

ENHANCEMENT OF HEAT TRANSFER IN SOLAR AIR HEATER USING POROUS MEDIA

Thesis

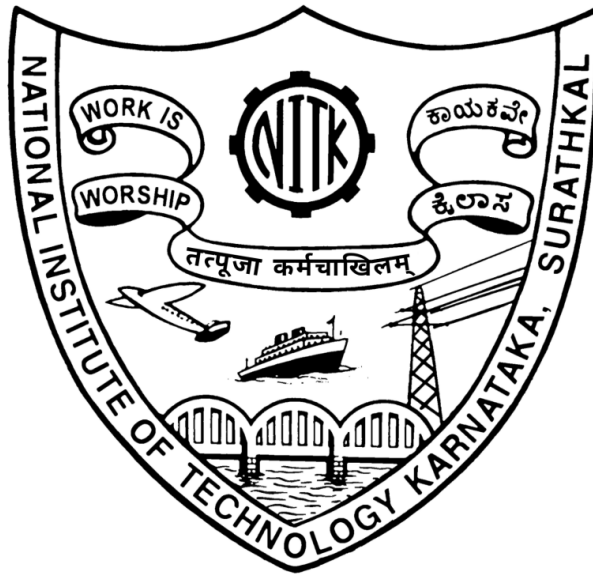
Submitted in partial fulfilment of the requirements for the degree of

DOCTOR OF PHILOSOPHY

by

RAWAL DIGANJIT SHASHIKANT

(207162ME027)



DEPARTMENT OF MECHANICAL ENGINEERING
NATIONAL INSTITUTE OF TECHNOLOGY KARNATAKA,
SURATHKAL, MANGALORE-575025

MAY 2024

ENHANCEMENT OF HEAT TRANSFER IN SOLAR AIR HEATER USING POROUS MEDIA

Thesis

Submitted in partial fulfilment of the requirements for the degree of

DOCTOR OF PHILOSOPHY

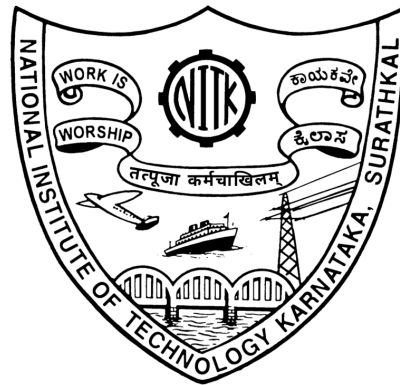
by

RAWAL DIGANJIT SHASHIKANT

(207162ME027)

Under the guidance of

Dr. N GNANASEKARAN



DEPARTMENT OF MECHANICAL ENGINEERING
NATIONAL INSTITUTE OF TECHNOLOGY KARNATAKA,
SURATHKAL, MANGALORE-575025

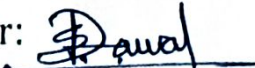
MAY 2024

DECLARATION

I hereby declare that the Research Thesis entitled “**ENHANCEMENT OF HEAT TRANSFER IN SOLAR AIR HEATER USING POROUS MEDIA**” which is being submitted to the **National Institute of Technology Karnataka, Surathkal** in partial fulfilment of the requirements for the award of the Degree of **Doctor of Philosophy in Mechanical Engineering** is a *bonafide report of the research work carried out by me*. The material contained in this Research Thesis has not been submitted to any other Universities or Institutes for the award of any degree.

Register Number: **207162ME027**

Name of the Research Scholar: **Rawal Diganjit Shashikant**

Signature of the Research Scholar: 

Department of Mechanical Engineering


Place: NITK Engineering

Date: 08/05/2024.

CERTIFICATE

This is to certify that the Research Thesis entitled “**ENHANCEMENT OF HEAT TRANSFER IN SOLAR AIR HEATER USING POROUS MEDIA**” submitted by **Mr. RAWAL DIGANJIT SHASHIKANT (Register Number:207162ME027)** as the record of the research work carried out by him, *is accepted as the Research Thesis submission* in partial fulfilment of the requirements for the award of the degree of **Doctor of Philosophy**.

Research Guide


08/05/2024

Dr. N Gnanasekaran

Associate Professor

Department of Mechanical Engineering

National Institute of Technology Karnataka, Surathkal


Chairman-DRPC

Department of Mechanical Engineering

National Institute of Technology Karnataka, Surathkal

Date: 08/05/2024.

ACKNOWLEDGMENT

It is my great pleasure to express my heartfelt gratitude to my research supervisor **Dr. N Gnanasekaran**, Associate Professor, Department of Mechanical Engineering, National Institute of Technology Karnataka (NITK), Surathkal, Mangalore, for his exemplary guidance and encouragement throughout my research work. He has been a constant inspiration with a keen interest in the progress of present research and valuable suggestions have increased my knowledge level, which led to the completion of my research work.

I am extremely grateful to our honourable director **Prof. Ravi B.** and former directors **Prof. Prasad Krishna** and **Prof. Udaykumar R. Yaragatti** for creating such assertiveness approach towards research for students. I am thankful to Professor **Prof. Ravikiran Kadoli** the Head, of the Department of Mechanical Engineering, for supporting and providing the facilities required for the successful completion of this research work. I take this opportunity to acknowledge the former HODs, Mechanical engineering, **Prof. Shrikantha S. Rao**, for their support and encouragement. It is an opportunity to thank the RPAC members, **Prof. Arun M.**, Professor, Department of Mechanical Engineering, **Dr. Ajay Kumar Yadav**, Associate professor, Department of Mechanical Engineering, and **Dr. Saumen Mandal**, Associate Professor, Department of Metallurgical and Materials Engineering for evaluating the work and their precise suggestions and extended support during my research work. I would like to convey my gratitude to **Dr. Kumar G N**, **Dr. Ranjith M.** and **Arumuga Perumal D** for the timely encouragement and knowledge they shared during my work. I express my earnest thanks to **Prof. Moghtada Mobedi**, Shizuoka University Japan for his valuable collaborative work and motivation during my research work.

I want to thank **Prof. Neelawar Shekar Vittal Shet** QIP coordinator of NITK Surathkal and **Prof. Arun Mohan Isloor**, former QIP coordinator of NITK Surathkal during the process of the academic and administrative process. I want to thank **Mr. Tushar** literate assistant CCE-QIP CELL and **Mr. Sarthak Shetty** literate assistant former QIP assistant for their kind support in executing the AICTE QIP process. Then, I would like to thank the non-teaching staff, **Avinash Devadiga**, **Vijaya K**, **Shubhavathi K**, **Nithyananda**, for providing all the facilities for my research work.

I would like to express my sincere thanks to All India Council for Technical Education (AICTE), Government of India, Department of Higher and Technical Education, Government of Maharashtra, Joint director of Technical Education Nashik Region for giving me an opportunity to carry out my research work at NITK under Quality Improvement Programme (QIP).

My special thanks to Principal and in charge Joint Director **Dr. Goraksh Vithoba Garje** for carrying out the research work and pursue Ph.D. at NITK. My deepest gratitude to former Principal and in charge Joint Director **Prof. Dyandev Nathe** for supporting and helping me in getting the deputation to pursue Ph.D. at NITK. I am extremely thankful to the department of Automobile Engineering, Government Polytechnic Nashik, Maharashtra, Faculty and non-teaching staff for providing the opportunity to carry out my research work at NITK. I also thank all the faculties of Government Polytechnic, Nashik for their kind words and constant support to pursue Ph.D. at NITK.

I feel happy to thank my Senior and friends **Dr. Anil Kadam, Dr. Parshuram R Chitragar, Dr. Shankar Katode, Dr. Harsha K, Dr. Banjara K, Dr. Narendran G, Dr. Anilkumar B C, Dr. Prakash Jadhav, Dr. Muthamil Selvan N, G Venkatapathy, Aditya Narkhede, Sayuj T** and list seems to be endless.

I bow down the feet of my parents **Shri. Shashikant Rawal** and **Smt. Vrushali Rawal** and my mother-in-law **Nita Rawal** for their continuous support for furnishing the needs to fulfil my wishes to achieve them. I would extremely thank my younger brother **Mr. Diganjay Rawal** and his family and my brother-in-law **Mr. Saurabh** for their valuable support with lot of joy.

Words cannot explain my gratitude to my wife, **Mrs. Vaishnavi** for supporting me and making my stay pleasant always. Finally, I wish to express my special thanks to all my family members, relatives, friends, and teachers who supported me throughout my life and made me reach this stage. I acknowledge with gratitude to all others who have helped directly or indirectly in completing my thesis successfully.

Rawal Diganjit Shashikant
Research Scholar (ME)

ABSTRACT

The solar air heater (SAH) is very much useful to dry the vegetables, fruits etc. It works on the basis of solar radiation available at the respective location. So, it saves the electricity i.e. reduces the dependency on the fossil fuel. SAH is easy to operate, simple in design. It has less maintenance. The limitations of the SAH are low thermal efficiency due to handling of large volume of air. Also, the air has low thermal capacity. Hence, this problem can be solved by using addition of different metal porous media of different porosities and pores per inch (PPI) inside the empty channel SAH.

Initially the empty channel rectangular domain single pass solar air heater (SPSAH) is designed analytically for 0.03 to 0.05 kg/s mass flow rates. The same has been validated with 2D geometry numerical study in ANSYS fluent software to observe the accuracy and performed the comparative study of thermal performance of SPSAH. Then, the discrete arrangement at equal distance of copper metal foam having thickness of 22, 44 and 88 mm of thicknesses with 10 ($\Phi=0.8769$), 20 ($\Phi=0.8567$), and 30 ($\Phi=0.92$) PPI has used to test the thermohydraulic performance parameter in order to enhance the heat transfer in SPSAH. The numerical study shows that the 22 mm thick metal foam is 5.02 % and 16.61 % higher THPP than 44 and 88 mm thick metal foam.

The 3D geometry further developed by Rosseland radiation model with solar ray tracing method has been used to account for solar radiation. Renormalization group (RNG) k-epsilon enhanced wall function with local thermal equilibrium (LTE) model has been considered to obtain the heat transfer characteristics in numerical study. Aluminium wire mesh samples with 3 ($\Phi=0.894$), 9 ($\Phi=0.812$), and 18 ($\Phi=0.917$) PPI has been used for numerical and experimental study. The configurations has been combined together to form graded wire mesh (GWM) including 3-9-18, 9-18-3 and 18-3-9 of 5 mm thickness for each wire mesh. The THPP of 9-18-3 PPI wire mesh are 13.04 % and 11.92 % higher than the other two cases. Later, 25 % of 9-18-3 GWM has been considered at four different locations, i.e. 0, 0.5, 1 and 1.5 m away from the inlet and analysed best location for efficient heat transfer. 1.5 m away from the inlet is the best location among the different locations. The experiment results of GWM at 1.5 m away from the inlet demonstrated 20.91 % and 23.32 % increase in thermal efficiency compared to empty channel for the 0.027 and 0.058 kg/s mass flow rates respectively.

Further investigations involve a comparative study of transverse arrangement of three layers of 9 ($\Phi=0.812$), and 18 ($\Phi=0.917$) PPI one over the another and same quantity of wire mesh of 50% is folded in the same direction. So, these combinations are (9-18, 18-9) T, (9-18, 18-9) L to obtain GWM in transverse and longitudinal direction, respectively. THPP of 9-18 L has an average of 2.45 % higher than all other combinations mentioned above. The thermal efficiency of 9-18 L has an average of 63.45 % higher than the empty channel for 0.05 and 0.08 mass flow rates. The GWM arrangement reduce the time of drying by 26.78 % and 55 % for tomato and onion respectively compared to empty channel SPSAH. The assessed simple payback period is 0.89 year which is shorter than lifespan of the SPSAH which is profitable. The present study was also focused on the solar panel battery operated fan and all the measuring instruments operated by battery which reduces the dependency on the external electric supply.

Keywords - Solar air heater, Discrete metal foam, Graded wire mesh, Thermal efficiency, Drying Onion and Tomato.

TABLE OF CONTENTS

Table of contents	i
List of Figures.....	ix
List of Tables	xvii
NOMENCLATURE.....	xix
CHAPTER 1	1
INTRODUCTION.....	1
1.1 SOLAR ENERGY.....	2
1.2 DETAILS OF SOLAR AIR HEATER	4
1.2.1 Advantages of Solar air heater.....	4
1.2.2 Applications of Solar air heaters	5
1.2.3 Importance of solar air heater	5
1.3 CLASSIFICATION OF THE SOLAR AIR HEATER.....	5
1.3.1 Selection parameters for enhancement of performance solar air heater.....	6
1.4 METAL POROUS MEDIA	8
1.4.1 Porosity (Φ).....	9
1.4.2 Permeability (K)	9
1.4.3 Form drag coefficient (C).....	10
1.4.4 Superficial velocity.....	10
1.5 FLOW THROUGH METAL POROUS MEDIUM.....	10
1.5.1 Darcy Law	10
1.5.2 Darcy Extended Forchheimer Law	11
1.6 HEAT TRANSFER THROUGH POROUS MATERIAL.....	11
1.6.1 Local Thermal Equilibrium Model.....	11

1.6.2 Local Thermal Non-Equilibrium Model.....	12
1.7 FRAMEWORK OF THESIS	13
CHAPTER 2.....	15
LITERATURE REVIEW	15
2.1 INTRODUCTION.....	15
2.2 EFFECT OF METAL FOAM as a POROUS MEDIA in solar air heater	16
2.2.1 Comparative study of metal foam and solid fin	16
2.2.2 Effect of addition of paraffin or nanofluids.....	17
2.2.3 Effect of different tilt angles of metal foam	18
2.3 EFFECT OF WIRE MESH POROUS MEDIA IN SOLAR AIR HEATER PERFORMANCE	20
2.3.1 Use of wire mesh in SPSAH.....	20
2.3.2 Use of wire mesh in DPSAH.....	22
2.3.3 Combined studies on single pass and double pass SAH	24
2.4 EFFECT OF ALTERNATIVE OPTIONS TO THE METAL FOAM AND WIRE MESH AS A POROUS MEDIA IN SOLAR AIR HEATER PERFORMANCE	25
2.5 APPLICATION OF WIRE MESH TO DRY THE VEGETABLES IN SOLAR AIR HEATER.....	25
2.6 OVERVIEW OF THE LITERATURE REVIEW	25
2.7 SUMMARY OF LITERATURE AND RESEARCH GAPS.....	40
2.8 MOTIVATION AND SCOPE OF THE PRESENT WORK.....	42
2.9 OBJECTIVES OF THE PRESENT RESEARCH WORK	43
2.10 CLOSURE.....	43
CHAPTER 3.....	45
RESEARCH METHODOLOGY	45
3.1 INTRODUCTION.....	45

3.2 PROBLEM STATEMENT	46
3.3 MATERIAL SELECTION AND DESIGN OF SINGLE PASS SOLAR AIR HEATER (SPSAH).....	47
3.4 DESIGN OF SPSAH BY ANALYTICAL METHOD	47
3.4.1 Assumptions considered during analytical method	50
3.4.2 Performance parameters of SPSAH for analytical method	51
3.5 TWO-DIMENSIONAL NUMERICAL DOMAIN, ITS BOUNDARY CONDITIONS AND GOVERNING EQUATIONS FOR SPSAH USING METAL FOAM.....	56
3.5.1 Details of geometry, meshing and boundary conditions	56
3.5.2 Governing equations and turbulent modelling considering LTNE method	59
3.5.3 Grid sensitivity analysis.....	61
3.6 THREE-DIMENSIONAL NUMERICAL DOMAIN, ITS BOUNDARY CONDITIONS AND GOVERNING EQUATIONS FOR SPSAH USING GAWM.....	63
3.6.1 Details of geometry, meshing and boundary conditions	63
3.6.2 Governing equations and turbulent modelling considering LTE method	68
3.6.3 Details of wire mesh as a porous media in SAH with its different arrangement and its geometrical parameters	72
3.6.4 Grid sensitivity analysis.....	75
3.7 THREE-DIMENSIONAL NUMERICAL DOMAIN, ITS BOUNDARY CONDITIONS AND GOVERNING EQUATIONS FOR SPSAH USING TRANSVERSE AND LONGITUDINAL DIRECTIONS OF GAWM.....	77
3.7.1 Details of wire mesh as a porous media in SAH with its transverse and longitudinal GAWM arrangements.....	77
3.7.2 Details of geometry, mesh generation and boundary conditions.....	78
3.7.3 Governing equations and turbulent modelling considering LTE method	81
3.7.4 Analysis of outlet temperature and pressure drop at different number of elements – evaluation of mesh refinement	81

3.8 EXPERIMENTAL SETUP	83
3.8.1 Experimental set up – details of 25 % of full-length test section at 1.5 m away from the inlet for the case 9-18-3 PPI of the GAWM	86
3.8.2 Experimental set up – details of 9-18 L GAWM (longitudinal direction 9-18 PPI AWM).....	90
3.9 PERFORMANCE PARAMETER FOR SPSAH.....	94
3.9.1 Evaluation of performance factor for the metal foam SPSAH in numerical method	94
3.9.2 Evaluation of Nusselt number, thermal efficiency and thermohydraulic efficiency of SPSAH in experimental method.....	95
3.9.3 Evaluation of exergy efficiency of SPSAH.....	96
3.9.4 Evaluation of moisture content and drying rate.....	96
3.9.5 Economic analysis	97
3.10 UNCERTAINTIES IN MEASUREMENT.....	98
3.10.1 Uncertainty for mass flow rate.....	98
3.10.2 Uncertainty for thermal efficiency	99
3.11 PRECAUTIONS CONSIDERED DURING THE NUMERICAL AND EXPERIMENTAL STUDIES.....	100
CHAPTER 4.....	101
NUMERICAL STUDY FOR ENHACEMENT OF HEAT TRANSFER USING DISCRETE METAL FOAM WITH VARYING THICKNESS AND POROSITY IN SPSAH BY LTNE METHOD.....	101
4.1 INTRODUCTION.....	101
4.2 VALIDATION OF ANALYTICAL AND NUMERICAL STUDY WITH PREVIOUS LITERATURE FOR SAME INPUT PARAMETERS.....	101
4.3 TEMPERATURE DISTRIBUTION AND VELOCITY DISTRIBUTION FOR DIFFERENT THICKNESS	103

4.4 VELOCITY DISTRIBUTION FOR DIFFERENT THICKNESS.....	103
4.5 EFFECT OF OUTLET TEMPERATURE AND ABSORBER PLATE TEMPERATURE	104
4.6 EFFECT OF NUSSELT NUMBER AND FRICTION FACTOR.....	107
4.7 EFFECT OF PERFORMANCE FACTOR AND DIFFERENT MATERIAL METAL FOAM	108
4.8 SUMMARY	109
4.9 CLOSURE.....	110
CHAPTER 5.....	111
THERMOHYDRAULIC EFFICIENCY OF A SOLAR AIR HEATER IN THE PRESENCE OF GRADED ALUMINIUM WIRE MESH – A COMBINED EXPERIMENTAL – NUMERICAL STUDY.	111
5.1 INTRODUCTION.....	111
5.2 VALIDATION OF NUMERICAL AND EXPERIMENTAL STUDY FOR SAME INPUT PARAMETERS.....	112
5.3 NUMERICAL RESULTS FOR DIFFERENT CASE STUDIES	113
5.4 COMPARATIVE STUDY OF TEMPERATURE RISE, NUSSELT NUMBER, FRICTION FACTOR, AND THPP	114
5.4.1 Effect of temperature rise and Nusselt number	114
5.4.2 Effect of friction factor and THPP	116
5.5 TEMPERATURE AND VELOCITY DISTRIBUTION IN THE 25 % LENGTH CASE AT A DISTANCE 1.5 M FROM THE INLET FOR SINGLE-PASS SAH.....	117
5.6 EXPERIMENTAL RESULTS OF EMPTY CHANNEL AND POROUS SAH.....	119
5.6.1 Thermal performance of porous bed SAH	119
5.6.2 Comparison of porous-bed SAH with empty-channel SAH	120
5.7 SUMMARY	122
5.8 CLOSURE.....	123

CHAPTER 6.....	125
ENERGY, EXERGY AND ECONOMIC ANALYSIS OF SOLAR AIR HEATER COMPARING DIFFERENT DIRECTIONS of GRADED WIRE MESH FOR DRYING ONION AND TOMATO.....	125
6.1 INTRODUCTION.....	125
6.2 VALIDATION OF NUMERICAL RESULTS WITH EXPERIMENTAL TESTING OUTCOMES.....	126
6.3 TEMPERATURE AND VELOCITY DISTRIBUTION FOR EMPTY CHANNEL AND 9-18 LONGITUDINAL GWM	127
6.4 Effect of DIFFERENT TRANSVERSE AND LONGITUDINAL POROUS ARRANGMENTS OF GWM in NUMERICAL STUDY	129
6.4.1 Effect of outlet temperature and Nusselt number	129
6.4.2 Effect of friction factor and THPP	131
6.5 EXPERIMENTAL OUTCOMES OF EMPTY CHANNEL AND 9-18 L GWM SAH	132
6.5.1 Effect of ambient temperature and solar radiation	132
6.5.2 Effect of rise in temperature and exergy efficiency	132
6.6 CHARACTERISTICS OF 9-18L GWM SAH WITH EMPTY CHANNEL SAH FOR DRYING THE ONION AND TOMATO.....	134
6.6.1 Effect of relative humidity.....	135
6.6.2 Effect of moisture content and moisture ratio and drying rate for empty channel and 9-18 L GWM SAH and open drying	136
6.7 ECONOMIC ANALYSIS.....	138
6.7.1 Annualized cost	138
6.7.2 Levelized cost of the dryer and simple payback period	139
6.8 SUMMARY	145
6.9 CLOSURE.....	145

CHAPTER 7.....	147
CONCLUSION and FUTURE SCOPE WORK.....	147
7.1 CONCLUSIONS.....	147
7.1.1 Significant outcome of numerical study for enhancement of heat transfer using discrete metal foam with varying thickness and porosity in SPSAH by LTNE method	147
7.1.2 Significant outcome of thermohydraulic efficiency of a solar air heater in the presence of graded aluminium wire mesh – a combined experimental – numerical study.	148
7.1.3 Significant outcome of energy, exergy and economic analysis of single pass solar air heater comparing transverse and longitudinal direction graded aluminium wire mesh for drying onion and tomato.....	149
7.1.4 Novel approach to scientific community.....	149
7.2 FUTURE SCOPE.....	150
7.3 CLOSURE.....	150
REFERENCES.....	151
LIST OF PUBLICATIONS based on Ph.D. research work	161
BIO-DATA.....	163

LIST OF FIGURES

Figure No.	Name of the Figure	Page No.
1.1	Under construction renewable energy source wise on March 2023 (Singh 2023b).	2
1.2	Uses of energy obtained from sun.	3
1.3	Schematic diagram of solar air heater (Sukhatme and Nayak 2018)	4
1.4	Selection parameters for enhancement of solar air heater	7
1.5	Metal foam porous media (a) Copper metal foam(Saedodin et al. 2017a) (b) Aluminium metal foam (Kamath et al. 2013) (c) Aluminium Wool (Sözen et al. 2021) (d) Aluminium Wire mesh available in the local market.	8
2.1	Details of the solar air heater study (a) Domain considered during testing as rectangular or circular, (b) Different metal porous media considered for the enrichment of thermal performance in solar air heater.	28
2.2	Different types of structures of single pass single glass solar air heater with different inlet and outlet shapes	29
2.3	Structure of the single pass and two glass cover for solar air heater	30
2.4	Different types of structures of double pass with single glass cover in SAH	30
2.5	Different types of structures of double pass with double glass cover in SAH	31
2.6	Different structures of the triple pass single glass cover of SAH	31
2.7	Literature of the different passes with single glass cover and double glass cover for single, double and triple pass studied papers	31
2.8	Different material used for the porous media (a) Metal foam, (b) Metal scrap, (c) Wire mesh	34
2.9	The thermal properties of the material used for metal porous media	34
2.10	Different arrangements of the porous media a) Parallel, b) Perpendicular and (c)Inclined to the absorber plate. (H is the height of the porous media and W is the width of the porous media)	35
2.11	Different arrangement of the porous media in the SAH (Parallel to absorber plate, perpendicular to absorber plate and Inclined to the absorber plate)	36

2.12	Different methodologies used by researchers to analyse the thermal performance of SAH.	37
2.13	Method of testing the thermal performance of SAH (a) Analytical Method, (b) Numerical Method	38
2.14	Comparison of the experimental studied of indoor and outdoor testing for single, double and triples SAH.	39
2.15	Effect of the mass flow rate and porosity on the thermal efficiency	39
2.16	Various aspects of heat transfer enhancement of solar air heater by metal porous media in the recent literature	40
2.17	Classification of method of drying products considered by metal porous media at recent studied literature	41
3.1.	Steps implemented to achieves the research objectives.	45
3.2.	Steps implemented to achieves the experimental objectives	45
3.3	Implementation strategy of the present research work	46
3.4	Significance of the selected material to manufacture the SPSAH	48
3.5	Detailed schematic layout of SAH: (1) wooden material for entrance section (in green line), (2) toughened glass (in yellow line), (3) Aluminium absorber plate (red line), (4) polyurethane foam (grey hatch line), (5) wooden material for exit section (green line), (6) M S steel stand for support (purple line), and (7) wooden material (green line) for the frame as an outer box of the solar air heater (all dimensions are in mm).	49
3.6	Two-dimensional geometry of SPSAH (a) empty channel, (b) 88 mm discrete metal foam at equal distances in the test section.	57
3.7	Schematic of SAH: (a) empty channel SAH, (b) 22 mm filled metal foam, (c) 44 mm filled metal foam (d) 88 mm filled metal foam in SPSAH.	57
3.8	Quadrilateral mesh of 88 mm metal foam block in solar air heater.	58
3.9	Layout of solar air heater with all its parts. (1) entrance section with PVC sheet (green colour line), (2) toughened glass (yellow colour line), (3) absorber plate (red colour line), (4) ceramic wool (grey colour hatch line), (5) exit section (green colour line), (6) support for SAH (purple colour	64

	line), and (7) base frame of SAH (green colour line); all dimensions are in mm.	
3.10	Numerical details of the 3D domain. (a) geometry of SPSAH for empty channel, (b) geometry of SPSAH for 9-18-3 PPI GWM with 25 % of the length of the WM full-length test section at 1.5 m from the inlet;	65
3.11	Quadrilateral mesh for 3D geometry for 9-18-3 PPI GWM with 25 % of the length of the WM full-length test section at 1.5 m from the inlet	65
3.12	Size and shape of Aluminium WM available on the local market. (a) diamond or expanded metal mesh—3 PPI, (b) diamond or expanded metal mesh—9 PPI, and (c) square mesh—18 PPI.	73
3.13	Detailed pictorial view of GWM arrangement in the channel of the SAH: (a) 3-9-18 PPI, (b) 9-18-3 PPI, and (c) 18-3-9 PPI.	74
3.14	Arrangement of WM in SAH. (a) empty channel, (b) case 1: 25% of the length of the WM of the full-length test section and at a distance of 0 m from the inlet, (c) case 2: 25% of the length of the WM of the full-length test section and at a distance of 0.5 m from the inlet, (d) case 3: 25% of the length of the WM of the full-length test section and at a distance of 1 m from the inlet, (e) case 4: 25% of the length of the WM of the full-length test section and at a distance of 1.5 m from the inlet, (f) case 9-18-3 PPI: WM with horizontal full length.	75
3.15	Grid-independence study for the empty channel and wire mesh at different nodes.	76
3.16	Geometry of 3D single pass SAH (a) empty channel SAH, (b) transverse graded wire mesh, (c) longitudinal graded wire mesh.	78
3.17	Quadrilateral meshing of SAH (a) the transverse graded wire mesh, (b) the longitudinal graded wire mesh type SAH	80
3.18	Schematic diagram of different arrangements of graded wire mesh (GWM) (a) 9-18 PPI transverse GWM, (b) 18-9 transverse GWM, (c) 9-18 longitudinal GWM, (d) 18-9 longitudinal GWM.	80
3.19	Variation in rise in temperature with change in number of mesh element at $Re = 4134$, Heat flux = 707 W/m^2 .	83

3.20	Flow chart for the experimental procedure	84
3.21	Details of the measuring instrument arrangement on the SPSAH (a) 1. PT 100 thermocouple for the ambient temperature (T_a), 2. for the inlet temperature (T_i), 3. for the outlet temperature (T_o), 4. for the temperature of the absorber plate at the inlet side (T_{absi}), 5. for the temperature of the absorber plate at the middle (T_{absm}), 6. for the temperature of the absorber plate at the outlet side (T_{abso}), 7. for the temperature of the glass at the inlet side (T_{gi}), 8. for the temperature of the glass at the middle (T_{gm}), 9. for the temperature of the glass at the outlet side (T_{go}), 10. Anemometer for measuring wind speed (WA), 11. Solar pyranometer (SPM), 12. Anemometer for measuring inlet air velocity (AA), 13. Pressure tap across the test section, i.e., at the inlet side (P_{in}) and at the outlet side (P_{out}), 14. Differential pressure transmitter (DPT), 15. Data logger (DL), 16. A 12 V DC fan, 17. A 12 V DC battery, 18. Solar panel (SP), 19. Charge controller. (b) Arrangement of PT 100 thermocouples kept on the glass and absorber plate (Kesavan et al. 2019; Rajarajeswari et al. 2018; Singh 2022).	89
3.22	Details of the experimental setup of SAH (a) front side view (b) backside view.	89
3.23	Weight of the product (a) Onion before drying, (b) Tomato before drying, (c) Onion after drying, (d) Tomato after drying.	92
3.24	A photo of the experimental set-up of SAH (a) front view, (b) back side view	93
4.1	Validation of analytical and numerical results of present empty channel SPSAH with (Rajarajeswari et al. 2018)	102
4.2	Contour of temperature for 30 PPI 0.92 porosity copper metal foam at 0.3779 velocity of (a) 22 mm, (b) 44 mm and (c) 88 mm thick metal foam.	103
4.3	Contour of velocity distribution for 30 PPI 0.92 porosity copper metal foam at 0.3779 m/s velocity for (a) 22 mm, (b) 44 mm and (c) 88 mm thick metal foam.	104
4.4	The temperature difference of the absorber plate and bulk mean temperature with varying the mass flow rate (a) Variation of temperature	106

	between absorber plate and bulk mean fluid temperature vs. mass flow rate.	
	(b) Variation of temperature between absorber plate and outlet temperature vs. mass flow rate. (c) Variation of a temperature difference between absorber plate and bulk fluid temperature for empty channel and 22 mm thickness 10 PPI 0.8769 porosity. (d) Variation of the temperature difference between absorber plate and outlet temperature for empty channel and 22 mm thickness 10 PPI 0.8769 porosity.	
4.5	Variation of (a)Nusselt number and (b) friction factor for different mass flow rates for different PPI and different thicknesses.	107
4.6	Variation of performance factors for different mass flow rates for (a) different PPI and different thicknesses, (b) different material.	108
5.1	(a) Variation in the rise in temperature with time. (b) Parity plot for validation of the thermohydraulic efficiency in numerical and experimental trials for the 0.027 kg/s and 0.058 kg/s mass flow rates.	112
5.2	Variation in the THPP vs. mass flow rate for the full length of 3-9-18 PPI, 9-18-3 PPI, and 18-3-9 PPI.	113
5.3	Comparison study between the 25 % length case at a distance of 0, 0.5, 1, and 1.5 m from the inlet for (a) temperature rise, (b) Nusselt number, (c) friction factor, and (d) THPP.	116
5.4	Temperature distribution of air for mass flow rate 0.027 kg/s and $I = 851.24 \text{ W/m}^2$ (a) along the plane and (b) in the 25 % length case at a distance 1.5 m from the inlet.	118
5.5	Velocity distribution of fluid for the 25 % length case at a distance 1.5 m from the inlet for mass flow rate 0.027 kg/s and $I = 851.24 \text{ W/m}^2$.	118
5.6	Variation in solar intensity and ambient temperature with time. (a) distribution of intensity of solar radiation during the experimental trials, (b) distribution of ambient temperature during the experimental trials.	119
5.7	Variation in the temperature difference with time for the empty channel and the 25 % length case at a distance 1.5 m from the inlet. (a) temperature rise parameter versus time of day, (b) temperature slip between the average absorber plate temperature and the outlet fluid temperature.	120

5.8	The variation in maximum thermal efficiency and maximum Nusselt number between the empty channel and the 25 % length case at a distance 1.5 m from the inlet.	120
6.1	(a) Validation of outlet temperature for numerical and experimental readings with varying the time for 0.05 and 0.08 kg/s mass flow rate on 17-05-2023 and 18-05-2023 respectively in empty channel SAH. (b) Parity plot for numerical and experimental outlet temperature result for 0.05 and 0.08 kg/s mass flow rate.	126
6.2	Temperature distribution of air at 0.35 m/s heat flux 707 W/m ² for (a) empty channel, (b) 9-18 L porous arrangement of GWM.	128
6.3	Velocity distribution of air at 0.35 m/s heat flux 707 W/m ² for (a) empty channel, (b) 9-18 L porous arrangement of GWM.	129
6.4	variation in outlet parameters for 9-18 T, 18-9 T, 9-18 L and 18-9 L arrangements of GWM at 0.05 kg/s and 0.08 kg/s (a) outlet temperature and Nusselt number, (b) friction factor and THPP	130
6.5	Variation of (a) ambient temperature, (b) solar intensity, (c) Temperature rise, and (d) exergy efficiency varying the time for 0.05 and 0.08 kg/s mass flow rate.	134
6.6	Variation in the Relative humidity of ambient, inlet and outlet humidity with respect to time for (a) 0.05 kg/s mass flow rate empty channel SAH, (b) 0.08 kg/s mass flow rate empty channel SAH, (c) 0.05 kg/s mass flow rate 9-18 L GAWM porous channel SAH, (d) 0.08 kg/s mass flow rate 9-18 L GAWM porous channel SAH.	135
6.7	Moisture content with drying time for (a) Onion and (b) Tomato for different mass flow rates in empty channel and 9-18 L GWM case	136
6.8	Effect of moisture removal varying with time for open sun drying, empty channel and 9-18 L GAWM for 0.05 and 0.08 kg/s mass flow rates.	137
6.9	Effect of drying rate with time for empty channel and 9-18 L porous channel varying mass flow rate	138

- 6.10 Colar of the Onion at different arrangement in (a) Onion before drying, (b) 142
Open Sun drying (c) empty channel SAH drying, (c) 9-18 L GAWM SAH
drying.
- 6.11 Colar of the Tomato at different arrangement in (a) Tomato before drying, 143
(b) Open Sun drying (c) empty channel SAH drying, (c) 9-18 L GAWM
SAH drying

LIST OF TABLES

Table. No	Name of the Table	Page No
2.1	Summary of analytical, numerical, and experimental investigations performed on SAH using metal foam by several researchers.	19
2.2	Common material used for wire mesh with its features.	32
2.3	Advantages and disadvantages of the different arrangements of the porous media	36
3.1	Material properties considered for simulation at 50 °C. (Fluent 2022; Kothandaraman and Subramanyan 2018; Rajarajeswari et al. 2018; Yadav and Bhagoria 2013).	50
3.2	Boundary conditions used during simulation in SAH (Rajarajeswari et al. 2018; Singh 2020; Singh et al. 2019; Sukhatme and Nayak 2018; Yadav and Bhagoria 2013).	58
3.3	Properties and its correlations of metal foam (Calmidi and Mahajan 2000; Jadhav et al. 2021).	62
3.4	Properties of Copper metal foam	62
3.5	Grid independent test.	62
3.6	Material properties considered for CFD analysis of the present SAH (Marin et al. 2019; Hu et al. 2013; Kothandaraman. and Subramanyan 2018; Nidhul et al. 2022; Parsa et al. 2021).	66
3.7	Boundary conditions used during simulation in the SAH.	67
3.8	Details of the Set up and solution in Numerical Study	71
3.9	Geometrical parameters of Aluminium wire mesh.	72
3.10	Results of grid-independence study for $Re = 11,544$.	76
3.11	Thermophysical and radiation properties of air and wire mesh (WM) (Kothandaraman and Subramanyan 2018).	79
3.12	Results of Grid study ($Re = 4134$, Heat flux = 707 W/m^2)	82
3.13	Specifications of SAH for experimental setup	85
3.14	The measuring instruments used during experimental trials	87

3.15	The measuring instruments used during drying application experimental trials	91
3.16	Uncertainties in measuring parameters during experimental work.	100
5.1	Comparison with previous similar type of rectangular single-pass SAH.	121
6.1	Average experimental measured reading of ambient temperature and solar intensity in the month of May 2023 for 0.05 and 0.08 kg/s mass flow rates.	133
6.2	Capacity of drying vegetables in kg per year	139
6.3	Capital cost of SPSAH (including GST, Labour and transportation charges)	140
6.4	Economic analysis of single pass solar air heater	141
6.5	Some comparative studies about development of capabilities of different solar air heaters and its drying application of Onion	143
6.6	Some comparative studies about development of capabilities of different solar air heaters and its drying application of Tomato	144

NOMENCLATURE

A_C	collector area in (m^2)
A_f	frontal area (m^2)
A_p	absorber plate area in (m^2)
a, b	constants for monthly average daily global radiation
a_{sf}	interfacial surface area (m^{-1})
C	Form drag coefficient or inertial coefficient (m^{-1})
C_C	capital cost of the SPSAH (Rs.)
C_m	total maintenance cost per year (Rs.)
C_O	total operational cost per year (Rs.)
C_p	specific heat of fluid (J/kg K)
C_r	the total cost of the raw material (Rs.)
D	depth of the porous bed (m)
D_h	hydraulic diameter (m)
d_f	fibre diameter (m)
d_p	pore diameter (m)
d_w	wire diameter (m)
EX_{in}	exergy inlet
EX_{out}	exergy outlet
ΔP	pressure drops across the collector (Pa)
f	friction factor
f_{WM}	friction factor of wire mesh
f_e	friction factor of empty channel
G_O	relative mass velocity
H	space between the absorber plate and glass (m)
h	heat transfer coefficient ($W/m^2 K$)
h_{sf}	interfacial heat transfer coefficient ($W/m^2 K$)
h_w	heat transfer coefficient for top cover ($W/m^2 K$)
I_T	total flux falling on a tilted surface at any instant (W/m^2)
J	Colburn j factor

K	permeability (m ²)
K _R	extinction coefficient
k _{air}	thermal conductivity of air (W/m K)
k _i	thermal conductivity of insulation material (W/m K)
L	length of the solar air heater (m)
L _C	loading capacity (kg)
L _f	life of the solar air heater (years)
L _W	labour cost per year (Rs.)
M _e	equilibrium moisture content (kg water/kg dry matter)
M _i	initial wet weight (kg)
MR	moisture ratio
M _t	instantaneous moisture content on wet basis at time 't' (kg water/kg dry matter)
ṁ	mass flow rate (kg/s)
N	pores per inch for WM
Nu	Nusselt number
Nu _{wm}	Nusselt number of wire mesh
Nu _e	Nusselt number of empty channels
n	day of the year
n _w	number of wire mesh layers
P	cost of the dried product per year (Rs.)
P _b	simple payback period (years)
P _{fan}	power of the fan (W)
P _K	packaging charges per year (Rs.)
Pr	Prandtl number
Pr _n	net profit of the product (Rs.)
P _S	product selling price in (Rs.)
P _t	pitch of wire mesh (mm)
P _W	the net weight of the product after drying per year (kg)
Q	volume flow rate (m ³ /s)
Q _s	rate of energy accepted by the absorber plate (W/m ²)

q	heat flux (W/m^2)
q_u	useful heat gain (W/m^2)
R_{air}	gas constant
Re	Reynolds number
Re_{df}	Reynolds number by fibre diameter
Re_{wm}	Reynolds number for wire mesh
r_h	hydraulic radius (m)
S	flux absorbed in the absorber plate (W/m^2)
T_a	ambient temperature ($^{\circ}\text{C}$)
T_{absi}	inlet side absorber plate temperature ($^{\circ}\text{C}$)
T_{absm}	middle side absorber plate temperature ($^{\circ}\text{C}$)
T_{abso}	outlet side absorber plate temperature ($^{\circ}\text{C}$)
T_{bm}	mean bottom plate temperature ($^{\circ}\text{C}$)
T_i	inlet temperature of the fluid ($^{\circ}\text{C}$)
T_o	outlet temperature of a fluid ($^{\circ}\text{C}$)
T_{pm}	mean plate temperature ($^{\circ}\text{C}$)
T_s	source temperature ($^{\circ}\text{C}$)
U	superficial velocity (m/s)
u	velocity of fluid (m/s)
V_{air}	average air velocity (m/s)
V_{sa}	salvage value per year (Rs.)
V_{∞}	wind velocity (m/s)
W	width of absorber plate (m)
w	total weight of the product (kg)
w_t	instantaneous weight of the product (kg)
w_d	weight of the dry product (kg)
η_{Ex}	exergy efficiency (%)
η_{fan}	fan efficiency (%)
η_{motor}	motor efficiency (%)
η_P	performance factor (%)

Greek symbols

Φ	porosity
α	absorptivity of the absorber plate
δ	declination
ε	emissivity of the material
β	slope of the solar air heater with the horizontal surface ($^{\circ}$)
ϕ	latitude of a location
λ_f	thermal conductivity of the fluid (W/m K)
k	thermal conductivity (W/m K)
ν	kinematic viscosity (m^2/s)
ρ	density of the fluid (kg/m^3)
$\bar{\rho}$	relative density of the diamond type of WM
τ	transmissivity of the cover system of solar air heater
τ_a	transmissivity obtained by considering only absorption
τ_r	transmissivity obtained by considering only reflection and refraction
μ	dynamic viscosity ($kg / m s$)
σ	Stefan Boltzmann constant

Subscript

abs	absorber
b	bulk mean fluid
f	fluid
i	inlet
max	maximum
o	outlet
s	solid

ABBREVIATIONS

1D	one dimensional
2D	two dimensional
3D	three dimensional

ANN	artificial neural network
CEA	current electricity authority
CFD	computational fluid dynamics
DAS	data acquisition system
DC	direct current
DEF	Darcy Extended Forchheimer
DPT	differential pressure transmitter
DPSAH	double pass solar air heater
DR	drying rate
FPSC	flat plate Solar collector
FDM	finite difference method
FVM	finite volume method
GAWM	graded Aluminium wire mesh
GI	Galvanized iron
LTE	local thermal equilibrium
LTNE	local thermal nonequilibrium
MATLAB	matrix laboratory
MC	Moisture content
MF	metal foam
MNRE	Ministry of New and Renewable Energy
MR	moisture ratio
MS Excel	Microsoft Excel
MS	Mild steel
NSEFI	National Solar Energy Federation India
PT100	Platinum 100
RTD	resistance temperature detector
PPI	pores per inch
PVC	polyvinyl chloride
RNG	Renormalization Group
SECI	solar energy corporation India
SPM	solar pyranometer

SPSAH	single pass solar air heater
SS	Stainless steel
SWH	solar water heater
T.I.	turbulent intensity
TPSAH	triple pass solar air heater
WM	wire mesh

CHAPTER 1

INTRODUCTION

The growth of the people and technology are very huge and very fast now a days. So, to compete the progress of people and technology, the utilisation of conventional fuels is very high with respect to the use of electrical appliances, food preservation devices etc. Production of electricity and heat are associated with burning of fossil fuels. It causes maximum unwanted gas emissions. Traditional method to supply electric current to rural or urban areas are created with the help of coal, oil, or gas, which generate carbon dioxide and nitrous oxide –that are greenhouse gases. As a result, the global earth surface temperature increases. So, reducing the dependency on fossil fuels and more utilisation of solar energy is a good solution to reduce the greenhouse gases.

The vision of the solar energy corporation India (SECI) limited is to make ‘Green India’ by utilizing ample solar radiation and to accomplish energy safety, protection for the country and the mission is to become the leader in the development of a greater number of solar installations. The mission of the Ministry of New and Renewable Energy (MNRE) India is energy security, more contribution to clean power, attainability and clearness, bareness and affordability. This mission is important to produce the progress in the solar energy utilization, formation of different solar systems to make the alternate option as alternate fuels and reduce the dependency on oil usage (MNRE Government of India 2023). According to the study entitled ‘Global market outlook for solar power 2023-2027’ with emphasize on South East Asia the installation done by the India is 17.4 GW approximately and stood in third position (Singh 2023a). The target of the National Solar Energy Federation of India (NSEFI) for yearly basis is to add at least 20 GW solar capacity every year. The main target of India is to achieve the 280 GW goal by 2030. India set a target to install an overall range of 4,886 MW of small solar power plants. India has also set the following targets for 2030: 1) Satisfy 50 % of energy need from renewable energy, 2) Achieve a non-fossil fuel range of 500 GW, 3) Diminish

carbon emissions by 1 billion tons, 4) Minimize the carbon intensity by 45 % (MNRE Government of India 2023).

1.1 SOLAR ENERGY

Solar energy is huge and inexhaustible form of energy. It is an unpolluted, uncontaminated good energy. It is unrestricted and convenient in enough quantities in almost all habitable parts of the world. The Sun transfer energy to the earth without medium which is beneficial for making any process. Hence, solar energy is easy to use and potential to process in the system. Solar energy has potential for all the available and upcoming energy demands across the globe on a regular support. The power of the Sun on the earth is approximately of the order of 1.8×10^{11} MW. This is thousand times more than the available rate of consumption on the earth of complete industrial energy roots (Garg and Prakash 2016; Sukhatme and Nayak 2018). According to announcement of the central electricity authority (CEA), India established renewable energy capacity more or less 125.16 GW. This shows that the India government has arranged to complete 500 GW of renewable energy capacity at the termination of 2030 (Singh 2023b).

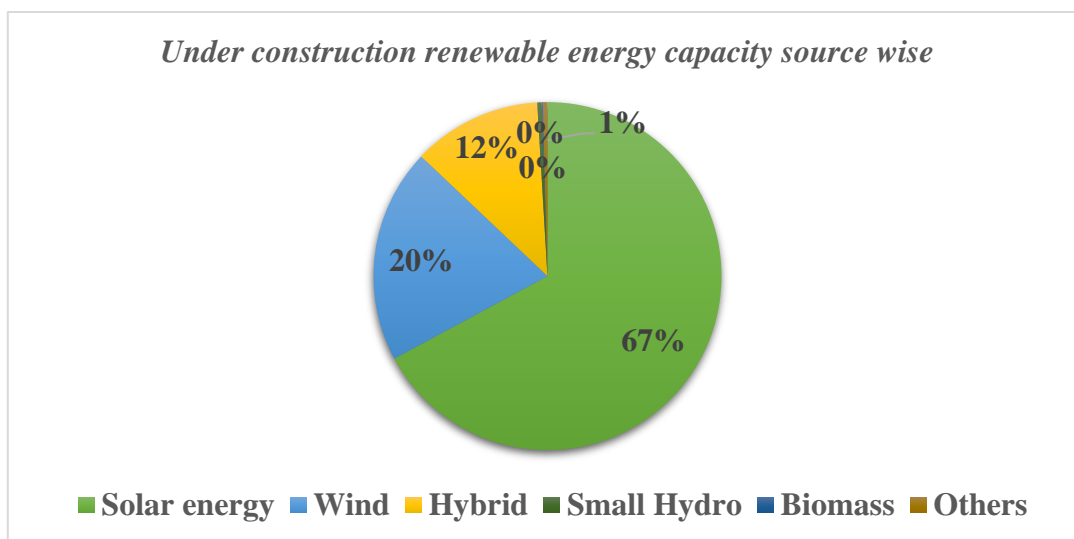


Figure 1.1 Under construction renewable energy source wise on March 2023 (Singh 2023b).

The source wise renewable energy which is under construction is shown in the Figure 1.1. Also, the use of sun for different applications is shown in the Figure 1.2. The applications shown in the Figure 1.2 are the alternative options for saving electricity and reduce the undesirable emissions i.e., reduce the carbon content in an environment. The maximum operating temperature for thermal collection devices is 40-100 °C, 40-130 °C, 40-90 °C, 10-400 °C and more than 400 °C for liquid flat plate collectors, evacuated tube collectors, solar air heaters, cylindrical parabolic concentrating collectors and paraboloid concentrating collectors, respectively (Sukhatme and Nayak 2018).

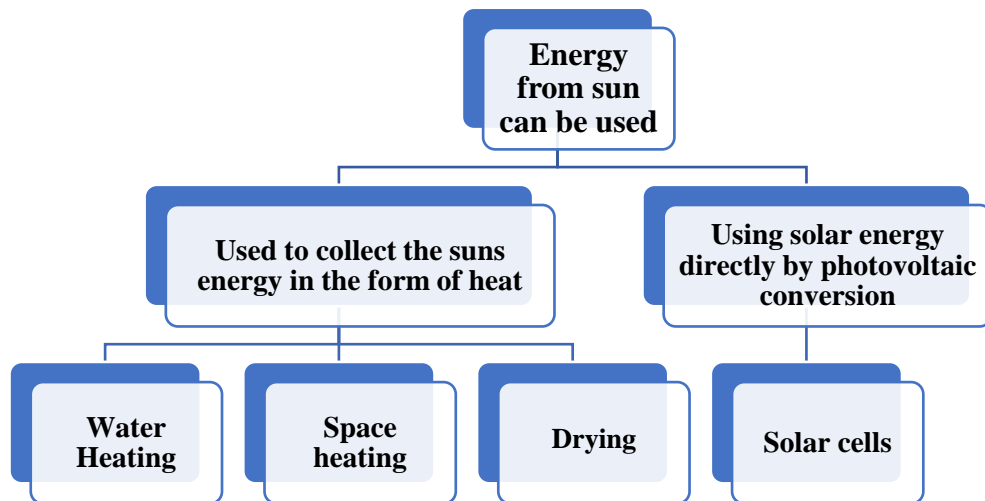


Figure 1.2 Uses of energy gained from sun.

The solar air heaters (SAH) have air as a working fluid. It is also available freely and easy to use. The operating temperature is lower compared to the other solar applications like solar water heaters, evacuated tube collectors, parabolic trough collectors. Therefore, the material required to carry the temperature is accessible with low-cost materials in comparison with other solar energy devices. Hence, the price of the solar air heater is less compared to other solar systems. The solar air heaters have less corrossions and lesser leakages in case of solar water heaters. The SAH does not need particular examination or observation for temperature lower than 0 °C (Sukhatme and Nayak 2018).

1.2 DETAILS OF SOLAR AIR HEATER

The *basic parts* that make up a conventional solar air heater (Garg and Prakash 2016; Sukhatme and Nayak 2018) are

- 1) The absorber Plate – a flat absorbing sheet, mostly metallic, on which the solar intensity arrived in different ways and it, adds more heat.
- 2) The transparent blanket (one or two sheet) – Glass, to diminish the heat loss in upward direction from the absorber plate.
- 3) The collector box – waterproof container to enclose the above components.
- 4) Thermal insulation contributed to diminish the heat losses at the rear and border of the absorber portion.

1.2.1 Advantages of Solar air heater

- It takes advantages of both beam and diffuse solar radiation. It has easy and non-movable design so that it requires little maintenance.
- It absorbs direct, diffuse, and reflected portion of solar radiation.
- It is stable in tilt and orientation and, thus there is no requirement of tracking the sun.
- It operates at comparatively high efficiency.

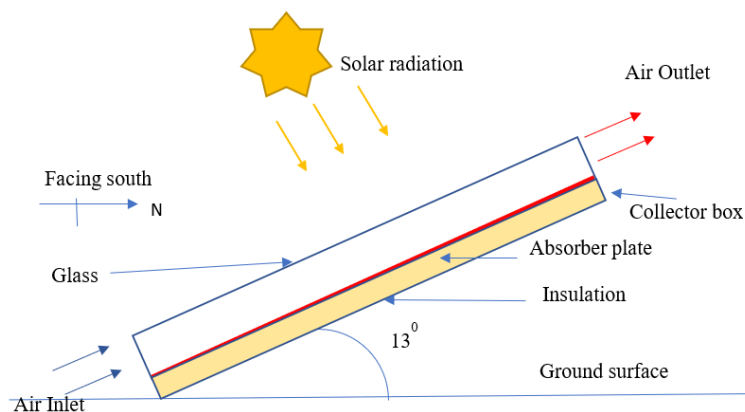


Figure 1.3 Simplified sketch of solar air heater (Sukhatme and Nayak 2018)

1.2.2 Applications of Solar air heaters

- Drying of vegetables, fruits etc.
- Factory or commercial heating operations
- Space heating purpose

1.2.3 Importance of solar air heater

Open sun drying having many disadvantages like dust dirt particles and pollution affects the quality of the products, rain, storm and dew can drop down the quality and quantity of drying, Animals and birds can spoil the drying product. Open sun drying is slower drying time process and time required is also more.

Secondly the device like Oven and heaters consumes more power and are costly. They require more skilled person and required maintenance time to time on scheduled basis. So, to overcome the above problems , solar air heater is the best option that consumes less maintenance with quality products can be obtained by designing a proper single pass solar air heater. By carefully choosing different parameter for drying the products such as average drying temperature, humidity, location etc. the SAH becomes more effective.

1.3 CLASSIFICATION OF THE SOLAR AIR HEATER

The solar air heater can be sorted according to its number of passes. The types are single pass, double pass with counter flow or parallel flow, triple pass etc. More the passes, more heat exchange takes place in channel. Air moves through channel twice or thrice in double or triple pass solar air heater. Double and triple pass improves the heat gain and finally more rise in temperature. Further, it can be classified according to number of covers. The covers of toughened glasses are useful to carry the solar radiation towards the absorber plate. As the number of covers increases, the value of products of transmissivity and absorptivity decreases. Thus, solar intensity absorbed by the absorbed plate is less so, heat gain is less when number of covers increase. Also, addition of more covers decreases the thermal efficiency (Sukhatme and Nayak 2018). Hence, single transparent cover is beneficial to make the model with selective absorber plate surface.

Considering above points, the single pass solar air heater has poor heat transfer coefficient between the absorber sheet and the working fluid. As a result, its efficiency is low. The solar air heater works only in daytime. It is less efficient in the rainy season. The downside of solar energy is that different solar intensity with time. Different solar intensity occurs daily because of the day night cycle and seasonally because of the earth's orbit about the sun. This change takes place at a specific location because of the local climatic conditions. The energy must be stored when the sun is gleaming. Further, it can be used when it is not obtainable. The requirement for storage also includes significantly to the cost of any system (Sukhatme and Nayak 2018). Hence, this lower efficiency can be enhanced by inserting roughened or longitudinal fins, baffles with different angles, metal porous media etc. There are plenty of materials used for enhancing the thermal efficiency of solar air heater. For example, fins, perforated sheet, wire mesh, metal foam, spherical marble balls etc. The porous material has benefits such as light in weight, higher surface area compared to solid fins, the intricate network of openings allows for better heat exchange with nearby fluid. Also, metal porous media ensure more uniform heat delivery across the surface, preventing localized hotspot.

1.3.1 Selection parameters for enhancement of performance solar air heater

Solar air heater is designed on the basis of design, operational, meteorological and environmental parameters. Some major parameters are listed below which influence the performance of solar air heater.

Selective surfaces – it should be desirable that the selective surface should absorb the maximum solar intensity coming from Sun. It must have less emissivity. The black paint to absorber plate is very much useful to absorb the maximum solar radiation. It is mostly the metal sheet with Al, GI or steel with thickness ranges from 0.5 to 1 mm.

Number of covers – More the number of transparent covers, lower the solar intensity absorbed by the absorber plate. So single transparent cover is more useful to obtain the optimum result of heat absorption by the absorber plate. It is mostly toughened glass and now days multiwall polycarbonate sheet is more common as a transparent cover.

Insulation – The insulation materials are preferably glass wool, ceramic wool, rockwool etc with thickness ranges from 5 to 8 cm.

Spacing – The spacing between the glass and the absorber plate must reduce the convective heat transfer coefficient.

Collector tilt- the angle of tilt of SPSAH is equal to the latitude of the location so that the absorber plate will absorb more solar intensity.

Collector area – The face area of the SPSAH should range from 1 to 2 m².

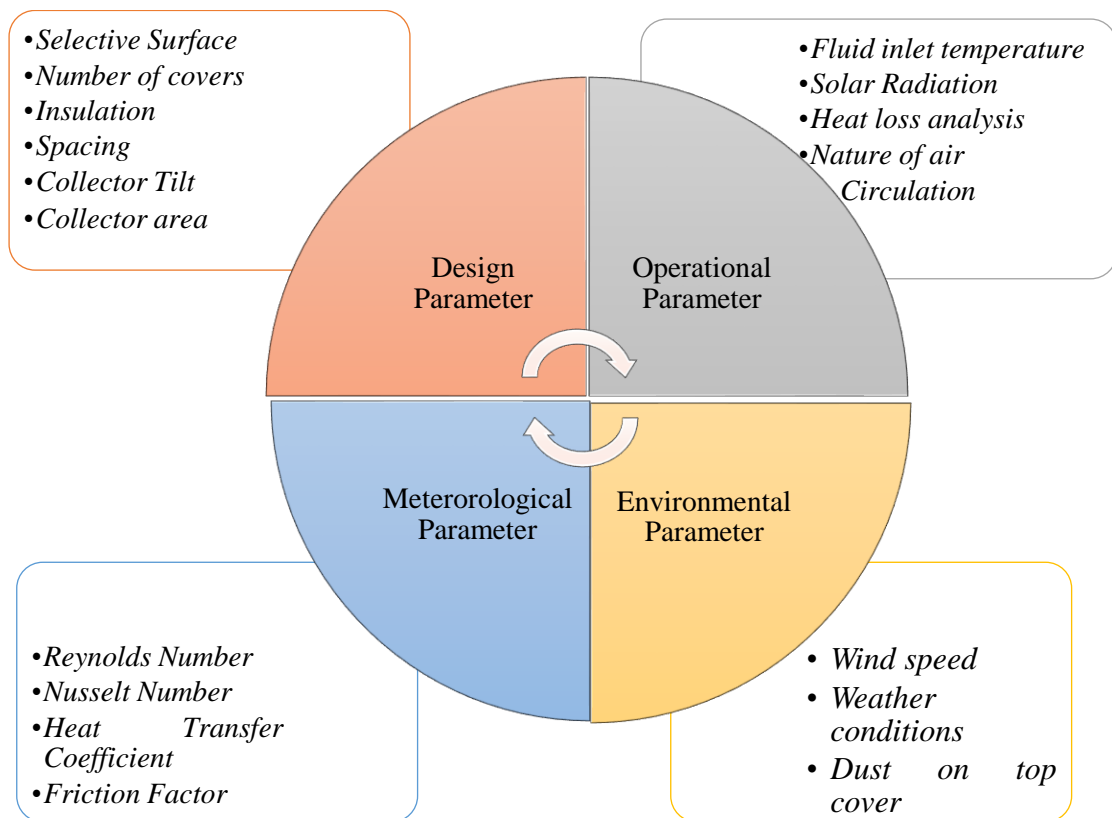


Figure 1.4 Selection parameters for enhancement of solar air heater

The operational parameters for enhancement of thermal performance of SPSAH are fluid inlet temperature, solar radiation, heat losses from the top cover, and nature of circulation of air. The SPSAH should work on lower fluid inlet temperature so that the top loss coefficient, temperature difference and heat loss will get reduced which increases the thermal efficiency of SPSAH. The nature of air circulation should be forced circulation to control the air flow as per requirement and to increase the thermal efficiency.

The environmental parameter for designing the SPSAH is dust on the transparent cover which should be less. Hence, regular cleaning of the glass is required. The test should run on sunny days to get maximum output of SPSAH.

The metrological parameters for analysis of performance of SPSAH are the heat transfer coefficient, Nusselt number which must be high and friction factor should be low so that thermohydraulic performance parameters will be high.

1.4 METAL POROUS MEDIA

A porous media is known as substance having of solid matrix with proximate, adjacent and varying gaps. The fluid moves via opening of the porous region, in elementary single-phase motion of openings are overloaded with particular fluid. The solid phase of the porous region may be firm, or it may undergo minor change in structure or shape. The examples of genuinely accessible porous substance are seashore sand, rye bread, sandstone etc. (Narashimhan 2020)

The metal porous media is available in the form of metal foam, wire mesh, steel balls, iron chips, etc. The pores per inch and the porosity are the measurement parameter considered during the manufacturing of the metal porous region. The applications of the metal porous region are useful to extract the heat in different thermal devices.

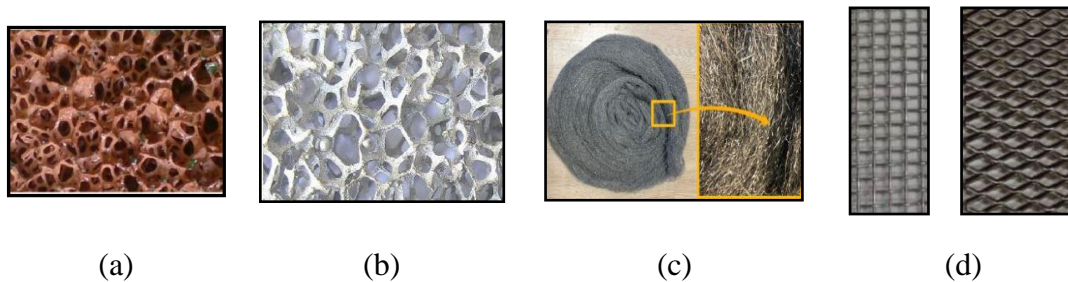


Figure 1.5 Metal foam porous media (a) Copper metal foam(Saedodin et al. 2017) (b) Aluminium metal foam (Kamath et al. 2013) (c) Aluminium Wool (Sözen et al. 2021) (d) Aluminium Wire mesh available in the local market.

Metal foam is used in heat exchangers, vertical channel, air plane, missiles, solar applications like solar water heating systems, solar air heaters, solar fuel cells, parabolic

trough collectors to enhance the heat exchange rate and to obtain the desirable output. Similarly, it is used in vehicle heaters or exhaust systems, gas turbines, energy utilization in different commercial processes such as heating systems, combined heat and power systems etc. Likewise, the wire mesh as a porous media is also useful in solar air heaters, solar distillation, solar cookers etc. Other than that, it is mostly used in civil area for constructing the buildings, as a fencing to walls etc.

1.4.1 Porosity (Φ)

It is known as the ratio of complete void volume to the entire volume of the porous region. Similarly, the surface porosity is known as the ratio of void area to the total area.

$$\Phi = \frac{V_{void}}{V_{total}} = 1 - \frac{V_{solid}}{V_{total}} \quad (1.1)$$

The metal porous media have the porosity from zero to 100 % and PPI varies as per requirement of the application in Industry. The porosity contributes noteworthy part in the forecast of variation in the pressure over the porous media (Narashimhan 2020).

1.4.2 Permeability (K)

It is known as the potential of the porous substances to enable the fluid to progress between the porous region. It depends on the porosity as well as appearance or formation of the porous structures. It is obtained from the Darcy law. The unit is in m^2 . The permeability of the porous region can be determined from experimental difference in the inlet and outlet pressure or mathematical expressions specified by numerous researchers for novel and new types of porous medium (Narashimhan 2020).

$$K = U \frac{\mu \Delta x}{\Delta P} \quad (1.2)$$

where U is known as the superficial velocity, μ is taken as the dynamic viscosity of the fluid and $\frac{\Delta P}{\Delta x}$ is considered as the pressure gradient across the porous region thickness.

The permeability of basic or easy geometries are determined by mathematical formula as given in Eqn. (1.3) as

$$K = d_p^2 \Phi^3 / 180(1 - \Phi)^2 \quad (1.3)$$

where d_p is known as fibre diameter or wire diameter in case of metal foam and wire mesh respectively. The constant 180 is considered from the most appropriate fit of observational facts and information which is tested by different experimental trails.

1.4.3 Form drag coefficient (C)

The Form drag coefficient depends on the construction and shape of the fibre or wire diameter and solid shape of the porous medium (Narashimhan 2020). Theoretically one can calculate the form drag coefficient by using Eqn. 1.4 as given below,

$$C = (\Delta P_f / L) / \rho u_p^2 \quad (1.4)$$

Where ΔP_f is pressure drop due to form drag.

1.4.4 Superficial velocity

The superficial velocity is the product of porosity and the average velocity of the fluid over the porous volume (Narashimhan 2020).

$$U = \Phi \bar{U} \quad (1.5)$$

Where \bar{U} is the average velocity of the fluid over the volume V_f

1.5 FLOW THROUGH METAL POROUS MEDIUM

1.5.1 Darcy Law

The elementary governing law of fluid flowing through the porous region is Darcy's law represented in Eqn. (1.6). It shows that the fluid flow rate through the porous region is proportional to pressure gradient and viscosity of the fluid over a given span (Narashimhan 2020).

$$\nabla P = - \frac{\mu \bar{u}}{K} \quad (1.6)$$

The Darcy law is authoritative only for small velocity incompressible and isothermal movement.

1.5.2 Darcy Extended Forchheimer Law

It is the addition of Darcy principle and states the inertial effects of the fluid motion, which interprets the form drag coefficient or inertial resistance coefficient as represented in Eqn. (1.7). The form drag coefficient depends on the inside construction of porous material, porosity and pore dimensions as per (Narashimhan 2020).

$$-\nabla P = \frac{\mu \vec{u}}{K} + \frac{\rho C}{\sqrt{K}} |\mathbf{u}| \mathbf{u} \quad (1.7)$$

Where C is called as form drag coefficient (Forchheimer coefficient).

1.6 HEAT TRANSFER THROUGH POROUS MATERIAL

There are two thermal models available for the prediction of heat exchange through the porous medium (i) local thermal equilibrium model (LTE) and (ii) local thermal non-equilibrium model (LTNE) (Narashimhan 2020). The local thermal non equilibrium model assumes that the medium and the fluid flow are not in thermal equilibrium in the porous medium. In this case temperature gradient is present between the solid and fluid interface. So, additional terms used in this method are interfacial area density and heat transfer coefficient between the solid and fluid phases in porous media. So, LTNE model accounts the effect of porosity and pore diameter. Further, the local thermal equilibrium considers the solid and fluid temperature gradient is zero. The conduction flux in the porous medium uses an effective conductivity and the transient term includes the thermal inertia of the solid region on the medium.

1.6.1 Local Thermal Equilibrium Model

Local thermal equilibrium model accepts that the solid and fluid parts of the porous region are in thermal equilibrium i.e., $T_s = T_f = T$. The net heat exchange between the stages of the porous medium is nothing i.e., nil since the heat conduction in both stages carried out synchronously.

$$\text{For solid} \quad (1 - \Phi)(\rho c)_s \frac{\partial T_s}{\partial t} - (1 - \Phi) \nabla \cdot (k_s \nabla T_s) + (1 - \Phi) q_s''' = 0 \quad (1.8)$$

For fluid
$$\Phi(\rho c_p)_f \frac{\partial T_f}{\partial t} + (\rho c_p)_f U \cdot \nabla T_f = \Phi \nabla \cdot (k_f \nabla T_f) + \Phi q_f''' \quad (1.9)$$

$$(\rho c)_{\text{eff}} \frac{\partial T}{\partial t} + (\rho c)_f U \cdot \nabla T = \nabla \cdot (k_{\text{eff}} \nabla T) + q_{\text{eff}}''' \quad (1.10)$$

where
$$(\rho c)_{\text{eff}} = (1 - \Phi)(\rho c)_s + \Phi (\rho c_p)_f \quad (1.11)$$

$$k_{\text{eff}} = (1 - \Phi) k_s + \Phi k_f \quad (1.12)$$

$$q_{\text{eff}}''' = (1 - \Phi)q_s''' + \Phi q_f''' \quad (1.13)$$

1.6.2 Local Thermal Non-Equilibrium Model

The local thermal non-equilibrium model thinks about the rise in temperature or drop at the fluid and solid area of the porous region. The heat exchange between the fluid and solid regions is evaluated by the convection condition exhibited in Eqn. (1.14) and (1.15) (Calmidi and Mahajan 2000).

For solid

$$(1 - \Phi)(\rho c)_s \frac{\partial T_s}{\partial t} = (1 - \Phi)\nabla \cdot (k_s \nabla T_s) + (1 - \Phi) q_s''' + h_{\text{sf}} a_{\text{sf}} (T_f - T_s) \quad (1.14)$$

For fluid

$$\Phi(\rho c_p)_f \frac{\partial T_f}{\partial t} + (\rho c_p)_f U \cdot \nabla T_f = \Phi \nabla \cdot (k_f \nabla T_f) + \Phi q_f''' + h_{\text{sf}} a_{\text{sf}} (T_s - T_f) \quad (1.15)$$

Where, interfacial surface area and heat transfer coefficient is described as (Mahmoudi and Karimi 2014)

$$a_{\text{sf}} = 6(1 - \Phi)/d_p \quad (1.16)$$

Interfacial heat transfer coefficient

$$Nu_{\text{sf}} = 2.0 + 1.1 \text{Pr}^{\frac{1}{3}} \text{Re}_p^{0.6} \left(\frac{\Phi d_p}{d_h} \right)^{0.6} \quad (1.17)$$

d_h is the pore scale hydraulic diameter in m.

1.7 FRAMEWORK OF THESIS

Chapter 1 narrates brief introduction about the current scenario of solar energy, different solar thermal systems, its applications, preface of solar air heaters, their types, importance of porous media and applications.

Chapter 2 is related with comprehensive and expository review of solar air heater with metal porous materials. It contains completely filled and partially filled porous material in solar air heater with different configurations. Also, it includes the study of different PPI and porosity of porous media as well as its thermohydraulic performance on solar air heater system. Moreover, this chapter includes the overview of the literature as well as research gaps, motivation and scope of the study. The objectives of the presented research works are also mentioned in this chapter.

Chapter 3 details the analytical, computational and experimental studies of solar air heater including and excluding porous materials to accomplish the objectives. The detailed information of geometry, meshing, material properties, boundary conditions, solution and set up are disclosed in this chapter. Also, dimensions of the experimental set up, measurement procedure, performance parameters for analysis revealed for the single pass solar air heater including and excluding porous materials.

Chapter 4 discussed about two-dimensional study of single pass solar air heater with or without metal foam. The arrangement of three different thicknesses of porous media is kept at equal distances in the single pass solar air heater. The thermohydraulic performance parameters are evaluated on the basis of different PPI and porosity. Also, three different materials are introduced for evaluation of thermohydraulic performance parameters.

Chapter 5 presents the computational and experimental studies of the partially filled graded aluminium wire mesh. Three unlike aluminium wire meshes are studied for heat transfer enhancement in the SPSAH. The numerical study is investigated with four different locations of the 25 % of entire-length of test section of the wire mesh. The Nusselt number, thermohydraulic performance parameters studied in detail for different location. The heat transfer enhancement in SAH are observed by comparing temperature rise in the empty channel and the GAWM SAH.

Chapter 6 represents the exergy, energy and economic analysis of the transverse and longitudinal direction of GAWM. The two different wire meshes are arranged in the transverse and longitudinal direction to obtain it GAWM. The thermohydraulic performance parameters are calculated for the four different configurations. The best model from the four types was considered for the experimental study. The empty channel and GAWM channel drying rate are compared for two different mass flow rates experimentally. The simple payback period is calculated for the present model.

Chapter 7 emphasizes the supreme and important conclusion of the current work. Future work is also mentioned in this section.

CHAPTER 2

LITERATURE REVIEW

2.1 INTRODUCTION

India is an agricultural nation which transport enormous amount of farming products. Solar energy is easy to use and anyone can use to produce electricity, to dry products like vegetables and fruits etc. Hence, the maximum utilisation of solar energy is more important in order to reduce the use of fossil fuel as well as dependency over the conventional commercial resources. The open sun drying has many drawbacks and problems like effect grime, smoke, insects or animals which reduces the quality of the drying products. Also, open sun drying is a lengthy, prolonged process. The alternative for this is electric ovens. But it has many downsides like dependency on electricity, skilled worker required to operate it. The maintenance is also high. The electricity production with fossil fuels creates unwanted gases which is harmful to environment. Therefore, the solar air heater (SAH) is the best option to dry products like vegetables, fruits etc. It reduces the usage of electric heaters, ovens etc. The cost of SAH is low; anyone can operate it, and maintenance is also low. The single-pass solar air heater has fewer parts and is simple to design and operate. It is made of one absorber plate, transparent cover, insulation and outer frame. The air flows through the space between the glass and the absorber plate. First, solar radiation falls on the glass which is coming from the Sun. It transmits through the glass cover and reaches the absorber plate. Due to the black paint of the absorber plate, it absorbs more radiation and gets heated. The air flows over the absorber plate, and absorbs heat from it. Therefore, the outlet temperature is higher than the inlet temperature of the fluid. This higher outlet temperature is used for drying the vegetables and the fruits which is useful to make powder and used for the eating purpose in different recipes. Hence, it can be handy, convenient, profitable for rural and non-rural areas across the world.

The efficiency of the solar air heater can be upgraded by inserting metal porous media, solid fins, baffles, novel extended surfaces or corrugated or wavy absorber plates in the entire channel of the system with different configurations. Many researchers are gaining

the awareness and curiosity on the metal foam and wire mesh as porous media to enhance the heat transfer rate and to make the system effective. They observed the system using fully filled and partially filled, changing the PPI and porosity of the porous media.

The solar air heater performance can be evaluated on the basis of different mass flow rate, which shows the type of fluid flow. Also, it depends on the Reynolds number. The researchers investigated the Nusselt number, friction factor to observe the thermal performance parameter. Further, many researchers focused on the thermal efficiency, exergy efficiency to check the moisture removal rate.

2.2 EFFECT OF METAL FOAM AS A POROUS MEDIA IN SOLAR AIR HEATER

The metal foam as porous media is used to enhance the heat transfer in solar air heater. The different combinations have been studied by different researcher in the previous studies. The main focus of the researchers is to increase the heat transfer and reduce the friction factor in order to increase the thermal performance parameter of the SAH. The different arrangements of thickness, PPI and porosity have introduced to evaluate the thermal efficiency and thermohydraulic performance parameter of SAH. Some researchers studied the different angular positions of metal foam, addition of nanofluids, paraffin etc. to observe the increase in temperature of SAH. These studies have compared mainly with the solid fin or without metal foam condition in order to observe the percentage increase in the thermal efficiency of SAH. The detailed summary of different configurations of metal foam have been explained as follows –

2.2.1 Comparative study of metal foam and solid fin

(Dukhan and Quinones 2003) observed that the effective conductivity and heat transfer of porous Aluminium metal foam is more than a solid fin by 4 % and 1.5 %, respectively. They considered 10, 20 and 30 PPI with the porosity of 95 % Aluminium metal foam for heat transfer enhancement in SAH. Further, it has been observed that the number of pores per inch increases when heat transfer is more for the same porosity.

(Naphon 2005) described that the addition of porous media in DPSAH improves the thermal efficiency 25.9 % compared to the empty channel DPSAH. The author used

implicit method of finite difference method to obtain the results. (Mancin et al. 2012) studied the experimental heat transfer coefficient and pressure drop for five different copper metal foam samples. They noticed that heat transfer coefficient was more for higher mass flow rate and that pressure drop reduced with reduced porosity. The copper metal foam with 10 PPI and 0.905 porosity was found to be the best option for electronic cooling applications compared to 5, 20, and 40 PPIs and different porosities. (Xu et al. 2014) studied the effect of LTE/ LTNE model including porous media in SAH numerically. The author obtained the porous fin with LTE model, which is more beneficial and useful in judging the performance. (Bayrak and Oztop 2015) studied the thermal performance of a solar air heater with Aluminium metal at different thicknesses experimentally. They concluded that the 6 mm thickness Aluminium metal foam has higher efficiency than 10 mm thickness metal foam for 0.025 kg/s mass flow rate. It is noted that Aluminium metal foam gives better results than empty channel solar air heater for the same velocity and heat flux conditions. (Jouybari and Lundström 2020) done the thermal and thermohydraulic investigation of SAH using Aluminium Oxide (Al_2O_3) ceramic porous media with 90 % porosity. The author reported five times increase in the thermal and thermohydraulic performance compared to without porous media SAH. (Kansara et al. 2021) performed experiments in FPSC with internal fins and porous media. The authors showed that porous media has the highest heat transfer compared to fins and conventional SAH.

2.2.2 Effect of addition of paraffin or nanofluids

(Chen et al. 2010) performed thermal performance analysis using combination of 90 % porosity aluminium metal foam and paraffin. The addition of foam increases the temperature up to 20 °C than without foam. (Jouybari et al. 2017) experimentally investigated the use of metal foam with the addition of nanofluid to improve thermal performance. The performance evaluation criteria are to reduce the pressure drop and increase the heat transfer. With the help of metal foam and nanofluid, the performance evaluation criteria increased more than 1 % for lower flow rate and thermal efficiency increases by 8.1 %. Further, the increase in nanofluid concentration increases the performance evaluation criteria. (Baig and Ali 2019) proposed an experimental study on thermal storage in solar air heaters with the help of paraffin wax combined with

Aluminium metal foam. The analysis included four different configurations: flat plate, two copper ducts, four copper ducts, and the fourth configuration as a flat plate with pre-heat. Usage of two and four copper ducts leads to more heat transfer than the other two configurations. A maximum efficiency of 97 % was achieved with the help of a flat plate pre-heat configuration without a fan and with the help of Aluminium foam and paraffin wax.

2.2.3 Effect of different tilt angles of metal foam

(Hussien et al. 2019) investigated the thermohydraulic performance of SAH with three types of metal foam configurations. The corrugated metal foam gives higher thermal and effectiveness efficiencies, rather than longitudinal and staggered. A high heat transfer rate obtained for a higher PPI. (Farhan et al. 2020) performed a comparative study on the solid fin and metal foam. These types were further arranged in longitudinal, staggered, and corrugated configurations to check the heat transfer enhancement rate. It was noticed that the corrugated arrangement gives more heat transfer than other arrangements. Also, it was observed that the exergy loss and efficiency depend on the solar intensity and the velocity of air flowing through the channel. (Taha and Farhan 2021) reported the thermal performance of SAH with herringbone porous metal foam. They kept foam at an angle of 30°, 60° and 90° for 0.01 to 0.05 m³/s mass flow rate. The author obtained highest thermal efficiency up to 87.7 % for 0.04 m³/s mass flow rate at 30° foam angle. (Mutar and Alaiwi 2023) studied the thermal efficiency of SPSAH using copper metal foam at an angle of 0° and 45° to the absorber plate and at four equal distances. The thermal efficiency is 51 % higher for 45° angle compared to 0° angle of metal foam to the absorber plate.

Hence from above all different configurations, the metal foam is found to be very useful for enhancement of heat transfer in solar air heater. Table 2.1 show Summary of analytical, numerical, and experimental investigations performed on SAH using metal foam by several researchers.

Table 2.1 Summary of analytical, numerical, and experimental investigations performed on SAH using metal foam by several researchers.

Ref.	Methodology, LTE/LTNE	Mass flow rate	Metal foam Material, (PPI)	Porosity	Type of arrangement of metal foam in SAH	Major outcomes compared with empty channel
(Dukhan and Quinones 2003)	Theo- 1D, NM	3.66 m/s	Al 10,20, 30	0.95	Horizontal	Heat transfer 4 times higher
(Chen et al. 2010)	Expt. and Num- 2D, LTE	-	Al, NM	0.90	Horizontal	Temperature rise 20 °C
(Bayrak and Oztop 2015)	Expt., NM	0.016, 0.025	Al, NM	NM	Vertical – Staggered	$\eta_{th} = 37 - 77 \%$
(Jouybari et al. 2017)	Expt., LTE	0.5 to 1.5 lit/min	Cu, 20	0.93	Horizontal	Improvement in $\eta_{th} = 8.1 \%$
(Baig and Ali 2019)	Expt., NM	-	Al, NM	NM	Horizontal	Max. $\eta_{th} = 97 \%$
(Hussien et al. 2019)	Expt., NM	0.01	Cu, 15, 20	NM	Fin longitudinal corrugated staggered	Max. $\eta_{th} = 86 \%$ (corrugated)
(Farhan et al. 2020)	Expt., NM	0.011 to 0.059	Cu, NM	NM	longitudinal corrugated, staggered	. $\eta_{ex} = 44 \%$
(Taha and Farhan 2021)	Expt., NA	0.01 to 0.05	Herringbone, 10	0.9	Corrugated angle	Max. $\eta_{th} = 87.7 \%$
(Jouybari and Lundström 2020)	2D Num. and Expt., LTE	Re= 4000 to 6000	Al ₂ O ₃ ceramic, NM	0.9	Horizontal	Thermal performance 5 % higher
(Kansara et al. 2021)	2D Num. and Expt., LTNE	0.0151, 0.0225, 0.0301, 0.0377	Al, NM	0.92	Horizontal	Temperature rise 16.17 % higher
(Mutar and Alaiwi 2023)	Expt., NA	0.0125, 0.025, 0.045	Cu, NM	NM	Angle with absorber plate is 0° and 45° .	Max. $\eta_{th} = 94.8 \%$ for MF = 45°

* NM = not mentioned

2.3 EFFECT OF WIRE MESH POROUS MEDIA IN SOLAR AIR HEATER PERFORMANCE

2.3.1 Use of wire mesh in SPSAH

2.3.1.1 Outdoor experimental trials and its findings in SPSAH

(Chiou et al. 1965) studied thermal performance of SAH by unidirectional, counter flow, cross flow arrangement of wire meshes. The author observed that the upper losses are less and thermal efficiency is high in unidirectional arrangement of wire mesh compared to counterflow and cross flow arrangement of wire mesh. The air is first travel with wire meshes and makes contact with the wire mesh upper surfaces. Hence the temperature is higher in unidirectional case. (Gupta and Garg 1967) investigated thermal performances of SAH with G I and Aluminium corrugated sheet and wire meshes. The author performed comparative study of G I, iron and Aluminium expanded metal screen. The corrugated type and wire mesh construction obtained 60 % and 50 % higher efficiency respectively. (Sharma et al. 1991) concluded that higher porosity with more transverse pitch achieved lowest outlet temperature compared to its lower porosity with lower transverse pitch. (Ahmad et al. 1996) studied thermohydraulic performance including iron wire screen matrices as absorber. The porosity of iron matrices for conducted experiment from 0.823, 0.946 and 0.968. The author observed thermohydraulic efficiency decreases with increase in the porous height to element size ratio and wire mesh porosity. (Varshney and Saini 1998) developed the heat transfer and friction factor correlations for rectangular domain SAH with ($\Phi = 88$ to 95 %) wire mesh. The author observed heat transfer coefficient and friction factor relies on the geometrical details of matrices. The correlations introduced for Colburn J factor and friction factor which is depends on heat transfer coefficient. The author considered six different porosity of wire meshes to develop the correlation. Similarly, (Thakur et al. 2003) developed heat transfer and friction factor interdependence for low porosity ($\Phi = 66.7$ to 88 %) WM porous SAH. (Prasad et al. 2009) concluded that the enhancement of efficiency of SAH is controlled by the mass flow rate and the porosity of wire mesh. The author observed that the heat transfer coefficient is more for lesser porosity of wire mesh. The author observed that the number of layers of wire mesh increases in the channel, then porosity decreases. It will give more tortuous flow in the channel. In the same time heat transfer area for passing the air is minimum, which gives higher

turbulence. Hence the temperature increases. (Velmurugan and Ramesh 2011) improved the thermal efficiency by 5 % using low carbon steel wire mesh at different mass flow rates. (Adnan Abed et al. 2017) studied the V type and U type porous absorber in solar air heater experimentally and mathematically. He observed that the V type is more effective in clear days compare to U type. He also notices that the U type is more effective at the time of sunrise and sunset.

(Devecioğlu et al. 2018) studied the thermal efficiency, thermohydraulic efficiency and exergetic efficiency of SAH using Copper wire mesh as porous media for different tilt angle and mass flow rate. The author observed that higher the mass flow rate, lower the tilt angle of solar air heater which gives better thermal and exergetic efficiencies of SAH. (Rajarajeswari et al. 2018) investigated numerical study on wire mesh and validation with experimental results. The diagonal arrangement of two wire mesh ($\Phi = 84.5$ and 92.5 %) improves thermal efficiency about 5–17 % and 5–20 %, respectively, with the mass flow rate ranging from 0.01 kg/s to 0.055 kg/s. (Sözen et al. 2020) studied thermal efficiency of tubular type SAH inserting iron wire mesh. The author noted that thermal efficiency increased by 11 % compared to without wire mesh. Further the same author studies the effect of Aluminium wire mesh. (Sözen et al. 2021) tested Aluminium wool as porous media in SAH. The author obtained 56.30 to 71.32 % average thermal efficiency. (Singh 2022) investigated the thermal performance of SAH with serpentine wavy WM. The thermohydraulic performance is 186 % higher than the conventional smooth channel.

2.3.1.2 Indoor experimental trials and its findings in SPSAH

Some researchers studied the thermal performance of SAH using indoor testing. (Luampon et al. 2019) reported the thermal efficiency of SAH with stainless steel wire mesh. The author obtained 5.10, 16.75 and 34.81 % more thermal efficiency than without wire mesh for 4, 8 and 12 PPI respectively. (Mahdi et al. 2021) investigated experimentally the performance enhancement criteria with insertions of copper wire mesh. The author obtained the 315 % increase in heat transfer coefficient by copper wire mesh. (Krittacom et al. 2022) studied heat transfer enhancement of SAH by inserting Stainless steel wire mesh. The author examined and noted that Nusselt number, friction factor and thermal enhancement factor (TEF) can be improved by

inserting Stainless steel wire mesh. (Mund et al. 2023) studied heat exchange and frictional performance of impinging jet integrated with wire mesh attached to the absorber sheet. The maximum efficiency is about 53.65 % at Re 4913.

2.3.1.3 Analytical and numerical trials and its findings in SPSAH

The thermal performance of SPSAH improved by many researchers using different analytical and numerical tools. The thermal efficiency is improved by (Singh and Panwar 2013), (Verma and Varshney 2015), (Chouksey and Sharma 2016), (Sharma et al. 2017) using the C++ language, (Ghritlahre and Prasad 2018) using ANN technique. (Singh and Panwar 2013) reported thermal performance of SAH by different thermal conductivity of wire meshes like Iron, Brass and Copper. He found that the thermal performance changes due to porosity and extinction coefficient of wire mesh. It is less depending on thermal conductivity of material for same porosity of different material because radiant energy absorption is small in this case. (Chouksey and Sharma 2016) observed that the more porous height decreases the heat transfer coefficient by increasing heat transfer area. This is due to less amount of conduction and radiation takes place at lower portion of porous bed. Hence air temperature is minimum. (Sharma et al. 2017) observed that the energy efficiency is directly proportional to mass flow rate and exergy efficiency is inversely proportional to mass flow rate.

2.3.2 Use of wire mesh in DPSAH

2.3.2.1 Outdoor experimental trials and its findings in DPSAH

The researchers performed the outdoor testing for DPSAH. The thermal efficiency are increased by 20 to 25 % and 30 to 35 % by making counter flow (Ramani et al. 2010), 72 to 85 % by using 2, 4 and 6 fins (El-khawajah et al. 2011), 11 to 17 % higher in counter type compared to parallel type of air movement (Dhiman et al. 2012), 80 % maximum thermal efficiency in serpentine packed bed wire mesh (Singh et al. 2019) compared to the without porous media double pass solar air heater.

2.3.2.2 Indoor experimental trials and its findings in DPSAH

(Sopian et al. 1999) introduced and reported that more outlet temperature and thermal efficiency by the second or lower channel compared to first or upper channel. (Ho et al. 2013) reported improvement in the DPSAH using wire mesh as a porous media by theoretically and experimentally. The author worked on SPSAH, DPSAH and DPSAH

with recycle ratio for 0.0107, 0.0161 and 0.0214 kg/s mass flow rates at different solar flux. The author noticed that the overall performance of the DPSAH is directly proportional to the recycle ratio. The excellent results of the DPSAH with wire mesh inserts are obtained at 0.5 to 1 recycle ratio to obtain a supreme overall performance of the system. (Velmurugan and Kalaivanan 2015) performed energy and exergy analysis of solar air heater by experimentally and theoretically. He compared result by finned plate dual pass SAH, roughened plate dual pass SAH, single pass flat plate SAH and wire mesh dual pass SAH. He further concluded that the v corrugated wire mesh arrangement is best among all other configurations. The wire mesh with V type arrangement in lower channel has turbulence intensity due to that heat transfer area increases, also path length increases. Hence the effect of rise in temperature at top cover is less so reduces the top losses.

(Singh and Dhiman 2018) studied the recycle type DPSAH. The wire mesh at the inserted above the absorber plate, and making flow arrangement like recycle flow, flow between two glass cover and compared the thermal and thermohydraulic efficiency. The thermal efficiency is higher for the air flow between glass and porous media compared to only porous media which is 81 to 86 %. Further, the author extended the work with wavy channel absorber plate with porous media. (Singh et al. 2019) The thermal efficiency of wavy channel with porous media is obtained 27 % more than the empty channel. (Jalil and Ali 2021) investigated the thermal efficiency using stainless steel and steel wool experimentally. The thermal efficiency more when the porous media is in lower channel. For lower porosity, air flow is less. Due to this, it increases the air path flow to remain in the porous media. Hence it gets higher temperature and the thermal efficiency increases.

2.3.2.3 Analytical and numerical trials and its findings in DPSAH

(Kumar 2012) studied the thermal performance of DPSAH using the counter and parallel flow type arrangement. The author reported that the counter pass is better than the parallel pass for the similar mass flow rates. The thermal efficiency is 90 % and 84 % for counter and parallel pass DPSAH. (Dehghan et al. 2015) studied the steady state model by semi analytically and finite difference method by numerically to observe the

thermal performance of porous media in the system. The author reported that the heat transfer can be improved using cellular porous media.

2.3.3 Combined studies on single pass and double pass SAH

(Mittal and Varshney 2006) observed that 0.937 porosity is best wire mesh for thermal performance of solar air heater among the 0.887, 0.902, 0.937, 0.939 and 0.958 porosity of wire meshes. The author further observed that the performance changes due to porosity but geometrical parameters of wire mesh acts as a measure role to change the thermal performance of it. (Omojaro and Aldabbagh 2010) evaluated the thermal performance of SAH using fins and steel wire mesh as an absorber plate for single and double pass. The author observed that the double pass is very much effective than single pass. The rise in temperature between outlet temperature and inlet temperature is higher in double pass than single pass due to preheating takes place in first channel then it goes to second channel. (Aldabbagh et al. 2010) studied the experimentally with the added wire mesh as a porous media. The author obtained 83.65 % higher efficiency with help of wire mesh and without including absorber plate.

(Singh 2020) extends his work and studied the same experiment with single and double pass SAH with serpentine wavy wire mesh with range of porosity is 85 % and 95 %. The enhancement with serpentine wire mesh is 24.33 % higher than flat wire mesh with the help numerical results. (Güler et al. 2020) studied numerically and experimentally double pass solar dryer without wire mesh and with iron wire mesh. The author concluded that the effect of wire mesh is positive and it reduces the time of drying the pepino fruit. (Chouksey et al. 2022) studied the woven wire mesh as porous media to enhance the heat transfer in SAH. The author optimizes the depth of bed using two-dimensional partial differential equation and their exact analytical solution. The results show that 15- and 22-mm depth of bed is good for the 0.0241 and 0.0248 m/s velocity. The maximum increase in efficiency for wire mesh SAH is 44 % and 54 % compare to conventional SAH. (Nowzari et al. 2021) reported the 30 mm, 50 mm and 70 mm bed heights for wire mesh porous solar air heater. The author also studied the comparison counter flow and single pass SAH with same bed height. The author noticed that the 70 mm bed height has maximum pressure drop in both the cases. The counter flow has 5.6

to 9.7 % higher efficiency than single pass in all the bed height. The efficiency is higher for 30 mm bed compared to 50 mm and 70 mm in single pass and counter flow SAH.

2.4 EFFECT OF ALTERNATIVE OPTIONS TO THE METAL FOAM AND WIRE MESH AS A POROUS MEDIA IN SOLAR AIR HEATER PERFORMANCE

Many researchers used metal porous media other than wire mesh to upgrade the working of solar air heater. (Mishra and Sharma 1981) used iron chips, Aluminium chips and pebbles, (Gill et al. 2012) used iron chips, (Tiwari et al. 2013) used iron chips to improve the overall operation of the solar air heater. The increase in the thermal efficiency is around 24.81- 32.85 %, 24.07 - 45.05 %, 55.3 - 70.3 % respectively.

2.5 APPLICATION OF WIRE MESH TO DRY THE VEGETABLES IN SOLAR AIR HEATER

The research shows the effectiveness of solar air heater using WM to dry the vegetables. The solar air heater has been used to dry tomatoes with the help of GI WM by (Rajarajeswari and Sreekumar 2014), potatoes with help of three different passes adding sand and wire mesh in it by (Kesavan et al. 2019), pepino with help of iron mesh by (Güler et al. 2020), carrot with help of iron mesh by (Sözen et al. 2020), onion with help of Aluminium wool by (Sözen et al. 2021), Teucrium polium with the help of iron wool porous plate adding PCM material by (Jahromi et al. 2023).

2.6 OVERVIEW OF THE LITERATURE REVIEW

The arrangement of metal foam as a porous media in SPSAH with partially filled is studied by (Bayrak et al., 2013; Bayrak and Oztop, 2015; Hussien et al., 2019; Jouybari and Lundström, 2020; Kansara et al., 2021; Mutar and Alaiwi, 2023; Saedodin et al., 2017). The authors investigated that; the metal foam is the best option to increase the heat transfer rate in SPSAH. In the recent literature different arrangements of MF, such as the different thicknesses of Al MF by staggered and sequence type (Bayrak et al. 2013; Bayrak and Oztop 2015), changing the thicknesses of MF from the absorber plate and insulation side (Saedodin et al. 2017), changing the corrugated, staggered and longitudinal arrangement of MF (Hussien and Farhan 2019), by arranging thin layer of MF at the top side (Jouybari and Lundström 2020), comparing fin and foam of different materials (Kansara et al. 2021), making 0° and 45° angle of MF to the absorber plate

(Mutar and Alaiwi 2023), were executed to increase the heat transfer rate in the SAH. The author improved the thermal efficiency of SPSAH on an average 20 to 60 % more than the empty channel using metal foam.

Another porous media is WM which is easily available in the local market which has cheaper price compared to MF. The recently studied literature shows that the wire mesh is useful and significant changes occurred to increase the thermal efficiency of SPSAH.

The author used different porosities of WM and also different material of WM to increase the thermal performance of SAH. For increasing the outlet temperature at the outlet of SAH, the author used fully filled single type of WM in the SPSAH of different porosities such as 87.5 to 95.3 (Sharma et al. 1991), 82.3 to 96.8 (Ahmad et al. 1996), 88.7 to 96 (Varshney and Saini 1998), 66.7 to 88 (Thakur et al. 2003), 68 to 80.3 (Tian et al. 2004), 88.7 to 96 (Mittal and Varshney 2006), 62 to 81.6 (Prasad et al. 2009, 2021), 82.3 to 89.6 (Singh and Panwar 2013), 87.5 to 95.3 (Chouksey et al. 2022; Sharma et al. 2017). The thermal efficiency increases due to these WM from an average 20 to 79 % compared to without filling of WM.

The fully filled WM has disadvantages like the increase in the pressure drop, so friction factor increases and finally lower the thermal performance. Hence, to reduce the pressure drop and saving the material cost, some researcher performed the optimization study for the partially filled WM in the SPSAH. The porosities used to improve the thermal efficiency of SPSAH are the same which are mentioned as above.

Similarly, certain researchers have investigated the insertion of a partially filled wire mesh with different orientations to improve the thermal performance of single-pass SAHs. Single-pass SAHs produced a better rise in temperature at the outlet by inserting a partially filled wire mesh in a number of studies: (Abed et al. 2017) utilised a 'U'-type arrangement of Aluminium wire mesh and compared it with 'V'-type soft steel wire mesh as a corrugated absorber; (Devecioğlu et al. 2018) utilised a Copper wire mesh at four equal distances in the vertical direction, i.e., keeping perpendicular to the absorber plate; (Ghritlahre and Prasad 2018) and (Rajarajeswari et al. 2018) utilised a mesh in the diagonal direction lower side at the inlet and upper side at the outlet of an SAH; (Sözen et al. 2020) utilised an Iron wire mesh, keeping at 100 mm equal intervals

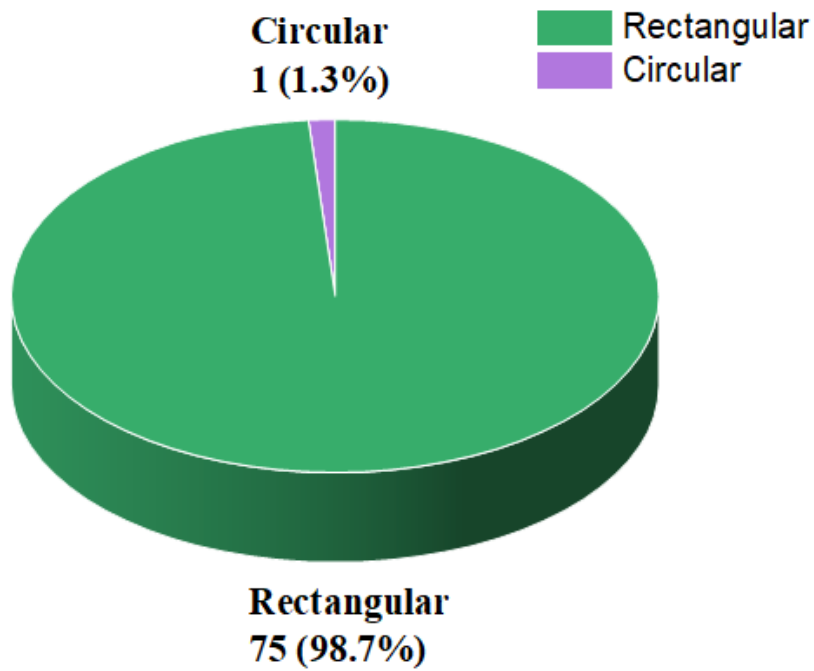
of distance perpendicular to the absorber plate; and (Jalil and Ali 2021) utilised steel wool and six layers at equal distances of stainless steel wire mesh, which improved the thermal performance of a SPSAH.

Recently, a partially filled wire mesh inserted into a SPSAH by different authors has been found to enhance the thermal efficiency. The thermal efficiency improved by 34 % to 82 %, keeping the wire mesh in vertical direction at four equal distances, in a study by (Devecioğlu et al. 2018); by 15 % to 88 % using a Copper wire mesh of different porosity in a study by (Rajarajeswari et al. 2018); and by 59.94 % to 67.69 % using an Iron mesh with hollow-tube SAH in a study by (Sözen et al. 2020). Similar improvements of 79.83 % and 76 % are found with steel wool and stainless-steel wire mesh, respectively, in a study by (Jalil and Ali 2021); and improvements of 56.32 % to 71.30 % for Aluminium wool are observed in a study by (Sözen et al. 2021), measuring the energy efficiency of SPSAH.

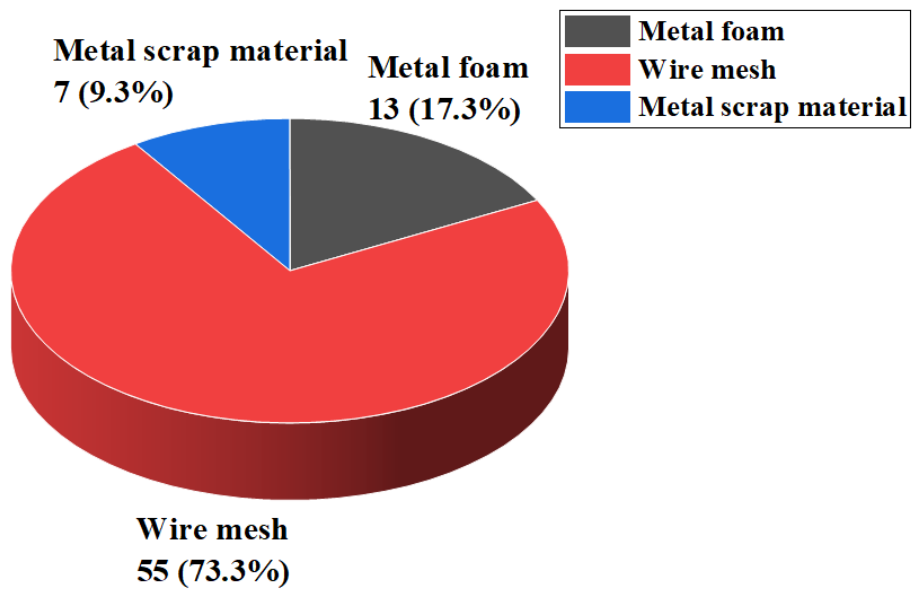
The arrangements of the WM are performed by different authors such as horizontal direction above the absorber plate in (Rajarajeswari and Sreekumar 2014), diagonal direction lower side at inlet and upper sides at outlet in (Chiou et al. 1965; Ghritlahre and Prasad 2018; Rajarajeswari et al. 2018), “V” type shape in (Abed et al. 2017), “U” type shape in (Abed et al. 2017), perpendicular to the absorber plate in (Krittacom et al. 2022; Sözen et al. 2020). The researchers noted that the average increase in the efficiency is from 15 to 88 % compared to empty channel SAH.

Figure 2.1 (a) show the geometrical domain considered for the SAH with metal porous media. The literature shows that rectangular domain is easy to design and develop. The rectangular model is easy to manufacture and simple in construction. Also, anyone can make it as per desirable dimensions. Figure 2.1 (b) shows the maximum study is performed with the help of wire mesh as porous media to enhance the heat transfer rate in the SAH.

The rectangular SAH is further categorised as single pass, double pass and triple pass SAH with metal porous media. This number of passes of SAH also grouped as single glass cover or double glass cover for single, double and triple pass SAH.



(a)



(b)

Figure 2.1 Details of the solar air heater study (a) Domain considered during testing as rectangular or circular, (b) Different metal porous media considered for the enrichment of thermal performance in solar air heater.

Few examples of the recent literature considered for the thermal performances are shown in Figures 2.2, 2.3, 2.4, 2.5 and 2.6 for single pass single glass cover, single pass double glass cover, double pass single glass cover, double pass double glass cover and triple pass single glass cover respectively. Figure 2.7 shows the number of studies with respect to number of passes of SAH considering single or double pass cover. Figure 2.7 shows that the single pass with single cover has been studied widely because of less parts in the system. When the number of passes increases, the material requirement is more and hence manufacturing cost as well as the weight increases. At the same time the maintenance increases with increase in the number of passes. Hence, SPSAH is less costly and easy to build due to less parts.

As the number of covers increases the system becomes more costly as well as maintenance requirement is also high. The efficiency is higher for the double pass compared to single pass but at the same time cost consideration, weight of the system is also major consideration during the design of the SAH. In the Figures 2.2, 2.3, 2.4, 2.5 and 2.6, the yellow line represents the glass cover, red represents the absorber plate, green represents the entrance zone, orange represents the exit zone. Also, the blue arrow represents the inlet side i.e., entrance and red arrow represents the outlet side i.e., exit of the SAH.

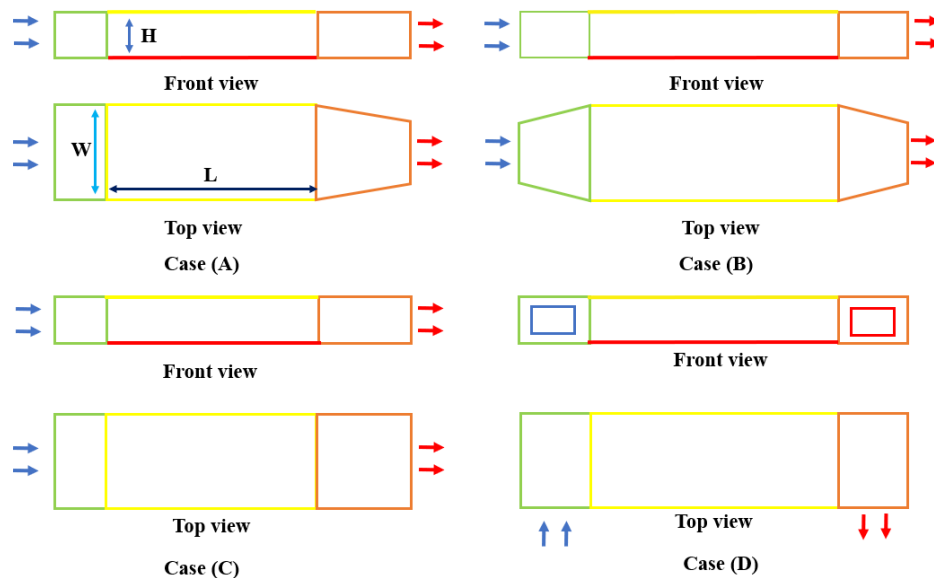


Figure 2.2 Different types of structures of single pass single glass SAH with different inlet and outlet shapes

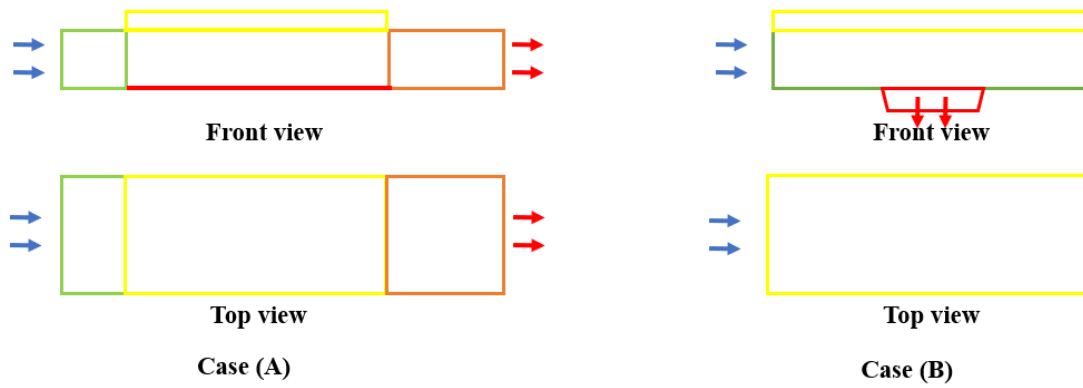


Figure 2.3 Structure of the single pass and two glass cover for solar air heater

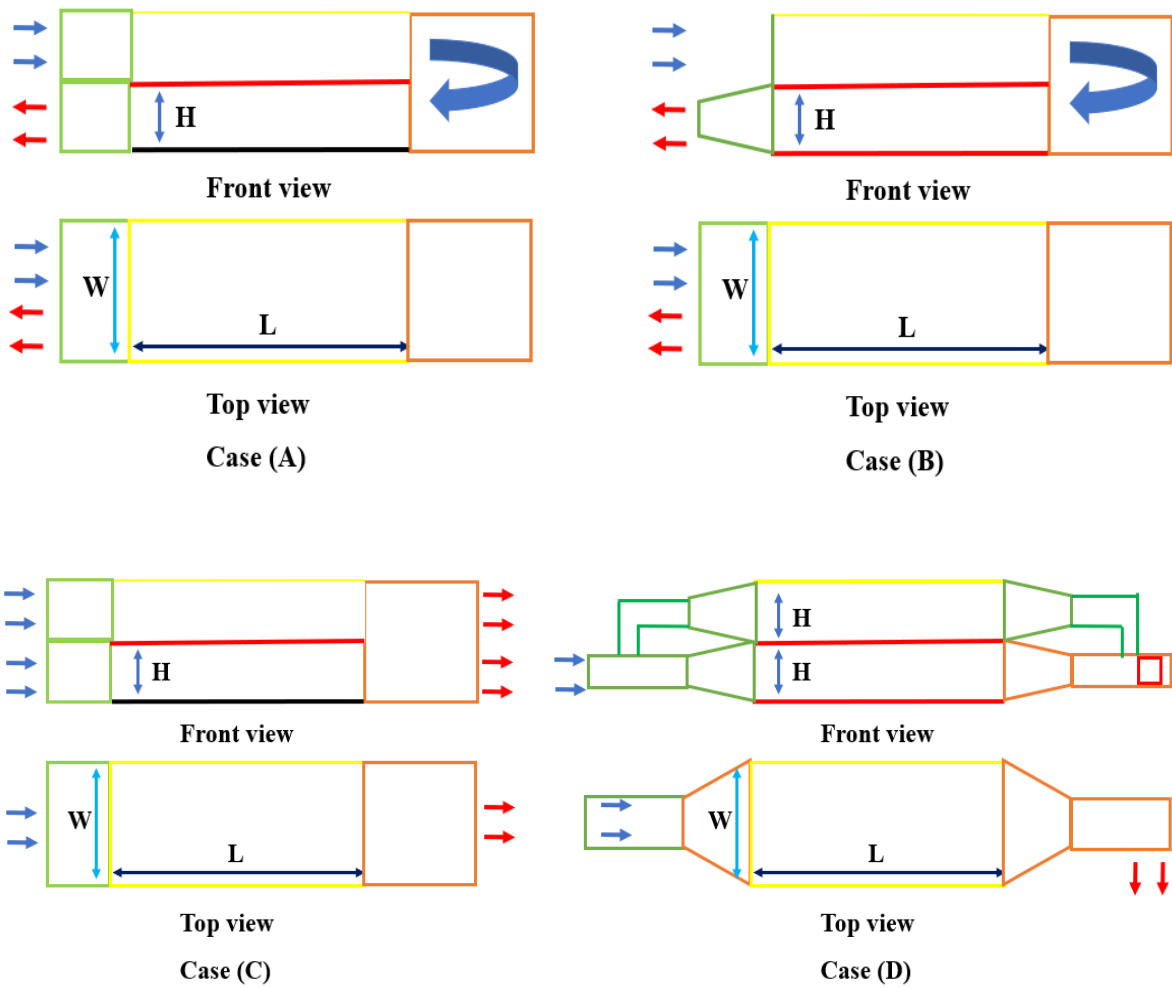


Figure 2.4 Different types of structures of double pass with single glass cover in SAH

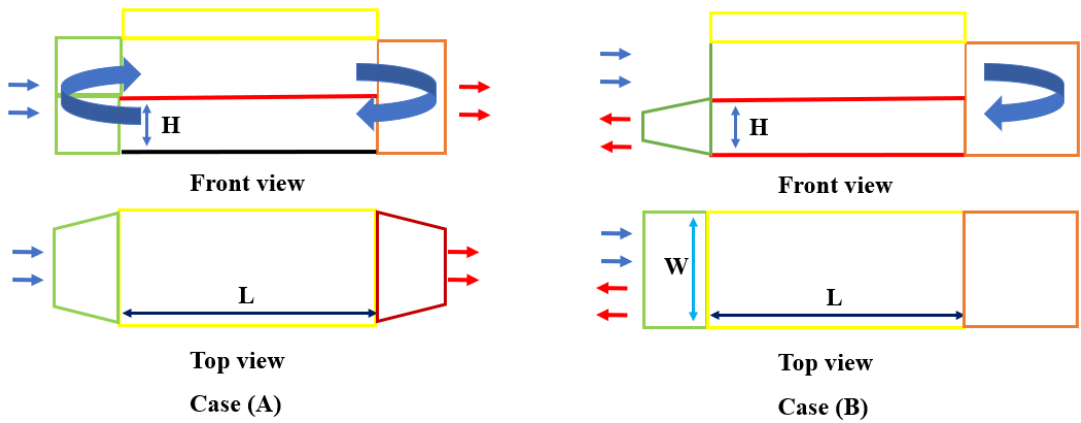


Figure 2.5 Different types of structures of double pass with double glass cover in SAH

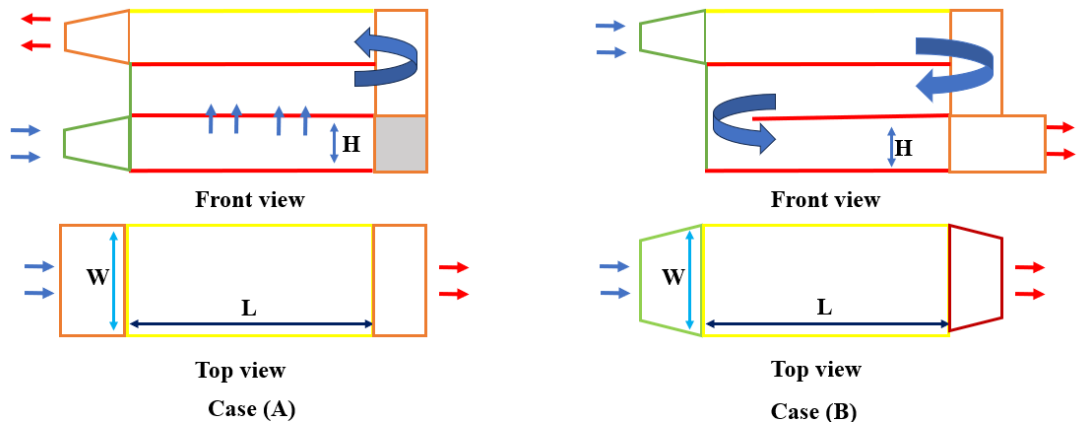


Figure 2.6 Different structures of the triple pass single glass cover of SAH

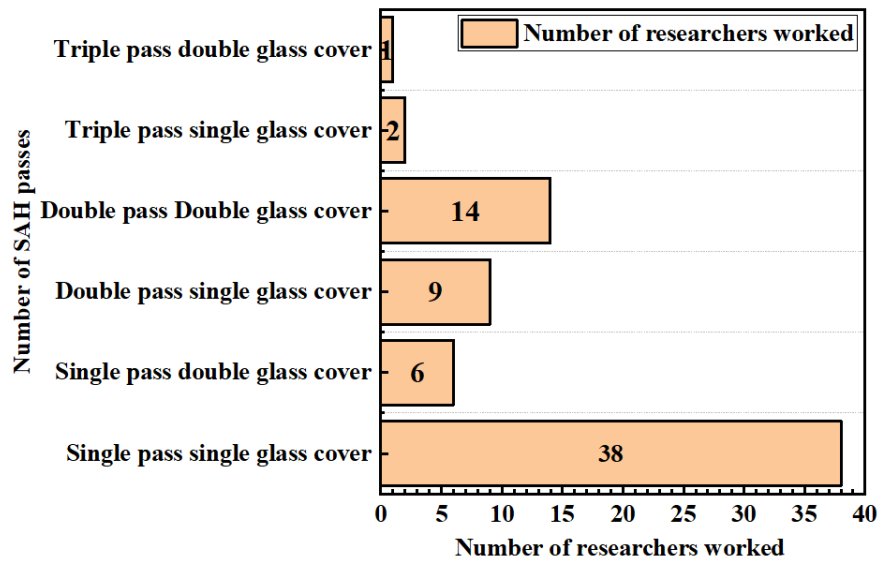


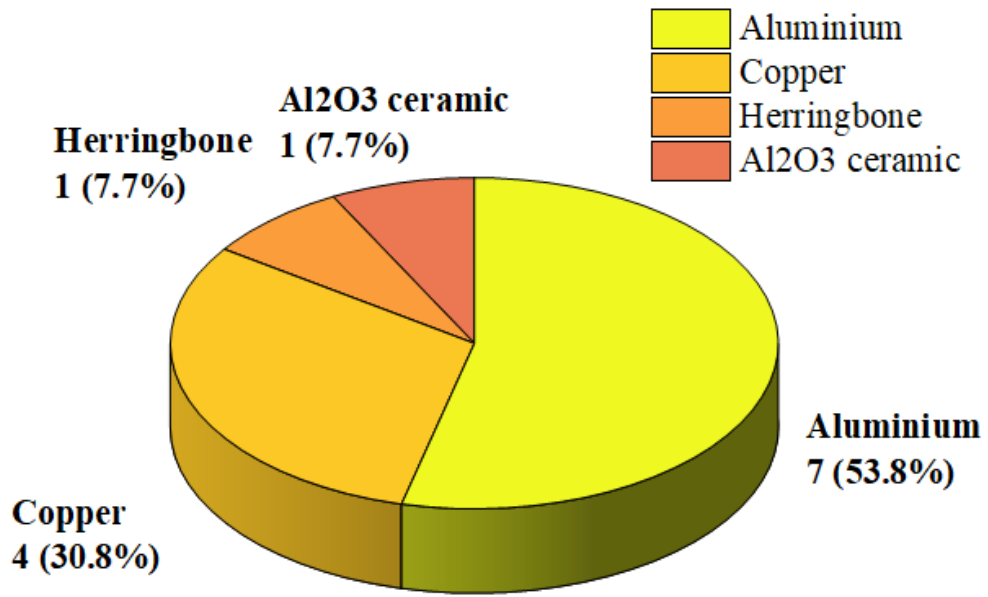
Figure 2.7 Literature of the different passes with single glass cover and double glass cover for single, double and triple pass studied papers.

So, the heat transfer rate in the above-mentioned different passes with number of covers changes according to area of the absorber plate, the percentage passing of solar radiation due to single cover or double cover. The enhancement in the heat exchange in the SAH increases because of more surface area due to porous media. The researcher used different materials to enhance the heat transfer in SAH.

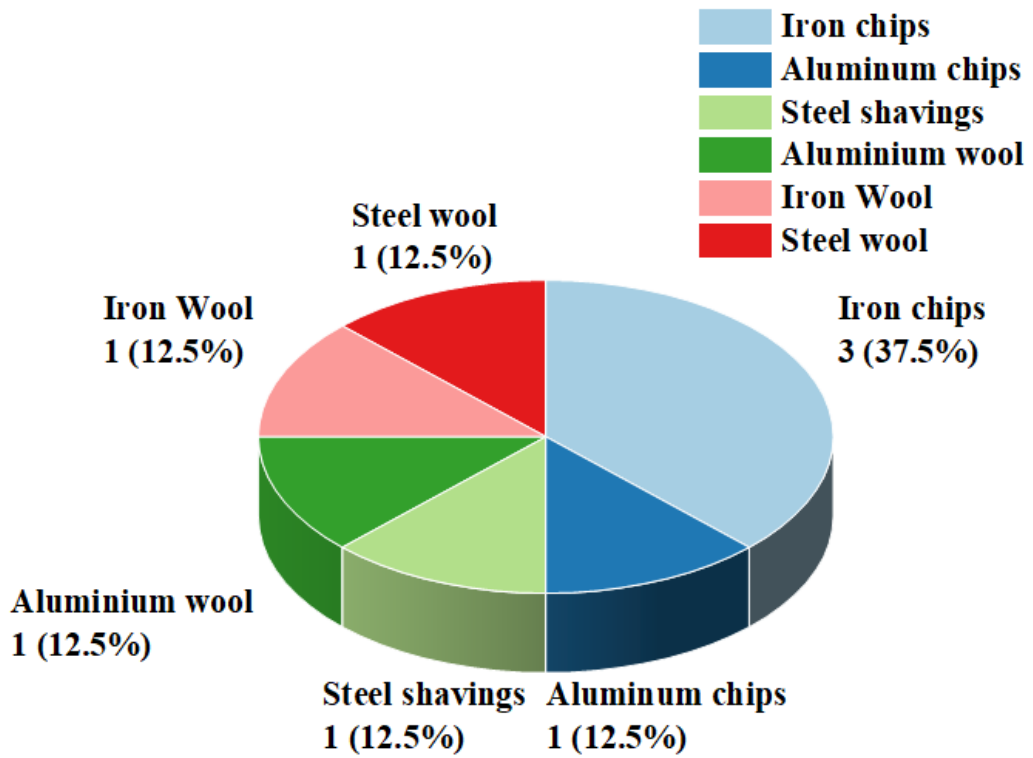
Figure 2.8 shows different materials of metal foam, metal scrap and wire mesh for the rise in temperature in the SAH. The majority of the availability and useful material in the metal foam is Aluminium and Copper. Both have higher thermal conductivity. The Aluminium has lower weight than the Copper. Hence, 53.8 % researchers used it in SAH application for the thermal performance improvement in the SAH. Further, few researchers used Iron, Steel and Aluminium scrap material to increase the thermal efficiency of the SAH. Similarly, more researchers used material like Steel, Copper, Aluminium, Galvanized Iron and Iron wire meshes for the thermal performance enrichment in the SAH. The material used for the wire mesh are metals like Aluminium (Al), Copper (Cu), Iron (Fe), etc. and alloys like Stainless Steel (SS), Brass from above study. The Stainless steel is alloy of Iron. The Brass is alloy of Copper and Zinc (70 % Cu and 30 % Zn). The Galvanised Iron (GI) is the process used of galvanization to avoid rusting of iron. The Aluminium has low weight, so transportation cost is less and also labour cost is less. The Copper cost is very high and weight is more. The stainless, Iron and GI are low thermal conductivity material, corrosion is more compared to Aluminium. The weight of the material and cost is also more compared to Aluminium material. Table 2.2 and Figure 2.9 shows that the Aluminium is the best option compared to Copper and Nickel.

Table 2.2 Common material used for wire mesh with its features.

Material	Copper	Aluminium	Nickel
Cost	High cost Rs 1020 /- per kg	Low cost Rs 320 / per kg	High cost Rs 1805 /- per kg
Weight	High weight	Low weight	High weight
Availability	Not easily available	Easily available	Easily Available
Thermal conductivity (Kothandaraman and Subramanyan 2018)	High Thermal conductivity k = 386 W/m K	Low thermal conductivity k = 204.2 W/m K	Low thermal conductivity k = 90 W/m K



(a)



(b)

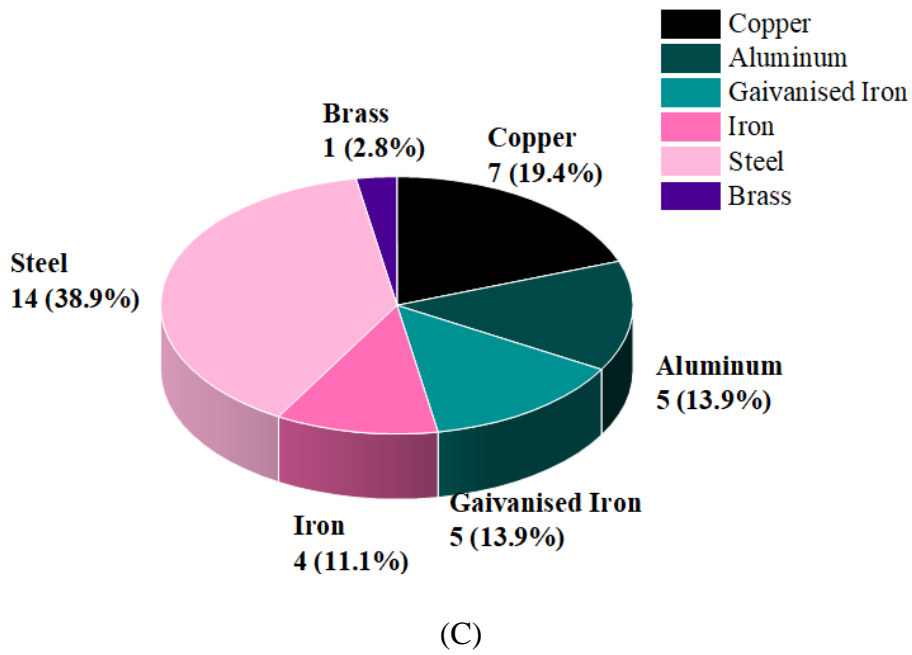


Figure 2.8 Different material used for the porous media (a) metal foam, (b) metal scrap, (c) wire mesh

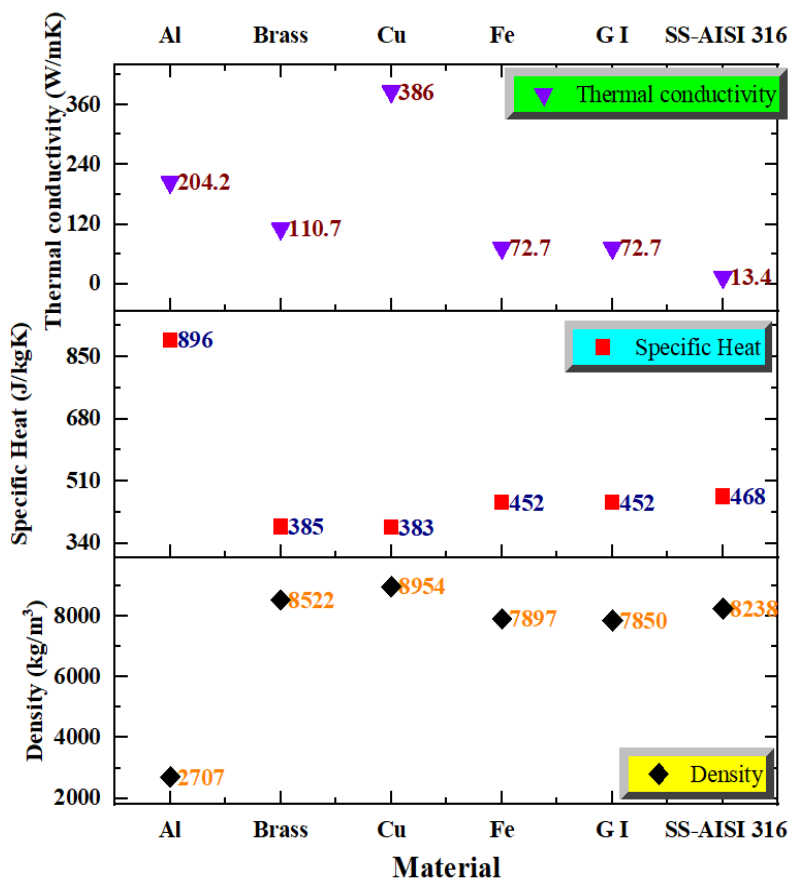


Figure 2.9 The thermal properties of the material used for metal porous media

So, till now, the above study overviewed best geometry or domain for SAH, then different porous media and its availability, the type of SAH studied till today with inserting metal porous media, the thermal properties and cost of the porous media in the local market. Now the second main part is the arrangement of the porous media in the SAH, so that optimum structure of the porous media is useful to upgrade the thermal performance of the SAH. The researchers studied different arrangements of metal foam, metal scrap and wire mesh with the absorber sheet to boost the heat transfer in the SAH.

The detailed merits and demerits are mentioned in the Table 2.3 for these different arrangements of the porous media. Figure 2.10, 2.11 and the Table 2.3 shows that the porous material parallel to the absorber plate is the best option compared to perpendicular or inclined to absorber plate in order to save the initial design, planning, construction and labour cost.

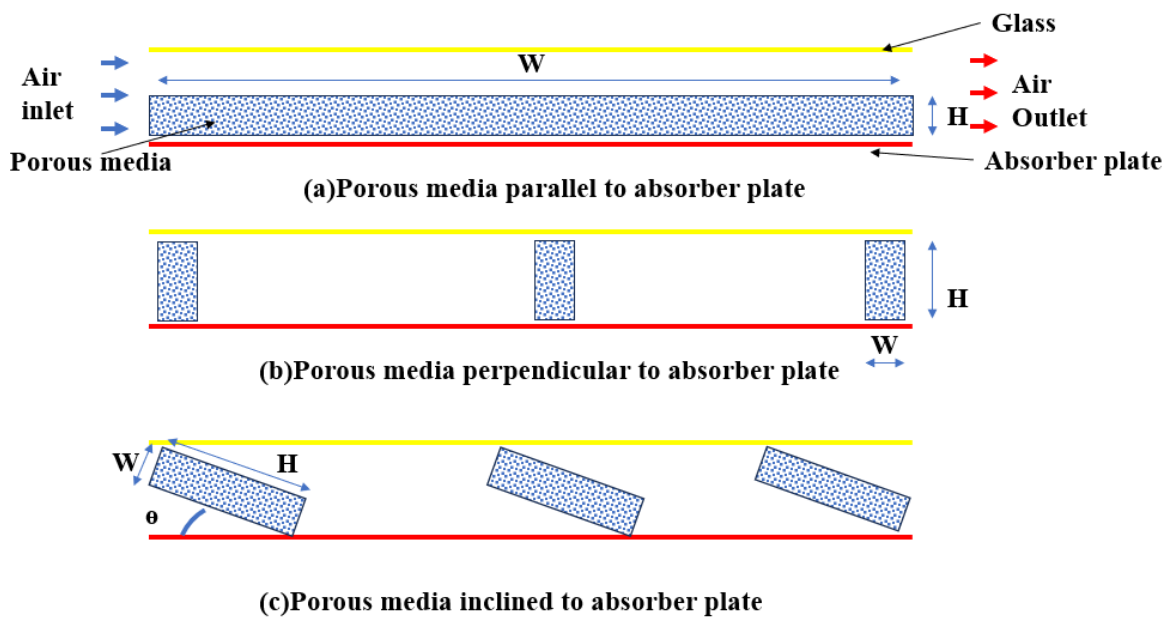


Figure 2.10 Different arrangements of the porous media a) parallel, b) perpendicular and (c) inclined to the absorber plate. (H is the height of the porous media and W is the width of the porous media)

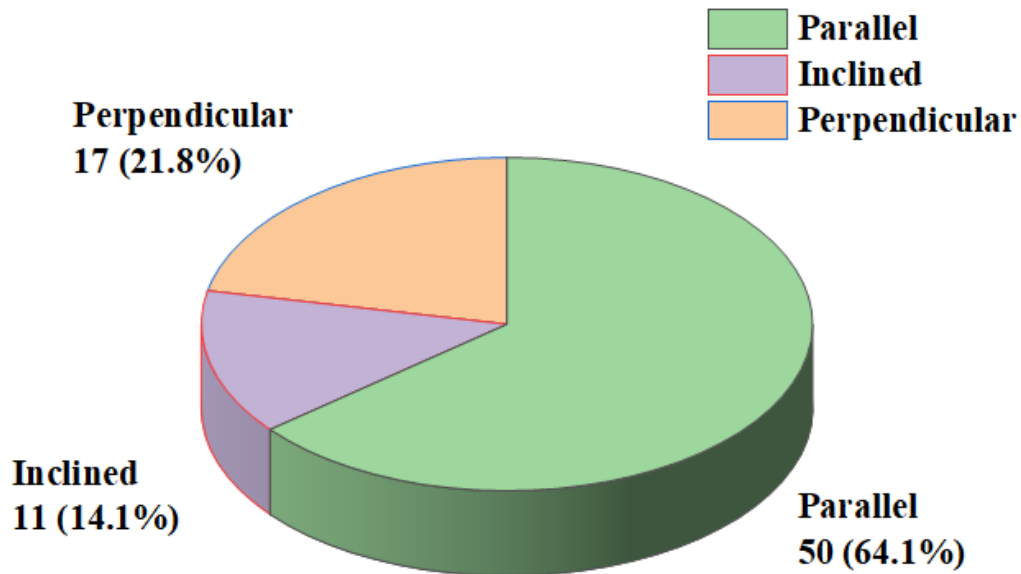


Figure 2.11 Different arrangement of the porous media in the SAH (parallel to absorber plate, perpendicular to absorber plate and inclined to the absorber plate)

Table 2.3 Advantages and disadvantages of the different arrangements of the porous media

Parallel to the absorber plate	Perpendicular or Inclined to the absorber plate
It is easy to mount or place the porous media in the space available between the glass and the absorber plate	It requires the initial arrangement and construction and planning for the mounting the porous media in the space available between the glass and the absorber plate.
It has less maintenance.	It requires the special care, changes in the dimensions of the porous media at middle due to sagging of the transparent glass.
The forced convection system does not affect the location of the porous media.	Due to forced convection, the location may change or difficult to maintain the space or extra glue is required to fixed the porous media so that at high velocity the porous media should not move the location.
It can be useful for direct method drying purposes.	It can be useful only for indirect method drying purposes.
It can be possible to add or remove the porous media from the system as per required average outlet temperature for drying purpose.	It cannot be possible to add or remove the porous media from the system as per required average outlet temperature for drying purpose.

From the above different arrangement of the metal porous media in SAH, the researchers performed studies like analytical, numerical and experimental method with indoor and outdoor testing. The methodology implemented by researchers is displayed in the Figure 2.12. Figure 2.12 and 2.13 shows the previously studied methodologies for the evaluation of the thermal performance of SAH. The experimental cost and time can be saved by the analytical and numerical trials. Hence, to observe the uniform flow, heat transfer contours, the CFD simulations plays significant role before manufacturing the experimental setup.

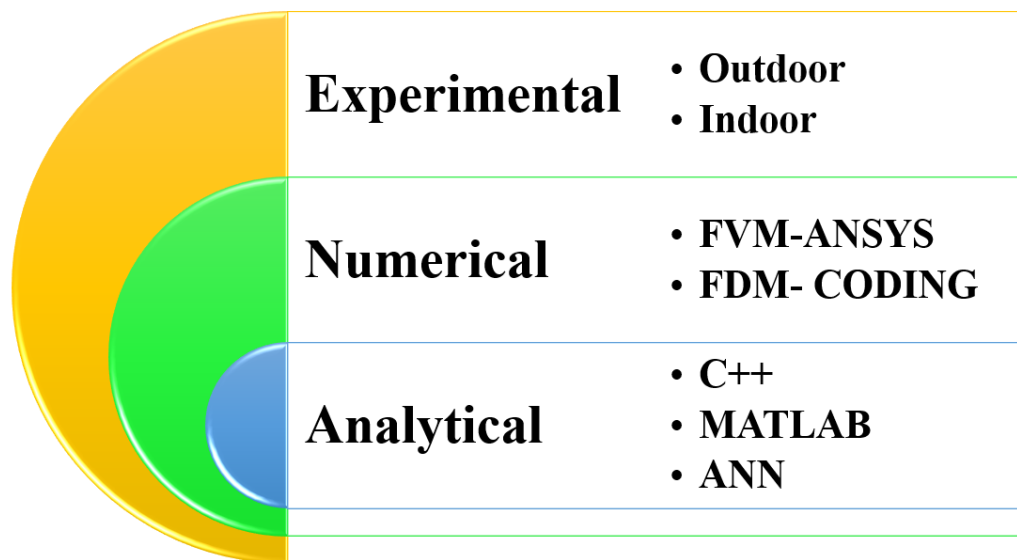
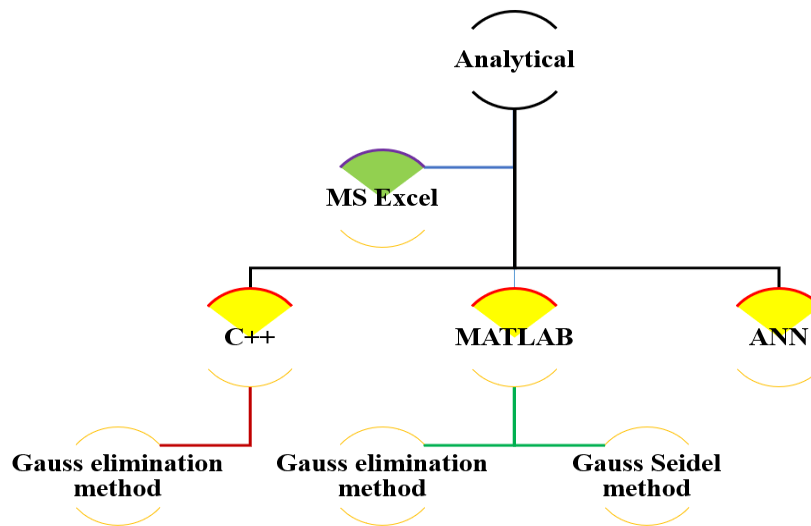


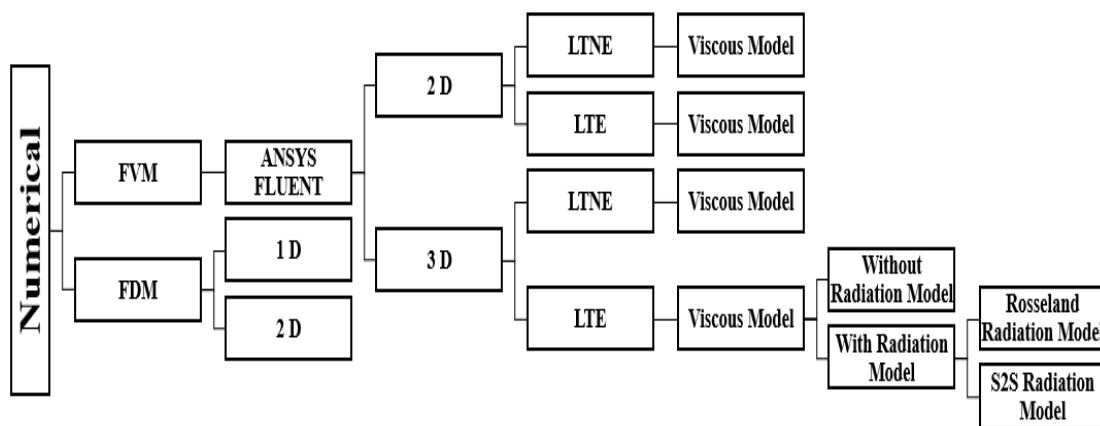
Figure 2.12 Different methodologies used by researchers to analyse the thermal performance of SAH.

The researcher performed the testing of SAH by different methodologies. The practical outdoor application is very important in any research. Figure 2.14 shows that the single pass outdoor studies are very much easy and practically it can be demonstrated by different metal porous media. 86.8 % of the researchers performed thermal performance studies of the SPSAH which is higher than the other types of SAH and also compared to indoor studies. Hence, the further focus of the output parameter is on the SPSAH with outdoor experimental work done by the previous researchers. The SAH has inlet parameters like inlet temperature, inlet area, outlet area, spacing between the glass and

absorber plate, absorber plate material, absorber area to absorb the solar radiation and mass flow rate or inlet velocity at inlet.



(a)



(b)

Figure 2.13 Method of testing the thermal performance of SAH (a) analytical Method, (b) numerical Method

Then, one can observe the outlet temperature, absorber plate temperature, solar radiation, of that particular time. and, the SAH evaluated on the basis of thermal efficiency, thermohydraulic efficiency, thermohydraulic performance parameter etc. The metal porous media with drying application is considered in order to evaluate the moisture ratio, drying rate and simple payback period. Figure 2.15 shows the recent

achievement in thermal efficiency of SAH using different types of WM. The authors obtained the thermal efficiency from 30 to 88 % with SPSAH.

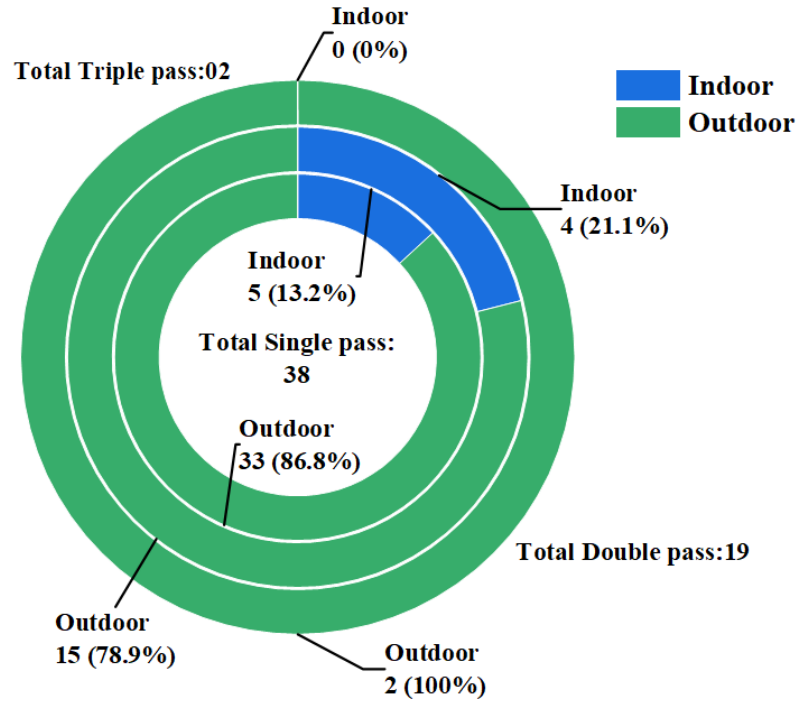


Figure 2.14 Comparison of the experimental studied of indoor and outdoor testing for single, double and triples SAH.

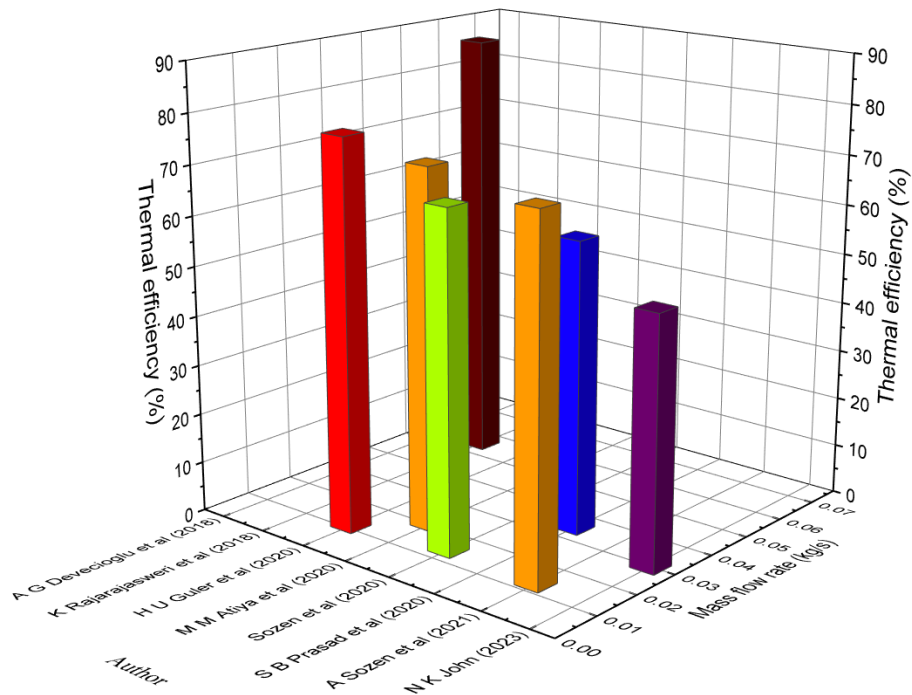


Figure 2.15 Effect of the mass flow rate and porosity on the thermal efficiency.

2.7 SUMMARY OF LITERATURE AND RESEARCH GAPS

The detailed investigation has been studied of metal porous media in solar air heater. Figure 2.16 shows various aspects which have been observed to enhance the heat transfer in solar air heater. Various researchers focused their study of SAH on number of passes, number of covers, variation in depth of channel, different absorber plate angles, flow directions and different insertion material like metal porous media etc.

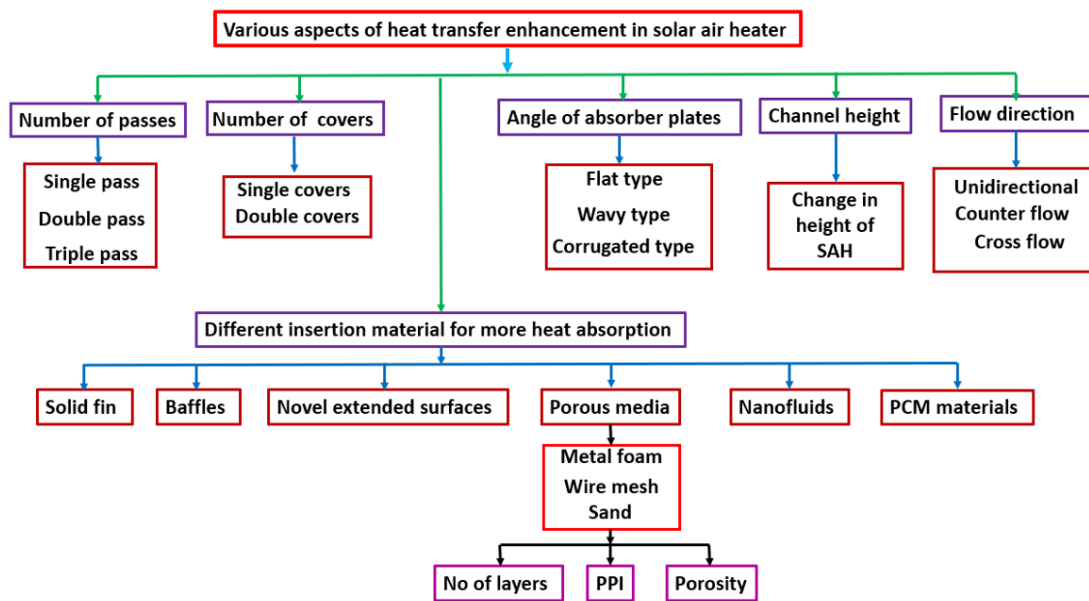


Figure 2.16 Various aspects of heat transfer enhancement of solar air heater by metal porous media in the recent literature.

The recent literature studied the maximum drying operation is with the active method generally controlled by the fan. The requirement of the temperature can be controlled by the fan speed to dry a particular product effectively. The open sun drying is a lengthy process and not effective compared to solar dryer process. The passive method is having lesser thermal efficiency than the active method hence the most of the literature considers active method due to higher thermal efficiency. The direct type is easy and low cost method. It saves cost of the extra drying chamber or box compared to indirect solar dryer. The recent different types of drying methods are shown in Figure 2.17.

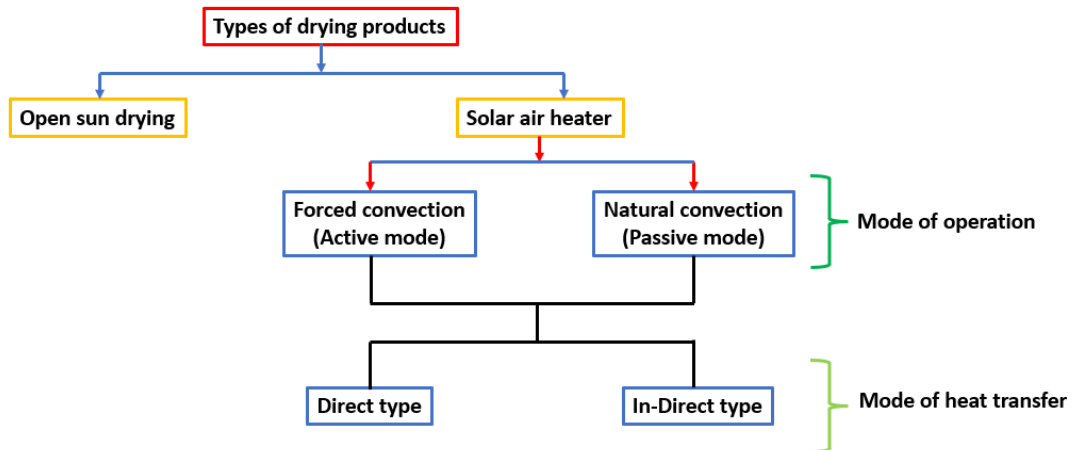


Figure 2.17 Classification of method of drying products considered by metal porous media at recent studied literature.

Based on the scrutiny of publications, it can be noted that the numerical analysis on wire mesh is required to understand the fluid flow and heat transfer characteristics through wire mesh. Further detailed research is required to understand the meaningful insights of fluid flow and heat transfer through the wire mesh. Also, the computational evaluation of parametric and optimization work of forced convection through highly permeable wire mesh are required but complex due to the construction of the permeable material.

The above literature survey shows that following points are not covered in the heat transfer enhancement of solar air heater.

1. The numerical and experimental studies on arrangements of different combinations of porosity of wire mesh material as a porous media are not performed for forced convection.
2. The numerical and experimental studies on arrangements of graded wire mesh different porosity material with combinations like Aluminium and nickel or Aluminium and Copper have not been analysed to increase the heat transfer and to decrease the pressure drop.
3. The numerical and experimental studies on combinations of different types of wire mesh like expanded type and square type have not been explored in the literature.
4. Optimization study of different heights of porous media for different combinations of structural properties is unaddressed so far.

2.8 MOTIVATION AND SCOPE OF THE PRESENT WORK

The above literature shows that the metal foam arrangement in SAH improves the heat transfer rate, while at the same time the pressure drop increases when the inlet velocity increases. Instead of fully filled metal foams in the SAH, a discrete arrangement of metal foam reduces the pressure drop with reasonable heat transfer. There always exists a trade-off between the heat transfer and pressure drop as the inlet velocity of the fluid increases.

- The SPSAH with a single-type horizontally arranged WM has been studied widely by many authors. Hence, from the literature, it can be observed that the single type of PPI, porosity, and pitch-to-wire diameter of the wire mesh inserted in SPSAHs have been studied, and a comparative analysis of SAHs' thermal efficiency and thermohydraulic efficiency has been conducted.
- The literature shows that wire mesh is the best option to enhance the heat transfer in the SAH because it is easily available, simple in design, low cost, has a lower transportation cost, and exhibits the appropriate pore structure. However, the literature shows that combinations of different PPIs, porosities, and pitch-to-wire diameters of the wire mesh have not been studied until today.
- The effect on the thermal performance of combining different PPIs and porosities has not been investigated numerically and experimentally till today. In particular, until today, the combination of three porosities of the same WM material in a SPSAH to improve its thermal efficiency has not been analysed in the research literature. Hence, to underline this situation, discrete metal foams with different thermal conductivity have been considered.
- The thickness of the metal foam in the discrete arrangement plays a significant role in heat transfer, the same has been varied while the distance between the discrete metal foams was kept constant. Moreover, the PPI of the metal foam is changed to see its effect in heat transfer and pressure drop.

2.9 OBJECTIVES OF THE PRESENT RESEARCH WORK

1. Design and development of rectangular domain type single pass solar air heater (SPSAH) to investigate thermal efficiency for different mass flow rates and to compare the results of thermal performance of SPSAH analytically and numerically.
2. To investigate the enhancement of heat transfer numerically in single pass solar air heater (SPSAH) using discrete porous media with varying thickness and porosity by local thermal non equilibrium method.
3. To evaluate the thermohydraulic efficiency of a single pass solar air heater (SPSAH) in the presence of wire mesh as a porous media and to compare the results for optimum configuration of wire mesh. To analyse the thermal efficiency of SPSAH experimentally with and without wire mesh.
4. Energy, exergy, economic (3E) analyses of single pass solar air heater (SPSAH) using graded wire mesh for drying vegetables by numerically and experimentally.

2.10 CLOSURE

The comparative study of fully and partially filled metal porous media in different types of solar air heater was overviewed in this chapter. The solar air heater has been compared with metal porous media and without porous media in order to check the thermal performance of SPSAH.

CHAPTER 3

RESEARCH METHODOLOGY

3.1 INTRODUCTION

This chapter deals with the detailed information of theoretical, numerical and experimental methodologies to achieve the aim of the proposed objectives. The research objectives fulfill the analytical, numerical (CFD) and experimental works. The complete steps and their details for theoretical, numerical and experimental study are given here. Figure 3.1 shows the research strategy implemented to carry out the objectives. Figure 3.2 shows the execution of the experimental objectives. The theoretical and numerical calculated values are validated with the experimental results. The sequence implemented is shown in the Figure 3.3 for the above methodologies.



Figure 3.1. Steps implemented to achieves the **research objectives**.

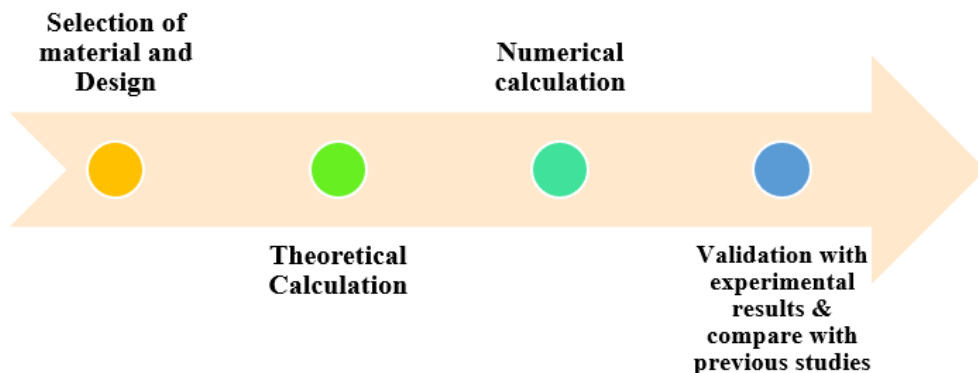


Figure 3.2. Steps implemented to achieves the **experimental objectives**.

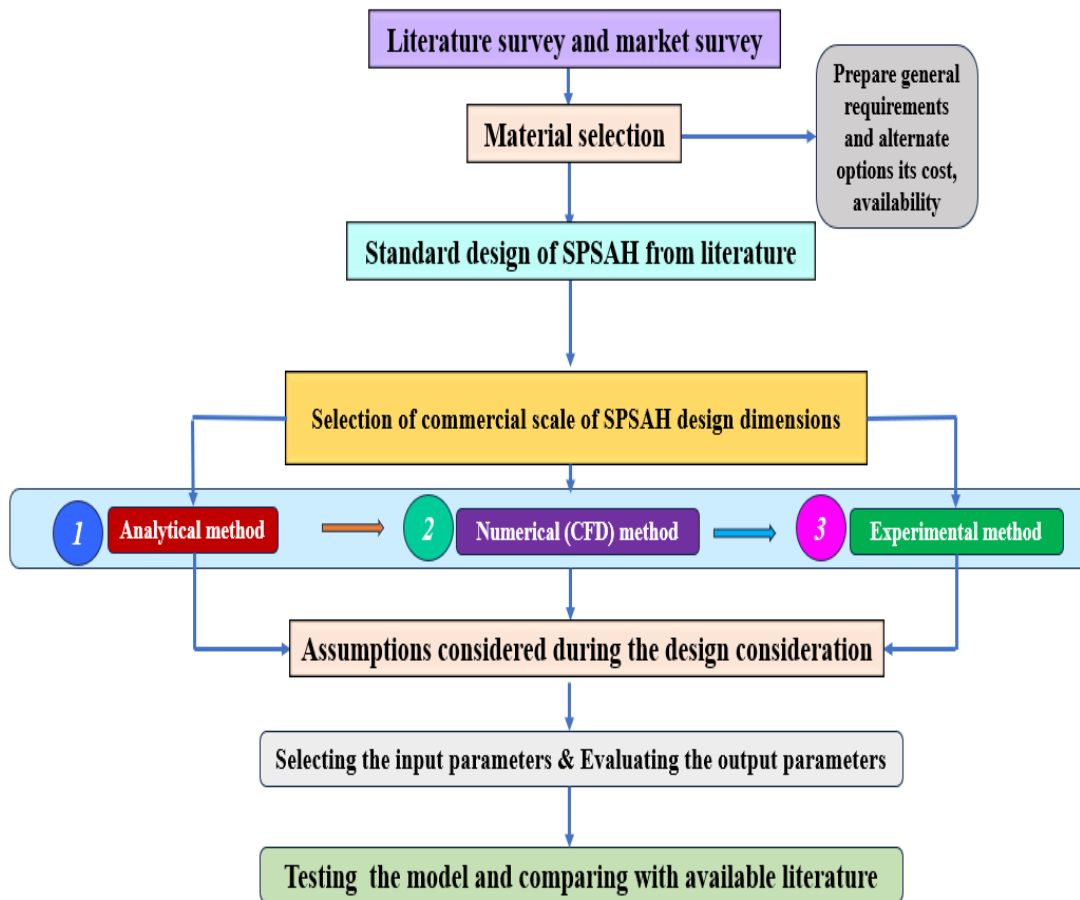


Figure 3.3 Implementation strategy of the present research work

3.2 PROBLEM STATEMENT

The main aim is to design SPSAH to dry the product like vegetables, fruits etc. for the location National Institute of Technology Karnataka, Surathkal Karnataka which is situated in southern India in the state of Karnataka. The location has a latitude of $13^{\circ} 0' 12''$ & longitude of $74^{\circ} 47' 24''$. Select the material and design the SPSAH based on open loop test in clear sky days. Evaluate the thermal efficiency and thermohydraulic performance factor of the SPSAH at different mass flow rates, solar radiation and ambient temperatures. Determine the maximum heat transfer enhancement and minimize the pressure drop numerically, by using different PPI, porosities and different thicknesses of metal foam or wire mesh. Test the best combination of graded wire meshes to dry the vegetables experimentally and compared it with empty channel performance.

3.3 MATERIAL SELECTION AND DESIGN OF SINGLE PASS SOLAR AIR HEATER (SPSAH)

The commercial scale of the SPSAH is 2m^2 . The material and designs have selected from the literature survey. The study performed by Rajarajeswari et al (Rajarajeswari et al. 2018) has considered as the reference work for the present study. The main parts of the SPSAH are absorber plate, transparent cover, insulation and outer frame. The criteria to select the material have chosen in such a way that it should give the maximum thermal performance and the cost of the material should be low. So that the capital cost of SPSAH is less. The Aluminium plate for absorber plate, toughened glass for transparent cover, ceramic wool for insulation, and polyvinyl chloride for outer frame has used to manufacture the SPSAH system. The matte black paint is applied on the absorber plate to absorb more solar radiation from the Sun. So that the heat carrying capacity of air increases. The characteristics of the selected material are shown in the Figure 3.4.

3.4 DESIGN OF SPSAH BY ANALYTICAL METHOD

The theoretical design of the SAH was developed at the location of Mechanical Engineering Department, National Institute of Technology Surathkal Karnataka, India. For the conventional SAH, the material and properties are considered as mentioned in (Kothandaraman C P 2018; Rajarajeswari et al. 2018). The dimensions mentioned in (Rajarajeswari et al. 2018) are considered additional design parameters. As given in (Sukhatme S P 2018), based on Klein's recommendation, the mean value for the month in April is 15. Hence the analytical solution for the empty channel is done on 15 April at 13:00 hours, because the solar radiation is maximum. The latitude and longitude of further study are $13^{\circ} 0' 12''$ N, $74^{\circ} 47' 24''$ E for the National Institute of Technology Karnataka, Surathkal. The analytical readings are considered during clear sky days in April 2022. Analytical studies are calculated under the climatic conditions of Surathkal, Karnataka, India (12.99° N, 74.81° E). The tilt angle of 13° with the ground surface facing south is taken for testing the SAH to achieve maximum solar radiation. The angle of tilt of SAH with the ground surface is equal to the latitude of the location. The facing south direction of SAH is beneficial for getting more solar radiation on the absorber plate. This 13° angle is prepared with the help of a strong frame made up of MS material to support the complete SAH. The angle of tilt is equal to the latitude of that location,

as mentioned in (Rajarajeswari et al. 2018). The constant a and b for monthly average daily global radiation are obtained for Mangalore city at 0.27 and 0.43, respectively, as mentioned in (Sukhatme and Nayak 2018).

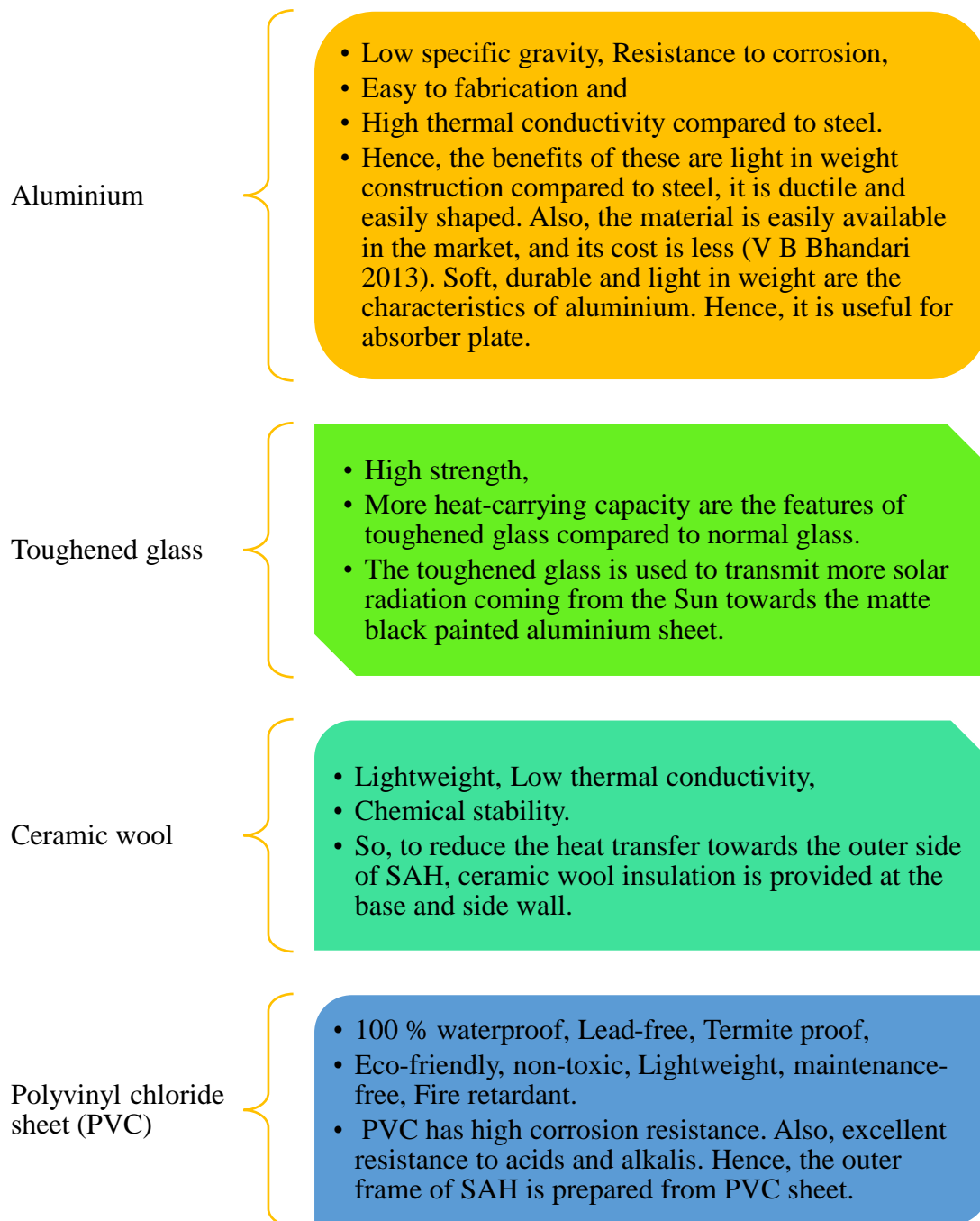


Figure 3.4 Significance of the selected material to manufacture the SPSAH

Table 3.1 Material properties considered for simulation at 50 °C. (Fluent 2022; Kothandaraman and Subramanyan 2018; Rajarajeswari et al. 2018; Yadav and Bhagoria 2013).

Material	Density kg/m ³	Specific Heat (J/kg K)	Thermal Conductivity (W/m K)	Kinematic Viscosity (m ² /s)	Prandtl Number	Emissivity	Absorptivity
Air	1.225	1006.43	0.0242	1.79×10^{-5}	0.702	-	-
Aluminium	2719	871	202.4	-	-	0.8	0.95
Glass	2500	670	0.7443	-	-	0.9	-
Wood	700	2310	0.173	-	-	-	-
Copper	8978	381	387.6	-	-	-	-
Nickel	8900	460.6	91.74	-	-	-	-

3.4.1 Assumptions considered during analytical method

In order to make the clarify the situation and to make predictions the assumptions are important to get the analytical results easily.

- The test is conducted for open loop in clear sky days.
- The specified limit of the solar radiation, ambient temperature, air flow rate, air inlet temperature and temperature rise across solar air heater are $\pm 50 \text{ W/m}^2$, $\pm 1 \text{ }^\circ\text{C}$, $\pm 1 \%$, $\pm 0.1 \text{ }^\circ\text{C}$, and $\pm 0.1 \text{ }^\circ\text{C}$, respectively, for a 15 min duration.
- The solar air heater is operated in steady state condition for the present study. The range of air velocity is less than 30 % of the Mach number. Hence, the density variation is very much less, due to a velocity which is below 5 %. So, the flow is assumed to be a steady-state, incompressible turbulent flow.
- Here, 15 April is the mean of the value of solar intensity (I_T) for the month of April. The average flux falling on the absorber plate for the month of April is 850 W/m^2 .
- The present study is selected for 0.2268, 0.2646, 0.3023, 0.3401, 0.3779 m/s velocities at inlet.
- The wind speed is assumed as 1 m/s.
- The properties of air (working fluid) are considered at the mean fluid temperature which is assumed as 50 °C.
- The material properties are isotropic.

- Side walls are adiabatic. Negligible heat loss from the bottom plate and the periphery envelope to the surroundings. Negligible heat loss from the inlet and outlet surfaces.

3.4.2 Performance parameters of SPSAH for analytical method

The analytical calculations of conventional SPSAH are done by the procedure mentioned in (Garg and Prakash 2016; Sukhatme and Nayak 2018) as follows-

The monthly average daily inclined irradiance is calculated by following Equation 3.1

$$\delta \text{ (in degree)} = 23.45 \sin [0.9863(284 + n)] \quad (3.1)$$

where n is the day of the year, the present study for analytical is 15 April hence, n = 105. δ is the declination.

Equation 3.2 below calculates the value of the angle between an incident solar beam flux and the normal to a plane surface. Considering surface of SAH is facing south ($\gamma = 0^\circ$)

$$\cos \theta = \sin \delta \sin (\phi - \beta) + \cos \delta \cos \omega \cos (\phi - \beta) \quad (3.2)$$

where θ is the angle between an incident solar beam flux and the normal to a plane surface. ϕ is latitude of a location. β is the slope of the SAH with the horizontal surface.

The magnitude of ω_{st} for an inclined surface facing south is calculated by Equation 3.3

$$|\omega_{st}| = \min[|\cos^{-1}(-\tan\phi \tan\delta)|, |\cos^{-1}\{-\tan(\phi - \beta)\tan\delta\}|] \quad (3.3)$$

The daily sunlight or sunshine hours per day is calculated from Equation 3.4 as

$$S_{\max} = \frac{2}{15} \omega_{st} \quad (3.4)$$

The daily radiation fall on a horizontal surface at the location is calculated by Equation 3.5 as

$$H_0 = \frac{24}{\pi} I_{sc} (1 + 0.033 \cos(\frac{360 n}{365})) (\sin \omega_s \sin \phi \sin \delta + \cos \phi \cos \delta \sin \omega_s) \quad (3.5)$$

From (Sukhatme S P 2018) constant a and b for Mangalore city in India are 0.27 and 0.43, respectively. Assuming the average sunshine hours per day are 9.5 h for April

month. The monthly average of the daily global radiation a horizontal surface is calculated by Equation 3.6 as

$$\frac{\overline{H_g}}{\overline{H_o}} = a + b\left(\frac{\overline{S}}{\overline{S_{max}}}\right) \quad (3.6)$$

The monthly average daily diffuse radiation is calculated by Equation 3.7 as

$$\frac{\overline{H_d}}{\overline{H_g}} = 0.8677 - 0.7365\left[\frac{\overline{H_g}}{\overline{H_o}}\right] \quad (3.7)$$

The hourly radiation on an inclined surface on n^{th} day between 1 h is calculated by Equation 3.8 as

$$I_o = 1.367 \left(1 + 0.033 \cos \left(\frac{360 n}{365} \right) \right) \sin \delta \sin(\phi - \beta) \quad (3.8)$$

$$+ \cos \delta \cos \omega \cos(\phi - \beta) \frac{\text{kW}}{\text{m}^2}$$

Normalizing factor f_c is mentioned in Equations 3.9 and 3.10

$$\frac{\overline{I_g}}{\overline{H_g}} = \frac{\overline{I_o}}{\overline{H_o}} \frac{(a+b \cos \omega)}{f_c} \text{kJ/m}^2\text{-h} \quad (3.9)$$

$$\text{Where, } f_c = a + 0.5b \left[\frac{\frac{\pi \omega_s}{180} - \sin \omega_s \cos \omega_s}{\sin \omega_s - \frac{\pi \omega_s}{180} \cos \omega_s} \right] \quad (3.10)$$

The monthly average hourly diffuse radiation is calculated by Equation 3.11 as

$$\frac{\overline{I_d}}{\overline{H_d}} = \frac{\overline{I_o}}{\overline{H_o}} \quad (3.11)$$

The diffuse radiation is calculated by Equation 3.12 as

$$\frac{\overline{I_{dg}}}{\overline{H_d}} = \frac{\overline{I_o}}{\overline{H_o}} \quad (3.12)$$

Choose the maximum value of diffuse radiation (I_d) between Equations 3.11 and 3.12 for further calculations.

The beam radiation is calculated by Equation 3.13 as

$$I_b = I_g - I_d \quad (3.13)$$

The tilt factor for beam radiation (r_b) is calculated by Equation 3.14

$$r_b = \frac{\cos \theta}{\cos \theta_z} = \frac{\sin \delta \sin(\theta - \beta) + \cos \delta \cos \omega \cos(\theta - \beta)}{\sin \theta \sin \delta + \cos \theta \cos \delta \cos \omega} \quad (3.14)$$

The tilt factor for diffuse radiation (r_d) is calculated by Equation 3.15

$$r_d = \frac{(1 + \cos \beta)}{2} \quad (3.15)$$

The tilt factor for reflector radiation (r_r) is calculated by Equation 3.16

$$r_r = \frac{\rho(1 - \cos \beta)}{2} \quad (3.16)$$

Assume ground reflectivity be 0.2 as mentioned in (Sukhatme 2018). The total flux (I_T) falling on tilted surface at any instant is calculated by Equation 3.17 as

$$I_T = I_b r_b + I_d r_d + (I_b + I_d) r_r \text{ (W/m}^2\text{)} \quad (3.17)$$

The total flux (I_T) falling on tilted surface at any instant is calculated by flux coming on the surface of absorber plate i.e., flux incident on the transparent glass is passing through glass towards the black painted absorber plate. This flux is the addition of beam and diffuse radiation coming directly on the absorber plate and the radiation reflected onto the surface from surroundings. Here, all the solar radiation coming from the sun is absorbed by the absorber plate. The heated absorber plate transfers heat as heat flux to moving air from inlet to outlet with help of conduction, a convection mechanism neglecting radiation heat transfer as mentioned in (Sukhatme and Nayak 2018). It is assumed that the heat flux i.e., solar intensity falling on the absorber plate is not more than $\pm 50 \text{ W/m}^2$ for a 15 min duration. Hence the solar air heater is working under a steady state condition.

The number of covers is considered for this SAH to be 1. The spacing between the plate is 120 mm. The top loss coefficient of SAH (U_t) is calculated by Equation 3.18,

$$U_t = \left[\frac{M}{\left(\frac{c}{T_{pm}}\right) \left(\frac{T_{pm} - T_a}{M+f}\right)^{0.252}} + \frac{1}{h_w} \right]^{-1} + \left[\frac{\sigma (T_{pm}^2 + T_a^2)(T_{pm} + T_a)}{\frac{1}{\varepsilon_p + 0.0425 M (1 - \varepsilon_p)} + \frac{2M+f-1}{\varepsilon_c} - M} \right] \quad (3.18)$$

$$\text{Where, } f_t = \left(\frac{9}{h_w} - \frac{30}{h_w^2} \right) \left(\frac{T_a}{316.9} \right) (1 + 0.091M) \quad (3.19)$$

$$C_t = 204.429 (\cos \beta)^{0.252} / d^{0.24} \quad (3.20)$$

d is spacing (in m) between cover plate and absorber plate, h_w is the convective heat transfer coefficient at the top cover, σ is the Stefan Boltzmann constant (5.67×10^{-8} in $\text{W/m}^2\text{K}^4$), ε_p and ε_c is the emissivity of the absorber plate surface and bottom surface respectively.

The convective heat transfer coefficient in $\text{W/m}^2 \text{K}$ at transparent cover is calculated by Equation 3.21

$$h_w = 5.7 + 3.8 V_\infty \quad (3.21)$$

The bottom loss coefficient of SAH (U_b) is calculated by Equation 3.22

$$U_b = \frac{k_i}{\delta_b} \quad (3.22)$$

where k_i is the thermal conductivity in W/m K of the insulation material and δ_b is the thickness of the insulation material in m. The side loss coefficient is assumed as zero.

The overall loss coefficient (U_L) in W/m² K is calculated by Equation 3.23

$$U_L = U_t + U_b + U_s \quad (3.23)$$

The transmissivity of the cover system of a SAH is calculated by Equation 3.24

$$\tau = \tau_r \tau_a \quad (3.24)$$

where τ_r is the transmissivity obtained by considering only reflection and refraction, τ_a is the transmissivity obtained by considering only absorption.

The value of the convective heat transfer coefficient h_{fp} in W/m² K is calculated by using Equation 3.25

$$h_{fp} = Nu \left(\frac{k_{air}}{\text{Hydraulic diameter } (d_h)} \right) \quad (3.25)$$

where Nu is Nusselt number, and k_{air} is the thermal conductivity of air in W/m K.

The Hydraulic diameter in m is calculated by Equation 3.26

$$\text{Hydraulic diameter}(D_h) = \frac{4 (W \times d)}{2 (W + d)} \quad (3.26)$$

where, W is the width of the absorber plate in m and d is the spacing between the glass and absorber plate in m.

The average air velocity in m/s is calculated by Equation 3.27

$$\text{Average air velocity} = \frac{\dot{m}}{\rho (W \times L)} \quad (3.27)$$

The Reynold number (Re) is calculated by Equation 3.28

$$Re = \frac{\rho v d_h}{\mu} \quad (3.28)$$

The radiative heat transfer coefficient (h_r) in W/m² K is calculated as Equation 3.29

$$h_r = \frac{\sigma}{\left(\frac{1}{\varepsilon_p} + \frac{1}{\varepsilon_b} - 1 \right)} (T_{pm} + T_{bm})(T_{pm}^2 + T_{bm}^2) \quad (3.29)$$

where h_r is the radiative heat transfer coefficient in $W/m^2 K$, T_{pm} and T_{bm} is the mean temperature of the absorber plate and the bottom plate in Kelvin. It can be taken to be equal to the mean fluid temperature T_{fm} in Kelvin.

The effective heat transfer coefficient (h_e) between the absorber plate and the air stream is calculated by Equation 3.30

$$h_e = h_{fp} + \frac{h_r h_{fb}}{h_r + h_{fb}} \quad (3.30)$$

The SAH efficiency factor is calculated by Equation 3.31

$$F' = \left(1 + \frac{U_L}{h_e}\right)^{-1} \quad (3.31)$$

The useful heat gain (q_u) in W for the SAH is calculated by Equation 3.32,

$$q_u = F_R A_P [S - U_L(T_{fi} - T_a)] \quad (3.32)$$

where F_R is the SAH heat removal factor, S is the flux absorbed in the absorber plate in W/m^2 .

$$F_R = \frac{\dot{m} C_p}{U_L A_P} \left[1 - \exp\left\{-\frac{F' U_L A_P}{\dot{m} C_p}\right\}\right] \quad (3.33)$$

$$S = I_T(\tau\alpha)_{avg} \quad (3.34)$$

The instantaneous efficiency of the SAH is calculated by Equation 3.35,

$$n_i = \frac{q_u}{I_T A_C} \quad (3.35)$$

The outlet temperature of the SAH is obtained by Equation 3.36,

$$q_u = \dot{m} C_p (T_{fo} - T_{fi}) \quad (3.36)$$

The above-mentioned equations are used to find the outlet temperature of SPSAH considering mentioned assumptions in the section 3.4.1. After the calculated outlet temperature, the comparison has done with the SPSAH of Rajarajeswari et al 2018. The advantages of the analytical method are to save the time, material cost, fabrication cost compared to direct experimental method. The analytical method serves as benchmark towards the validation of the numerical work. Then the next primary stage is to calculate the outlet temperature from the two-dimensional numerical domain of the same SPSAH, considering the same assumptions. Next, the 2D numerical model is simple to design and easy to observe the temperature variations, velocity distribution etc. The 2D

numerical model has lesser mesh quantity as a result the computational time to obtain the results is less. The analysis of thermal performance is also easy.

3.5 TWO-DIMENSIONAL NUMERICAL DOMAIN, ITS BOUNDARY CONDITIONS AND GOVERNING EQUATIONS FOR SPSAH USING METAL FOAM

In this section the empty channel two dimensional SPSAH is designed as per Figure 3.5. Then to increase the heat transfer enhancement in the SPSAH, the discrete metal foam is added at equal distances of 22, 44 and 88 mm thicknesses. The outlet temperature is calculated with insertion of metal foam and it has compared with the empty channel SAH. Also, the thermohydraulic performance parameter is evaluated for different PPI and porosities of metal foam.

3.5.1 Details of geometry, meshing and boundary conditions

All the design and analysis are performed in ANSYS Fluent 2022 R2 software. The two-dimensional geometry is considered for the numerical analysis. The minimum computational time, to obtain simple meshing with high quality in less time and easy visualization are the benefits of the two-dimensional (2D) geometry compared to the three-dimensional (3D) geometry analysis. Hence the first stage the numerical analysis is performed with 2D study. The geometry consists of three parts i.e., entrance zone, test zone and exit zone. The entrance zone has inlet and exit zone has the outlet. The air is flowing from the inlet to the outlet of SPSAH. The reference work of SPSAH is considered as shown in the Figure 3.5.

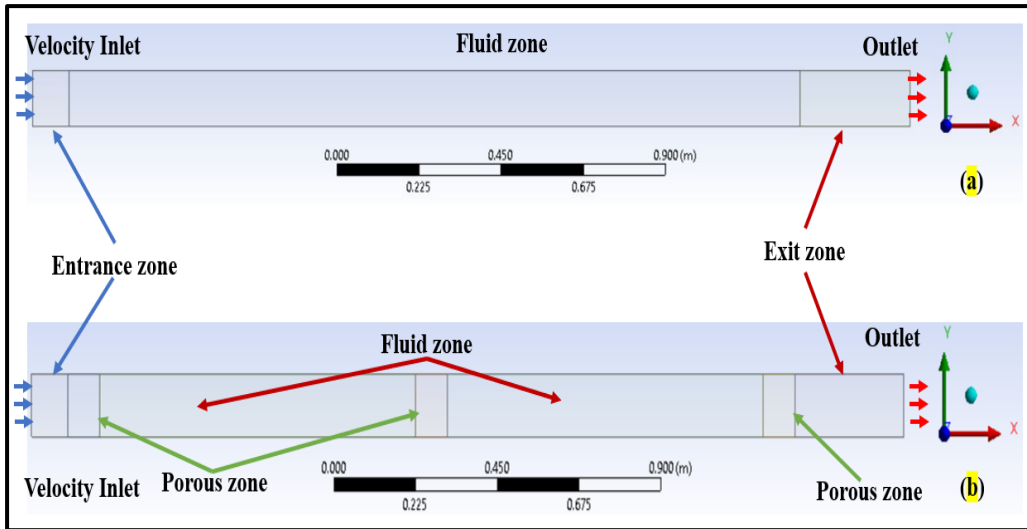


Figure 3.6 Two-dimensional geometry of SPSAH (a) empty channel, (b) 88 mm discrete metal foam at equal distances in the test section.

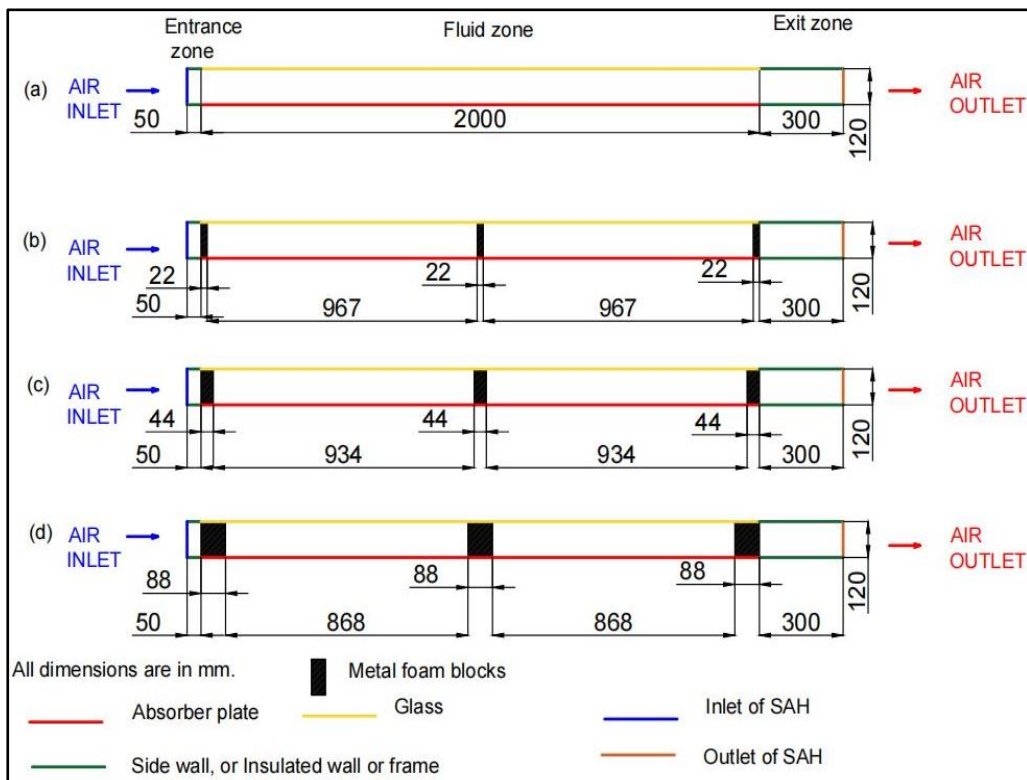


Figure 3.7 Schematic of SAH: (a) empty channel SAH, (b) 22 mm filled metal foam, (c) 44 mm filled metal foam (d) 88 mm filled metal foam in SPSAH.

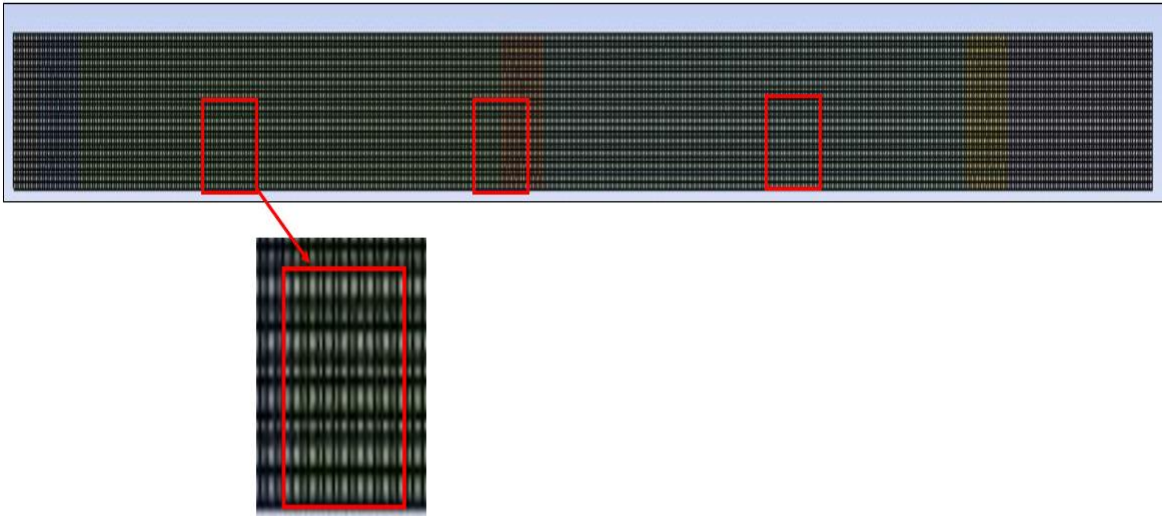


Figure 3.8 Quadrilateral mesh of 88 mm metal foam block in solar air heater.

Figure 3.6 shows the geometry of the empty channel and 88 mm discrete metal foam at equal distance in the test section. Similarly, the 22 and 44 mm discrete metal foams are arranged in the test section to enhancement of heat transfer in the SPSAH. Figure 3.7 shows the metal foam arrangement adopted for numerical study. The empty channel and porous bed analysis are done for the same heat flux, i.e., the same solar intensity falling on the SAH. Figure 3.8 shows the meshing for 88 mm metal foam thicknesses. The material properties and assumptions are considered as mentioned in the Table 3.1 and section 3.4.1 respectively. The detailed boundary conditions used during simulation are mentioned in Table 3.2. The planar-space steady-state pressure-based solver with double precision is considered for 2D analysis. The Renormalization group (RNG) k - ϵ viscous model with enhanced wall function is used in ANSYS Fluent for this study. A Green Gauss node-based method is used for the gradient to discretize the convection and diffusion terms. A second order upwind scheme is applied to discretize pressure, momentum, Turbulent kinetic energy, turbulent dissipation. The under-relaxation factors for pressure, momentum, turbulent kinetic energy, turbulent dissipation rate, turbulent viscosity, and energy are taken as 0.3, 0.7, 0.8, and 1, respectively. The relaxation factors for other terms are kept in unity by default. In solution initialization, standard initialization method is selected with computing from the inlet. The convergence criteria set for energy is 10^{-6} , while for other terms it is set as 10^{-4} .

Table 3.2 Boundary conditions used during simulation in SAH (Rajarajeswari et al. 2018; Singh 2020; Singh et al. 2019; Sukhatme 2018; Yadav and Bhagoria 2013).

	Momentum	Thermal
Inlet	Velocity magnitude as 0.3779, 0.3401, 0.3023, 0.2646, 0.2268, m/s	Inlet temperature = 27 °C
Outlet	Pressure outlet as zero	Back flow temperature = 27 °C
Absorber plate	Stationary wall No slip shear condition	Heat flux = 850 W/m ² Material = Aluminium Wall Thickness = 0.0005 m Bottom of the wall
Glass	Stationary wall No slip shear condition	Mixed Heat transfer coefficient (HTC) = 9.5 W/m ² K as wind speed assumed as 1 m/s Where, $h_w = 5.7 + (3.8 V_\infty)$ Free stream temperature = 27 °C External emissivity = 0.88 External radiation temperature = 27 °C Wall thickness = 0.004 m
Side wall and other wall	Stationary wall No slip shear condition	Heat flux = zero W/m ² i.e., adiabatic wall Material = wood Wall thickness = 0.018 m

3.5.2 Governing equations and turbulent modelling considering LTNE method

For fluid flow in SPSAH, continuity and Reynolds-Averaged-Navier-Stocks (RANS) equations are used. In this study, the Renormalization group (RNG) k-ε turbulence model with enhanced wall treatment is used, as it improves the performance.

Continuity equation for empty channel is mentioned in Equation 3.37,

$$\frac{\partial(\rho u_j)}{\partial x_i} = 0 \quad (3.37)$$

Continuity equation for metal foam is mentioned in Equation 3.38,

$$\frac{\partial(\rho \epsilon u_j)}{\partial x_i} = 0 \quad (3.38)$$

Momentum equation for empty channel is mentioned in Equation 3.39

$$\frac{\partial}{\partial x_j}(\rho u_i u_j) + \frac{\partial p}{\partial x_i} = \frac{\partial}{\partial x_j} \left[\mu \left(\frac{\partial u_i}{\partial x_j} + \frac{\partial u_j}{\partial x_i} \right) \right] \quad (3.39)$$

Momentum equation for metal foam channel is mentioned in Equation 3.40

$$\frac{\partial}{\partial x_j}(\rho u_i u_j) + \epsilon \frac{\partial p}{\partial x_j} = \frac{\partial}{\partial x_j} \left[\mu \left(\frac{\partial u_i}{\partial x_j} + \frac{\partial u_j}{\partial x_i} \right) - \epsilon \left(\frac{\mu_{\text{eff}}}{K} \mu_i + \rho C |u| u_i \right) \right] \quad (3.40)$$

Here, K is the permeability and C is the inertia coefficient.

Energy equation for fluid in empty channel,

$$\frac{\partial}{\partial x_i}(\rho u_j T) - \frac{\partial}{\partial x_j} \left[\lambda_f \frac{\partial T}{\partial x_j} \right] = 0 \quad (3.41)$$

To model flow through porous media in non-equilibrium thermal model, for simulations solid porous zone and fluid zone are not in thermal equilibrium. Hence, these two zones are interacted with heat transfer only.

For fluid zone equation as:

$$\epsilon \frac{\partial(\rho C_p u_j T)}{\partial x_j} = \lambda_{fe} \epsilon \frac{\partial}{\partial x_j} \left(\frac{\partial T_f}{\partial x_j} \right) + h_{sf} a_{sf} (T_s - T_f) \quad (3.42)$$

For solid zone equation as:

$$\lambda_{se} (1 - \epsilon) \frac{\partial}{\partial x_j} \left(\frac{\partial T_s}{\partial x_j} \right) = h_{sf} a_{sf} (T_s - T_f) \quad (3.43)$$

Where, $\lambda_{fe} = \lambda_f \cdot \epsilon$ and $\lambda_{se} = \lambda_s \cdot (1 - \epsilon)$ (3.44)

The properties of metal foam, for example fiber diameter, permeability, pore size and inertial coefficient are determined by Table 3.3. The detailed information on porous media metal foam is described in (Calmidi and Mahajan 2000; Jadhav et al. 2021, 2022). Table 3.4 gives the copper metal foam properties considered for present study.

The volume of the present porous metal foam block is considered a continuum with homogenous properties with respect to porosity and pore size. The similar homogeneous properties are considered in previous literature. The solid metal foam assumed here is gray and optically thick considering its absorption, isotropic scattering and emission properties throughout the length is same. The flow of air in metal foam is laminar and incompressible. The volume difference between metal foam before heating and after heating due to solar intensities are ignored (Sharma and Talukdar 2022).

In this study, to obtain the characteristics of porous media for SAH, a Darcy Extended Forchheimer (DEF) flow model is considered. The source term is added with the help of a viscous loss term and an inertial loss term. The DEF model is further joined with momentum equation as a source term. The inertial and viscous loss terms are calculated with the help of permeability and form drag coefficient of porous media. Calmidi and Mahajan (Calmidi and Mahajan 2000) have proposed metal foam properties as superficial area density and interfacial heat transfer coefficient, which are given by Equations 3.45 and 3.46.

Superficial area density

$$a_{sf} = \frac{3\pi d_f (1 - \exp^{-\frac{1-\varepsilon}{0.04}})}{(0.59d_p)^2} \quad (3.45)$$

Interfacial heat transfer coefficient

$$\frac{h_{sf} d_f (1 - \exp^{-\frac{1-\varepsilon}{0.04}})}{\lambda_f} = \begin{cases} 0.76 Re_{df}^{0.4} Pr^{0.37}, & (1 \leq Re_{df} \leq 40) \\ 0.52 Re_{df}^{0.5} Pr^{0.37}, & (40 \leq Re_{df} \leq 10^3) \\ 0.26 Re_{df}^{0.6} Pr^{0.37}, & (10^3 \leq Re_{df} \leq 2 \times 10^5) \end{cases} \quad (3.46)$$

where λ_f is the thermal conductivity of working fluid in W/m K, Pr is the Prandtl number, Re_{df} is known as Reynolds number calculated by the fibre diameter of the metal foam.

$$Re_{df} = \left\{ u d_f \left(\frac{1 - \exp^{-\frac{1-\varepsilon}{0.04}}}{\varepsilon v} \right) \right\} \quad (3.47)$$

where d_f is the fiber diameter in m, and d_p is the pore diameter in m.

3.5.3 Grid sensitivity analysis

The minimum size of the mesh is achieved by grid sensitivity analysis. Table 3.5 shows the details of the number of elements and its skewness. The simulations are performed

for four different mesh sizes. The temperature variation and change in pressure are shown in Table 3.5. The maximum number of elements is set as baseline and other elements are compared with it. 125,280 elements are preferred for further computational investigation because it has lesser deviation than other mesh sizes.

Table 3.3 Properties and its correlations of metal foam (Calmidi and Mahajan 2000; Jadhav et al. 2021).

Sr. No	Properties	Correlations
1	Pore size (d_p)	$d_p = \frac{0.0254}{PPI}$
2	Fiber diameter (d_f)	$\frac{d_f}{d_p} = 1.18 \sqrt{\frac{(1-\varepsilon)}{3\pi}} \left(\frac{1}{1 - e^{\left(\frac{1-\varepsilon}{0.04}\right)}} \right)$
3	Permeability (K)	$K = 0.00073(1-\varepsilon)^{-0.224} \left(\frac{d_f}{d_p}\right)^{-1.11} d_p^2$
4	Inertial/form coefficient (CI)	$CI = 0.00212(1-\varepsilon)^{-0.132} \left(\frac{d_f}{d_p}\right)^{-1.63}$

Table 3.4 Properties of Copper metal foam (Kamath et al. 2011, 2013)

PPI	Fiber Diameter	Pore Diameter	Porosity	Viscous Resistance	Inertial Resistance	Interfacial Area Density	Heat Transfer Coefficient
10	0.687	4.644	0.8769	1.742×10^{-7}	176.75	824.2496	85.8858
20	0.619	3.837	0.8567	2.490×10^{-7}	217.04	1106.8362	91.2402
30	0.703	4.732	0.92	1.644×10^{-7}	148.97	936.38	178.908

Table 3.5 Grid independence test

Number of elements	Max Skewness	Outlet Temperature, T_{out} , K	Pressure Drop ΔP , Pa	T_{out} Deviation (%)	ΔP Deviation (%)
70,499	0.273	334.41	0.053	0.2	0
92,652	0.278	334.45	0.053	0.009	0
125,280	0.004	334.47	0.053	0.002	0
180,480	0.0036	334.48	0.053	Baseline	

3.6 THREE-DIMENSIONAL NUMERICAL DOMAIN, ITS BOUNDARY CONDITIONS AND GOVERNING EQUATIONS FOR SPSAH USING GAWM

In the previous section the empty channel two dimensional SPSAH which is designed as per Figure 3.5 is modified for the standard commercial scale purposes. In the present section slightly modified the dimensions of the absorber plate to $2 \text{ m} \times 1 \text{ m}$ because of commercial scale, while the similar dimensions are as per (Rajarajeswari et al. 2018). Then to increase the heat transfer enhancement in the SPSAH, the combinations of the three different Aluminium wire mesh are added at different locations and compared it numerically. The outlet temperature is calculated with insertion of GAWM and it has compared with the empty channel SAH. Also, the thermohydraulic performance parameter is evaluated for combinations of different PPI and porosities of GAWM. The 3D geometry is the beneficial for getting realistic, practical characterization, for getting true and more accurate fluid flow and heat transfer visualization. Hence the 2D geometry is converted into 3D geometry in this section.

3.6.1 Details of geometry, meshing and boundary conditions

The standard commercial size of SAH is considered as 2 m^2 . The present SAH is developed based on the recent works of (Abed et al. 2017; Aldabbagh et al. 2010; Nowzari et al. 2015; Nowzari and Aldabbagh 2017; Omojaro and Aldabbagh 2010; Rajarajeswari et al. 2018). According to Rajarajeswari et al. (Rajarajeswari et al. 2018), where the absorber plate was considered to be $2 \text{ m} \times 0.9 \text{ m}$, the authors in the present study slightly modified the dimensions of the absorber plate to $2 \text{ m} \times 1 \text{ m}$ because of commercial scale, while the other dimensions are as per (Rajarajeswari et al. 2018). The detailed dimensions of the SPSAH are shown in the Figure 3.9. The air flow is in the x-direction. The quadrilateral mesh is selected for all of the entrance, test, or porous and exit zones. Figure 3.10 shows the geometry for empty channel and for the case of 25 % of the length of the WM of the full-length test section at a distance 1.5 m from the inlet. Figure 3.11 shows the quadrilateral mesh of the SPSAH for the case of 25 % of the length of the WM of the full-length test section at a distance 1.5 m from the inlet. The thermophysical properties of the fluid and wire mesh, as well as the surface radiation properties, can be found in Table 3.6. The material properties are calculated at a mean fluid temperature of $47.5 \text{ }^\circ\text{C}$. Similar considerations have been mentioned in previous works (Debnath et al. 2022; Kohol  et al. 2021; Nidhul et al. 2020, 2022; Patel

et al. 2021). The properties are assumed to be the same throughout the day. The boundary conditions for the momentum and energy equations, as well as for thermal radiation, are given in Table 3.7.

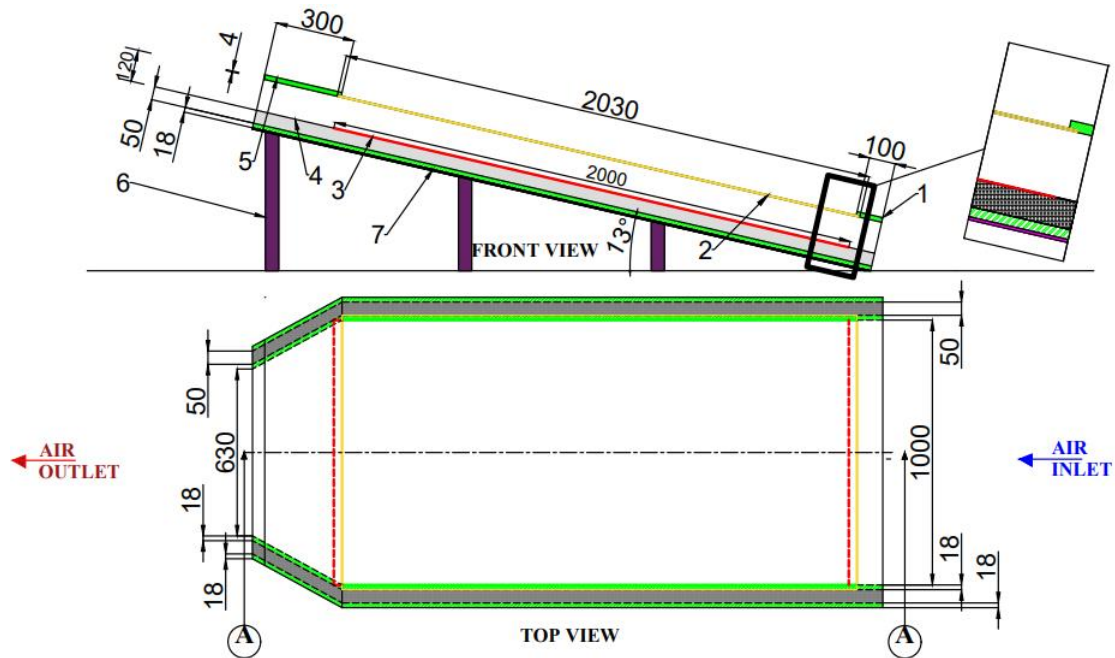
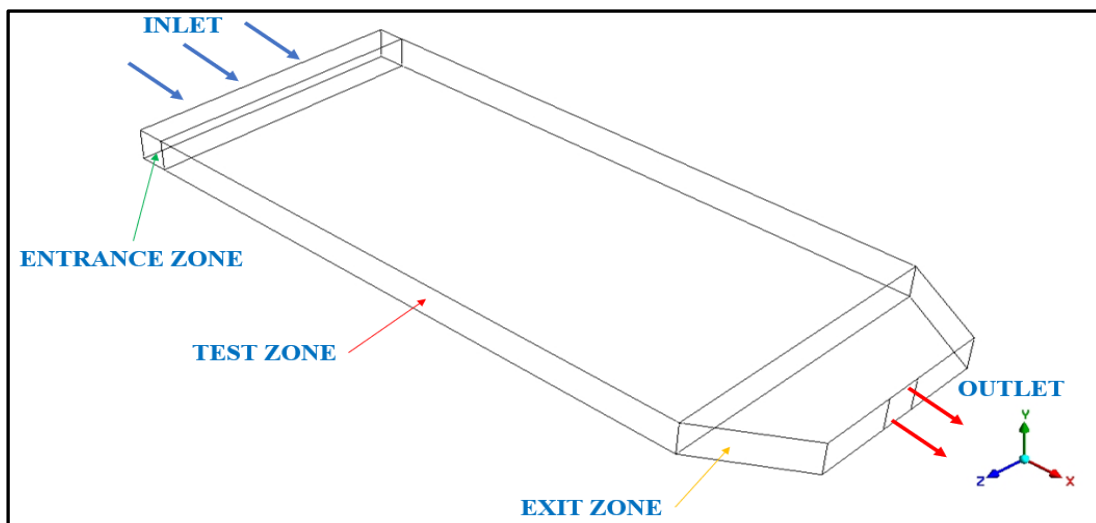
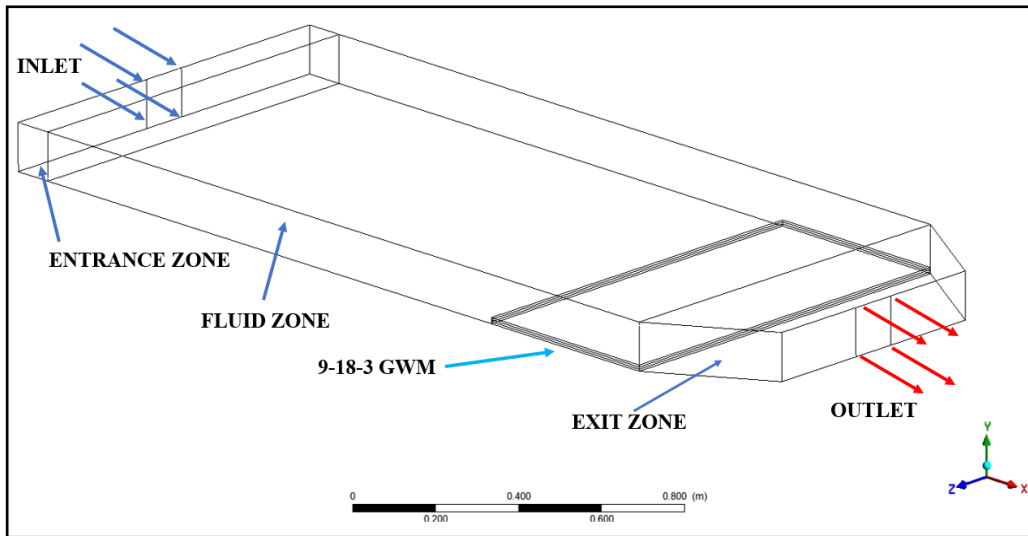


Figure 3.9 Layout of solar air heater with all its parts. (1) entrance section with PVC sheet (green colour line), (2) toughened glass (yellow colour line), (3) absorber plate (red colour line), (4) ceramic wool (grey colour hatch line), (5) exit section (green colour line), (6) support for SAH (purple colour line), and (7) base frame of SAH (green colour line); all dimensions are in mm.

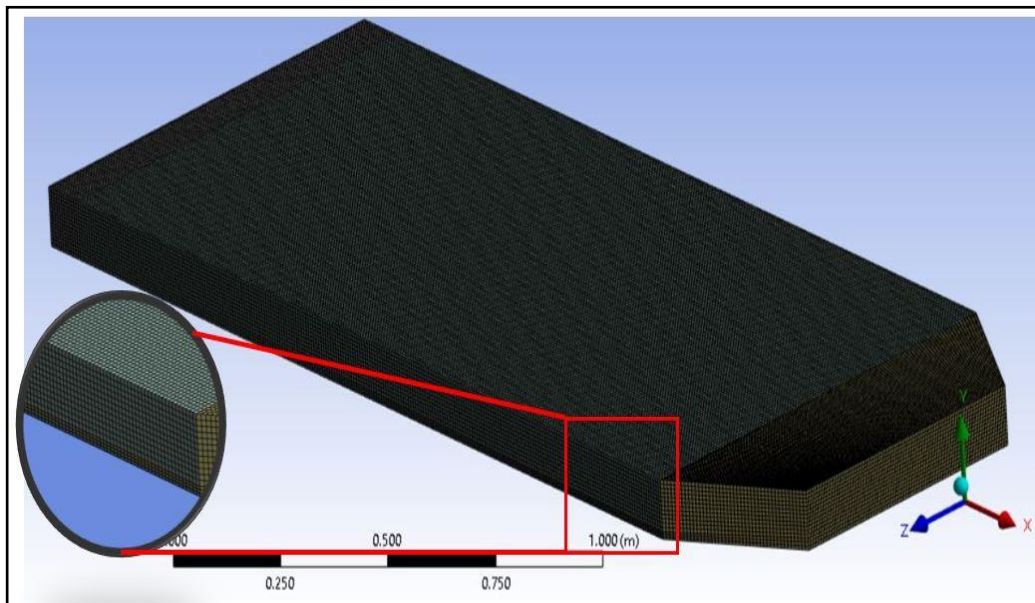


(a)



(b)

Figure 3.10 Numerical details of the 3D domain. (a) geometry of SPSAH for empty channel, (b) geometry of SPSAH for 9-18-3 PPI GWM with 25 % of the length of the WM full-length test section at 1.5 m from the inlet;



(c)

Figure 3.11 Quadrilateral mesh for 3D geometry for 9-18-3 PPI GWM with 25 % of the length of the WM full-length test section at 1.5 m from the inlet

Table 3.6 Material properties considered for CFD analysis of the present SAH (Marin et al. 2019; Hu et al. 2013; Kothandaraman. and Subramanyan 2018; Nidhul et al. 2022; Parsa et al. 2021).

Properties	Aluminium	Toughened Glass	Polyvinyl Chloride Board Sheet (PVC)	Ceramic Wool	Air 47.5 °C
Density (ρ) kg/m ³	2719	2500	0.55	64	1.1035
Specific heat capacity (Cp) J/kg K	871	670	900	1246	1005
Thermal conductivity (k) W/m K	202.4	0.7443	0.05	0.20	0.02805
Dynamic viscosity (μ) Ns/m ²	-	-	-	-	1.95×10^{-5}
Absorptivity	0.95	0.06	-	-	-
Emissivity	-	0.88	-	-	-
Transmissivity	-	0.90	-	-	-
Absorption coefficient	-	-	-	-	1
Refractive index	-	-	-	-	1

The computational domain consists of two parts, the first one is the empty part in which air flows and the second consists of a WM in which air flows between the gap of wires. The governing equations for these two parts are different. The governing equations for the empty part are traditional three-dimensional continuity, momentum, and energy equations in a cartesian coordinate system.

In the present study, 1.7 and 3.6 m/s are the flow velocities of air, which is less than 30 % of the speed of sound, i.e., the Mach number of flow is less than 0.3. Thus, the change in density due to fluid velocity is less than 5 %. Hence, the flow is assumed to be incompressible (Cengel 2006; Parsa et al. 2021; Sukhatme S P 2018). The experimental parameter assumed for global radiation incident on the SAH, ambient temperature, fluid flow rate, temperature rise across SAH, and fluid inlet temperature are assumed to be within $\pm 50 \text{ W/m}^2$, $\pm 1 \text{ }^\circ\text{C}$, $\pm 1 \%$, $\pm 1 \text{ }^\circ\text{C}$, and $\pm 1 \text{ }^\circ\text{C}$, respectively, within a 15 min duration (Sukhatme S P 2018). Thus, the system is assumed to be in a steady state. The obtained velocities measured via the anemometer and hydraulic diameter are used to

calculate the Reynolds number. The calculated Reynolds numbers are 11,544 and 24,447. Hence, the flow is turbulent in the entire channel in the conventional SAH or non-porous region. The recent literature shows that the Renormalisation group (RNG) $k-\epsilon$ viscous model with enhanced wall function is very much suitable for providing accurate results as per the experimental results of (Azad et al. 2021; Fluent 2022; Parsa et al. 2021; Yadav and Saini 2020; Zhao et al. 2021).

Table 3.7 Boundary conditions used during simulation in the SAH.

	Momentum	Thermal	Radiation
Absorber plate	Stationary wall No slip condition	Heat flux is flux absorbed by the absorber plate in W/m^2 which is equal to the product of $I_T (\tau\alpha)$ (Hu et al. 2013; Zhao et al. 2021). Absorber plate material is Aluminium and wall thickness is 0.0005 m	Opaque BC type and absorptivity is 0.95
Glass	Stationary wall No slip condition	Bottom of the wall Mixed (Hu et al. 2020; Hung et al. 2017; Jia et al. 2021) $h_w = 5.7 + (3.8 V_\infty)$ in W/m^2 (Jia et al. 2021; Kansara et al. 2021) Free stream temperatures are ambient temperature External emissivity is 0.88 External radiation temp is ambient temperature Wall thickness is 0.004 m	BC type—semi-transparent wall Absorptivity is 0.1 Transmissivity is 0.9
Side wall and other walls	Stationary wall No slip condition	Heat flux is zero W/m^2 , i.e., adiabatic wall Wall Material is PVC Wall thickness is 0.018 m	BC type is opaque and does not participate in solar ray tracing
Inlet	Velocity magnitude as 1.7 and 3.6 m/s, with turbulent intensity as 4.9696 and 4.5247, respectively, and hydraulic diameter as 0.12	Inlet temperature is obtained from experimental reading	Radiation condition is participating and factor is 1
Outlet	Pressure outlet as zero and hydraulic diameter as 0.12	Back flow temperature in the initial case same as inlet temperature	Radiation condition is participating and factor is 1

The advantages of this model are (i) the two equations produce a balance in CFD accuracy and time compared to other viscous models; (ii) the average absolute deviation is minimum relative to other viscous models (Yadav and Saini 2020); (iii) an additional term in its k-ε equation increases the accuracy for rapid flows; and (iv) the effect of the swirl on turbulence is involved in the RNG model which is more accurate for swirling flows (Fluent 2019). Hence, the RNG k-ε model with enhanced wall function is selected to obtain a higher accuracy in the present numerical study. The Reynolds number in the porous media is calculated. The calculated Reynolds number for porous media ranges from 26.92 to 1874. The Reynolds numbers are below 4000 ($Re_p < 4000$). The flow inside the porous media is laminar. Hence, in the computational steps, the flow in the porous region is selected as the laminar zone (Fluent 2019).

3.6.2 Governing equations and turbulent modelling considering LTE method

The Rosseland radiation model is simple for solving radiative heat transfer and preferred for optically thick media, where the optical thickness is greater than one (Marin et al. 2019). In the present study, the WM is considered as an optically thick media which takes part in the majority of the absorption of the incident solar radiation (Anirudh and Dhinakaran 2020).

The governing equation for the empty channel can be written as follows,

The continuity equation is Equation (3.48) (Jadhav and Gnanasekaran 2021),

$$\frac{\partial(\rho_f u_i)}{\partial x_i} = 0 \quad (3.48)$$

The momentum equation is Equation (3.49) (Jadhav and Gnanasekaran 2021),

$$\frac{\partial}{\partial x_j} (\rho_i u_i u_j) + \frac{\partial p}{\partial x_i} = \frac{\partial}{\partial x_j} \left[(\mu_f + \mu_t) \left(\frac{\partial u_i}{\partial x_j} + \frac{\partial u_j}{\partial x_i} \right) \right] \quad (3.49)$$

The energy equation with the LTE model is Equation (3.50) (Anirudh and Dhinakaran 2021; Gill et al. 2021),

$$\frac{\partial}{\partial x_i} (\rho_f u_j T) - \left(\frac{16\sigma T^3}{3K_R} + k \right) \frac{\partial}{\partial x_j} \left[\frac{\partial T}{\partial x_j} \right] = 0 \quad (3.50)$$

where σ is the Stefan–Boltzmann constant and K_R is the extinction coefficient.

The turbulent kinetic energy equation and rate of energy equations are Equations (3.51) and (3.52) (Fluent 2022),

$$u_j \frac{\partial k}{\partial x_j} = -u'_i u'_j \frac{\partial u_i}{\partial x_j} + \frac{\partial}{\partial x_j} \left(\frac{k_m \partial k}{\sigma_k \partial x_j} \right) - \varepsilon \quad (3.51)$$

$$u_j \frac{\partial \varepsilon}{\partial x_j} = -C_{\varepsilon 1} \frac{\varepsilon}{k} u'_i u'_j \frac{\partial u_i}{\partial x_j} + \frac{\partial}{\partial x_j} \left(\frac{k_m \partial \varepsilon}{\sigma_\varepsilon \partial x_j} \right) - C_{\varepsilon 2} \frac{\varepsilon^2}{k} \quad (3.52)$$

$$\text{where } \mu_t = \rho C_\mu \frac{k^2}{\varepsilon} \text{ and } k_m = \nu \left[1 + \left(\frac{C_\mu}{\nu} \right) \frac{k}{\varepsilon^{0.5}} \right]^2 \quad (3.53)$$

The values of the constants of the above equation are $C_\mu = 0.09$, $\sigma_k = 1.0$, $\sigma_\varepsilon = 1.30$, $C_{\varepsilon 1} = 1.44$, and $C_{\varepsilon 2} = 1.92$.

The governing equations for the second part of the computational domain in which wires are located in continuity, momentum, and energy equations for the fluid (air) and solid (wire mesh). Darcy extended Forchheimer is used in the momentum equation to include the effect of the porous media. The air and solid temperature are assumed to be equal in the porous zone; hence, the current study assumed the local thermal equilibrium (LTE) (Anirudh and Dhinakaran 2020; Jadhav and Gnanasekaran 2021; Rajarajeswari et al. 2018; Saedodin et al. 2017; Tian et al. 2004). The continuity equation,

$$\frac{\partial(\rho_f \Phi(u_i))}{\partial x_i} = 0 \quad (3.54)$$

The momentum equation for laminar flow (Jadhav and Gnanasekaran 2021),

$$\frac{\partial(\rho_f u_i u_j)}{\partial x_j} = -\phi \frac{\partial P}{\partial x_i} + \frac{\partial}{\partial x_j} \left\{ \mu_f \left(\frac{\partial u_i}{\partial x_j} + \frac{\partial u_j}{\partial x_i} \right) \right\} - \phi \left(\frac{\mu_{\text{eff}}}{K} u_i + \frac{\rho_f C_F}{\sqrt{K}} |u| u_i \right) \quad (3.55)$$

The momentum equation for turbulent flow (Jadhav and Gnanasekaran 2021),

$$\begin{aligned} \frac{\partial(\rho_f u_i u_j)}{\partial x_j} = & -\phi \frac{\partial P}{\partial x_i} + \frac{\partial}{\partial x_j} \left\{ (\mu_f + \mu_t) \left(\frac{\partial u_i}{\partial x_j} + \frac{\partial u_j}{\partial x_i} \right) \right\} \\ & - \phi \left(\frac{\mu_{\text{eff}}}{K} u_i + \frac{\rho_f C_F}{\sqrt{K}} |u| u_i \right) \end{aligned} \quad (3.56)$$

The energy equation with the LTE model (Anirudh and Dhinakaran 2021; Gill et al. 2021; Howell 2002),

$$\frac{\partial}{\partial x_i} (\rho_f C_{Pf} \langle u \rangle_j \langle T \rangle) - \left(\frac{16\sigma \langle T \rangle^3}{3K_R} + k \right) \lambda_{\text{eff}} \frac{\partial}{\partial x_j} \left[\frac{\partial T_f}{\partial x_j} \right] = 0 \quad (3.57)$$

where the effective viscosity is,

$$\mu_{\text{eff}} = \mu_f \quad (3.58)$$

Effective heat capacity is,

$$(\rho C_P)_{\text{eff}} = \Phi(\rho C_P)_f + (1 - \Phi)(\rho C_P)_s \quad (3.59)$$

Effective thermal conductivity is

$$\lambda_{\text{eff}} = \Phi\lambda_f + (1 - \Phi)\lambda_s \quad (3.60)$$

where K is considered as permeability and C_F is considered as inertia coefficient, respectively. The K_R has dependency on the location. In the porous media, the viscous resistance ($1/K$) and inertia coefficient (C_F) (Ansys Fluent 2022) are calculated by Equations (3.61) and (3.62),

$$(1/K) = \frac{d_w^2}{150} \frac{\Phi^2}{(1 - \Phi)^2} \quad (3.61)$$

$$C_F = \frac{3.5}{d_w} \frac{(1 - \Phi)}{\Phi^2} \quad (3.62)$$

where d_w and Φ are the wire diameter and porosity of the WM respectively.

The porosity (Φ) of the square WM is determined by Equation (3.63) (Chouksey and Sharma 2016; Rajarajeswari et al. 2018),

$$\Phi = 1 - \frac{\pi n d_w^2}{2 p_t D} \left(1 + \frac{d_w^2}{p_t^2}\right)^{1/2} \quad (3.63)$$

The porosity (Φ_d) of the diamond or expanded metal WM can be obtained by Equation (3.64) (Tian et al. 2004),

$$\Phi_d = 1 - \bar{\rho} \quad (3.64)$$

The relative density of the diamond ($\bar{\rho}$) type WM can be decided by Equation (3.65),

$$\bar{\rho} \equiv \frac{\rho}{\rho_s} = \frac{\pi N d_w^2}{2(1/n)} \sqrt{1 + \left(\frac{1}{1 + w/d_w}\right)^2} \quad (3.65)$$

The pore per inch (N) can be obtained by the following Equation (3.66),

$$N = \frac{1}{d_w + w} \quad (3.66)$$

The Reynolds number for the WM region (Re_Φ) can be determined by Equation (3.67) (Varshney and Saini 1998),

$$\text{Re}_p = \frac{4r_h G_0}{\mu} \quad (3.67)$$

The hydraulic radius (r_h) for the WM can be evaluated by Equation (3.68) (Varshney and Saini 1998),

$$r_h = \frac{\Phi d_w}{4(1 - \Phi)} \quad (3.68)$$

The relative mass velocity (G_0) can be found by Equation (3.69),

$$G_0 = \frac{\dot{m}}{A_f \Phi} \quad (3.69)$$

The turbulent intensity (T.I.) for the inlet velocity and pressure outlet boundary condition can be defined by Equation (3.70) (Ansys Fluent 2022),

$$\text{T.I.} = 0.16 (\text{Re})^{-1/8} \quad (3.70)$$

The general steps in the setup of ANSYS fluent tool has selected as 3D space, steady state condition, option of pressure-based solver choosing double precision. Also, serial processing option and absolute velocity formulation are selected. This is used in conjunction with coupled method for pressure velocity coupling scheme. The solution information adopted in the solving the numerical problem has given in Table 3.8.

Table 3.8 Details of the setup and solution in Numerical study

Pressure-velocity coupling scheme	Coupled
Spatial discretization -Gradient	Least square cell
Pressure	Second order
Momentum, Turbulent kinetic energy, turbulent dissipation rate, Energy	Second order upwind
Pseudo Time method	Global
Under relaxation factor in pressure, momentum, Turbulent kinetic energy, turbulent dissipation rate, Energy	0.3, 0.7, 0.8, 0.8
Monitors residuals absolute criteria for energy	10^{-6}
Monitors residuals absolute criteria for others	10^{-4}

3.6.3 Details of wire mesh as a porous media in SAH with its different arrangement and its geometrical parameters

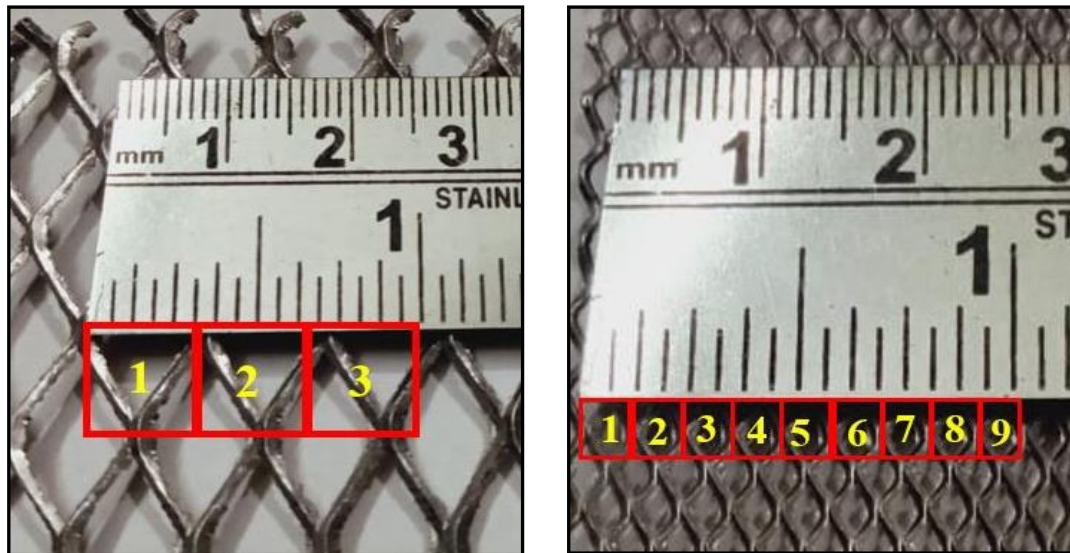
In the literature, researchers have mainly used Copper and Aluminium WM because of their high thermal conductivity and low weight compared to Iron, steel, and GI WM. In this study, Aluminium WM is selected, which is readily available in the market. Aluminium has a high thermal conductivity and a low cost compared to Iron, GI, and Brass WMs and a low weight compared to Copper, Iron, GI, and Brass WMs. Table 3.9 presents the detailed specifications of the Aluminium WM. It shows the types of WM and its properties.

Table 3.9 Geometrical parameters of Aluminium wire mesh.

Type of Wire Mesh	Diamond or Expanded Metal Mesh	Diamond or Expanded Metal Mesh	Square Mesh
Pore per inch (PPI)	3	9	18
Wire diameter d_w (mm)	0.91	0.48	0.21
Pitch P_t (mm)	6.862	1.7	1.26
Thickness of single-layer WM (mm)	1.804	1.176	0.618
Porosity Φ	0.894	0.812	0.917
Viscous resistance (1/K) (m^{-2})	2,546,508.72	34,898,955.12	30,116,606.43
Inertial resistance (C_F) (m^{-1})	570.58	2560.5	1865
P_t/d_w	7.54	3.54	6
The number of layers used to achieve 5 mm thickness	3	4	8
$1/n\Phi$	0.37	0.31	0.14

Figure 3.12 shows details of the size and shape of the Aluminium WM. The porosity of the WM is calculated as per the expression mentioned in (Devecioğlu et al. 2018; Nowzari et al. 2015, 2021; Sharma et al. 2017). The absorption of a greater solar intensity and maximum outlet temperature of air is ensured by applying matte black paint on the WM. Case 9-18-3 PPI indicates that a WM of 9 PPI is kept horizontally at the lower side, while a WM of 18 PPI and a WM of 3 PPI are kept above the WM of 9 PPI, respectively. Thus, the case acts as a GWM which has a different PPI porosity structure. The height of each WM is fixed as 5 mm in the present study. The length is 500 mm and the width is 985 mm to avoid scratches on the side walls and WM bending. The detailed pictorial view of GWM is shown in Figure 3.13 Case 9-18-3 PPI with a

full horizontal length and at 25 % of the length of the WM of the full-length test section arrangements of WM kept at four different locations are shown in Figure 3.14.



(a) 3 PPI, $\Phi = 0.894$

(b) 9 PPI, $\Phi = 0.812$



(c) 18 PPI, $\Phi = 0.917$

Figure 3.12 Size and shape of Aluminium WM available on the local market. (a) diamond or expanded metal mesh—3 PPI, (b) diamond or expanded metal mesh—9 PPI, and (c) square mesh—18 PPI.

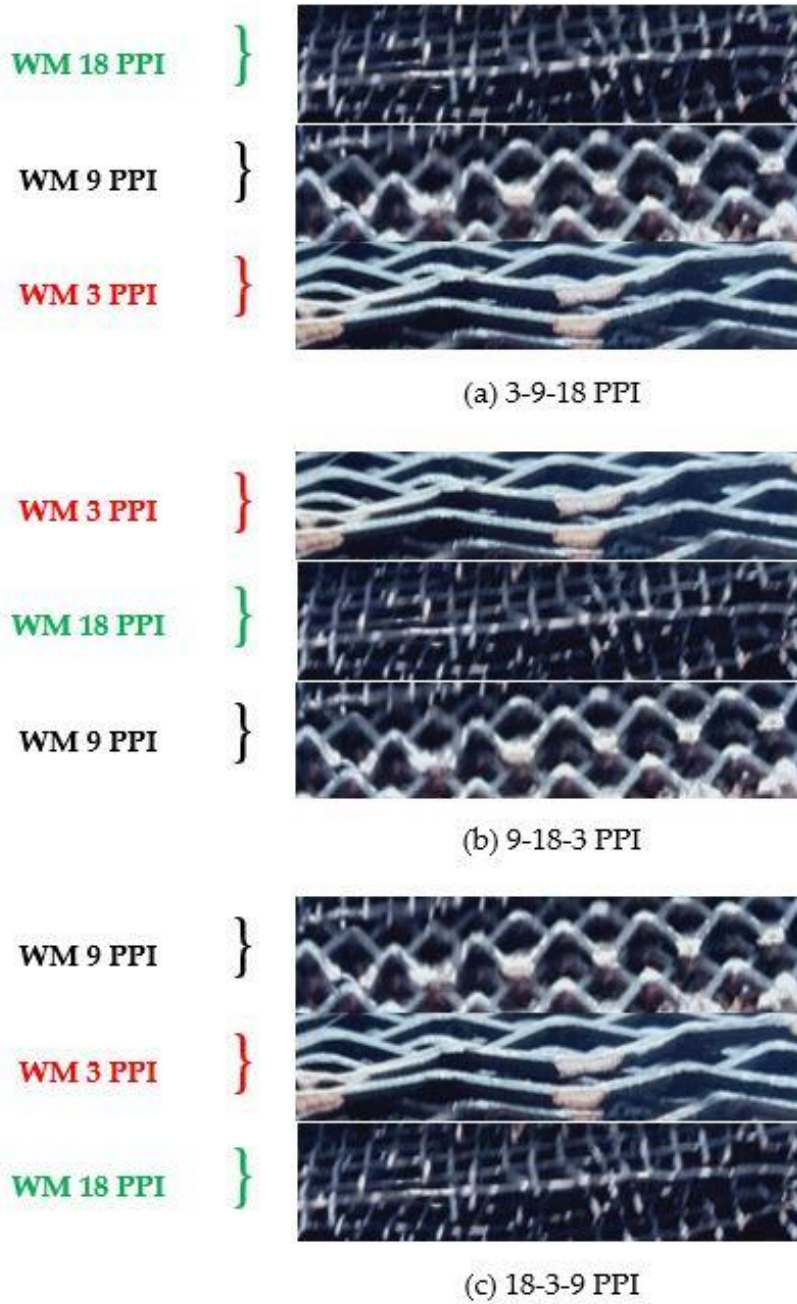


Figure 3.13 Detailed pictorial view of GWM arrangement in the channel of the SAH: (a) 3-9-18 PPI, (b) 9-18-3 PPI, and (c) 18-3-9 PPI.

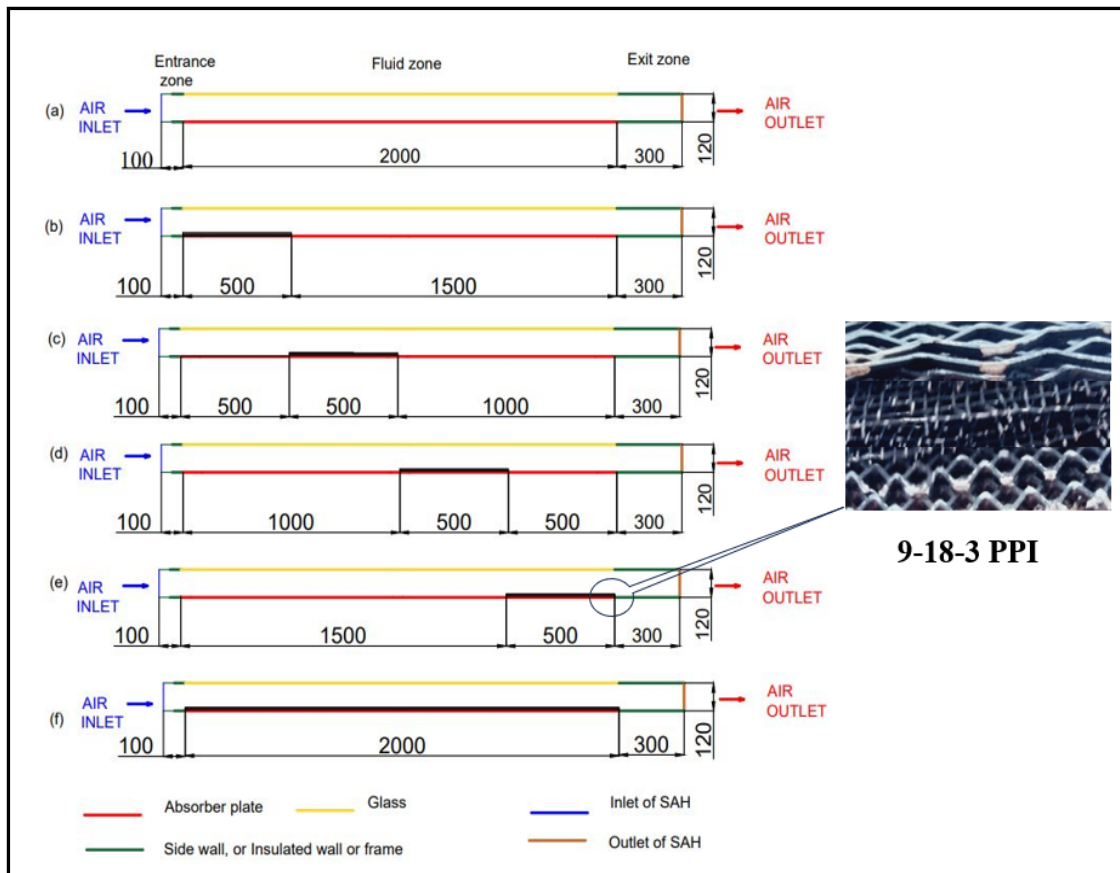


Figure 3.14 Arrangement of WM in SAH. (a) Empty channel, (b) case 1: 25 % of the length of the WM of the full-length test section and at a distance of 0 m from the inlet, (c) case 2: 25 % of the length of the WM of the full-length test section and at a distance of 0.5 m from the inlet, (d) case 3: 25 % of the length of the WM of the full-length test section and at a distance of 1 m from the inlet, (e) case 4: 25 % of the length of the WM of the full-length test section and at a distance of 1.5 m from the inlet, (f) case 9-18-3 PPI: WM with horizontal full length.

3.6.4 Grid sensitivity analysis

The grid study is significant for fixing the number of grids required to obtain the optimum temperature and pressure of the system. A uniform structured mesh with rectangular elements is used in the meshing of geometry. Table 3.10 shows the results of a grid study for different numbers of nodes. In total, 400,365 nodes for the empty channel and 409,136 nodes for the WM channel have lower deviation from the baseline. The percentage deviation is 0.01 % and 0.048 % for the outlet temperature and a 1.25 % and 0 % pressure drop in the empty channel SAH and WM SAH, respectively. Hence,

numerical analysis is performed with 400,365 and 409,136 nodes for the empty channel and the WM channel for further study. The grid-independence study for the outlet temperature is shown in Figure 3.15.

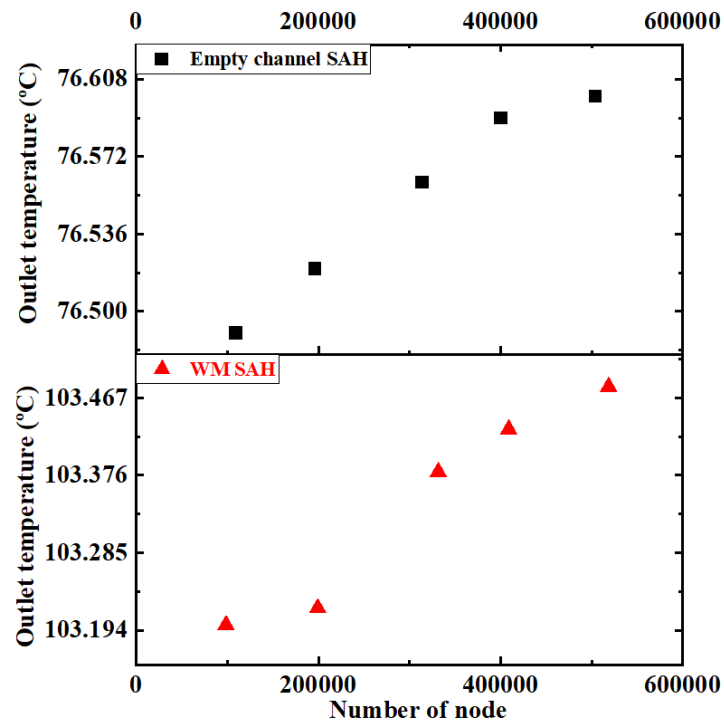


Figure 3.15 Grid-independence study for the empty channel and wire mesh at different nodes.

Table 3.10 Results of grid-independence study for $Re = 11,544$.

Case	Number of Nodes	Outlet Temperature in °C	Pressure Drop (ΔP) in Pa	% Deviation for $ T_o $	% Deviation for $ \Delta P $
Empty channel SAH	109,200	76.49	1.62	0.14	2.53
	196,224	76.52	1.62	0.11	2.53
	314,160	76.56	1.63	0.05	3.16
	400,365	76.59	1.60	0.01	1.25
	504,192	76.60	1.58	Baseline	
WM SAH	98,560	103.2	1.64	0.27	0.61
	199,281	103.22	1.64	0.25	0.61
	331,500	103.38	1.64	0.097	0.61
	409,136	103.43	1.65	0.048	0
	518,500	103.48	1.65	Baseline	

3.7 THREE-DIMENSIONAL NUMERICAL DOMAIN, ITS BOUNDARY CONDITIONS AND GOVERNING EQUATIONS FOR SPSAH USING TRANSVERSE AND LONGITUDINAL DIRECTIONS OF GAWM

In the previous section the empty channel three dimensional SPSAH is designed in the ANSYS fluent software then using meshing, setup and solution criteria the system is evaluated for the further thermal analysis of SPSAH. In the present section slightly modified the arrangement of the GWM as the transverse and longitudinal direction using 9 and 18 PPI as GAWM.

3.7.1 Details of wire mesh as a porous media in SAH with its transverse and longitudinal GAWM arrangements

The 9 and 18 PPI with full horizontal length each 3 layers kept above the absorber plate such as 9-18 PPI and 18-9 PPI as GWM in the transverse direction one over the other. After that the full length 3 layers are folded to have 50 % WM and made as 6 layers. Then, again 9-18 PPI and 18-9 PPI made as graded wire mesh in longitudinal direction one in front of another and compared it numerically. The types of WM and their properties are shown in the Figure 3.8. Case 9-18 PPI indicates that WM 9 PPI is kept horizontally at lower side, WM 18 PPI is kept above the 9 PPI. So, this acts as GWM which has different PPI and porosity structure. The layer of each WM in transverse direction is fixed as 3 in the present study. The length is 2000 mm and the width is 985 mm to avoid the scratches on side walls and WM bending. The detailed pictorial view of GWM is shown in Figure 3.16. The best combination is used for experimental trials. Also, it is used for practical application to dry the tomatoes and onions.

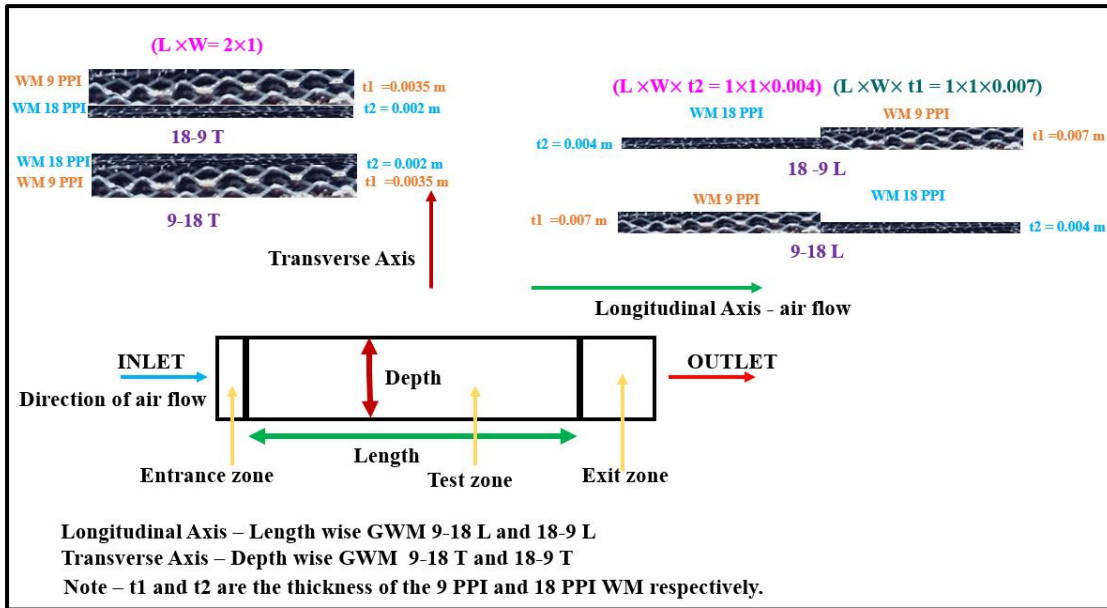


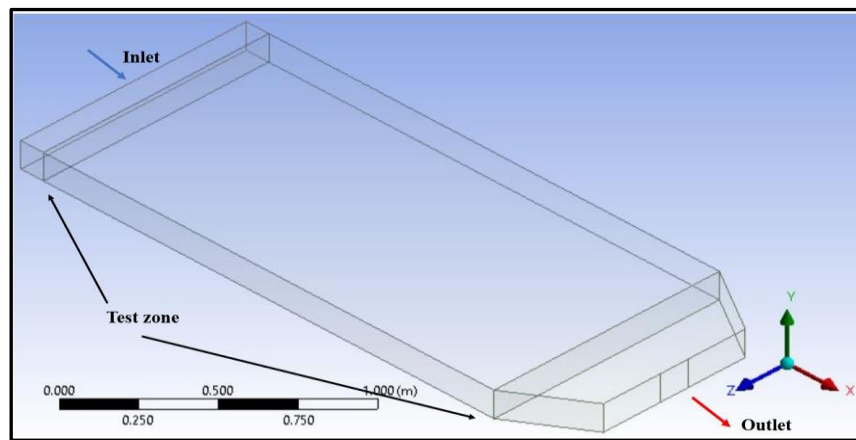
Figure 3.16 Schematic diagram of different arrangements of GWM (a) 9-18 PPI transverse GWM, (b) 18-9 transverse GWM, (c) 9-18 longitudinal GWM, (d) 18-9 longitudinal GWM.

3.7.2 Details of geometry, mesh generation and boundary conditions

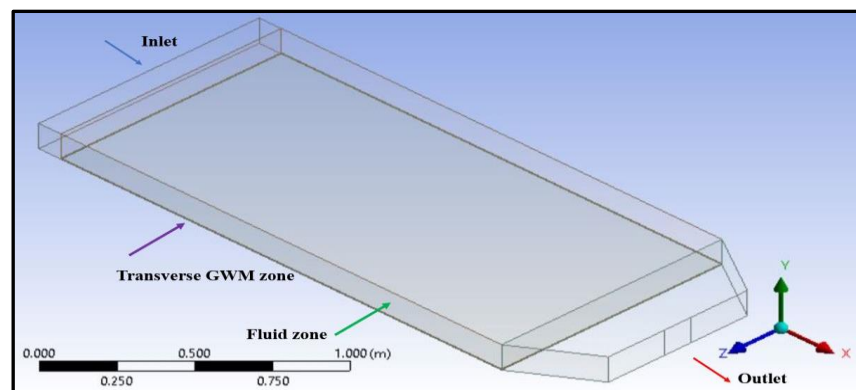
The computational fluid dynamics (CFD) analysis is done by ANSYS Fluent 2022 R2 software in 3-dimensional geometry. The entrance, test or porous and exit zones were the main parts of 3D geometry. The air was flowing with X -direction. The thermophysical and radiation properties of air and wire mesh are mentioned in Table 3.11. The properties of air are decided at the mean fluid temperature of 46.97 °C which is obtained from the empty channel experimental trails. Figure 3.17 and 3.18 shows the geometry and meshing of the 18-9 PPI WM respectively. The quadrilateral mesh was selected for all zones.

Table 3.11. Thermophysical and radiation properties of air and wire mesh (WM) (Kothandaraman and Subramanyan 2018).

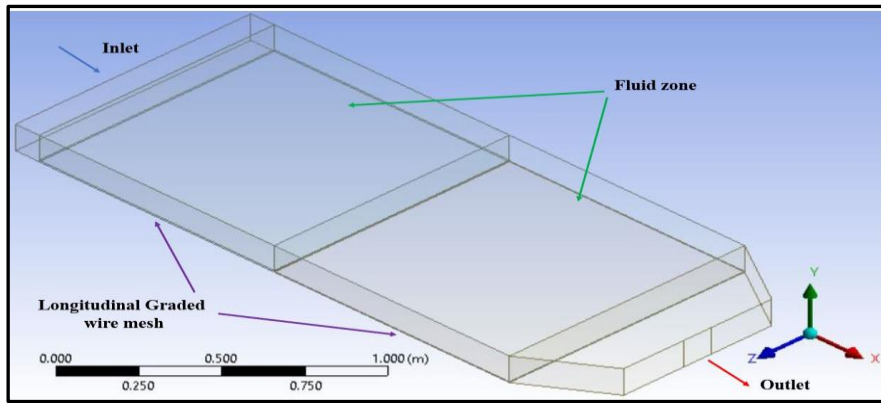
Properties	Aluminium	Toughened glass	Polyvinyl chloride board sheet (PVC)	Air 46.97 °C
Density (ρ) kg/m ³	2707	2500	0.55	1.1035
Specific Heat capacity (Cp) J/kg K	896	670	900	1005
Thermal conductivity (k) W/m K	204.2	0.7443	0.05	0.02805
Dynamic Viscosity (μ) Ns/m ²	-	-	-	1.95E-05
Absorptivity (α)	0.95	0.06	-	-
Emissivity (ϵ)	-	0.88	-	-
Transmissivity (τ)	-	0.90	-	-
Absorption coefficient	-	-	-	1
Refractive index	-	-	-	1



(a)

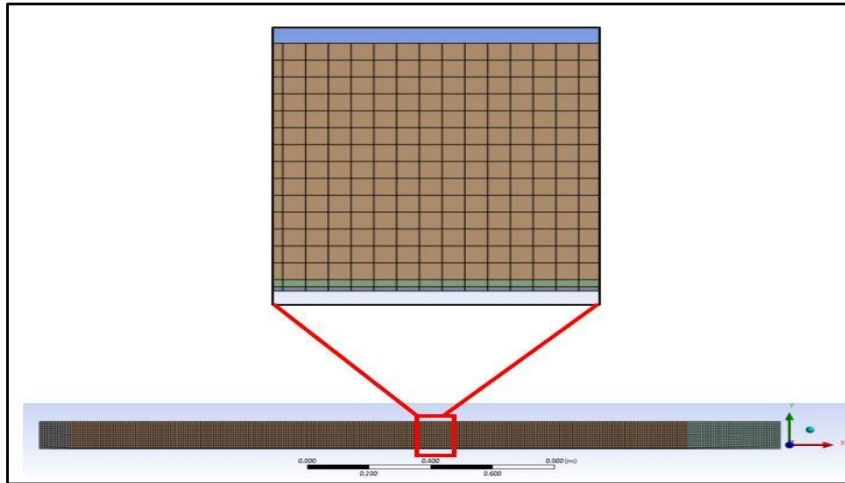


(b)

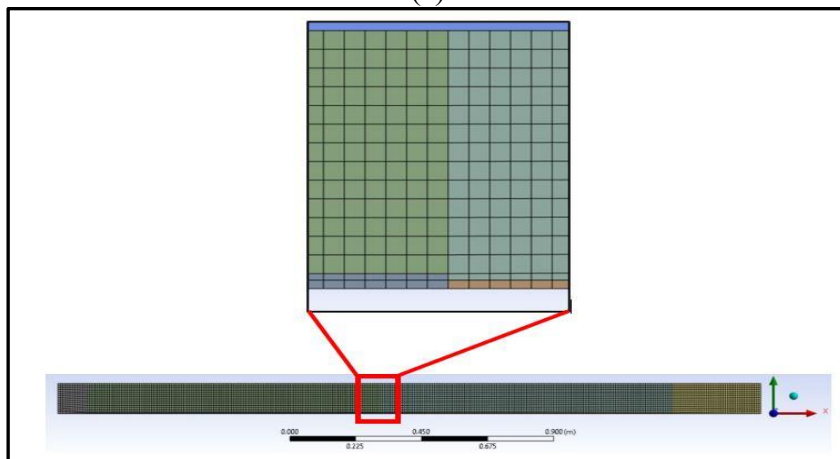


(c)

Figure 3.17 Geometry of 3D single pass SAH (a) empty channel SAH, (b) Transverse graded wire mesh, (c) Longitudinal graded wire mesh.



(a)



(b)

Figure 3.18 Quadrilateral meshing of SAH (a) the transverse graded wire mesh, (b) the longitudinal graded wire mesh type SAH.

The implementation of boundary conditions is applied as mentioned in the Table 3.6 which is mentioned in section 3.6.1. The set up and solution criteria as mentioned in the section 3.6.1.

3.7.3 Governing equations and turbulent modelling considering LTE method

The governing equations and LTE method are used as mentioned in the previous section 3.6.2.

3.7.4 Analysis of outlet temperature and pressure drop at different number of elements – evaluation of mesh refinement

The optimum mesh size is calculated from different number of mesh elements. The temperature rise is calculated at six different number of mesh elements. The change in temperature rise is observed by drawing the graph of number of elements to temperature rise for each configuration. It is observed that, as the number of mesh increases, the deviation in temperature rise is lower. Also, the accuracy increases. The final mesh size is selected on the basis of change in the temperature rise. The deviation has been calculated with respect to base line value.

The evaluation of mesh refinement is essential in the numerical simulation in order to get the solution near to the actual solution. The change in the rise in temperature and pressure drop with their deviation with respect to base line for number of elements is shown in the Table 3.12 for Reynolds number 4134 and heat flux 707 W/m^2 . The grid studies for empty channel, 18-9 L, 9-18 L, 18-9 T and 9-18 T are shown in Figure 3.19 for rise in temperature in the form of graph. Five different number of elements are considered to examine the deviation in the temperature and pressure drop. 376278, 387436, 188320, 378000, 386295 are the selected number of elements for the further numerical study because of less deviation compared to baseline for empty channel, 18-9L, 9-18L, 18-9 T, 9-18 T respectively.

Table 3.12 Results of grid study (Re = 4134, Heat flux = 707 W/m²)

Number of elements	Avg. skewness	Rise in temperature ΔT (°C)	Pressure drop ΔP (Pa)	% Deviation in $ \Delta T $	% Deviation in $ \Delta P $
SAH with empty channel					
96111	2.73E-02	33.16	1.06	0.33	37.66
191290	2.74E-02	33.14	0.89	0.27	15.58
280644	2.73E-02	33.05	0.86	0	11.69
<u>376278</u>	<u>2.71E-02</u>	<u>33.05</u>	<u>0.84</u>	<u>0</u>	<u>9.09</u>
466500	2.73E-02	33.05	0.77	Base line	
SAH with porous channel 18-9 PPI longitudinal direction					
95040	3.63E-2	58.26	1.11	0.03	44.15
209280	3.28E-2	58.28	0.97	0	25.97
299000	3.23E-2	58.28	0.86	0	11.69
<u>387436</u>	<u>3.26E-2</u>	<u>58.28</u>	<u>0.76</u>	<u>0</u>	<u>1.30</u>
465450	3.28E-2	58.28	0.77	Base line	
SAH with porous channel 9-18 PPI longitudinal direction					
92070	3.73E-2	57.54	1.01	0.02	46.38
<u>188320</u>	<u>3.54E-2</u>	<u>57.54</u>	<u>0.86</u>	<u>0.02</u>	<u>24.64</u>
277264	3.41E-2	57.54	0.96	0.02	39.13
364420	3.29E-2	57.49	0.86	0.07	30.43
469800	3.43E-2	57.53	0.69	Base line	
SAH with porous channel 18-9 PPI transverse direction					
83655	3.04E-2	57.45	1.14	0.05	52
185736	2.97E-2	57.47	0.99	0.02	32
304584	2.89E-2	57.48	0.85	0	13.33
<u>378000</u>	<u>2.99E-2</u>	<u>57.48</u>	<u>0.81</u>	<u>0</u>	<u>8</u>
467152	2.86E-2	57.48	0.75	Base line	
SAH with porous channel 9-18 PPI transverse direction					
78228	3.16E-2	57.45	1.14	0.05	52
184884	2.98E-2	57.47	0.98	0.02	30.7
309288	2.92E-2	57.47	0.83	0.02	10.7
<u>386295</u>	<u>2.94E-2</u>	<u>57.48</u>	<u>0.78</u>	<u>0</u>	<u>4</u>
467152	2.86E-2	57.48	0.75	Base line	

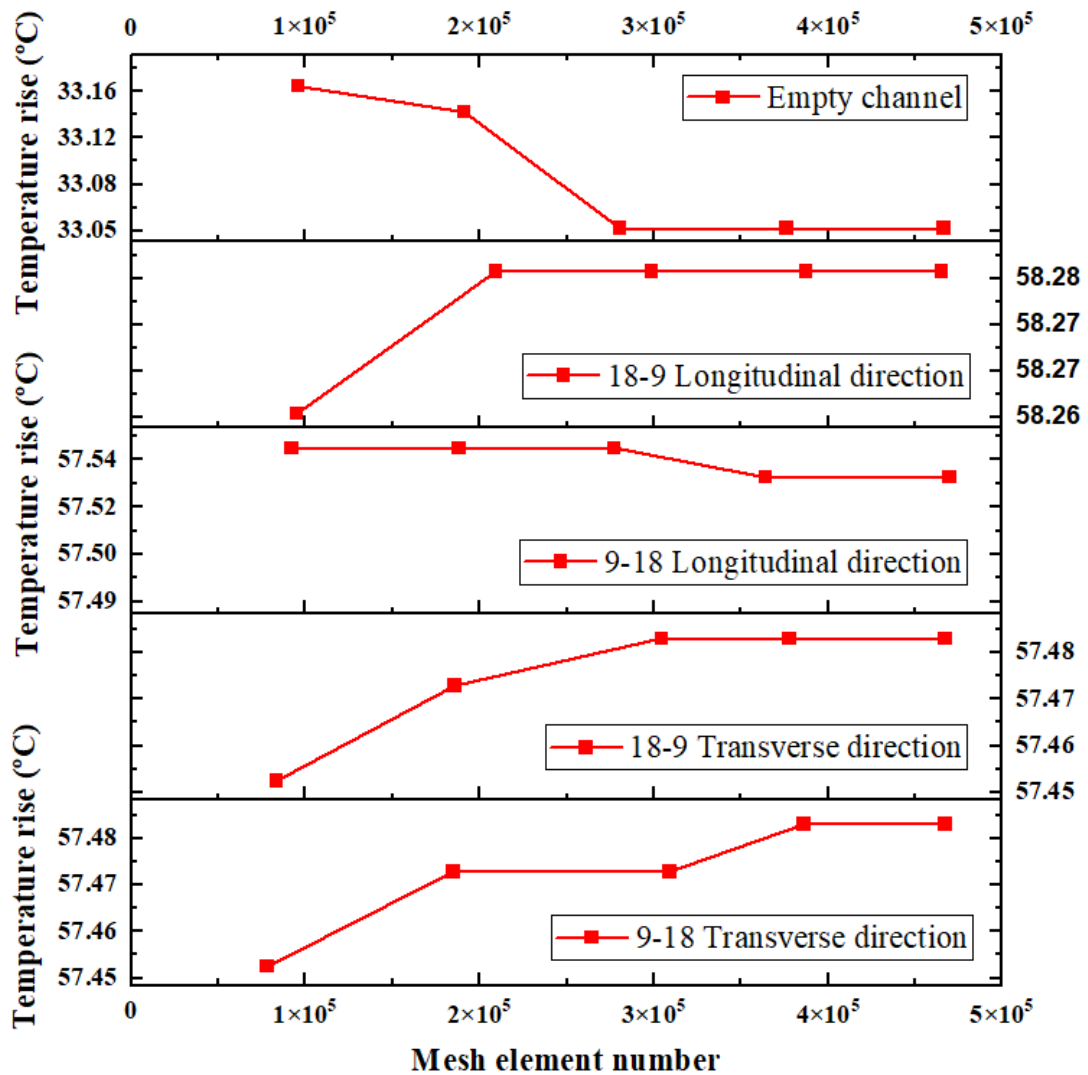


Figure 3.19 Variation in rise in temperature with change in number of mesh element at $Re = 4134$, Heat flux = 707 W/m^2 .

3.8 EXPERIMENTAL SETUP

The experimental trails are required to observe the actual performance of the SPSAH, which is helpful for practical application. The first stage is analytical method, then numerical design of 2D and 3D SPSAH had analysed with respect to performance factor and thermal efficiency of it. Then it has compared with the previous literature to check the quality and capacity of the outlet parameters. After getting true results of analytical and numerical study, comparing with the literature, one can start to build the prototype or actual model of the system. The detailed flowchart to present the experimental procedure is shown in figure 3.20.

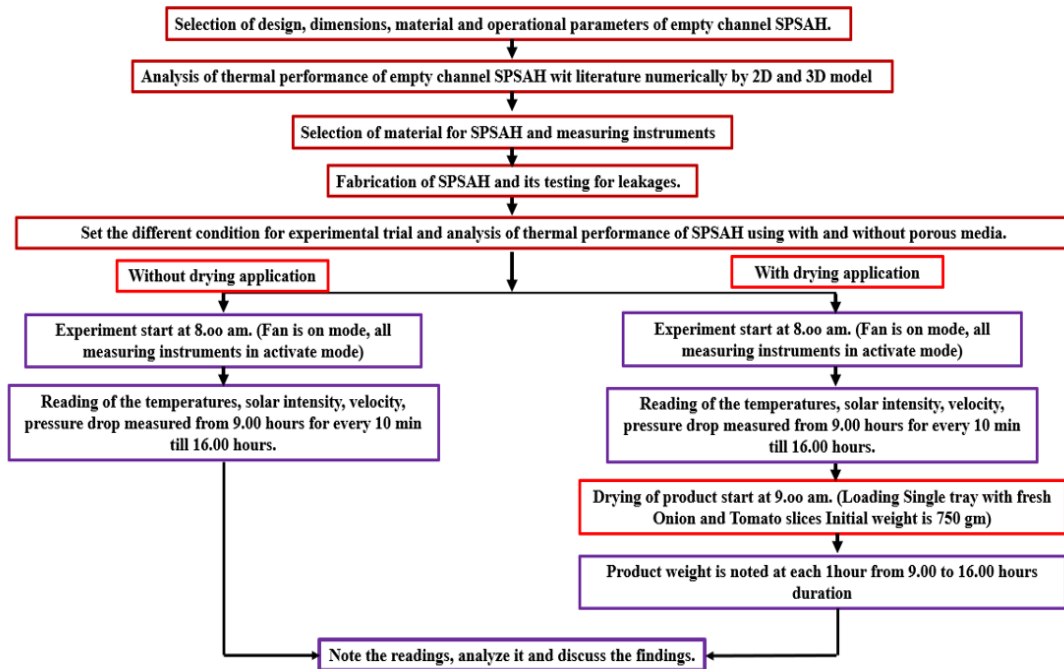
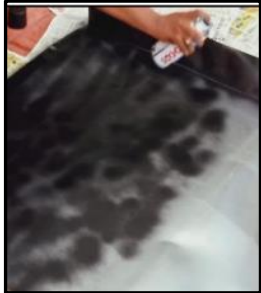






Figure 3.20 Flow chart for the experimental procedure

The SAH design is made up of one toughened piece of glass that acts as a transparent cover and an Aluminium plate that acts as an absorber plate. The insulation material considered is ceramic wool, and the outer box is composed of a polyvinyl chloride (PVC) sheet. Air flows between the transparent cover and the absorber plate. The Aluminium plate is painted with matte black spray paint to obtain a high absorptivity and to reduce the reflection of solar radiation from the Aluminium plate. Insulation with a thickness of 50 mm reduces the heat losses from the bottom and side walls. The frame of a mild steel angle is used to provide support to the experimental SAH. The detailed sizes of different parts of SAH with a pictorial view are mentioned in Table 3.12.

The WM layers are placed horizontally above the absorber plate between the transparent cover and the absorber plate. A soap bubble test is performed to check for leakages present in between the joints. An epoxy compound and silicon sealant is used to avoid leakages in the joints. Figure 3.9 shows the dimensions and the type of materials of the SAH. The trapezium-type section is provided at the exit section to mix the hot air.

Table 3.13 Specifications of SAH for experimental setup

Description of main SAH parts, Medium, and Size (mm) (L × W × t)	Pictorial view
Absorber plate, Matte black-painted Al, 2000 × 1000 × 0.5	
Transparent cover, Toughened glass, 2030 × 1030 × 4	
Insulation, Ceramic wool, For the base wall- 2000 × 1000 × 50, For both side walls- 2000 × 170 × 50	
Outer body, Polyvinyl chloride, For the base wall - 2400 × 1172 × 18 For both side walls- 2400 × 170 × 18	
Matte black paint	

The assembly of different parts are connected with the help of screws, nut and bolt arrangement as per the required size and shape. The angle of tilt of SAH with the ground surface is equal to the latitude of the location. The tilt angle equals the location's

latitude, as mentioned in (Devecioğlu et al. 2018; Garg and Prakash 2016; Kesavan et al. 2019; Omojaro and Aldabbagh 2010; Prasad et al. 2009; Rajarajeswari et al. 2018; Sukhatme and Nayak 2018). The facing south direction of SAH is beneficial for getting more solar radiation on the absorber plate. The experimental readings are considered under the climatic conditions of Surathkal, Karnataka, India (12.991° N, 74.81° E). This 13° angle is prepared with the help of a strong frame made up of MS material to support the complete SAH.





3.8.1 Experimental set up – details of 25 % of full-length test section at 1.5 m away from the inlet for the case 9-18-3 PPI of the GAWM

The experimental readings are taken during partly cloudy days in September 2022. It is impossible to achieve clear sunny days for full days and months. Hence, the average solar intensity of all experimental days is compared with clear sunny days. Thus, the average sunshine factor is 0.66 for all experimental readings. The reading is taken from 9:00 hr to 16:00 hr (Güler et al. 2020; Nowzari et al. 2021) for each velocity for three days. The temperature, solar radiation, wind speed is measured every 10 min and considered for evaluating the thermal efficiency of SAH. A 12 V DC battery which operates an exhaust fan is used to flow the air from the inlet to the outlet of the SAH. The mass flow rate is maintained as constant using a speed controller attached to the exhaust fan. The experimental trials are performed for two different air flow rates containing a minimum and a maximum of 0.027 and 0.058 kg/s, respectively. Similarly, in the recent literature, experiments are performed for two mass flow rates (Nowzari and Aldabbagh 2017; Sözen et al. 2020). The exhaust fan is started well before taking the reading to obtain a steady state flow of ambient air.

A PT100 RTD sensor is connected to the universal data logger to measure the temperature of the SAH at different locations. The fluid temperatures are measured at the inlet and outlet of the SAH. The temperatures for the absorber plate and glass cover are measured at the beginning, middle, and end, respectively. The ambient temperature is measured below the solar air heater. The data from the logger are evaluated by the DAS software version 10.4 (Ranake 2021.). The anemometer is used to measure the velocity across the square section of 120 mm at the entrance section. A differential pressure transmitter and solar radiation sensor are used to measure the pressure drop across the absorber plate and the incident solar radiation, respectively. The details of

the measuring instruments are mentioned in Table 3.14. The details of the locations of the measuring instruments are shown in Figure 3.21. The experimental setup front view and back side view are shown in Figure 3.22.

Table 3.14 The measuring instruments used during experimental trials

Name of the Instrument	Model
<p>RTD PT-100 thermocouples Make- Heatron industrial heater, Baikampadi, Mangalore, India. Model- class 1/3 rod type and Flat type or surface mounting. Quantity – Rod type – Nine numbers, Flat type – Six numbers. Range -0 to 1200 °C. Accuracy – ± 1 °C. Role of the instrument – To measure the temperature at a particular location.</p>	
<p>Wind speed sensor Make - Sunsui process system, Pune, India. Model -Mini Cup anemometer - OC ANEMO 01, Quantity – One. Range and Accuracy – 0 to 50 m/s, 2 %. Role of the instrument – To measure the wind speed of air in the atmosphere.</p>	
<p>Solar radiation sensor Maker - Solar radiation sensor, Model - Pyra 300 V, Quantity – One. Range and Accuracy - 0 to 1800 W/m², ± 5 %. Role of the instrument – To measure solar intensity.</p>	
<p>Differential pressure transmitter Make – Sunsui process system, Pune, India (Sensocn) Model – Series 211 Quantity – One Range and Accuracy – -250 to +250 Pa, 0.5 % or 0.25 % Role of the instrument – To measure the pressure drop across the absorber plate, i.e., test section.</p>	

Vane probe anemometer,
 Make- Mextech Mumbai, India.
 Model -AM 4208
 Quantity- One
 Range and Accuracy- 0.4–45 m/s, $\pm 2\%$
 Role of the instrument- To measure the velocity at inlet
 of the duct



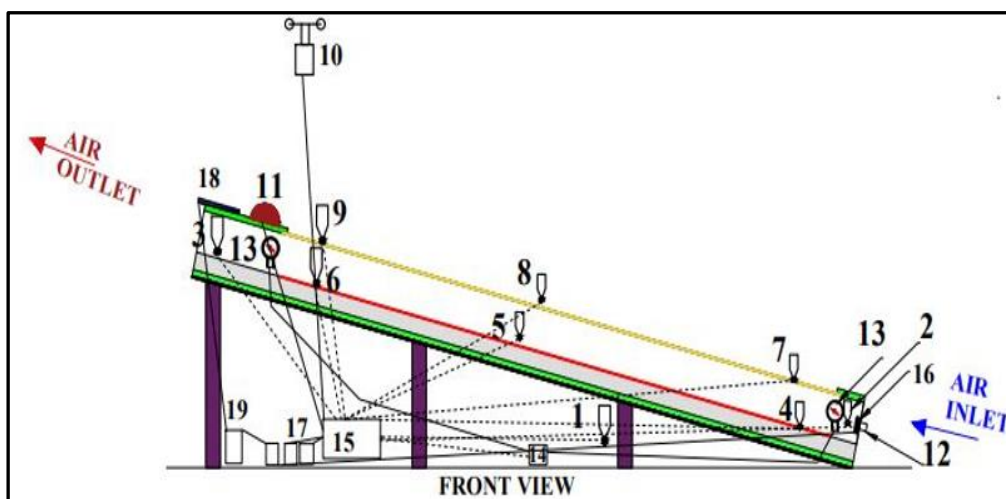
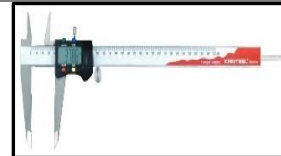
Universal data logger
 Make - Sunsui process system, Pune, India.
 Model- Touch screen data logger (DL -35-16 channel)
 Quantity – Two
 Range and Accuracy – -200 to 300 °C, 0.1 %.
 Role of the instrument -To convert the readings into
 digital format and display and save the reading.



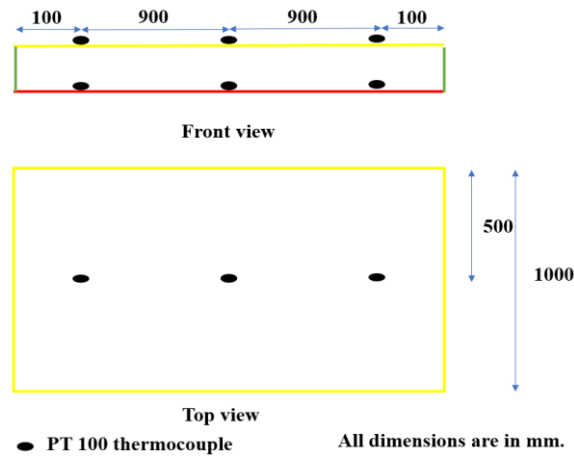
Measuring tape
 Make- Venus-Stylo
 Model- 5 m
 Quantity – one
 Range and Accuracy- 0 to 5 m, ± 0.001 m
 Role of the instrument - To measure the length, width,
 and height of the parts.



Digital textile Vernier Calliper
 Make- Kristeel-Shinwa
 Model- 3982
 Quantity- one
 Range and Accuracy- 0 to 0.015 m, ± 0.01 m
 Role of the instrument- To measure the internal and
 external dimensions of the object.



(a)



(b)

Figure 3.21 Details of the measuring instrument arrangement on the SPSAH (a) 1. PT 100 thermocouple for the ambient temperature (T_a), 2. for the inlet temperature (T_i), 3. for the outlet temperature (T_o), 4. for the temperature of the absorber plate at the inlet side (T_{absi}), 5. for the temperature of the absorber plate at the middle (T_{absm}), 6. for the temperature of the absorber plate at the outlet side (T_{abso}), 7. for the temperature of the glass at the inlet side (T_{gi}), 8. for the temperature of the glass at the middle (T_{gm}), 9. for the temperature of the glass at the outlet side (T_{go}), 10. Anemometer for measuring wind speed (WA), 11. Solar pyranometer (SPM), 12. Anemometer for measuring inlet air velocity (AA), 13. Pressure tap across the test section, i.e., at the inlet side (P_{in}) and at the outlet side (P_{out}), 14. Differential pressure transmitter (DPT), 15. Data logger (DL), 16. A 12 V DC fan, 17. A 12 V DC battery, 18. Solar panel (SP), 19. Charge controller. (b) Arrangement of PT 100 thermocouples kept on the glass and absorber plate (Kesavan et al. 2019; Rajarajeswari et al. 2018; Singh 2022).







Figure 3.22 Details of the experimental setup of SAH (a) front side view (b) backside view.

3.8.2 Experimental set up – details of 9-18 L GAWM (longitudinal direction 9-18 PPI AWM)

The experimental tests are supervised in May month during sunny days. The experimental test readings took from morning 9.00 hrs to evening 16.00 hrs. for all days. The experiments were performed in the morning at 8.00 hrs for all tests to achieve a steady state. Solar radiation coming from the Sun travels through the toughened glass. The matte black-painted absorber plate absorbs the solar rays coming from the Sun. Therefore, the absorber plate gets heated. The air is flowing through the inlet towards the outlet because of 12 V DC exhaust fan in forced convection systems. The 3 W solar panel with a charge controller and 12 V DC operated battery are attached to the 12 V DC exhaust fan. Due to the convection process, the air acquires heat inside the entire channel of SAH while flowing over the absorber plate. Thus, the outlet temperature of SAH is obtained higher than the inlet temperature of SAH. Thus, all the measuring instruments are joined to the touch screen universal data logger as per the instructions in the manual associated with the wiring of each measuring instrument. 12 V DC two batteries joined in sequence to create a 24 V DC supply and attached to the universal data logger. Thus, the data logger is started by the batteries for the entire experimental test. The measured readings are recorded into the pen drive. Then it observed with the help of data acquisition software (DAS) (Ranake 2021.) for comparative study. The accuracy, range, role of the instrument, make and model are given in the Table 3.14. In addition to that, the other instruments during drying application are mentioned in details in Table 3.15.

The product drying is performed for Onion and Tomato which are collected from the local market. The analysis is done with 250 gm of each configuration by open channel, empty channel and 9-18 L GAWM. In the initial stage, tomatoes are washed with water and cleaned. The Onions used with removing initial covers and then good onions are used to dry. The Onions and Tomatoes are cut in equal slices by using special machine. The weight of the Onion and Tomato before and after drying is performed by weighing machine which is shown in the Figure 3.23. The detailed experimental set up is shown in Figure 3.24.

Table 3.15 The measuring instruments used during drying application experimental trials

Name of the instrument	Model
<p>Air velocity transmitter Make and Model- Sunsui process system, Pune, India, EE 75. Quantity – One Range and Accuracy – 0 to 40 m/s, ± 0.20 m/s + 2% Role of the instrument – To measure the air velocity inside the channel.</p>	
<p>Temperature Humidity Sensor Make - Sunsui process system, Pune, India. Model- THX 32 CHB Quantity – Two Range – Temperature 0 to 50 °C, Humidity 0 to 100 %. Accuracy – +/- 0.3 °C, $\pm 2\%$ RH from 20 to 80 % RH; $\pm 3.5\%$ RH below 20 and above 80 % RH @ 22 °C. Role of the instrument -To measure the temperature and humidity at ambient and inlet of SAH.</p>	
<p>Temperature Humidity Sensor Make - Sunsui process system, Pune, India. Model- Rotronic XB3 OEM Series Quantity – One Range – Temperature 0 to 200 °C, Humidity 0 to 100 %. Accuracy – +/- 0.2 °C, $\pm 1\%$ RH @ 23 °C. Role of the instrument -To measure the temperature and humidity at the outlet of SAH.</p>	
<p>Weighing machine Make –Samsung Model- S10 Quantity-One Range and Accuracy– 0 to 10 kg, ± 0.03 kg Role of the instrument- To measure the weight of the product</p>	



(a)



(b)

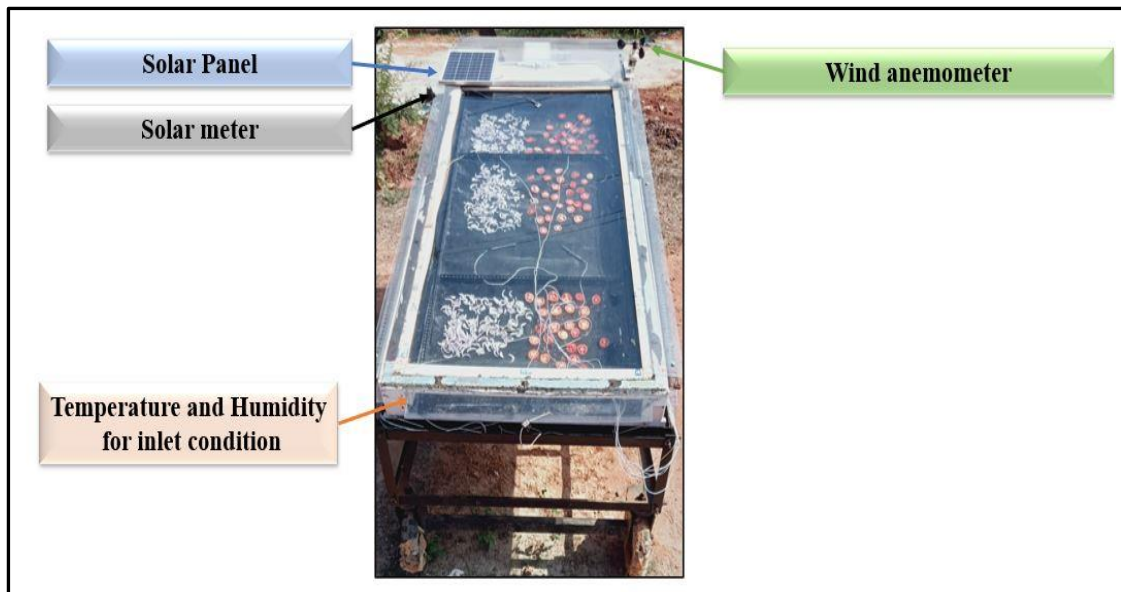


(c)

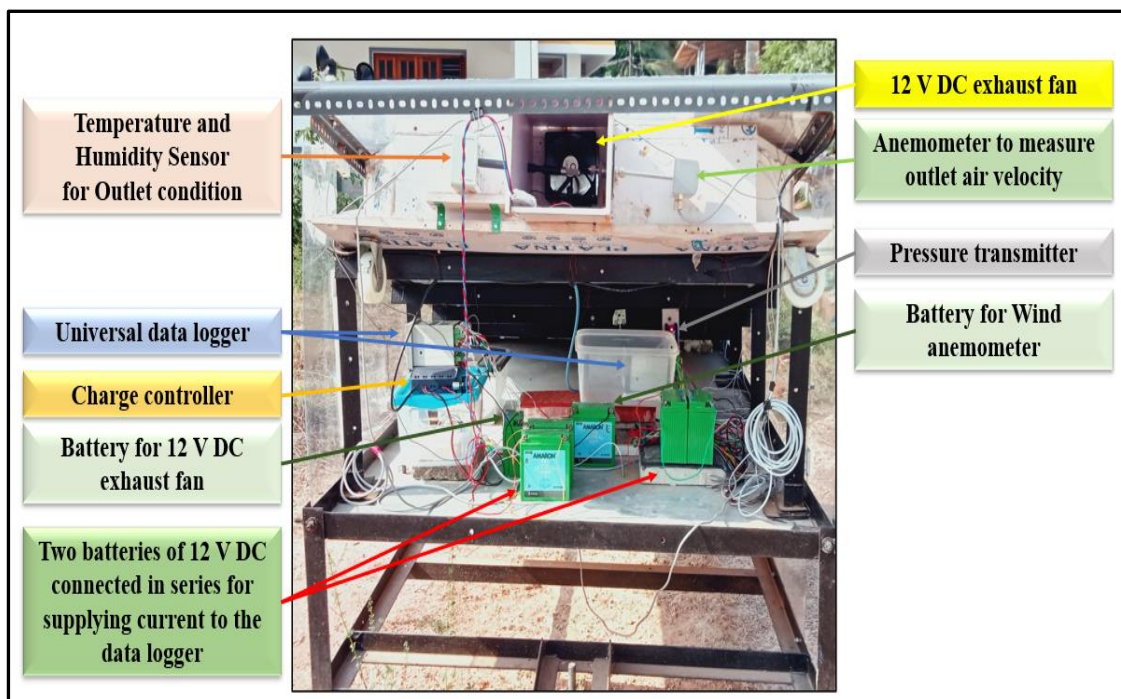


(d)

Figure 3.23 Weight of the product (a) Onion before drying, (b) Tomato before drying, (c) Onion after drying, (d) Tomato after drying.



(a)



(b)

Figure 3.24. A photo of the experimental set-up of SAH (a) front view, (b) back side view.

The single tray is prepared from GI slotted bar and with Aluminium wire mesh attached to it. The single tray with $2\text{m} \times 0.91\text{m}$ is assembled and rollers are attached to easily move the SAH in different location. The three sections are prepared and 250 gm of Onion and Tomato in each section are dried at three different locations. The three

locations are inlet side, middle side and outlet side. The average of all the 750 gm of product were considered for evaluation purposes. The moisture content of the product is measured from 9.00 hrs to 16.00 hrs for every one hour duration. The performance is evaluated on the basis of moisture content, moisture ratio and drying rate of the product.

3.9 PERFORMANCE PARAMETER FOR SPSAH

3.9.1 Evaluation of performance factor for the metal foam SPSAH in numerical method

The average air velocity (V_{air}), is determined by Equation 3.71

$$\text{Average air velocity} = \frac{\dot{m}}{\rho (W \times L)} \quad (3.71)$$

The Hydraulic diameter can be obtained by Equation 3.72

$$\text{Hydraulic diameter}(D_h) = \frac{4 (W \times H)}{2 (W + H)} \quad (3.72)$$

The Reynold number is determined by Equation 3.73

$$Re = \frac{\rho V D_h}{\mu} \quad (3.73)$$

The bulk mean fluid temperature (T_b) is calculated as mentioned in Equation 3.74

$$T_b = \frac{T_i + T_o}{2} \quad (3.74)$$

The convective heat transfer coefficient (h) in $W/m^2 K$ is calculated by Equation 3.75

$$h = \frac{q_w}{T_{pm} - T_b} \quad (3.75)$$

The Nusselt number is calculated by the Equation 3.76

$$Nu = \frac{h D_h}{k_{air}} \quad (3.76)$$

The friction factor (f) across the SAH is calculated by Equation 3.77

$$f = \frac{2 \rho_f \Delta P D_h}{u^2 L} \quad (3.77)$$

The performance factor is determined by Equation 3.78

$$\eta_P = \frac{Nu_{wm}}{Nu_e} / \left(\frac{f_{wm}}{f_e} \right)^{\frac{1}{3}} \quad (3.78)$$

3.9.2 Evaluation of Nusselt number, thermal efficiency and thermohydraulic efficiency of SPSAH in experimental method

The thermal efficiency of both the empty and the porous channels can be calculated by following the definition given in (Sukhatme 2018),

$$\eta_{th} = \frac{q_u}{I_T \times A_c} \quad (3.79)$$

where I_T and A_c are the solar intensity entering the SAH and area of the SAH, respectively, and η_{th} shows the thermal efficiency of the SAH.

The thermohydraulic efficiency of the SAH can be found by Equation 3.80 (Singh 2022),

$$\eta_{the} = \frac{q_u - P_{fan}}{I_T \times A_c} \quad (3.80)$$

where P_{fan} represents the power of the fan used in the system. It shows that the power needed to force the air through the channel is calculated by Equation 3.81 (Singh 2022),

$$P_{fan} = \frac{P_{flow}}{\eta_{fan} \times \eta_{motor}} \quad (3.81)$$

where the η_{fan} and η_{motor} are the efficiencies of the fan and motor, assumed as 70 % and 90 %, respectively (Singh 2022).

P_{flow} can be calculated as (Singh 2022),

$$P_{flow} = \frac{\dot{m} \times \Delta P}{\rho} \quad (3.82)$$

The heat transfer coefficient (h) for the entire channel with or without a WM is calculated by Equation 3.83 (Cengel 2006),

$$h = \frac{q_u}{A_p \times (T_{pm} - T_b)} \quad (3.83)$$

where T_b is the bulk temperature and T_p is the absorber plate temperature is calculated by averaging all of the temperatures of thermocouples near to the inlet, in the middle, and near to the outlet location, each one kept above the absorber plate. Similar arrangements have been performed in the recent literature for glass and absorber plates (Kesavan et al. 2019; Nowzari et al. 2021; Rajarajeswari et al. 2018).

The average temperature for the absorber plate is calculated by Equation 3.84 as,

$$T_{Pm} = \frac{T_{absi} + T_{absm} + T_{abso}}{3} \quad (3.84)$$

where T_{absi} , T_{absm} , and T_{abso} are the temperatures measured at the inlet, middle, and outlet side of the absorber plate as shown in the Figure 3.17 b.

Nusselt number (Nu) for the entire channel is calculated by Equation 3.85 (Cengel 2006)

$$Nu = \frac{h \times D_h}{k} \quad (3.85)$$

3.9.3 Evaluation of exergy efficiency of SPSAH

The Exergy inlet of the SPSAH can be determined by Equation 3.86 (Kesavan et al. 2019),

$$Ex_{in} = \dot{m}C_p \left((T_i - T_a) - T_a \ln \left(\frac{T_i}{T_a} \right) \right) \quad (3.86)$$

Where, i and a are the suffixes for inlet and ambient temperature.

The Exergy outlet of the SPSAH can be solved by Equation 3.87 (Kesavan et al. 2019),

$$Ex_{out} = \dot{m}C_p \left((T_o - T_a) - T_a \ln \left(\frac{T_o}{T_a} \right) \right) \quad (3.87)$$

The Exergy efficiency can be measured by Equation 3.88 (Kesavan et al. 2019),

$$\eta_{Ex} = \frac{Ex_{out}}{Ex_{in}} \quad (3.88)$$

3.9.4 Evaluation of moisture content and drying rate

Moisture content helps to compare the results of final dried product in open sun drying as well as beginning mass of the product before drying. Moisture content on the dry basis can be calculated by

$$MC_{db} = \frac{M_i - M_d}{M_d} \times 100 \quad (3.89)$$

Instantaneous Moisture available on wet basis can be calculated by

$$M_t = \frac{W_t - W_d}{W} \times 100 \quad (3.90)$$

Where, W is the total weight of the Onion or Tomato in kg, W_t is the instantaneous weight of the product in kg and W_d is the weight of dry Onion or Tomato in kg.

Moisture ratio (MR) is the ratio of moisture available at time of instant 't' and at the beginning moisture available in the Onion or Tomato.

Moisture Ratio can be calculated by

$$MR = \frac{M_t - M_e}{M_i - M_e} \quad (3.91)$$

The drying rate of the Onion or Tomato can be determined by

$$DR = \frac{dM}{dt} = \frac{M_{t+\Delta t} - M_t}{\Delta t} \quad (3.92)$$

Where, M_t is the moisture available in the Onion or Tomato and Δt is the time required.

3.9.5 Economic analysis

Economic analysis of solar air heater is required to compare conventional system in terms of initial cost and operational cost. Solar energy has high initial cost but low operational cost. There are three approaches namely capital cost, net profit per year, Pay-back period for an economical evaluation of solar air heater. This is useful for making profit-oriented application. The levelized cost of drying (LCOD) is decided on the basis of all costs incurred over the life time of an energy system over its life time. LCOD may be considered as minimum cost at which the drying product must be sold in order to break even over the life time of the system (Sukhatme and Nayak 2018). The total cost of the system is calculated by Equation 3.93 as

$$P = C_r + C_o + C_m + L_w + P_k \quad (3.93)$$

Where, C_r is the total cost of the raw material per year, C_o is the total operational cost per year, C_m is the total maintenance cost per year, L_w is the labour cost per year, and P_k is the packaging charges per year.

The net weight of the product after drying per year is

$$P_w = \frac{\text{(Total weight of the Onion per year/Weight of the Onion after drying per batch)}}{\text{Weight of the Onion per batch}} \quad (3.94)$$

The dried product selling price can be calculated by Equation 3.95

$$P_s = P_w \times \text{Selling price in Rs. Per kg in the local market} \quad (3.95)$$

The net profit of the product can be calculated by

$$P_{r_n} = P_s - P \quad (3.96)$$

The simple payback period of the SAH is determined by

$$P_b = P/P_s \quad (3.97)$$

The levelized of cost of dryer (LCOD) is calculated by equation 3.98

$$\text{LCOD} = \frac{\text{Total Cost} - \text{benefits}}{\text{Dried product produced by the system per year}} \quad (3.98)$$

Where total costs includes the installation costs, maintenance charges, manpower charges, raw material charges and packaging charges. The benefits consist of the net profit of the drying vegetables. Dried product produced by the system is calculated by Equation 3.99 as

$$\begin{aligned} &\text{Dried product produced by the system} \\ &= \text{Total kg dried per year} \times \text{number of hours per day} \times \text{number of days per year} \times \text{annual capacity factor of the system} \end{aligned} \quad (3.99)$$

The annual capacity factor is calculated by the Equation 3.100

$$\text{ACF} = \frac{\text{Annual dried weight in kg of the dried product}}{\text{Annual initial total weight of the product in kg}} \quad (3.100)$$

3.10 UNCERTAINTIES IN MEASUREMENT

During experiments, different measuring instruments are utilized for measuring different parameters. The details of the accuracy of the devices are given in the Table 3.12 and Table 3.13. An uncertainty analysis is performed to ascertain the standard error in the measurement of the mass flow rate and thermal efficiency (Holman 1994; Kumar and Layek 2022; Saravanan et al. 2021).

3.10.1 Uncertainty for mass flow rate

The fractional uncertainty in experimental results such as for mass flow rate, $\omega_{\dot{m}}$, is obtained as follows.

The mass flow rate (\dot{m}) can be calculated by Equation 3.101 as in (Holman 1994; Singh 2020),

$$\dot{m} = \rho Q \quad (3.101)$$

where ρ is the density of the air and Q is the volume flow rate.

The density of the air (ρ) is obtained by Equation 3.102 as in (Holman 1994).

$$\rho = \frac{P}{R_{\text{air}} T_a} \quad (3.102)$$

Here, R_{air} is the gas constant which has a constant value. Therefore, the density of the air depends on the pressure and temperature values.

The uncertainty in the result is considered as w_R , and $w_1, w_2 \dots w_n$ are the uncertainties in the independent variables. Thus, the uncertainty in the independent variables can be calculated by Equation 3.103 as in (Holman 1994),

$$w_R = \left[\left(\frac{\partial R}{\partial X_1} w_1 \right)^2 + \left(\frac{\partial R}{\partial X_2} w_2 \right)^2 + \dots + \left(\frac{\partial R}{\partial X_n} w_n \right)^2 \right]^{1/2} \quad (3.103)$$

where X_1, X_2 , and X_n are the independent variables.

Using the above Equation 3.100, the uncertainty for the mass flow rate is calculated by Equation 3.104 as,

$$\omega_{\dot{m}} = \left[\left(\frac{\partial \dot{m}}{\partial T_a} \omega_{T_a} \right)^2 + \left(\frac{\partial \dot{m}}{\partial P} \omega_P \right)^2 + \left(\frac{\partial \dot{m}}{\partial Q} \omega_Q \right)^2 \right]^{1/2} \quad (3.104)$$

The volume flow rate (Q) is calculated by Equation 3.105 as,

$$Q = A_f \times u_{\text{air}} \quad (3.105)$$

where A_f is the frontal area and u_{air} is the velocity of air at the inlet. As the frontal area is constant, \dot{m} is a function of T_a, p , and u in the air. It is calculated according to the method explained in Refs. (Azad et al. 2021; Yadav and Saini 2020), and the uncertainty in the mass flow rate is calculated by Equation 3.106 as,

$$\omega_{\dot{m}} = \left[\left(\frac{\partial \dot{m}}{\partial T_a} \omega_{T_a} \right)^2 + \left(\frac{\partial \dot{m}}{\partial P} \omega_P \right)^2 + \left(\frac{\partial \dot{m}}{\partial u_{\text{air}}} \omega_{u_{\text{air}}} \right)^2 \right]^{1/2} \quad (3.106)$$

3.10.2 Uncertainty for thermal efficiency

The fractional uncertainty in thermal efficiency $\omega_{\eta_{\text{th}}}$ is calculated by the below Equation 3.107,

$$\frac{\omega_{\eta_{\text{th}}}}{\eta_{\text{th}}} = \left[\left(\frac{\omega_{\dot{m}}}{\dot{m}} \right)^2 + \left(\frac{\omega_{\Delta T}}{\Delta T} \right)^2 + \left(\frac{\omega_{I_T}}{I_T} \right)^2 \right]^{1/2} \quad (3.107)$$

The obtained values of uncertainty for the mass flow rate and thermal efficiency are shown in Table 3.15.

Table 3.16 Uncertainties in measuring parameters during experimental work.

Uncertainty in measurement	Uncertainty	Unit
Mass flow rate, \dot{m}	$\pm 1.47\% - 1.03\%$	kg/s
Thermal efficiency, η_{th}	± 3.48	%

As can be seen from the above table, the errors in the trials conducted are a result of the uncertainties in the instruments, which must be known to report an uncertainty analysis. It is well known that uncertainty analysis must be performed for measured experimental readings to obtain the errors in the measured values of mass flow rate, temperature, solar intensity, and calculated thermal efficiency.

3.11 PRECAUTIONS CONSIDERED DURING THE NUMERICAL AND EXPERIMENTAL STUDIES

The orthogonality for the all-numerical model maintained near about 99 % so that it improves the numerical stability and accuracy. It is also useful to get better representation of the flow and heat transfer in the system. It solves the problem with high-speed convergence and cost effective and energy saving computation.

The soap bubble test is performed to observe the leakages in the joints. The silicon sealant and epoxy resin are used for joints.

3.12 CLOSURE

In this chapter, details of the analytical, computational and experimental studies of solar air heater including and excluding porous materials to accomplish the objectives. The detailed information of geometry, meshing, material properties, boundary conditions, solution and set up are disclosed in this chapter. Also, dimensions of the experimental set up, measurement procedure, performance parameters for analysis revealed for the single pass solar air heater including and excluding porous materials.

CHAPTER 4

NUMERICAL STUDY FOR ENHANCEMENT OF HEAT TRANSFER USING DISCRETE METAL FOAM WITH VARYING THICKNESS AND POROSITY IN SPSAH BY LTNE METHOD

4.1 INTRODUCTION

As single pass solar air heater (SPSAH) has less manufacturing and maintenance cost compared to double pass and triple pass SAH. Hence, the SPSAH is selected for the present study. The outlet temperature has calculated with help of trial-and-error method and it is the systematic standard process which is useful to calculate the thermal performance accurately. Then the numerical analysis was performed for the same input parameters with two dimensional CFD simulation process. The velocities considered for this study are 0.2268, 0.2646, 0.3023, 0.3401 and 0.3779 m/s at inlet velocity which is referred in Rajarajeswari et al 2018. The heat transfer enhancement was performed with the addition of discrete metal foam of 10 ($\Phi = 0.8769$), 20 ($\Phi = 0.8567$), and 30 ($\Phi = 0.92$) PPI of 22-, 44 and 88 mm thicknesses at equal distances. The discrete metal foam with different thickness was compared with empty channel SPSAH.

The analytical method, computational domain, meshing and boundary conditions etc are mentioned in section 3.4 and 3.5 respectively. The results are compared with the previous literature to observe the rise in temperature, velocity and temperature contours, effect of Nusselt number, friction factor, performance parameter in order to check the thermal performance.

4.2 VALIDATION OF ANALYTICAL AND NUMERICAL STUDY WITH PREVIOUS LITERATURE FOR SAME INPUT PARAMETERS.

The analytical and numerical results of the present study are similar to the conventional SAH (Rajarajeswari et al. 2018). The average deviation between the analytical and CFD results with (Rajarajeswari et al 2018) is 9.66 %. Figure 4.1 shows that as the mass flow rate increases, the temperature difference between outlet and inlet gives less deviation.

The analytical and numerical studies show a similar trend. The average deviation between the analytical and CFD results is 2.78 %.

The present study is performed with Renormalisation group (RNG) k-epsilon model with enhanced wall function for the same input parameters. The analytical and numerical results having deviation less than 5 % shows that the assumed conditions for analytical and numerical test are correct. The numerical results are higher than the experimental results of (Rajarajeswari et al. 2018) because the experimental results are having instrumental error, heat losses due to sudden change in the environmental conditions. But the deviation is also less than 10 % hence the assumed conditions are correct. Same is the case for the porous channel.

The temperature rise for the empty channel is from the 17 to 30 °C and it decreases with increase in mass flow rate. The thermal efficiency of the empty channel SAH is obtained between 48 and 67 % for the mass flow rate of 0.03 and 0.05 kg/s. The Rajarajeswari et al. 2018 noted that the empty channel thermal efficiency for 0.01 to 0.055 mass flow rates are 37 to 62 %. Hence, it shows that the analytically and numerically developed model is correct and result are within the range compared with literature (Rajarajeswari et al. 2018).

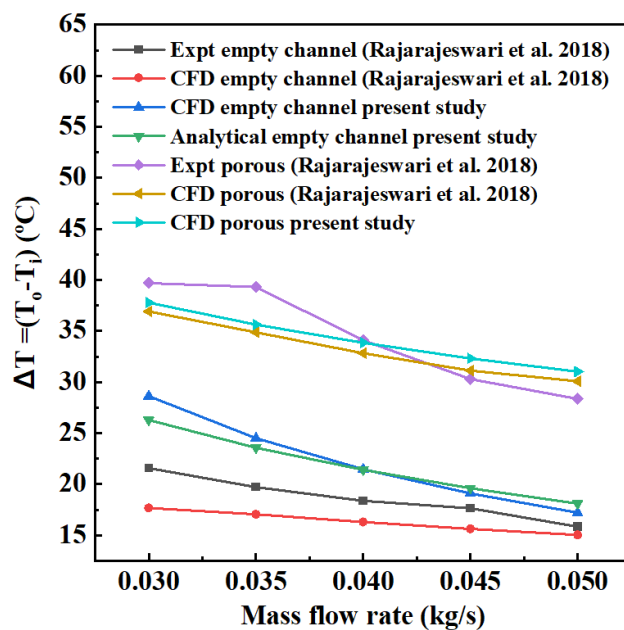


Figure 4.1 Validation of analytical and numerical results of present empty channel SPSAH with (Rajarajeswari et al. 2018)

4.3 TEMPERATURE DISTRIBUTION AND VELOCITY DISTRIBUTION FOR DIFFERENT THICKNESS

Figure 4.2 a–c presents the temperature contour relative to 0.92 porosity 30 PPI Copper metal foam for 0.3779 m/s velocity for the thicknesses of 22, 44, and 88 mm. In the case of porous media such as metal foam, the maximum temperature represents the temperature near the absorber plate. In the case of the lower thickness of the metal foam, the absorber plate temperature is higher, as shown in 4.2. The temperature is uniform throughout the channel except near the absorber plate. For the same PPI and porosity, as the thickness of the metal foam increases, the absorber plate temperature decreases due to more heat transfer area.

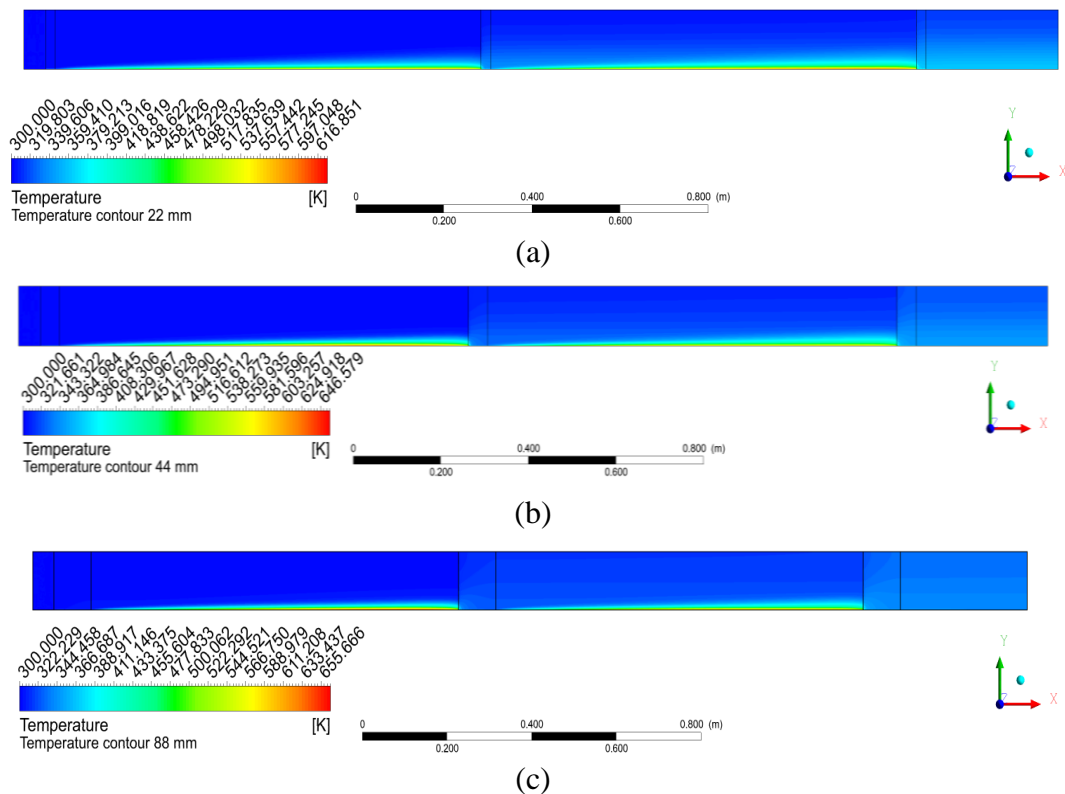


Figure 4.2 Contour of temperature for 30 PPI 0.92 porosity copper metal foam at 0.3779 velocity of (a) 22 mm, (b) 44 mm and (c) 88 mm thick metal foam.

4.4 VELOCITY DISTRIBUTION FOR DIFFERENT THICKNESS

Figure 4.3 represents the velocity distribution for 0.3779 m/s velocity for 30 PPI 0.92 porosity copper metal foam at (a) 22 mm, (b) 44 mm and (c) 88 mm thick metal foam. Figure 4.3 a–c shows the maximum velocity in the middle of the channel. The velocity near the wall is close to zero because of the shear resistance effect.

4.5 EFFECT OF OUTLET TEMPERATURE AND ABSORBER PLATE TEMPERATURE

Figure 4.4 a, b shows the variation of temperature with varying mass flow rate from 0.03 to 0.05 kg/s. With 10 PPI with porosity of 0.8769, 20 PPI with a porosity of 0.8567, and 30 PPI with porosity of 0.92 for 22 mm, 44 mm, and 88 mm metal foam thicknesses are considered.

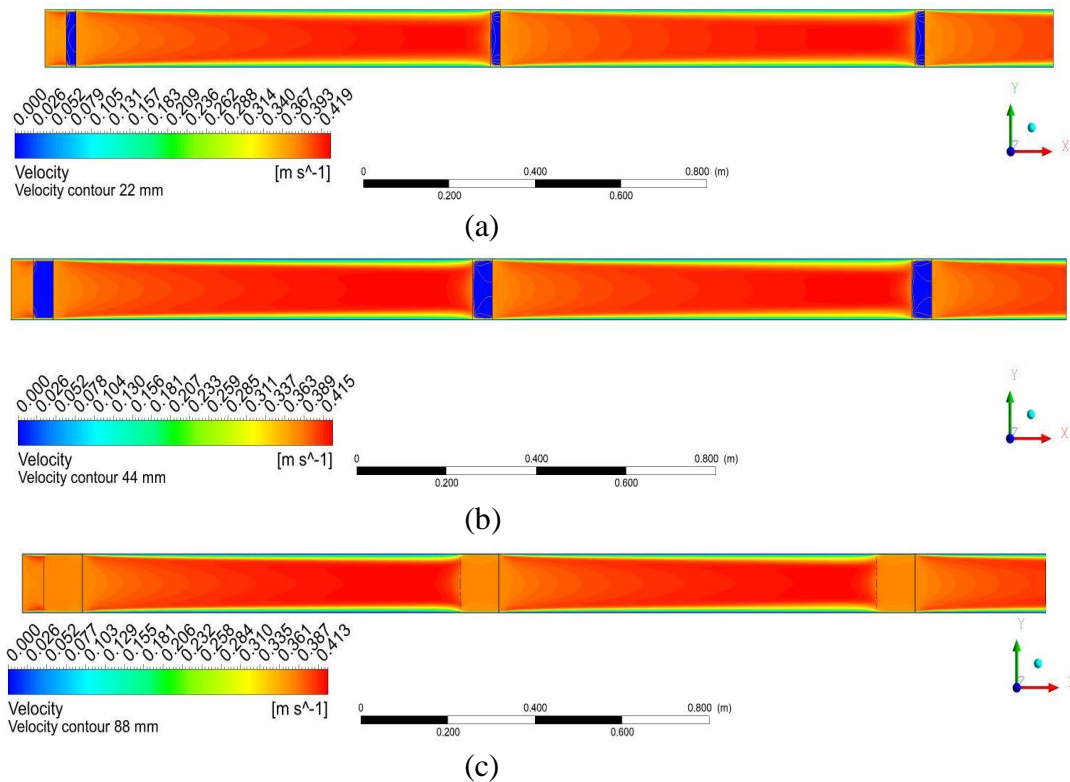
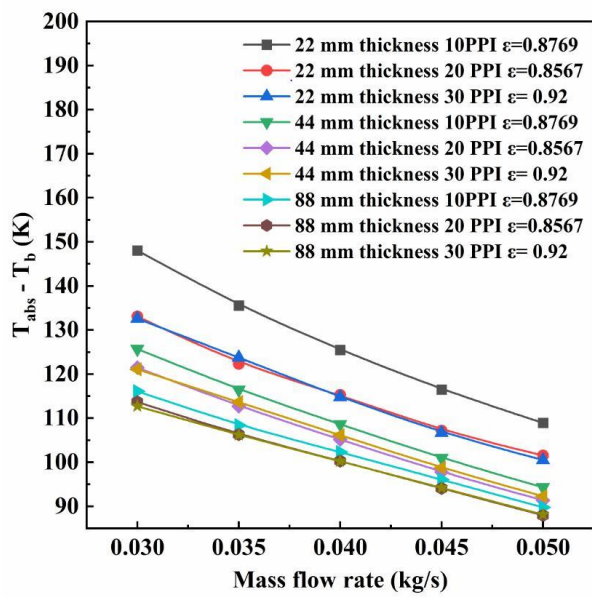


Figure 4.3 Contour of velocity distribution for 30 PPI 0.92 porosity copper metal foam at 0.3779 m/s velocity for (a) 22 mm, (b) 44 mm and (c) 88 mm thick metal foam.

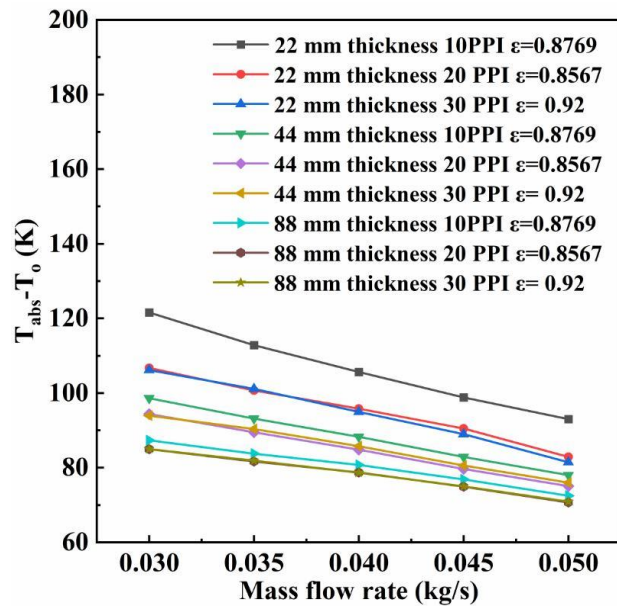
It shows that as the mass flow rate and thickness of the metal foam increases, the difference between the absorber plate temperature and bulk fluid temperature reduces. A similar trend is observed for the difference in the absorber plate and outlet temperatures with an increase in mass flow rate. Due to turbulent flow and velocity of air, the difference in the absorber plate and bulk fluid temperatures change. The lower velocity takes more time to travel in the channel, so that the temperature difference increases. Figure 4.4 a show that the 22 mm 10 PPI copper metal foam has an 8.79 % and 11.45 % higher average temperature difference of absorber plate temperature and bulk fluid temperature compared to the metal foam of 20 and 30 PPI, respectively. The

44 mm 10 PPI copper metal foam has the same percentage of increase in an average temperature difference of absorber plate temperature and bulk fluid temperature, which is about 3.30 % and 3.04 % increase for 20 PPI and 30 PPI, respectively. The same trend is observed in 88 mm thickness for 10 PPI compared to 20 PPI and 30 PPI, which is 2.03 % and 2.46 % higher than 20 PPI and 30 PPI, respectively.

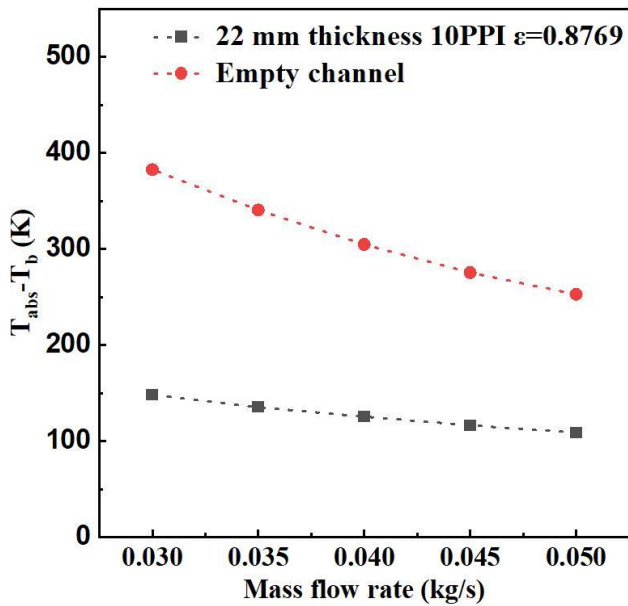
Figure 4.4 b shows that the average temperature difference for 22 mm thickness 10 PPI is higher than all other PPI and all other thicknesses. As the thickness of metal foam increases, the temperature difference between the absorber plate and outlet temperature decreases. As the mass flow rate increase, the temperature difference also decreases. The 22 mm thickness of 10 PPI metal foam is having 10.86 % and 14.32 % more average temperature difference than 20 PPI and 30 PPI, respectively, for the same thickness. The 44 mm, 10 PPI copper metal foam has 4.22 % and 3.90 % increase in average temperature difference than 20 PPI and 30 PPI, respectively, for the same thickness. The average temperature difference between absorber temperature and outlet temperature of 10 PPI is 2.26 % and 3.26 % higher than the 20 PPI and 30 PPI of 88 mm metal foam thicknesses. The above discussion concludes that 10 PPI has a higher temperature difference than 20 PPI and 30 PPI because of more interfacial surface area of the metal foam. As the thickness of metal foam increases, more conduction occurs near the absorber plate, and hence more heat is transferred to metal foam. So, it is noticed that the average temperature reduces as the thickness of metal foam increases. The empty channel has high average absorber plate temperature than the porous media channel.



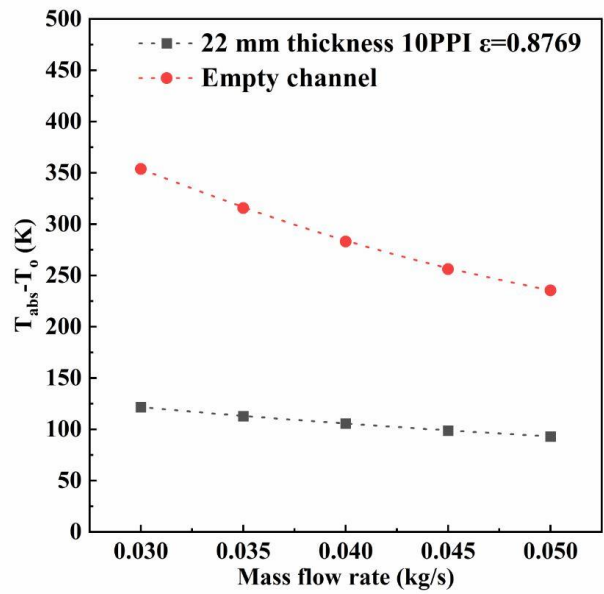
(a)



(b)



(c)



(d)

Figure 4.4 The temperature difference of the absorber plate and bulk mean temperature with varying the mass flow rate (a) variation of temperature between absorber plate and bulk mean fluid temperature vs. mass flow rate. (b) variation of temperature between absorber plate and outlet temperature vs. mass flow rate. (c) variation of a temperature difference between absorber plate and bulk fluid temperature for empty channel and 22 mm thickness 10 PPI 0.8769 porosity. (d) variation of the temperature difference between absorber plate and outlet temperature for empty channel and 22 mm thickness 10 PPI 0.8769 porosity.

4.6 EFFECT OF NUSSLETT NUMBER AND FRICTION FACTOR

Figure 4.5 (a) shows that the Nusselt number is directly proportional to the mass flow rate. As the mass flow rate increases, the Nusselt number also increases. With an increase in thickness, the Nusselt number also increases. Figure 4.5 (a) observes that the 20 PPI of 0.8567 and 30 PPI of 0.92 porosity has a higher Nusselt number compared to 10 PPI of 0.8769 porosity metal foam for 22, 44, and 88 mm thickness of the metal foam. The Nusselt number for 30 PPI of 0.92 porosity is 11.70 %, 2.86 %, and 2.32 % more compared to 10 PPI of 0.8769 porosity for 22, 44, and 88 mm, respectively. The Nusselt number for 20 PPI 0.8567 porosity and 30 PPI 0.92 porosity is almost in the same range for 22, 44, and 88 mm thickness of the metal foam. The results show that with an increase in porosity, the Nusselt number increases because more fluid is flowing through the metal foams.

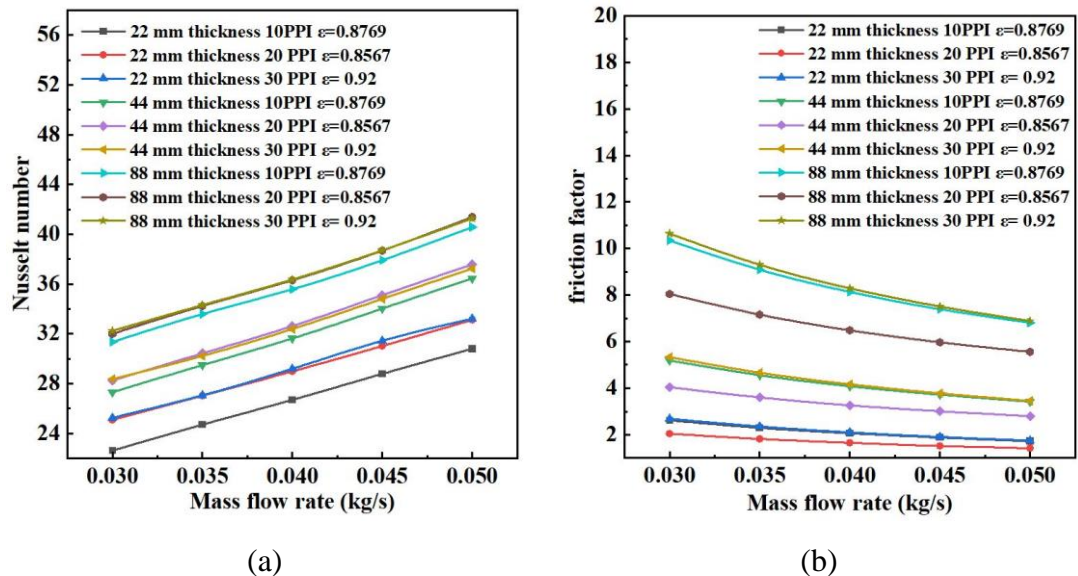


Figure 4.5 Variation of (a) Nusselt number and (b) friction factor for different mass flow rates for different PPI and different thicknesses.

Figure 4.5 (b) shows that the friction factor decreases with an increase in mass flow rate. As the thickness of metal foam increases, the friction factor also increases. The 30 PPI 0.92 porosity metal foam has 31 % and 2.62 % higher friction factor than 20 PPI 0.8567 porosity and 10 PPI 0.8769 porosity copper metal foam for 22, 44, and 88 mm thickness of the metal foam. As the thickness of metal foam increases with twice the value of the previous thickness, the friction factor increases with the same percentage. Hence, it shows that more the PPI, the higher the disturbance to flow, which gives a

higher friction factor. More the thickness of the metal foam, greater the disturbance of the fluid flow; hence, an increase in friction factor.

4.7 EFFECT OF PERFORMANCE FACTOR AND DIFFERENT MATERIAL METAL FOAM

Figure 4.6 (a) shows the performance factor distribution with an increase in mass flow rate. The figure shows that the 22 mm thickness of 20 PPI 0.8567 porosity metal foam is higher than other 44 mm and 88 mm metal foam thickness for 10 PPI 0.8769 porosity and 30 PPI 0.92 porosity. The maximum performance factor for the 20 PPI 0.8567 porosity is 0.0055, 0.0050, and 0.0044 at 22, 44, and 88 mm metal foam thickness, respectively. It is noticed that the performance factor has the maximum value near to 0.0055 at a lower mass flow rate and reduces as the mass flow rate increases.

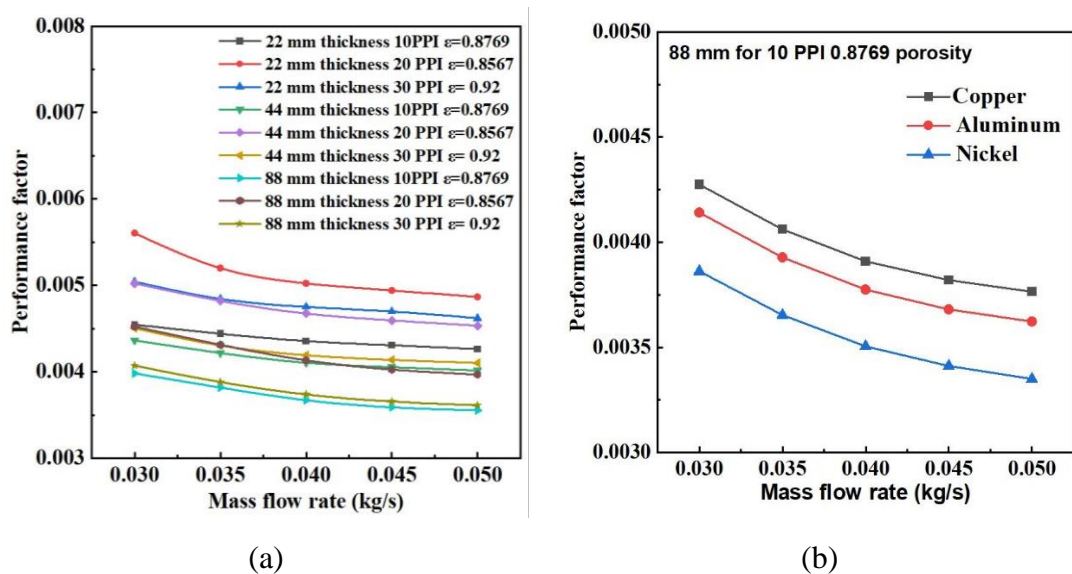


Figure 4.6 The variation of performance factors for different mass flow rates for (a) different PPI and different thicknesses, (b) different material for 88 mm 10 PPI 0.8769 porosity

Figure 4.6 (b) shows the difference between different material performance factors. The material considered for comparison is copper, Aluminium, and nickel. Figure 4.8 shows the performance factor for nickel is minimal compared to Aluminium and copper. Since copper has high thermal conductivity, the absorber plate and outlet temperature difference are less than nickel. It is observed that the temperature difference reduces as the thermal conductivity increases. The copper metal foam has 3.13 % and 9.63 % lesser

mean temperature difference of the absorber plate temperature and bulk mean fluid temperature than Aluminium and Nickel, respectively, for 88 mm thick metal foam.

4.8 SUMMARY

The two-dimensional rectangular channel was modelled to evaluate the effect of partial filling of different porosity of copper metal foam in SPSAH. The complete length of the rectangular channel was 2.35 m, and the height was 0.120 m. The computational analysis was performed for three different thicknesses with variation in PPI and porosity of the copper metal foam. Based on the current investigation, the following points are observed:

- With increasing mass flow rate, the outlet temperature decreases for the empty channel as well as for the partially filled porous channel in all cases of PPI and porosity. The same is achieved for different thickness of metal foam. The average temperature difference between the absorber plate and bulk mean fluid temperature is lowest for 88 mm thick metal foam than 22 and 44 mm thick metal foam.
- The Nusselt number is higher at higher mass flow rate and rises with increasing PPI and thickness of metal foam. The Nusselt number is highest for 88 mm metal foam, rather than 22 and 44 mm thick metal foam. The Nusselt number for 22, 44, and 88 mm thicknesses is 157.64 %, 183.31 %, and 218.60 %, respectively, higher than the empty channel.
- The pressure drop increases with higher thickness and it increases with increase in mass flow rate. Amongst the 10, 20 and 30 PPI copper metal foam, the 20 PPI gives a lesser pressure drop than 10 and 30 PPI metal foam for 22, 44, and 88 mm thickness. The highest pressure drop belongs to 30 PPI, having 28 % and 2 % more average pressure drop than 20 and 10 PPI, respectively, for 22, 44, and 88 mm thickness.
- The performance factor is higher for lower velocity, irrespective of PPI and porosity. The 20 PPI 0.8567 porosity with 22 mm thick metal foam has highest performance factor compared to all 10 and 30 PPI metal foam. For mass flow rate of 0.03 kg/s, the maximum performance factor for the 20 PPI 0.8567 porosity is 0.0055, 0.0050, and 0.0044 at 22, 44, and 88 mm metal foam thickness, respectively.

- The temperature difference of the absorber plate and the bulk mean fluid temperature depend on thermal conductivity of material. The copper has lowest temperature difference of the absorber plate and bulk mean fluid temperature compared to Aluminium and Nickel because of its thermal conductivity.
- With respect to performance factor, 22 mm 20 PPI 0.8567 porosity is best in terms of pressure drop and cost involved in manufacturing the solar air heater.

4.9 CLOSURE

This chapter explicated the complete information of heat transfer enhancement using discrete metal foam with different PPI, porosities and different thicknesses in SPSAH forced convection system. Three different thickness with three different PPI and porosities were used to check the thermal performance of SPSAH and same is compared with the empty channel SPSAH. The next chapter deals with the GAWM of different PPI and porosities for the thermal performance evaluation and experimental study of the SPSAH using wire mesh as porous media.

CHAPTER 5

THERMOHYDRAULIC EFFICIENCY OF A SOLAR AIR HEATER IN THE PRESENCE OF GRADED ALUMINIUM WIRE MESH – A COMBINED EXPERIMENTAL – NUMERICAL STUDY.

5.1 INTRODUCTION

The wire mesh as porous media has many advantages like easily available, easy to manufacture, less cost compared to metal foam. Hence, this chapter included with the different PPI and porosities combined together to form graded wire mesh (GWM) configuration and to increase the heat transfer rate in the SPSAH instead of metal foam. In order to check the thermal performance, the outlet temperature, pressure drop has calculated with help of three-dimensional numerical analysis using Rosseland radiation model with RNG k- ϵ enhanced wall treatment. First the experimental trials were tested for two different velocities such as maximum and minimum inlet velocities. Then this empty channel numerical and experimental results are validated for the same input parameters with three dimensional CFD simulation process. The velocities considered for this study are 1.7 and 3.6 m/s at inlet velocity which is measured at inlet of the SPSAH by anemometer. The heat transfer enhancement was performed with the addition of combined graded wire mesh of 3 ($\Phi = 0.894$), 9 ($\Phi = 0.812$), and 18 ($\Phi = 0.917$) PPI for four different locations from inlet such as 0, 0.5, 1 and 1.5 m away from inlet. The best combination out of four locations of GWM was compared with empty channel SPSAH. The computational description and experimental details are mentioned in section 3.6 and 3.8.1 respectively. The results are compared with the previous literature to observe the rise in temperature, velocity and temperature contours, effect of Nusselt number, friction factor, performance parameter in order to check the thermal performance.

5.2 VALIDATION OF NUMERICAL AND EXPERIMENTAL STUDY FOR SAME INPUT PARAMETERS.

Comparisons between numerical and experimental results are performed, and the agreement between them validates both the obtained numerical and experimental results. Figure 5.1 a show the change in the temperature difference between the inlet and outlet during two days in September 2022 for two different values of air mass flow rate for the empty channel. As can be seen, there is a good agreement between the measured experimental and obtained numerical results, and the deviation in the temperature rise between the numerical and experimental value is 4 %. Furthermore, the thermohydraulic efficiency of the experimental and numerical setups are calculated and shown for scenarios of 0.027 kg/s and for 0.058 kg/s in Figure 5.1 b. The deviation between them do not exceed $\pm 8\%$ for 0.027 kg/s and for 0.058 kg/s for the empty channel. The validation for the temperature rises via the thermohydraulic efficiency for the numerical and experimental trials is between $\pm 8\%$. A similar average range of deviation is considered in the work of Singh (Singh 2022).

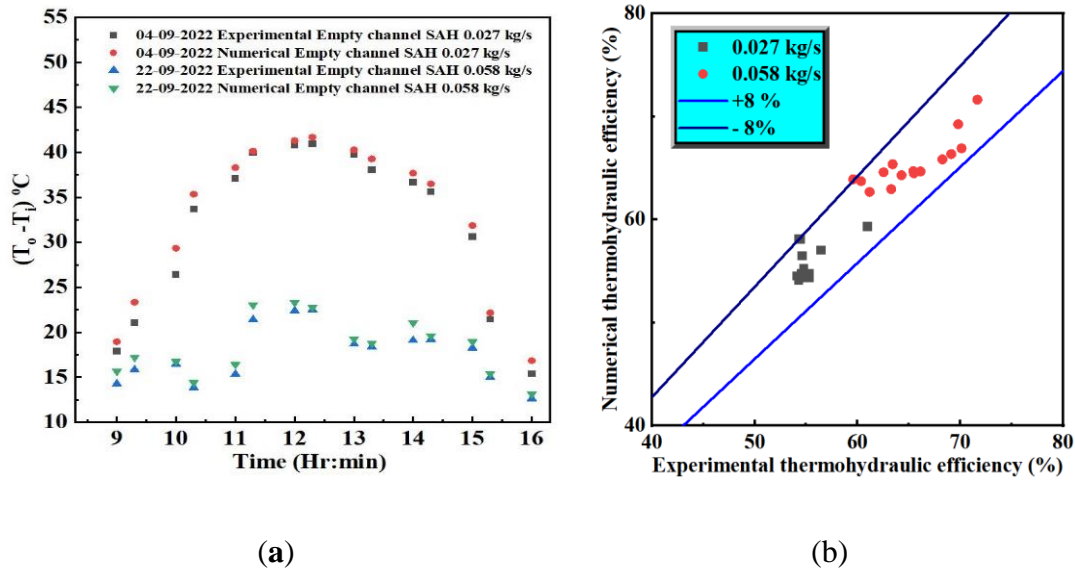


Figure 5.1 (a) Variation in the rise in temperature with time. (b) Parity plot for validation of the thermohydraulic efficiency in numerical and experimental trials for the 0.027 kg/s and 0.058 kg/s mass flow rates.

A numerical analysis is performed for the date 4 September 2022 at 13.00 hr with a sunshine factor as 0.809 (Rajarajeswari et al. 2018; Tian et al. 2004). The experimental inlet temperature, ambient temperature, and solar intensity are considered for numerical

study on the same day. The average temperature of the absorber plate and glass plate of the empty channel is considered as the inlet temperature for the WM SAH in the numerical simulation (Rajarajeswari et al. 2018).

5.3 NUMERICAL RESULTS FOR DIFFERENT CASE STUDIES

A numerical comparison of Cases 3-9-18, 9-18-3, and 18-3-9 is performed for 0.027 and 0.058 kg/s. Figure 5.2 shows that the THPP for the full length of Case 9-18-3 is 13.04 % and 11.92 % higher than for Case 3-9-18 and 18-3-9 PPI case, respectively. The 9-18-3 PPI case has porosities of 0.812, 0.917, and 0.894, respectively.

The lower porosity contains more material. Hence lower porosity near the wall (i.e., near to absorber plate) absorbs more heat from the absorber plate towards WM and then to the air which is available in the channel (Gill et al. 2012; Gupta and Garg 1967). Further, the lower porosity occupies a greater specific area density and increases the volumetric heat transfer coefficient. For this reason, there is a greater heat transfer to the working fluid which minimizes the absorber plate temperature, reducing the thermal losses to the atmosphere; therefore, the thermal efficiency increases. Hence, the sequence from the absorber plate side is a 0.812 porosity near to the wall, then 0.917 and 0.894 porosities of Al WM, as the porosity for the 18 and 3 PPI is nearly identical.

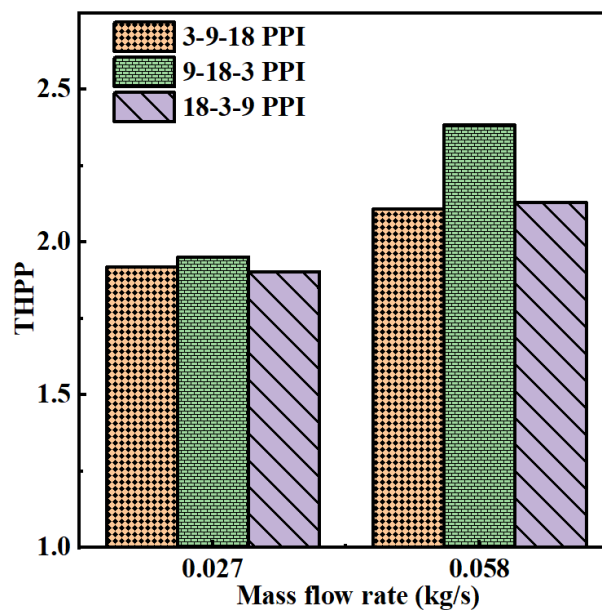


Figure 5.2 Variation in the THPP vs. mass flow rate for the full length of 3-9-18 PPI, 9-18-3 PPI, and 18-3-9 PPI.

For the same porosity, the decreasing gradient in PPI from the absorber plate side minimizes the thickness of the thermal boundary layer which lowers the pressure drop and ultimately reduces the friction factor and increases the thermohydraulic performance parameter. The pitch-to-wire diameter ratios for the 9-18-3 PPI case are 3.54, 6, and 7.54, respectively. For the 0.917 and 0.894 porosities, the pitch-to-wire diameter ratios are 6 and 7.54 respectively. The friction factor is less for the 0.917 porosity and the pitch-to-wire diameter ratio of 6 occurs due to a reduced pressure drop. A similar trend is observed in the work of (Prasad et al. 2009; Varshney and Saini 1998). For the 18 and 3 PPI cases, the ratios of the pitch-to-wire diameter are 6 and 7.54, which is nearly the same. The $1/n\Phi$ ratios for 9-18-3 PPI are 0.31, 0.14, and 0.37, respectively. For the same pitch-to-wire diameter ratio, the $1/np$ ratio increases and the friction factor also increases; hence, the 18 PPI should be near to the absorber plate to obtain a higher THPP. The results were similar for the 9 and 3 PPI Al WM; the $1/n\Phi$ ratios are 0.31 and 0.37, which are very similar. For the same $1/n\Phi$ ratio, the friction factor is lower for lower values of the pitch-to-wire diameter ratio, and hence the THPP is high. The same consideration was investigated in the literature (Prasad et al. 2009; Varshney and Saini 1998). Thus, the present numerical analysis calculated and presented in Figure 5.2 is correct. Hence, further simulations consider Case 9-18-3 to be the full-length WM condition and the results are compared with a WM of 25 % of the length of the full-length test section for four different scenarios, i.e., 0, 0.5, 1, and 1.5 m from the inlet.

5.4 COMPARATIVE STUDY OF TEMPERATURE RISE, NUSSOLT NUMBER, FRICTION FACTOR, AND THPP

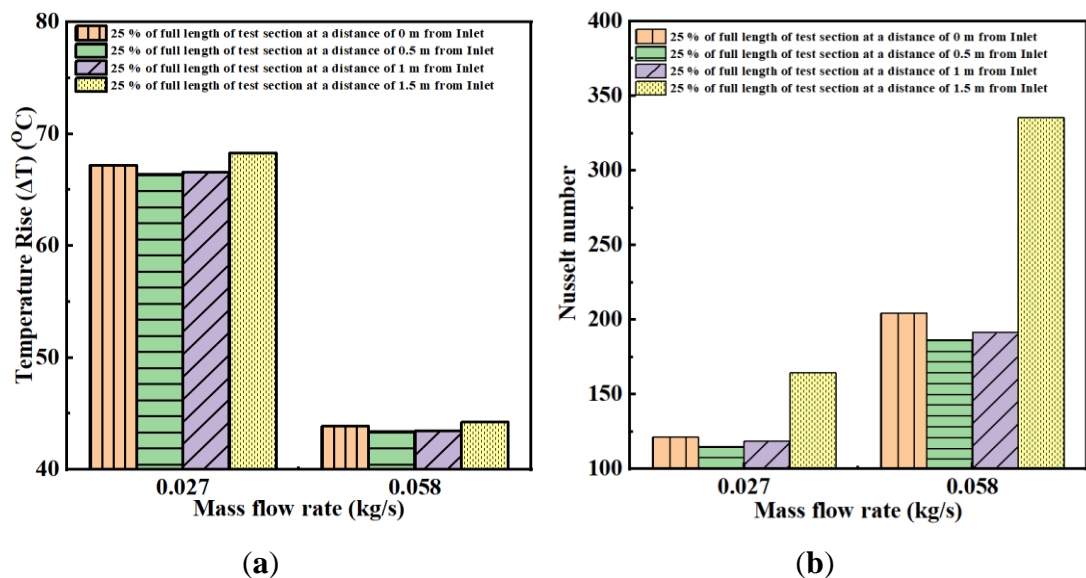
The case of a WM of 25 % of the length of the WM of the full-length test section is simulated at four different locations for the same input conditions. The thermal performance of SPSAH is evaluated on the basis of temperature rise, Nusselt number, friction factor and THPP.

5.4.1 Effect of temperature rise and Nusselt number

The outlet side has a higher temperature in the absorber plate compared to the inlet side; keeping the GWM at the outlet side, it absorbs more heat from the plate due to more

material towards the outlet and when air passes through it, the velocity of the air is minimized, which increases the residence time. Hence it absorbs more heat, and finally the temperature at the outlet is higher. So, temperature rise is more for 25 % of full length of test section at a distance of 1.5 m from inlet. The heat transfer coefficient is higher for this case because the mean absorber plate temperature is lower and bulk mean fluid temperature is higher. Hence, temperature difference between the mean absorber plate temperature and bulk mean fluid temperature is lower which gives higher heat transfer coefficient. Figure 5.3b shows that the Nusselt number is higher for the 25 % of full length of test section at a distance of 1.5 m from inlet.

Figure 5.3 a, b shows the temperature rise and Nusselt number variation for the 0.027 and 0.058 kg/s mass flow rates. The 25 % length case at a distance of 1.5 m from the inlet shows a greater temperature rise and a greater heat-transfer enhancement compared to other 25 % length cases at distances 0, 0.5, and 1 m from the inlet. The average temperature rise and average Nusselt number for the 25 % length case at a distance 1.5 m from the inlet is 2.34 % and 38.65 % higher for the 0.027 kg/s mass flow rate and 1.51 % and 72.60 % higher at the 0.058 kg/s mass flow rate, respectively, comparing all other cases.



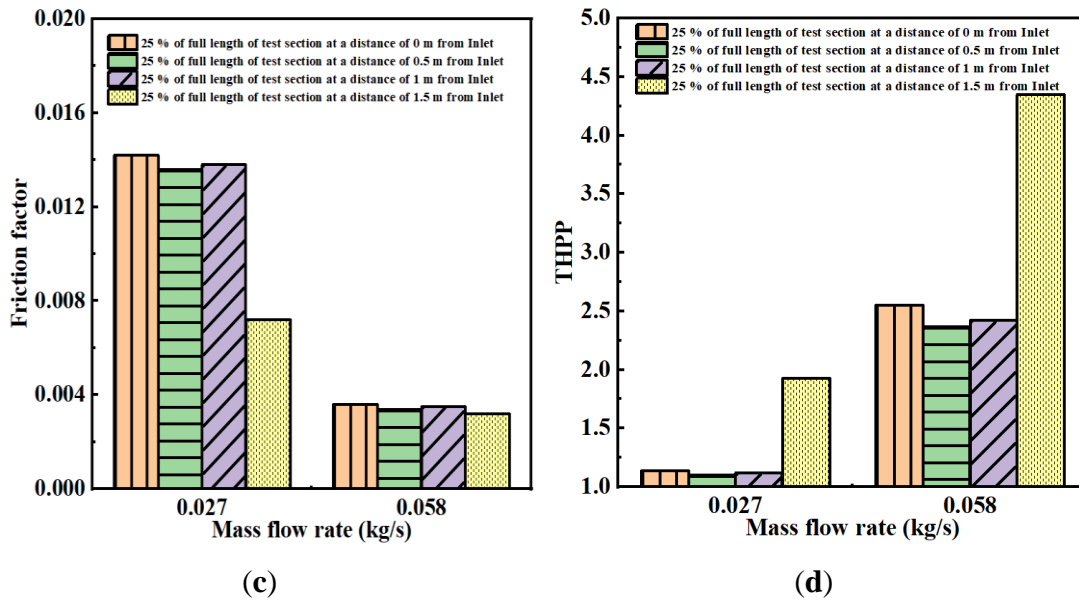


Figure 5.3 Comparison study between the 25 % length case at a distance of 0, 0.5, 1, and 1.5 m from the inlet for (a) temperature rise, (b) Nusselt number, (c) friction factor, and (d) THPP.

5.4.2 Effect of friction factor and THPP

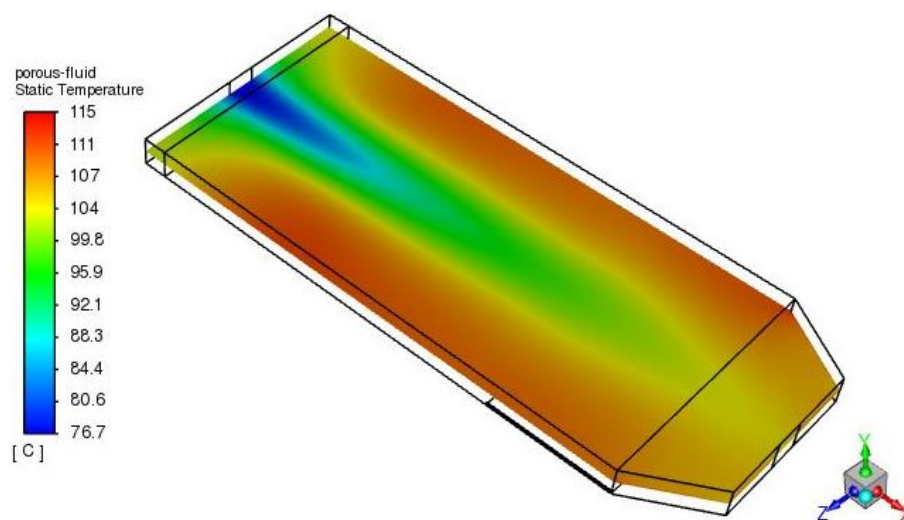
The GWM at the outlet is helpful to lower the resistance of incoming air, and is better for reducing the pressure distribution which gives a reduced pressure drop (Jadhav et al. 2021). Hence, the 25 % length case at a distance of 1.5 m from the inlet is lower friction factor than the other cases in Figure 5.3 C. THPP is higher for the higher Nusselt number and lower friction factor. Hence, 25 % length case at a distance of 1.5 m from the inlet is having higher THPP than all other cases in Figure 5.3 d.

Figure 5.3 c shows a lower friction factor for the 25 % length case at a distance 1.5 m from the inlet compared to all of the other cases. It has a lower friction factor by an average of 48 % and 8.5 % for the 0.027 and 0.058 kg/s mass flow rates, respectively. The temperature rise reduces as the mass flow rate increases; this is because at high mass flow rate, the travel time for air is lower, hence it absorbs less heat. The 25 % length case at a distance of 1.5 m from the inlet had a better THPP value compared to distances of 0, 0.5, and 1 m away from the inlet for the 0.027 and 0.058 kg/s mass flow rates, as shown in Figure 5.3 d. It is an average THPP that is 72.69 % and 77.83 % higher than the all of the other cases. The outlet side has a higher temperature in the absorber plate compared to the inlet side; keeping the GWM at the outlet side, it absorbs

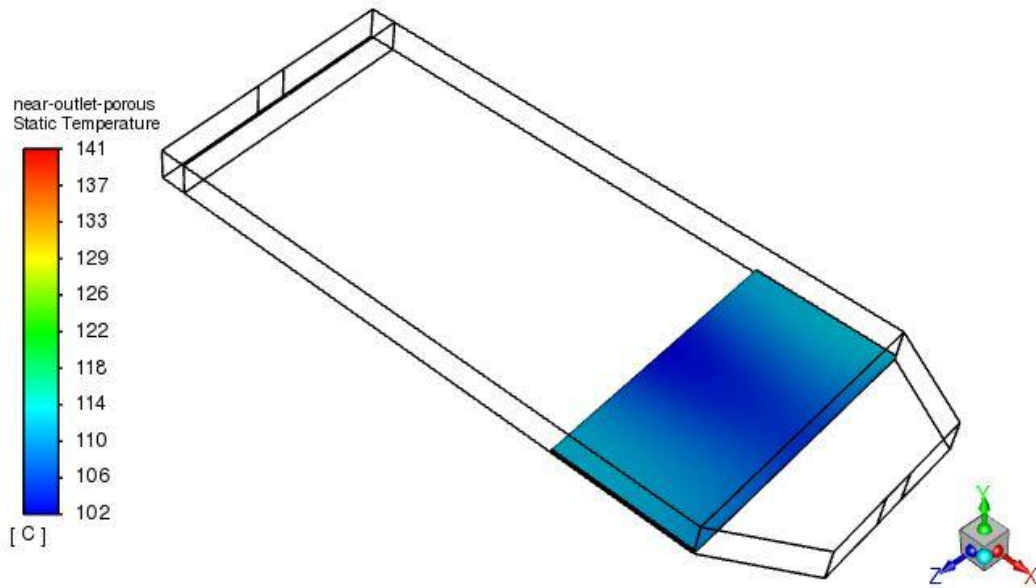
more heat from the plate and when air passes through it, the velocity of the air is minimized, hence it absorbs more heat, and finally the temperature at the outlet is higher. The GWM at the outlet is helpful to lower the resistance to incoming air, and it is better for reducing the pressure distribution which gives a reduced pressure drop (Jadhav et al. 2021). Hence, the 25 % length case at a distance of 1.5 m from the inlet is better than the other cases. Hence, a WM of 25 % of the full-length WM at a distance of 1.5 m from the inlet is selected for experimental analysis.

5.5 TEMPERATURE AND VELOCITY DISTRIBUTION IN THE 25 % LENGTH CASE AT A DISTANCE 1.5 M FROM THE INLET FOR SINGLE-PASS SAH

Figure 5.4 a, b shows the fluid temperature distribution along the plane and in the 25 % length case of porous media near the outlet, respectively. It shows that the temperature is more homogenous in the porous zone. The heat transfer from the absorber plate to the WM and from the WM to the fluid is uniform. A 15 mm thickness of GWM at the outlet side gives a uniform temperature distribution. Figure 5.5 shows the velocity distribution along the plane in the porous SAH. The velocity in the porous zone is more uniform. Due to the lower velocity in the WM, a greater amount of heat is being absorbed; hence, there is an increase in the outlet temperature.



(a)



(b)

Figure 5.4 Temperature distribution of air for mass flow rate 0.027 kg/s and $I = 851.24 \text{ W/m}^2$ (a) along the plane and (b) in the 25 % length case at a distance 1.5 m from the inlet.

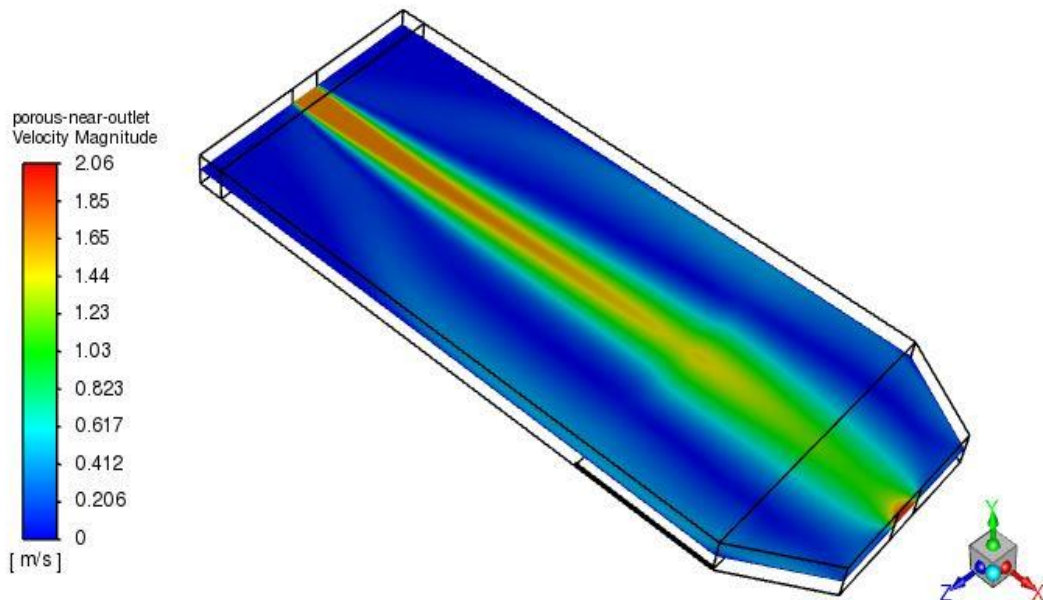


Figure 5.5 Velocity distribution of fluid for the 25 % length case at a distance 1.5 m from the inlet for mass flow rate 0.027 kg/s and $I = 851.24 \text{ W/m}^2$.

5.6 EXPERIMENTAL RESULTS OF EMPTY CHANNEL AND POROUS SAH

5.6.1 Thermal performance of porous bed SAH

Figure 5.6 a, b shows the solar intensities and ambient temperature variation from 9.00 hr to 16.00 hr during the experimental trials. Figure 5.6 a shows the maximum solar radiation ranges from 11.00 hr to 14.00 hr. The average solar radiation is obtained between 700 to 800 W/m². The ambient temperature range during the experimental trials is 29 °C to 37 °C. Figure 5.7 a show the temperature rise in the porous media for the 0.027 and 0.058 kg/s mass flow rates. For the 0.027 and 0.058 kg/s mass flow rates, the outlet air temperature ranges between 43 °C to 80.4 °C and 39.7 °C to 64 °C, respectively. The maximum temperature rise attained is 43.9 °C for the 0.027 kg/s mass flow rate. Figure 5.7 b shows the difference between the average absorber plate and the outlet air temperature for the empty and porous channel with a maximum mass flow rate of 0.058 kg/s. The average absorber and outlet air temperature difference is greater for the empty channel. Hence, the heat-transfer rate is higher for the graded WM compared to the empty channel.

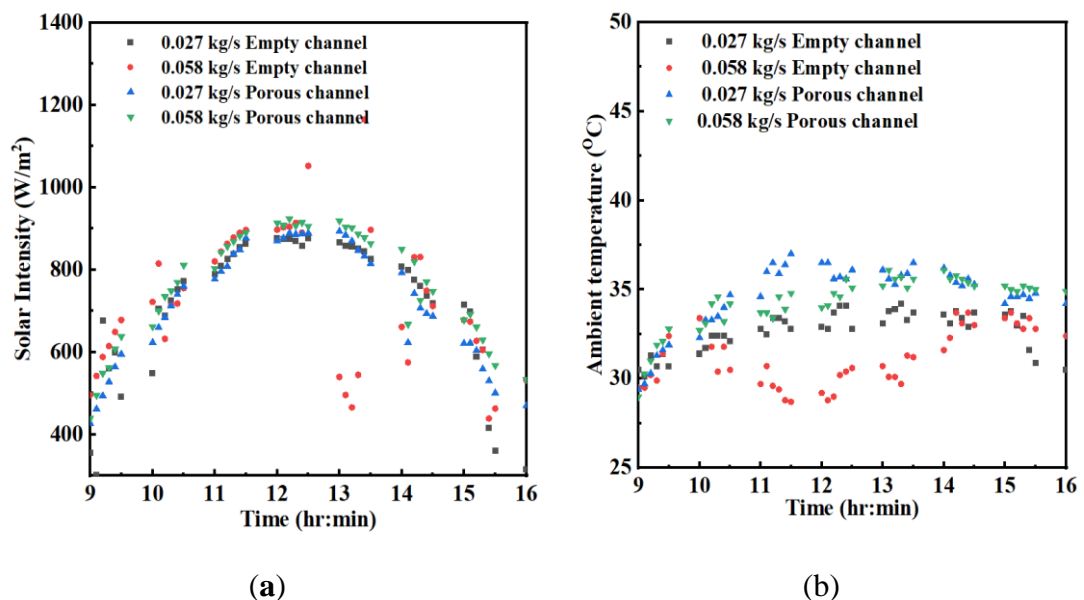


Figure 5.6 Variation in solar intensity and ambient temperature with time. (a) distribution of intensity of solar radiation during the experimental trials, (b) distribution of ambient temperature during the experimental trials.

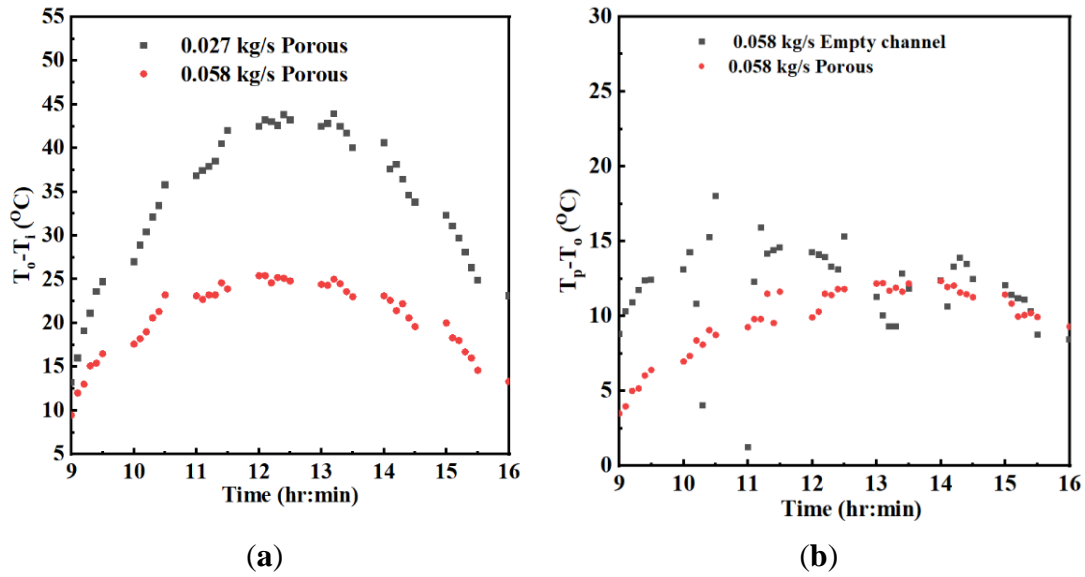


Figure 5.7 Variation in the temperature difference with time for the empty channel and the 25 % length case at a distance 1.5 m from the inlet. (a) temperature rise parameter versus time of day, (b) temperature slip between the average absorber plate temperature and the outlet fluid temperature.

5.6.2 Comparison of porous-bed SAH with empty-channel SAH

For the same average solar intensity, the percentage increase in the thermal efficiency of the GWM is 20.91 % at 0.027 kg/s and 23.32 % at 0.058 kg/s greater than the empty channel, as shown in Figure 5.8.

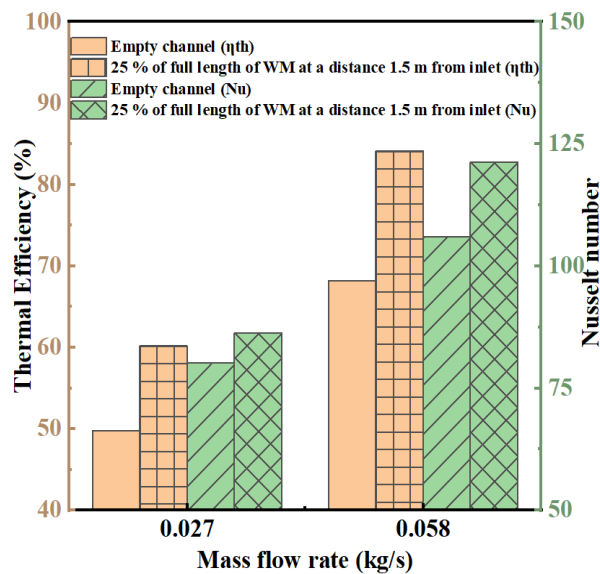


Figure 5.8 The variation in maximum thermal efficiency and maximum Nusselt number between the empty channel and the 25 % length case at a distance 1.5 m from the inlet.

Table 5.1 Comparison with previous similar type of rectangular single-pass SAH.

Author Year and Ref.	Mass Flow Rate (kg/s)	Different Porous Absorbers	Thermal Efficiency (%)
(Gupta and Garg 1967)	1.22×10^{-3} g/cm ² s	Aluminium expanded metal mesh with carbon black coating	50
(Omojaro and Aldabbagh 2010)	0.012 to 0.038	WM with longitudinal fins	Max. 59.62
(Aldabbagh et al. 2010)	0.012 to 0.038	WM without absorber plate	Max. 45.93
(Singh and Panwar 2013)	0.02281	Iron Brass Copper	61.47, 64.42, 64.42
(Nowzari et al. 2015)	0.011, 0.032	WM with different covers	48
(Nowzari and Aldabbagh 2017)	0.011, 0.032	Partially perforated cover with WM	55
(Adnan Abed et al. 2017)	0.033	U and V corrugated WM absorber	NM
(Rajarajeswari et al. 2018)	0.01 to 0.055	Cu WM	15–88
(Gill et al. 2012)	0.011 to 0.020 m/s	Iron chips	37.45
Present study	0.027 and 0.058	Partially filled Al WM with different PPI and porosity	35.8 to 69.5 for 0.027 kg/s and 53.8 to 84.12 for 0.058 kg/s

The heat transfer enhancement in the GWM is demonstrated in terms of the Nusselt number in Figure 5.8. The Nusselt number increases with the Reynolds number. For 0.027 kg/s and 0.058 kg/s, the Nusselt numbers are 86.33 and 121.29, respectively, for the same input condition in the GWM. The increase in performance is due to the temperature rise in the GWM because of the lower velocity in the GWM. Table 5.1 shows a comparative study of the present study with recently studied literature using different configurations of wire mesh as a heat-transfer enhancement media. It shows that the resulting 69.5 % and 84.12 % thermal efficiency is better than the wire mesh material cost and the performances of all of the other references mentioned in the Table 5.1.

5.7 SUMMARY

The present study involves experiments and analysis of the 3D geometry of single-pass SAHs by a numerical finite volume method. The flow inside the SPSAH is assumed to be incompressible and steady state. The Rosseland radiation model with a solar ray tracing method is considered to evaluate the thermal performance of the SPSAH using a WM as a porous media. The properties of air are calculated at a bulk mean temperature and assumed to be constant throughout the length. Al WMs with three different porosities is combined together to enhance the heat-transfer rate in single-pass forced convection SAH. The Al WM is assumed to be isotropic, homogenous, and non-deformable. The wire mesh length, width, and thickness of each porosity is assumed to be $500 \times 985 \times 5$ mm (i.e., 25 % of the full length of the test section) in the present study. A local thermal equilibrium method was applied for the heat transfer from the WM to the air inside it. Experiments are performed for the 0.027 and 0.058 kg/s mass flow rates. The following results have been obtained based on the present work:

- For the full-length case, 9-18-3 PPI is the best suitable combination compared to Cases 3-9-18 and 18-3-9 PPI in terms of maximum outlet temperature, Nusselt number and THPP. Case 9-18-3 PPI has 7.62 % and 7.22 % higher average THPP than Case 3-9-18 and 18-3-9, respectively, for both the mass flow rate.
- The 25 % length of the GWM of the full-length test section was kept at four different locations (i.e., 0, 0.5, 1, and 1.5 m from the inlet) in numerical analysis. The thermal performance was analysed with respect to temperature, Nusselt number, friction factor, and THPP at these four locations. It shows that the rise in the outlet temperature was nearly the same for all of the cases. The Nusselt number is higher in the WM of 25 % of the length of the full-length test section than all other cases considered above as a result of the changes in the absorber plate temperature and bulk mean fluid temperature. The friction factor was lower and THPP was higher for the case of 25 % of the length of the WM of the full-length test section among all of the other cases.
- The 25 % length of the WM of the full-length test section at a distance 1.5 m from the inlet is more valuable than all other cases in terms of the overall performance of porous SAH. As the mass flow rate increases, thermal efficiency also increases.

The enhancement in the thermal efficiency was 23.32 % higher for 0.058 kg/s than the empty channel.

5.8 CLOSURE

This chapter deals with the graded aluminium wire mesh for heat transfer enhancement in the SPSAH. The 25 % of full length of test section 1.5 m away from the inlet gives higher THPP and which can be useful for drying application. The transverse and longitudinal graded aluminium wire mesh partially filled porous media and its effect on heat transfer and THPP are clarified in the next chapter.

CHAPTER 6

ENERGY, EXERGY AND ECONOMIC ANALYSIS OF SOLAR AIR

HEATER COMPARING DIFFERENT DIRECTIONS OF GRADED WIRE

MESH FOR DRYING ONION AND TOMATO.

6.1 INTRODUCTION

The present study involves the single pass solar air heater (SPSAH) operated by forced convection. The 9 and 18 PPI Al wire mesh of porosity 0.812 and 0.917, respectively, are kept in the channel of SPSAH. Single pass solar air heater equipped with wire mesh structure is one of the low-cost technologies to harness the solar energy in an efficient way to dry vegetables. Solar air heater is constructed with 9 and 18 pore per inch (PPI) Al wire mesh of porosity 0.812 and 0.917, respectively to improve heat transfer performance. This wire meshes are arranged one wire mesh over the other wire mesh in the transverse direction and the same quantity of wire mesh is folded to 50 % length and kept one after the other in a longitude direction. So, these combinations are (9-18, 18- 9)T, (9-18, 18-9)L to obtain gradient wire mesh in transverse and longitudinal directions, respectively. The numerical study is performed with the Rosseland radiation model with the solar ray tracing method. The Renormalisation group k- ϵ with enhanced wall function viscous model is used for further 3D analysis because the calculated Reynolds numbers are 4134 and 7398. The computational description and experimental details are mentioned in section 3.7 and 3.8.2 respectively. The results are compared with the previous literature to observe the rise in temperature, velocity and temperature contours, effect of Nusselt number, friction factor, performance parameter in order to check the thermal performance. Also, economic investigation is studied to get the simply payback period.

6.2 VALIDATION OF NUMERICAL RESULTS WITH EXPERIMENTAL TESTING OUTCOMES

The comparison between numerically simulated results with experimental testing outcomes has performed to observe the accuracy and correctness of the steps implemented during each method. Figure 6.1(a) shows the outlet temperature during two different days in May 2023 for two different values of air mass flow rate tested in empty channel. The deviation is between $\pm 10.5\%$ for 0.05 kg/s and 0.08 kg/s for empty channel as displayed in Figure 6.1 (b).

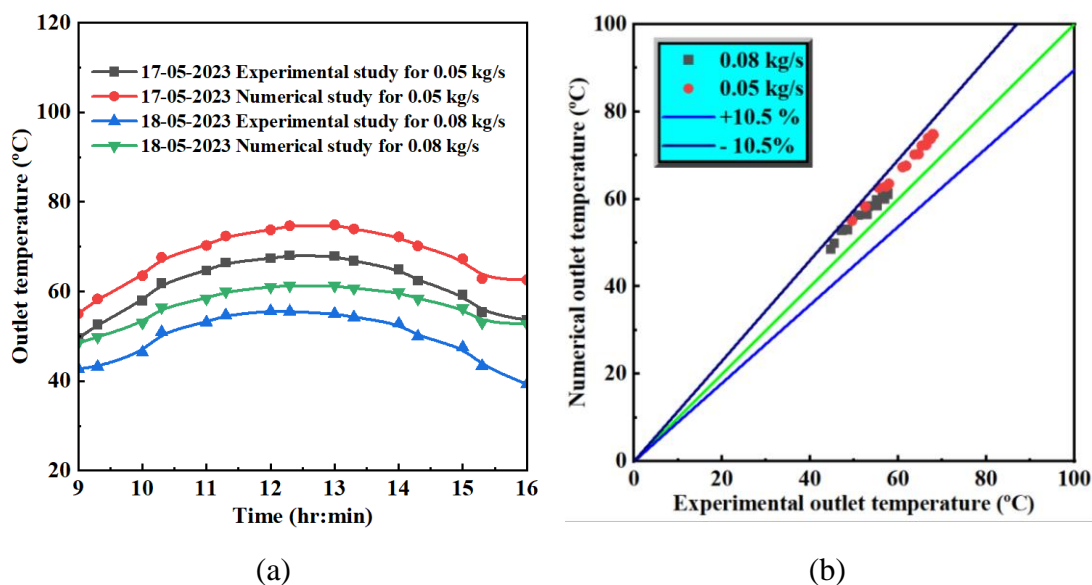


Figure 6.1. (a) Validation of outlet temperature for numerical and experimental readings with varying the time for 0.05 and 0.08 kg/s mass flow rates on 17-05-2023 and 18-05-2023 respectively in empty channel SAH. (b) Parity plot for numerical and experimental outlet temperature result for 0.05 and 0.08 kg/s mass flow rates.

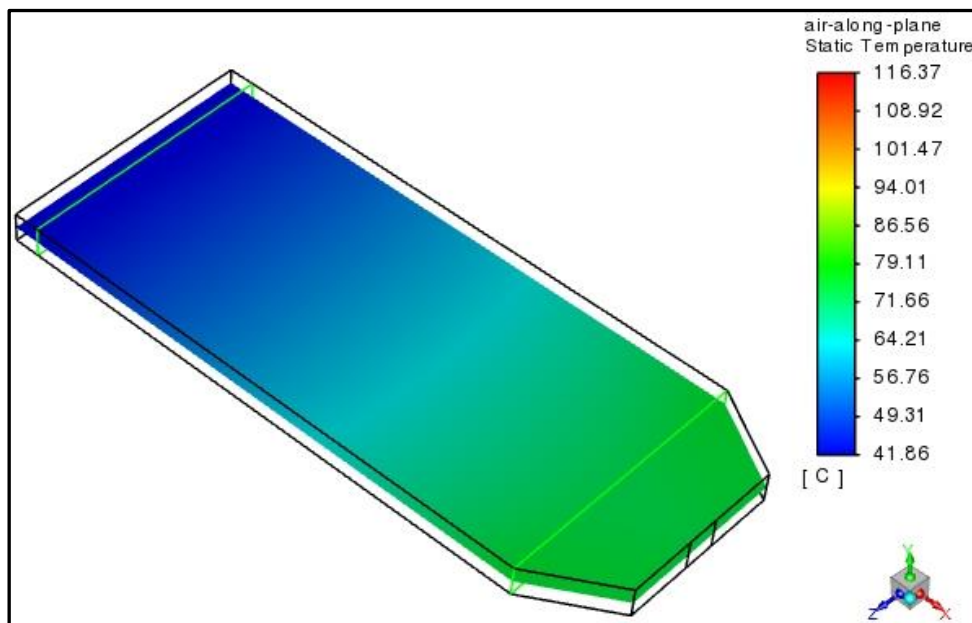
The average deviation between numerically simulated results with experimentally testing outcomes has 5.59 % which is acceptable. In Figure 6.1, the numerical readings are calculated with assumptions and input parameters which represent the predicted output parameters. The actual experimental readings are affected by instrumental errors. Also, the boundary conditions and the thermophysical properties of air are considered constant but in actual experimental setup, the material properties may change. The outer box is considered as the adiabatic wall but in actual experiments few losses to atmosphere can happen. The numerical model assumes the constant heat flux

throughout the plate but in actual experimental trial, it is not possible. Hence, the experimental readings are lower than the numerical readings.

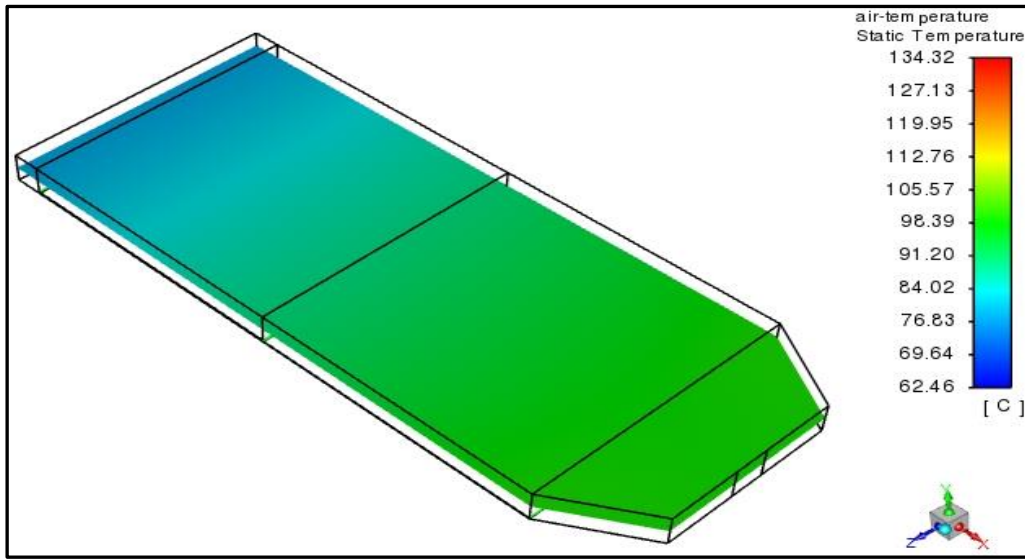
The maximum solar intensity of the day is obtained at 1300 hr. Hence, further numerical study is performed based on the 17th May 2023 at 1300 hr. Recent studies used similar conditions at 1300 hr. (Alic et al. 2021; Rajarajeswari et al. 2018; Shetty Shreyas, N. Madhwesh 2021)

6.3 TEMPERATURE AND VELOCITY DISTRIBUTION FOR EMPTY CHANNEL AND 9-18 L LONGITUDINAL GWM

Figure 6.2 (a) and (b) shows the temperature distribution in the empty channel and 9-18 L GWM temperature distribution in the SPSAH. Figure 6.2 b is having higher temperature distribution compared to Figure 6.2a empty channel. Figure 6.2 a show that 50 % of the empty channel is less than 50 °C temperature and Figure 6.2 b shows that 50 % of the test section are above 50 °C. This is because of the GWM kept inside the test section. The air flowing in between wire mesh is having lower velocity from inlet to outlet. Hence, the incoming fluid absorbs more heat while moving in the porous media. Figure 6.3 (a) and (b) shows the velocity distribution in the empty channel and 9-18 L GWM porous media. The porous media has lower velocity compared to empty channel.

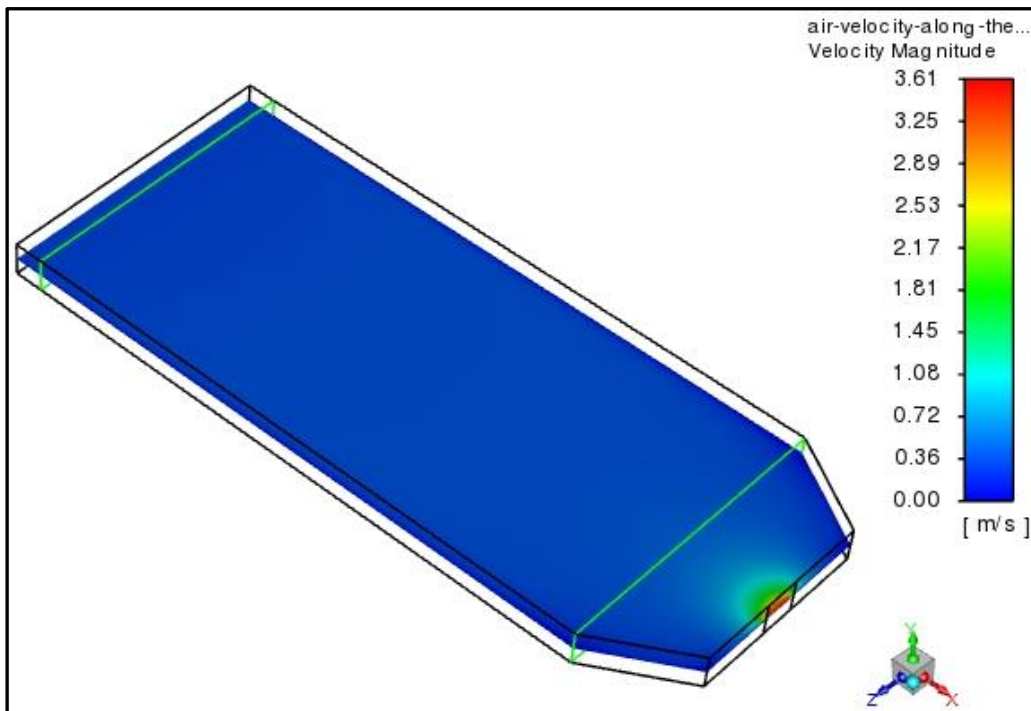


(a)

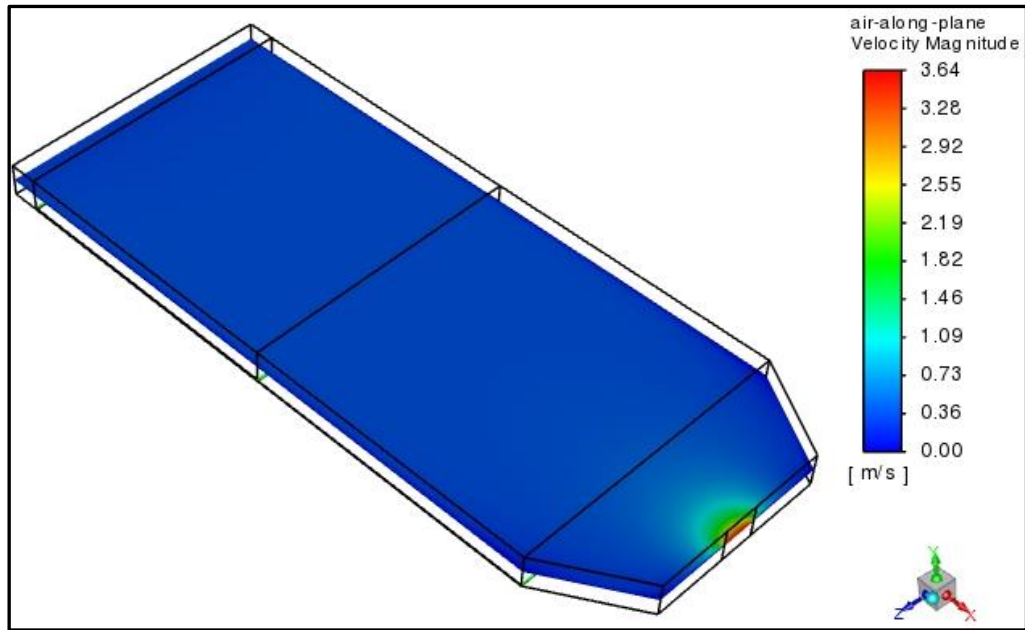


(b)

Figure 6.2 Temperature profile of air at 0.35 m/s heat flux 707 W/m^2 for (a) empty channel, (b) 9-18 L porous arrangement of GWM.



(a)



(b)

Figure 6.3 Velocity distribution of air at 0.35 m/s heat flux 707 W/m^2 for (a) empty channel, (b) 9-18 L porous arrangement of GWM.

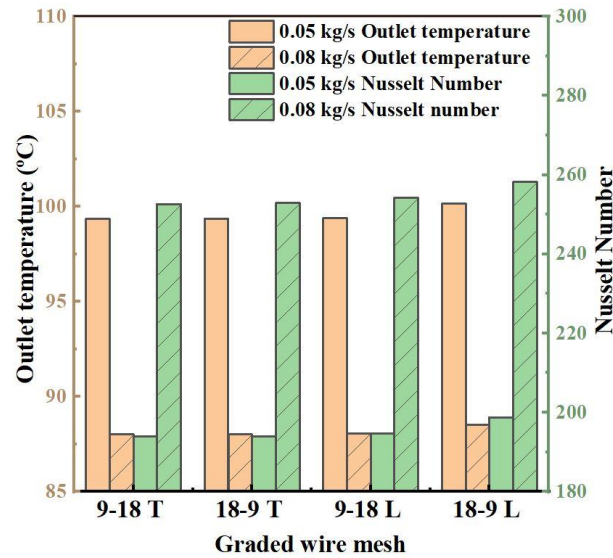
6.4 EFFECT OF DIFFERENT TRANSVERSE AND LONGITUDINAL POROUS ARRANGMENTS OF GWM IN NUMERICAL STUDY

Figure 6.4 (a) and (b) shows the difference as well as change in outlet temperature, Nusselt number, friction factor and thermohydraulic performance parameter for 9-18 T, 18-9 T, 9-18 L and 18-9 L arrangements of GAWM for 0.05 and 0.08 kg/s mass flow rates respectively.

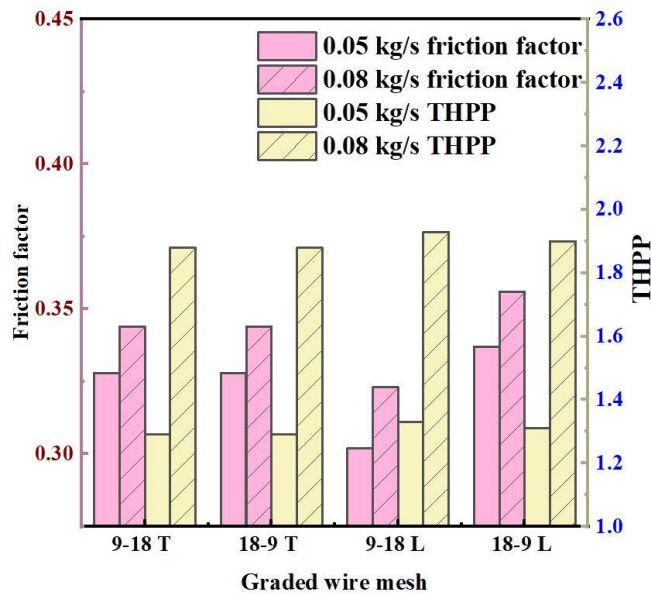
6.4.1 Effect of outlet temperature and Nusselt number

The outlet temperature is higher for 18-9 L GWM compared to all other cases, then 9-18 L GWM has higher outlet temperature than 9-18 T and 18-9 T GWM. 9 PPI has less porosity and has more material. The lower porosity has smaller pores in WM which reduces the velocity of air. The residence time of air in 9 PPI WM is more. The thickness in longitudinal GWM is more compared to transverse GWM. So, more air obstruction happens in longitudinal GWM. In longitudinal case, 9 and 18 PPI is having twice the thickness of transverse GWM case. The obstacles to air flow are high so the residence time is more and more heat is absorbed by the incoming fluid. Hence, the outlet temperature is higher for longitudinal case. The absorber plate temperature is

lower in longitudinal case compared to transverse case. Hence, heat transfer coefficient is higher in longitudinal case. Thus, Figure 6.4 shows that the Nusselt number is higher for longitudinal case than transverse GWM.



(a)



(b)

Figure 6.4 variation in outlet parameters for 9-18 T, 18-9 T, 9-18 L and 18-9 L arrangements of GWM at 0.05 kg/s and 0.08 kg/s (a) outlet temperature and Nusselt number, (b) friction factor and THPP

6.4.2 Effect of friction factor and THPP

The friction factor is lower for higher mass flow rate and lower with increase in porosity of WM. The transverse GWM has same thickness throughout the channel so no deviation in the velocity and porosity from the start of the absorber plate to end of it. Hence there is no change in the friction factor. In case of 9-18 L GWM the porosity at inlet and outlet are 0.812 and 0.917, respectively. The first half of test section with lower porosity i.e. 0.812 has more material and smaller opening compared to 0.917 porosity material. Hence, the residence time is more for air in the first half of test section. So, in the first half section air absorbs more heat and enters into the higher porosity region i.e. 0.917. The higher porosity region is having larger opening than first half of test section. Air will flow with higher velocity than the first case which reduces the friction factor. The Figure 6.4 shows that the 9-18 L is having lesser friction factor than 18-9 L.

Figure 6.4 (a) and (b) indicated that the outlet temperature, Nusselt number and friction factor are higher for 18-9 L arrangement of GWM compared to all other cases. But, in order to obtain the higher thermohydarulic performance, friction factor should be less. Figure 6.4 (b) the 9-18 L arrangement of GWM has lower friction factor compared to all other cases, in both mass flow rates. The friction factor for 9-18 L arrangement is 8.83 % and 7.39 % lower than average friction factor for all other three GWM arrangement in 0.05 and 0.08 kg/s mass flow rates respectively. Hence, further it is noticed that 9-18 L arrangement of GWM has average 2.45 % increase in the THPP compared to average of all THPP of all three cases i.e., 9-18 T, 18-9 T and 18-9 L GWM arrangement. Results presents that as rise in mass flow rate, outlet temperature decreases, and Nusselt number, friction factor, THPP increases.

Figure 6.4 (b) shows the higher THPP for the case 9-18 L than all other cases in both the mass flow rate and THPP is higher for the higher Nusselt number and lower friction factor. THPP increases with increasing porosity with increase in mass flow rate. 9-18 L case is having lower porosity towards inlet side and higher porosity towards the outlet side. It results in reduced friction factor as increase in porosity with increase in mass

flow rate. Higher porosity has lower resistance to air flow. So, the best configuration comparing with Nusselt number, friction factor and THPP is 9-18 L GWM.

6.5 EXPERIMENTAL OUTCOMES OF EMPTY CHANNEL AND 9-18 L GWM SAH

In the initial stage, the experimental testing has been conducted for two times for each mass flow rate. It is very difficult to obtain the same ambient temperature and solar intensity for all the days. The environmental conditions may be varying time to time. Table 6.1 shows the average reading of solar intensity and ambient temperature for complete day which was measured for empty channel and 9-18 L GWM. The mass flow rates are 0.05 and 0.08 kg/s for empty channel and 9-18 L GWM porous media. From the Table 6.1, it represents that the solar intensity on 25-05-2023 and 23-05-2023 is more or less the similar for 0.05 kg/s mass flow rate. Similarly, on 27-05-2023 and 24-05-2023 same average solar intensity and surrounding temperature are observed for 0.08 kg/s mass flow rate. Therefore, Figure 6.5 represents the graph of change in (a) ambient temperature, (b) solar intensity, (c) rise in temperature, (d) exergy efficiency, varying with respect to time for the same date.

6.5.1 Effect of ambient temperature and solar radiation

The range of surrounding temperature and solar intensity measured in experimental testing are 33 to 38 °C and 220 to 860 W/m² respectively. The maximum effect of solar radiation is from 11.00 hrs. to 14.00 hrs. for all the day of the experimental trials as shown in the Figure 6.5 (b). The solar intensity first increases till 13.00 hrs. and then it decreases. The peak of the solar intensity starts from 12.30 hrs. to till 13.00 hrs. which ranges from 800 to 860 W/m².

6.5.2 Effect of rise in temperature and exergy efficiency

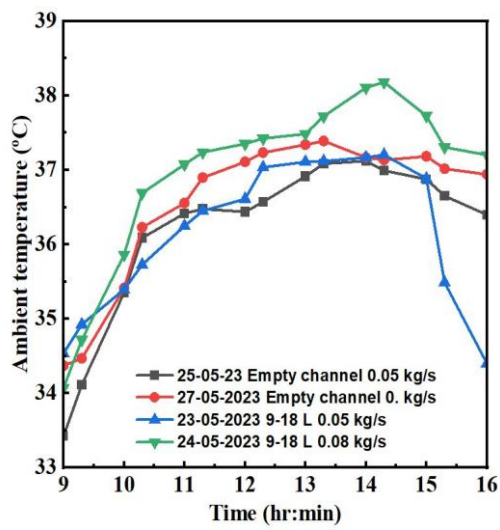
The rise in temperature increases as the mass flow rate reduces for the both cases in empty channel and 9-18 L GWM arrangement. But the rise in temperature for 9-18 L GWM is higher than empty channel in both mass flow rate as heat transfer area increases due to wire mesh insert in the test zone. The rise in temperature for 9-18 L GWM is 12.44 % and 15.98 % higher than the empty channel for 0.05 and 0.08 kg/s mass flow rates. The empty channel where there is no porous media, air moves quickly in the test zone and absorbs less heat, hence the outlet temperature of without WM is

less. In 9-18 L GWM channel, when air moves through the wire mesh, velocity reduces due to small gaps in the wire mesh and absorbs more heat so outlet temperature of the air is more. The range of rise in temperature for 9-18 L GWM for 0.05 and 0.08 kg/s mass flow rates are from 9.84 to 31.60 °C and 8.95 to 26.97 °C respectively.

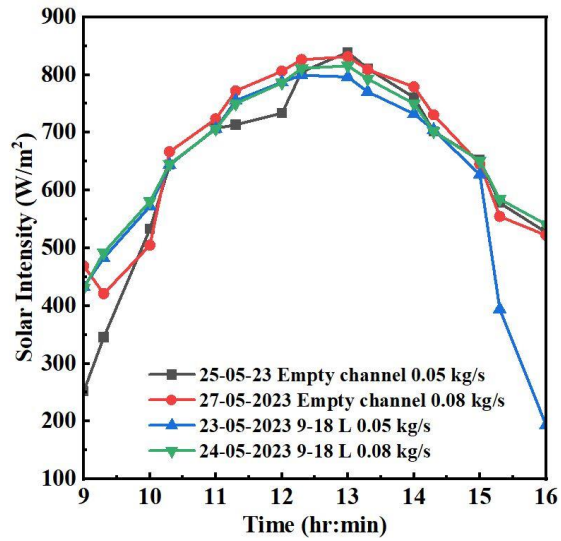
The exergy values are obtained for maximum solar intensity from 11.00 hrs. to 14.00 hrs. The exergy efficiency of dryer is more with lower temperature rise between the inlet and outlet temperature of SPSAH. So, higher mass flow rates have higher exergy efficiency and similar trend in empty channel and 9-18 l GWM cases are seen.

Table 6.1. Average experimental measured reading of ambient temperature and solar intensity in the month of May 2023 for 0.05 and 0.08 kg/s mass flow rates.

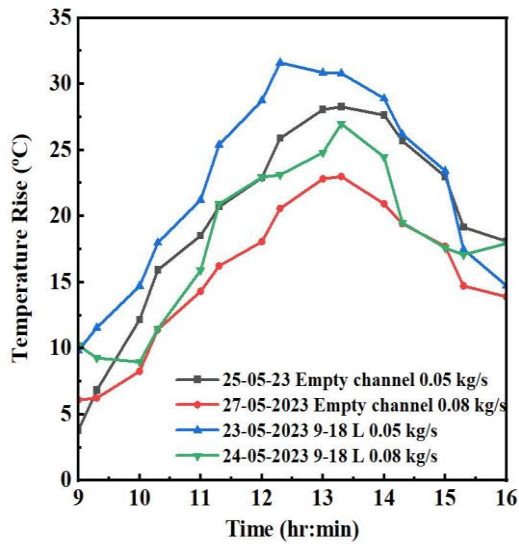
SAH	Mass flow rate (kg/s)	0.05		0.08	
Empty channel	Date	25-05-2023	28-05-2023	26-05-2023	27-05-2023
	Avg. Solar intensity (W/m ²)	<u>652.71</u>	686	594.71	<u>678.88</u>
	Avg. Ambient temperature (°C)	36.26	36.52	36.08	36.61
9-18 L GWM	Date	21-05-2023	23-05-2023	22-05-2023	24-05-2023
	Avg. Solar intensity (W/m ²)	696.6	<u>645.2</u>	707	<u>679</u>
	Avg. Ambient temperature (°C)	37.05	36.25	36.04	37.02



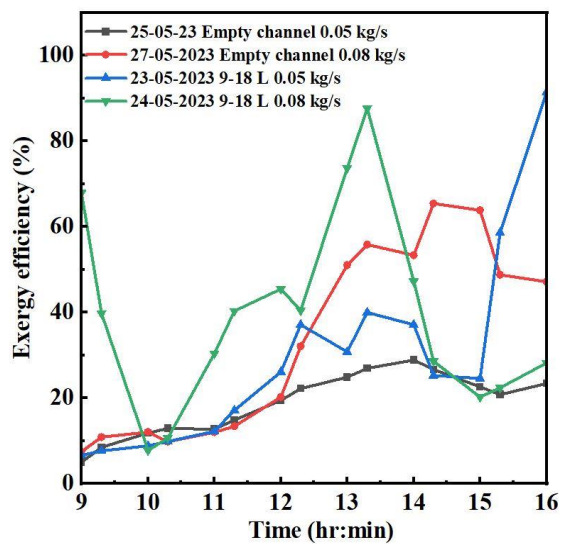
(a)



(b)



(c)



(d)

Figure 6.5 Variation of (a) ambient temperature, (b) solar intensity, (c) temperature rise, and (d) exergy efficiency varying the time for 0.05 and 0.08 kg/s mass flow rates.

6.6 CHARACTERISTICS OF 9-18L GWM SAH WITH EMPTY CHANNEL SAH FOR DRYING THE ONION AND TOMATO

Onions and Tomatoes are dried in the empty channel and 9-18 L GWM SAH for 0.05 and 0.08 kg/s mass flow rates. The actual practical trials have been conducted for two days. The weight of the Onion and Tomato has kept 0.750 kg to dry.

6.6.1 Effect of relative humidity

Figure 6.6 shows the changes in ambient, inlet and outlet relative humidity of air. The variation of relative humidity was 60 to 70 %, 47 to 62 % and 10 to 49 % for the ambient, inlet and outlet of the air respectively. The relative humidity reduces first from 9.00 hr. to 13.00 hr. then increases again. Similar trend is observed for empty and GWM SAH.

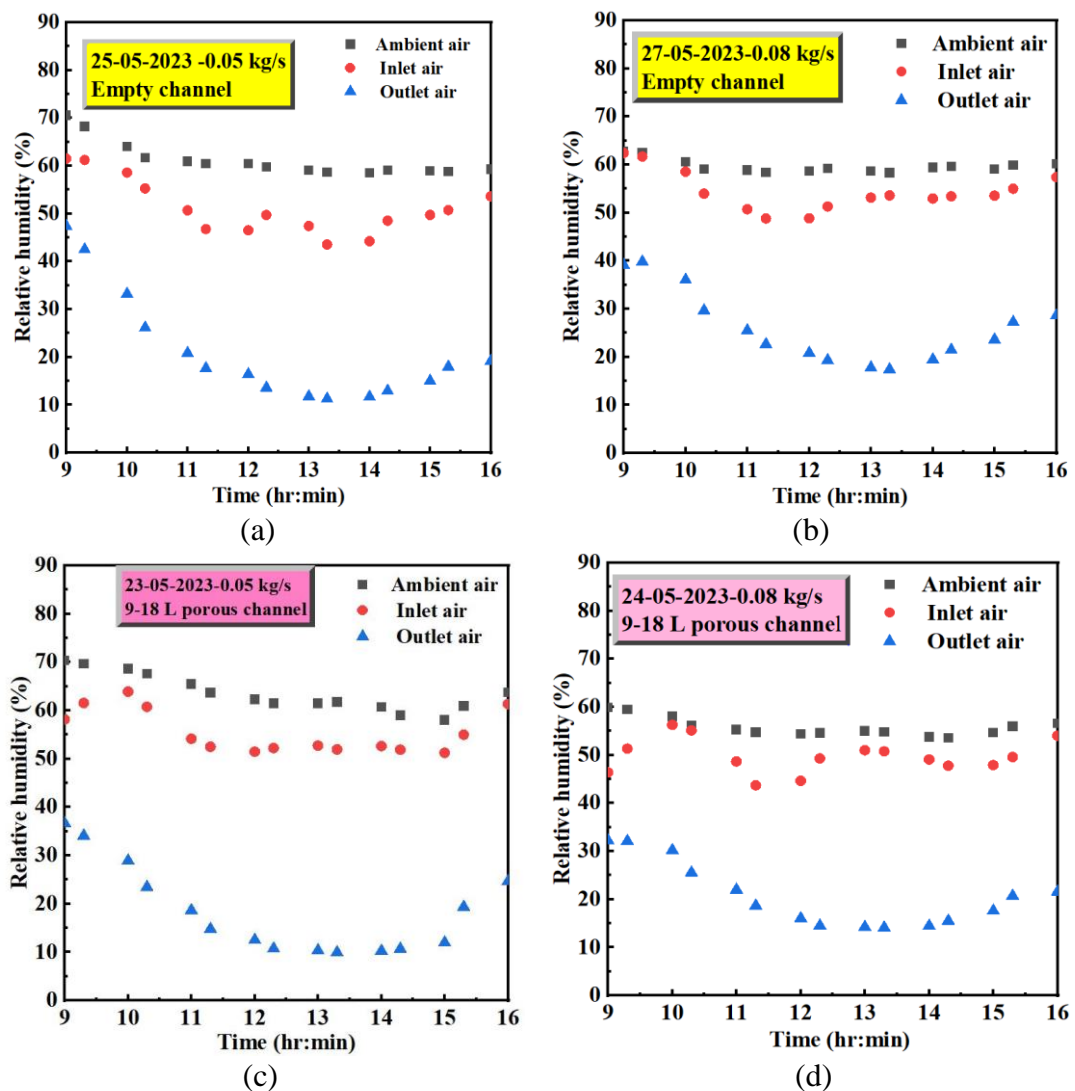


Figure 6.6 Change in the Relative humidity of ambient, inlet and outlet humidity with respect to time for (a) 0.05 kg/s mass flow rate empty channel SAH, (b) 0.08 kg/s mass flow rate empty channel SAH, (c) 0.05 kg/s mass flow rate 9-18 L GAWM SAH, (d) 0.08 kg/s mass flow rate 9-18 L GAWM SAH.

The relative humidity is low at the higher temperature because higher the temperature more the moisture extraction rate. 9-18 L GWM SAH is having 14.53 % and 25.46 % lower outlet relative humidity than the empty channel SAH due to the higher temperature in the GWM channel.

6.6.2 Effect of moisture content and moisture ratio and drying rate for empty channel and 9-18 L GWM SAH and open drying

The drying time is determined by moisture content on the dry basis. As the temperature increases the relative humidity decreases for both mass flow rates and for both empty channel and 9-18 L GWM SAH. The moisture removal rate from 9.00 hrs. till 11.00 hrs. is less due to lesser solar intensity. As the solar intensity increases, the temperature inside the channel increases and relative humidity reduces, so moisture removing rate is higher from 11.00 hrs to 14.00 hrs. The maximum moisture removal occurs in this time duration. The average drying time for the Onion and Tomato are 380 and 240 min respectively. The Figure 6.7 shows moisture content with drying time for Onion and Tomato for different mass flow rates in empty channel and 9-18 L GWM case.

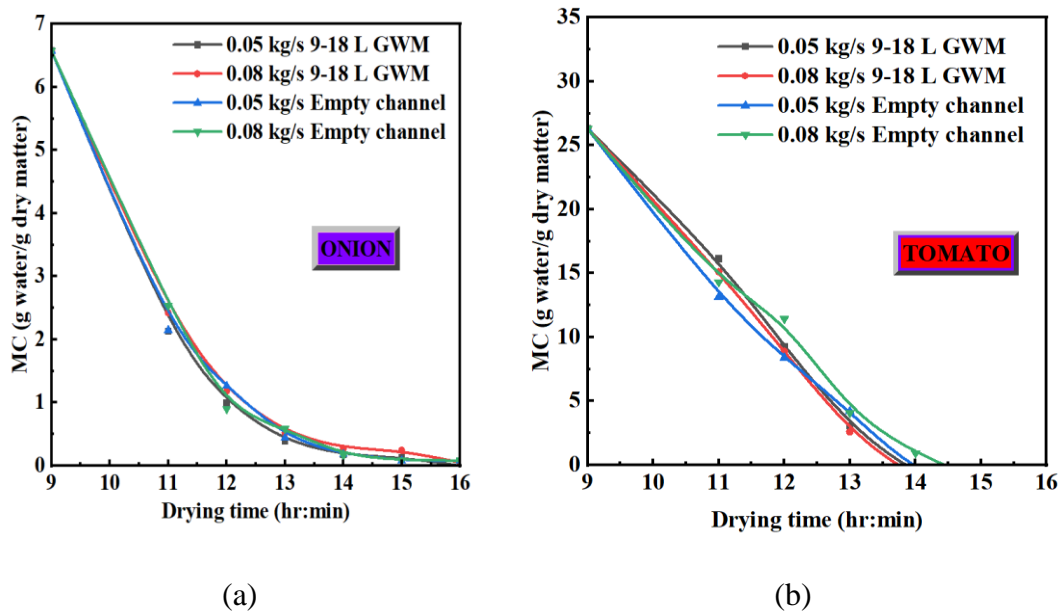


Figure- 6.7 Moisture content with drying time for (a)Onion and (b)Tomato for different mass flow rates in empty channel and 9-18 L GWM case.

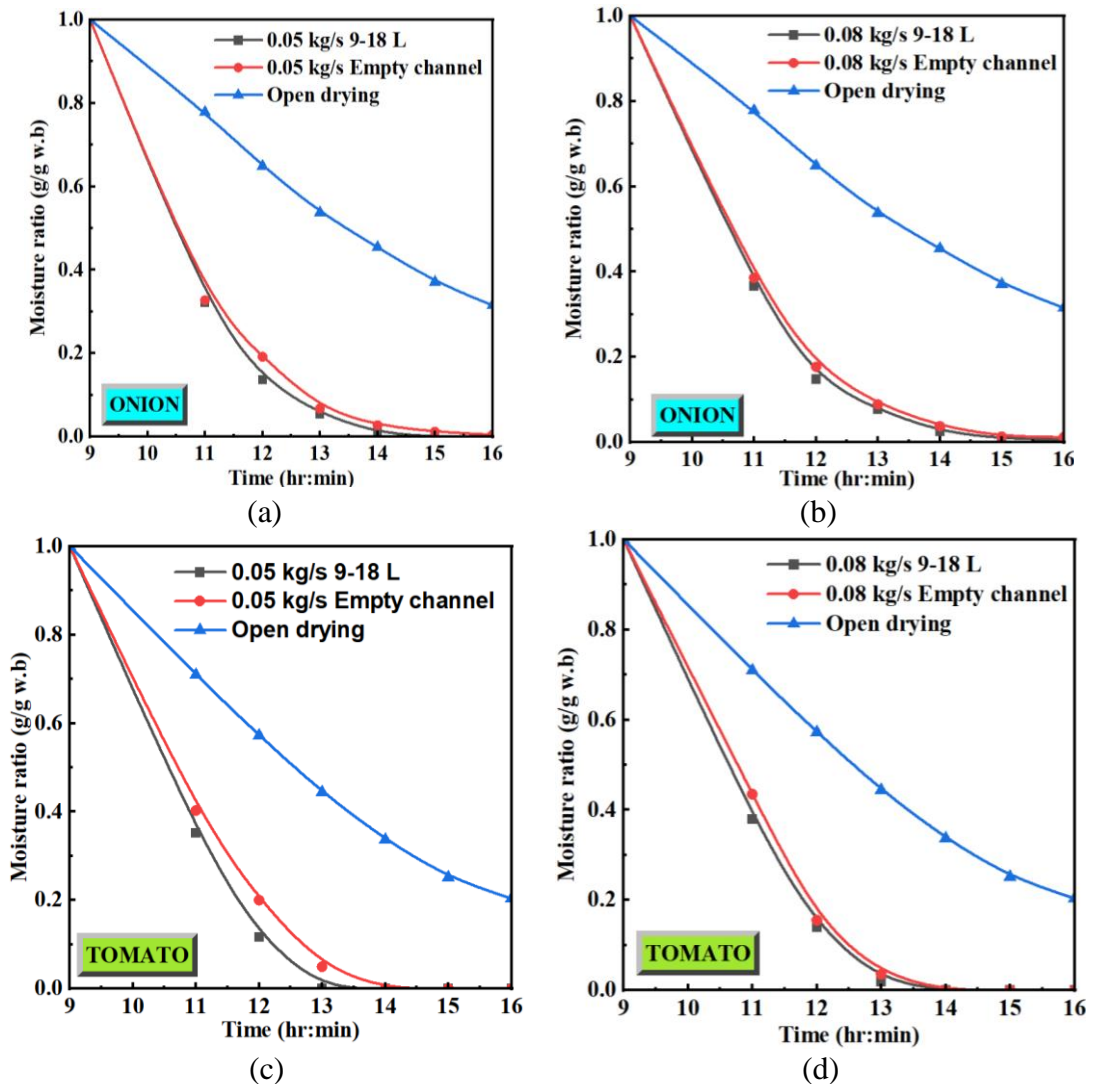


Figure 6.8 Effect of moisture removal varying with time for open sun drying, empty channel and 9-18 L GAWM for 0.05 and 0.08 kg/s mass flow rates.

Figure 6.8 shows the change in moisture ratio with time for open drying, empty channel and 9-18 L GWM SAH. The initial weight before drying of the Onion and Tomato is 250 gm for open sun drying, empty channel and 9-18 L GWM. The experiments are started at 8.00 hr i.e., one hour before to get steady state. Then, at 9.00 hr the product placed in the dryer. In the morning the moisture ratio is higher and then it decreases to zero as shown in Figure 6.8. In the first 120 min, the moisture ratio is nearly same. As the solar radiation increase from 11.00 am onwards, the moisture ratio decreases as the moisture removal is higher at higher temperature. The moisture ratio of Onion and Tomato has similar pattern as observed from Figure 6.8. Also same is the pattern for

drying rate in Figure 6.9. The product dries quickly in the initial 120 min and then it reduces gradually due to quick surface moisture exchange rate at the beginning. The total average drying hours for the slices of Onions and Tomatoes are 5 and 4 hours respectively. The GWM arrangement reduces the time of drying by 26.78 and 55 % for tomato and onion respectively compared to empty channel SAH comparing both mass flow rates.

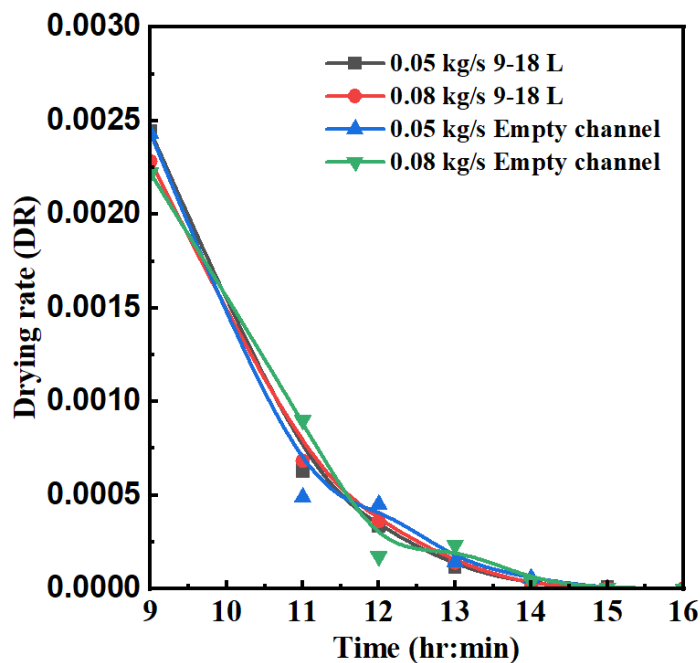


Figure 6.9. Effect of drying rate with time for empty channel and 9-18 L GWM SAH varying mass flow rates

6.7 ECONOMIC ANALYSIS

The parameters chosen for the present study in the economic investigations are annualized cost, net profit and payback duration. These categories are explained as follows-

6.7.1 Annualized cost

For twelve-month capital cost has been considered by using the purchased material to build the SAH, labor required to transport it and the special assembly done by special machining and its costing. The sum of these includes the annual capital cost. The twelve-month maintenance cost of the SAH is 10 % of the annual capital cost. The salvage value is 10 % of the twelve-month capital cost. The SAH operated days in a year considered as 250 days for the calculation purposes (Kesavan et al. 2019). The

dryer was operated on the 12 V DC solar panel operated exhaust fan; hence the electricity charges are zero. The amount of Onion and Tomato drying processed in a year at SAH is 660 kg and 260 kg respectively. The price of the dried 1 kg of Onion and Tomato slices is equivalent to the price of same product available in the market. So, 1 kg dried Onion and Tomato selling price considered as Rs.305 and Rs. 585 respectively. The capital cost of the studied single pass SAH is shown in the Table 6.2.

6.7.2 Levelized cost of the dryer and simple payback period

A solar air heater has been running 7 hours per day from 9.00 hours to 16.00 hours. The working days are 250 per year. The total weight of the product in initial state before drying is 20 kg which shows that the loading capacity of tray.

Table 6.2 Capacity of drying vegetable in kg per year

Vegetable Type	Onion		Tomato	
	Empty channel	9-18 L GWM	Empty channel	9-18 L GWM
Per day capacity of the loading tray at initial stage (kg)	20	20	20	20
Yearly capacity of the tray in kg	5000	5000	5000	5000
Per day running time of the system (minutes)	420	420	420	420
Complete duration of drying 20 kg of vegetables (minutes)	420	378	282	240
Weight of the initial loaded vegetables after drying	2.64	2.64	1.04	1.04
Per year drying vegetable weight	660	660	260	260
Extra time available to dry vegetable on the same day (minutes)	0	42	138	180
The extra loading capacity factor on the same day (kg)	0	0.11	0.49	0.75
The extra loading capacity per year	0	73	127	195
The extra initial vegetable required per year (kg)	0	550	2447	3750
Total dried vegetable weight per year (kg)	660	733	387	455
Yearly initial loading capacity of the tray with extra loading (kg)	5000	5550	7447	8750

The time required to complete dry the vegetables are 420, 378, 282 and 240 min for empty and 9-18 L GWM channel, in case of Onion and Tomato respectively. The dried product weight for one day after completion of test is 2.64 kg and 1.04 kg for Onion and Tomato respectively. The yearly capacity to drying vegetables in kg is noted in the Table 6.2. Table 6.2 shows that the 9-18 L has 11 % and 17.50 % more drying capacity than empty channel for Onion and Tomato respectively. At the same time the initial loading fresh vegetables increases as per modification done in SPSAH. The capital cost of the SPSAH is shown in Table 6.3. The capital cost of empty channel and 9-18 L SPSAH are Rs. 29216 and Rs. 32345 respectively. The capital cost includes GST charges, Labour charges and transportation charges.

Table 6.3 Capital cost of SPSAH (including GST, Labour and transportation charges)

Name of the part	Material	Price (Rs)
Absorber plate	Aluminium (Al)	1780
Transparent cover	Toughened glass	4050
Insulation	Ceramic wool	3100
Outer frame	Polyvinyl Chloride (PVC) sheet	9500
Black paint	Matte black paint	1160
Wire mesh	Aluminium (Al)	3129
Exhaust fan	12 V DC	738
Battery	12 V 9 A	2200
Solar panel and accessories	20 W capacity + Battery charge controller + wiring	1700
Miscellaneous	Nut + bolt + washer + Silicon sealant + Wires + Insulation tape.	2000
Angular Support for SAH	Mild Steel (MS)	3600
Tray (Slotted bar)	Galvanized Iron (GI)	1088
	Total	32345

The net profit is calculated from the price of dried product per year and selling value of dried product per year. The levelized cost of the dryer for Onion is 0.19 Rs/kg h and 0.18 Rs/kg h for empty channel and 9-18 L GWM. Also, for Tomato it is 0.22 Rs/kg h and 0.18 Rs/kg h for empty channel and 9-18 L GWM. The levelized cost of dryer minimized with addition of wire mesh by 5.26 % and 18.18 % compared to empty channel. It shows that the system is the best with wire mesh and useful for future application. The assessed average simple payback duration is 0.89 year which is shorter

Table 6.4 Economic analysis of single pass solar air heater

Vegetable	Onion		Tomato	
	Empty channel	9-18 L GWM	Empty channel	9-18 L GWM
Type of SPSAH	Empty channel	9-18 L GWM	Empty channel	9-18 L GWM
Capital cost (C _C) (Rs)	29216	32345	29216	32345
Maintenance charges (10% of C _M) (Rs)	2921.6	3234.5	2921.6	3234.5
Man power charges (Rs. 300 per day per unit for 250 days) (C _L) (Rs)	75000	75000	75000	75000
Raw material charges (Cr) (Rs)				
(Rs 20 kg/ per day × rate of product × 250 days in year)	100000	111000	74470	87500
Packaging charges (P _k) (Rs)	5000	5000	5000	5000
Total cost (P)	212138	226580	186608	203080
Initial total weight of the vegetable per year	5000	5550	7447	8750
Number of hours required for drying per day (Considered single batch of the vegetables so no addition of the product in between)	7	7	7	7
Number of days system operated per year	250	250	250	250
Annual dried weight of the vegetable in kg	660	733	387	455
Annual capacity of factor of the system	0.13	0.13	0.05	0.05
Cost of the dried vegetable per year (Rs)	305	305	585	585
Dried product fresh selling price per year (Rs)	201300	223443	226530	266175
Net benefits	-10838	-3137	39922	63096
Levelized cost of Dryer (LCOD)	0.19	0.18	0.22	0.18
Simple payback period (SPP)	1.05	1.01	0.82	0.76
Average SPP	for empty channel		0.94	
	9-18 L		0.89	
	GWM			

than lifespan of the SAH. The addition of the wire mesh reduces the payback period by 5.26 %. Hence the present manufactured single pass SAH is profitable, fruitful,

monetary useful for the drying vegetables and fruits in the rural areas. The details of the localized cost of dryer and simple payback period are shown in the Table 6.4.



(a) Onion before drying



(b) Open Sun drying



(c) Empty channel SAH drying



(d) 9-18 L GAWM SAH drying

Figure 6.10 Color of the Onion at different arrangement in (a) Onion before drying, (b) Open Sun drying (c) Empty channel SAH drying, (c) 9-18 L Al GWM SAH drying.



(a) Tomato before drying



(b) Open Sun drying



(c) Empty channel SAH drying

(d) 9-18 L GAWM SAH drying

Figure 6.11 Colar of the Tomato at different arrangement in (a) Tomato before drying, (b) Open Sun drying (c) Empty channel SAH drying, (c) 9-18 L Al GWM SAH drying.

Table 6.5 Some comparative studies about development of capabilities of different solar air heaters and its drying application of Onion

Ref.	Dryer type	Modification type	Mass flow rate kg/s	η_{th}	η_{Ex}	Weight of the product (g)	Drying time (min)
(Beye et al. 2019)	Direct	Greenhouse dryer	-	-	-	-	360–600
(Sözen et al. 2021)	Indirect	Tubular absorber with inserting Aluminium wool	0.010, 0.013	56.32–71.30	NM	100	180
(Hadibi et al. 2022)	Direct	geo-exchange energy assisted-insulated north wall solar dryer	0.018	1.48%–48.90%	-	5000	28 hr
(Tuncer et al. 2023)	Indirect	PVT dryer with grooved absorber surface, baffles and spherical turbulators	0.009, 0.014	61.32–77.49	59.16–68.31	-	220–320
Present study	Direct	Graded Aluminium wire mesh	0.05, 0.08	-	20-70	750	280

Table 6.6 Some comparative studies about development of capabilities of different solar air heaters and its drying application of Tomato

Ref.	Dryer type	Modification type	Mass flow rate (kg/s)	η_{th} (%)	η_{Ex} (%)	Weight of the product (g)	Drying time (min)
(Rajkumar et al. 2007)	Indirect	Vacuum assisted	-	-	-	-	360-600
(Hossain et al. 2008)	Indirect	Reflector and thermal storage system	-	22.35 -	-	79-139	88 hr
(Dorouzi et al. 2018)	Indirect	liquid desiccant-assisted SAH equipped with a PV-T regeneration system	-	-	-	500	250
(Ebadi et al. 2021)	Indirect	Hybrid compound parabolic concentrator	0.01, 0.025, 0.04	11-25	1-6	5-10	231
(Gupta et al. 2022)	Indirect	PVT thermal dryer		34.93	44.66	5000	13 hr
(Ahmad et al. 2023)	Direct	Green house SAH with thermal storage	0.06	50.20	-	4000	300
Present study	Direct	Graded Aluminium wire mesh	0.05, 0.08	-	20-70	750	240

Figure 6.10 and 6.11 shows the picture of before drying, open sun drying, empty channel and 9-18 L GAWM drying for Onion and Tomato respectively. It shows that within one day time period from 8.00 hr. to 17.00 hr. with even partly sunny days drying the product with SAH is very effective and the product dried in less time compared to open sun drying system. Table 6.5 and 6.6 shows the results of present research work

and previous investigations were performed by researchers. The present study has acceptable agreement with literature studies for both Onion and Tomato drying.

6.8 SUMMARY

The three-dimensional numerical analysis was performed with ANSYS fluent software. The Rosseland radiation model was used with solar ray tracing approach. The forced convection SPSAH was used to dry Onion and Tomato in the present study for two different mass flow rates as 0.05 and 0.08 kg/s numerically and experimentally. The improvement in the empty channel SPSAH is performed by adding GAWM of 9-18 in longitudinal direction.

- The empty channel experimental trials performed for 0.05 and 0.08 kg/s mass flow rates and average rise in temperature is from 9 °C to 32 °C and solar radiation was observed 300 to 950 W/m².
- The different combinations of GAWM were studied numerically to observed the temperature rise, Nusselt number, friction factor and finally thermal performance parameter of SPSAH. The 9-18 L is the best combination amongst 9-18 T, 18-9 T, 9-18 L and 18-9 L different configurations. The 9-18 L has an average of 2.45 % higher thermohydraulic performance than all other combinations mentioned above four types.
- The 9-18 L GWM case has an average of 63.45 % higher thermal efficiency than the empty channel for both mass flow rates.
- The GWM arrangement reduces the time of drying by 26.78 and 55 % for tomato and onion respectively compared to empty channel SAH.
- The assessed simple payback duration is 0.89 years which is good deal for rural application. Hence, the studied manufactured SPSAH is profitable, fruitful, monetary useful for the drying vegetables and fruits in the rural areas.

6.9 CLOSURE

This chapter deals with the transverse and longitudinal GAWM for heat transfer enhancement in the SPSAH. The use of graded aluminium wire mesh shows the good results for drying application. The simple payback period for Onion and Tomato is average 0.89 year which is good comparing the average life of the system.

CHAPTER 7

CONCLUSION AND FUTURE SCOPE WORK

7.1 CONCLUSIONS

The dominant priority of the present investigation is to design and develop a suitable and efficient single pass solar air heater for drying the vegetable and fruits etc. purposes. In this thesis, the main focus was to enhance the heat transfer in the entire channel by using metal foam or wire mesh as a metal porous media. Different thicknesses, PPI and porosities of metal foam and wire mesh were considered in order to evaluate the thermal performance of SPSAH. To mitigate the testing of SAH on the conventional electric supply and solar panel battery-operated testing was employed in this investigation.

7.1.1 Significant outcome of numerical study for enhancement of heat transfer using discrete metal foam with varying thickness and porosity in SPSAH by LTNE method

The two-dimensional rectangular channel was modelled to evaluate the effect of partial filling of different PPI and porosity of copper metal foam in SPSAH numerically. Based on the current investigation, the following points are concluded:

- The Nusselt number is highest for 88 mm metal foam, rather than 22 and 44 mm thick metal foam. The Nusselt number for 22, 44, and 88 mm thicknesses is 157.64%, 183.31%, and 218.60%, respectively, higher than the empty channel.
- Amongst the 10, 20 and 30 PPI copper metal foam, the 20 PPI gives a lesser pressure drop than 10 and 30 PPI metal foam for 22, 44, and 88 mm thickness. The highest pressure drop belongs to 30 PPI, having 28 % and 2 % more average pressure drop than 20 and 10 PPI, respectively, for 22, 44, and 88 mm thickness.
- The 20 PPI 0.8567 porosity with 22 mm thick metal foam has highest performance factor compared to all 10 and 30 PPI metal foam. For mass flow rate of 0.03 kg/s, the maximum performance factor for the 20 PPI 0.8567 porosity is 0.0055, 0.0050, and 0.0044 at 22, 44, and 88 mm metal foam thickness, respectively.

- With respect to performance factor, 22 mm 20 PPI 0.8567 porosity is best in terms of pressure drop and cost involved in manufacturing the solar air heater.

7.1.2 Significant outcome of thermohydraulic efficiency of a solar air heater in the presence of graded aluminium wire mesh – a combined experimental – numerical study.

This study involves experiments and analysis of the 3D geometry of SPSAH by a numerical finite volume method. The flow inside the SPSAH is assumed to be incompressible and steady state. The Rosseland radiation model with a solar ray tracing method is considered to evaluate the thermal performance of the SPSAH using LTE method for WM porous media. The properties of air are calculated at a bulk mean temperature and assumed to be constant throughout the length. Al WMs with three different porosities is combined together to enhance the heat-transfer rate in single-pass forced convection SAH. The Al WM is assumed to be isotropic, homogenous, and non-deformable. The wire mesh length, width, and thickness of each porosity is assumed to be $500 \times 985 \times 5$ mm (i.e., 25% of the full length of the test section) in the present study. Experiments are performed for the 0.027 and 0.058 kg/s mass flow rates. The following results have been obtained:

- For the full-length case, 9-18-3 PPI is the best suitable combination compared to Cases 3-9-18 and 18-3-9 PPI in terms of maximum outlet temperature, Nusselt number and THPP. Case 9-18-3 PPI has 7.62 % and 7.22 % higher average THPP than Case 3-9-18 and 18-3-9, respectively, for both the mass flow rate.
- The 25 % length of the GWM of the full-length test section was kept at four different locations (i.e., 0, 0.5, 1, and 1.5 m from the inlet) in numerical analysis. The thermal performance was analysed with respect to temperature, Nusselt number, friction factor, and THPP at these four locations. The Nusselt number is higher in the WM of 25 % of the length of the full-length test section than all other cases considered above as a result of the changes in the absorber plate temperature and bulk mean fluid temperature. The friction factor was lower and THPP was higher for the case of 25 % of the length of the WM of the full-length test section among all of the other cases.

- The 25 % length of the WM of the full-length test section at a distance 1.5 m from the inlet is more valuable than all other cases in terms of the overall performance of porous SAH. The enhancement in the thermal efficiency was 23.32 % higher for 0.058 kg/s than the empty channel.

7.1.3 Significant outcome of energy, exergy and economic analysis of single pass solar air heater comparing transverse and longitudinal direction graded aluminium wire mesh for drying onion and tomato.

The forced convection single pass SAH was used to dry Onion and Tomato in the present study for two different mass flow rates as 0.05 and 0.08 kg/s numerically and experimentally. The improvement in the empty channel SPSAH is performed by adding graded Aluminium wire mesh of 9-18 in longitudinal direction.

- The different combinations of graded wire mesh were studied numerically to observe the temperature rise, heat transfer coefficient, friction factor and finally thermal performance parameter of SPSAH. The 9-18 L is the best combination amongst 9-18 T, 18-9 T, 9-18 L and 18-9 L different configurations. The 9-18 L has an average of 2.45 % higher THPP than all other combinations mentioned above four types.
- The 9-18 L GWM case has average of 63.45 % higher thermal efficiency than the empty channel for both mass flow rates.
- The GWM arrangement reduces the time of drying by 26.78 and 55 % for tomato and onion respectively compared to empty channel SAH.
- The assessed simple payback duration is 0.89 years which is good deal for rural application. Hence, the studied manufactured single pass SAH is profitable, fruitful, monetary useful for the drying vegetables and fruits in the rural areas.

7.1.4 Novel approach to scientific community

The present thesis involves some of the novel scientific approach which would be helpful to industry as well as house hold applications.

- Design of SAH according to industrial scale
- Use of solar panel battery-operated data logger
- Portable SAH for easy mobility

- Novel arrangements of wire meshes in SAH to improve the efficiency
- Focus is on drying of vegetables

7.2 FUTURE SCOPE

The following are the future plans in the area of SAH:

- Design and development of compact SAH as per the industry requirements.
- Waste to wealth concept: to use maximum waste material to make SAH.
- Integrating PCM and wire mesh in SAH for energy storage purpose.
- Analysis of different suitable conditions for drying of different vegetables.

7.3 CLOSURE

This work shows that the thermohydraulic performance parameter and thermal efficiency can be improved by porous media. This chapter provides the major outcome of the complete research work carried out to check the thermal performance of SAH by numerical and experimental methods. Also, this chapter gives further development related to SAH.

REFERENCES

- Adnan Abed, Q., Badescu, V., Ciocanea, A., Soriga, I., and Bureștea, D. (2017). "Models for new corrugated and porous solar air collectors under transient operation." *Journal of Non-Equilibrium Thermodynamics*, 42(1), 79–97.
- Ahmad, A., Prakash, O., Kumar, A., and Hussain, M. S. (2023). "Drying Kinetics and Performance Analysis of Thermal Storage-Based Hybrid Greenhouse Dryer for Uniform Drying of Tomato Flakes." *J Therm Sci Eng Appl*, 15(5).
- Ahmad, A., Saini, J. S., and Varma, H. K. (1996). *Thermohydraulic performance of packed-bed solar air heaters. ~ Pergamon Energy Convers. Mgmt.*
- Aldabbagh, L. B. Y., Egelioglu, F., and Ilkan, M. (2010). "Single and double pass solar air heaters with wire mesh as packing bed." *Energy*, 35(9), 3783–3787.
- Alic, E., Das, M., and Akpınar, E. K. (2021). "Design, manufacturing, numerical analysis and environmental effects of single-pass forced convection solar air collector." *J Clean Prod*, 311.
- Anirudh, K., and Dhinakaran, S. (2020). "Performance improvement of a flat-plate solar collector by inserting intermittent porous blocks." *Renew Energy*, 145, 428–441.
- Anirudh, K., and Dhinakaran, S. (2021). "Numerical analysis of the performance improvement of a flat-plate solar collector using conjugated porous blocks." *Renew Energy*, 172, 382–391.
- Ansys Fluent. (2022). "Ansys Fluent Theory Guide, ANSYS Inc. Canonsburg." *version 2022* (Oct. 6, 2023).
- Avila-Marin, A. L., Fernandez-Reche, J., and Martinez-Tarifa, A. (2019). "Modelling strategies for porous structures as solar receivers in central receiver systems: A review." *Renewable and Sustainable Energy Reviews*, Elsevier Ltd.
- Azad, R., Bhuvad, S., and Lanjewar, A. (2021). "Study of solar air heater with discrete arc ribs geometry: Experimental and numerical approach." *International Journal of Thermal Sciences*, 167.
- Baig, W., and Ali, H. M. (2019). "An experimental investigation of performance of a double pass solar air heater with foam aluminum thermal storage medium." *Case Studies in Thermal Engineering*, 14.
- Barghi Jahromi, M. S., Kalantar, V., Sefid, M., Samimi Akhijahani, H., and Iranmanesh, M. (2023). "Energy and exergy analysis of an unglazed transpired collector connected to a dryer with a porous plate and phase change material." *J Energy Storage*, 60.

- Bayrak, F., and Oztop, H. F. (2015b). “Experimental analysis of thermal performance of solar air collectors with aluminum foam obstacles.” *J. of Thermal Science and Technology*, 35, 11–20.
- Bayrak, F., Oztop, H. F., and Hepbasli, A. (2013). “Energy and exergy analyses of porous baffles inserted solar air heaters for building applications.” *Energy Build*, 57, 338–345.
- Beye, N. F., Kane, C., Ayessou, N., Kebe, C. M. F., Talla, C., Diop, C. M., and Sène, A. (2019). “Modelling the dehydration kinetics of four onion varieties in an oven and a solar greenhouse.” *Heliyon*, 5(9).
- Calmidi, V. V., and Mahajan, R. L. (2000). “Forced convection in high porosity metal foams.” *J Heat Transfer*, 122(3), 557–565.
- Cengel, Y. A. (2006). *Heat transfer a practical approach*.
- Chen, Z., Gu, M., and Peng, D. (2010). “Heat transfer performance analysis of a solar flat-plate collector with an integrated metal foam porous structure filled with paraffin.” *Appl Therm Eng*, 30(14–15), 1967–1973.
- Chiou, J. P., El-Wakil, M. M., and Duffie, J. A. (1965). “A slit-and -expanded aluminum-foil matrix solar collector.” *Solar Energy*, 9(2), 73–80.
- Chouksey, V. K., and Sharma, S. P. (2016). “Investigations on thermal performance characteristics of wire screen packed bed solar air heater.” *Solar Energy*, 132, 591–605.
- Chouksey, V. K., Singh Yadav, A., Raha, S., Shrivastava, V., and Shrivastava, S. P. (2022). “A theoretical parametric analysis to optimize the bed depth of packed bed solar air collector.” *Int J Green Energy*, 19(7), 775–785.
- Debnath, S., Das, B., and Randive, P. (2022). “Energy and exergy analysis of plain and corrugated solar air collector: effect of seasonal variation.” *International Journal of Ambient Energy*, 43(1), 2796–2807.
- Dehghan, M., Rahmani, Y., Domiri Ganji, D., Saedodin, S., Valipour, M. S., and Rashidi, S. (2015). “Convection-radiation heat transfer in solar heat exchangers filled with a porous medium: Homotopy perturbation method versus numerical analysis.” *Renew Energy*, 74, 448–455.
- Devecioğlu, A. G., Oruc, V., and Tuncer, Z. (2018). “Energy and exergy analyses of a solar air heater with wire mesh-covered absorber plate.” *International Journal of Exergy*, 26(1–2), 3–20.
- Dhiman, P., Thakur, N. S., and Chauhan, S. R. (2012). “Thermal and thermohydraulic performance of counter and parallel flow packed bed solar air heaters.” *Renew Energy*, 46, 259–268.

- Diganjit, R., Gnanasekaran, N., and Mobedi, M. (2022). “Numerical Study for Enhancement of Heat Transfer Using Discrete Metal Foam with Varying Thickness and Porosity in Solar Air Heater by LTNE Method.” *Energies (Basel)*, 15(23), 8952.
- Dorouzi, M., Mortezaipoor, H., Akhavan, H. R., and Moghaddam, A. G. (2018). “Tomato slices drying in a liquid desiccant-assisted solar dryer coupled with a photovoltaic-thermal regeneration system.” *Solar Energy*, 162, 364–371.
- Dukhan, N., and Quinones, P. D. (2003). Convective heat transfer analysis of open cell metal foam for solar air heaters.
- Ebadi, H., Zare, D., Ahmadi, M., and Chen, G. (2021). “Performance of a hybrid compound parabolic concentrator solar dryer for tomato slices drying.” *Solar Energy*, 215(May 2020), 44–63.
- El-khawajah, M. F., Aldabbagh, L. B. Y., and Egelioglu, F. (2011). “The effect of using transverse fins on a double pass flow solar air heater using wire mesh as an absorber.” *Solar Energy*, 85(7), 1479–1487.
- Farhan, A. A., Obaid, Z. A. H., and Hussien, S. Q. (2020). “Analysis of exergetic performance for a solar air heater with metal foam fins.” *Heat Transfer - Asian Research*, 49(5), 3190–3204.
- Fluent, A. (2019). “Ansys Fluent.” *version 2019*, <<https://ansyshelp.ansys.com/>>.
- Garg, and Prakash. (2016). *Solar Energy Fundamentals and Applications*. Mc Graw Hill.
- Ghritlahre, H. K., and Prasad, R. K. (2018). “Investigation of thermal performance of unidirectional flow porous bed solar air heater using MLP, GRNN, and RBF models of ANN technique.” *Thermal Science and Engineering Progress*, 6(December 2017), 226–235.
- Gill, R. S., Hans, V. S., and Singh, R. P. (2021). “Optimization of artificial roughness parameters in a solar air heater duct roughened with hybrid ribs.” *Appl Therm Eng*, 191(October 2020), 116871.
- Gill, R. S., Singh, S., and Singh, P. P. (2012). “Low cost solar air heater.” *Energy Convers Manag*, 57, 131–142.
- Güler, H. Ö., Sözen, A., Tuncer, A. D., Afshari, F., Khanlari, A., Şirin, C., and Gungor, A. (2020). “Experimental and CFD survey of indirect solar dryer modified with low-cost iron mesh.” *Solar Energy*, 197, 371–384.
- Gupta, A., Das, B., Biswas, A., and Mondol, J. D. (2022). “An environmental and economic evaluation of solar photovoltaic thermal dryer.” *International Journal of Environmental Science and Technology*, 19(11), 10773–10792.
- Gupta, C. L., and Garg, H. P. (1967). “Performance studies on solar air heaters.” *Solar Energy*, 11(1), 25–31.

- Hadibi, T., Boubekri, A., Mennouche, D., Benhamza, A., Mazouzi, K., Kumar, A., Xiao, H. W., and Allaf, K. (2022). “Energy, environmental, economic, and color analysis of geo-exchange energy assisted-insulated north wall solar dryer for onion slices under relatively cloudy and rainy conditions.” *Solar Energy*, 236, 1–16.
- Ho, C. D., Lin, C. S., Chuang, Y. C., and Chao, C. C. (2013). “Performance improvement of wire mesh packed double-pass solar air heaters with external recycle.” *Renew Energy*, 57, 479–489.
- Hossain, M. A., Amer, B. M. A., and Gottschalk, K. (2008). “Hybrid solar dryer for quality dried tomato.” *Drying Technology*, 26(12), 1591–1601.
- Howell, R. S. & J. (2002). *Thermal radiation heat transfer*. Taylor & Francis.
- Hu, J., Guo, M., Guo, J., Zhang, G., and Zhang, Y. (2020). “Numerical and experimental investigation of solar air collector with internal swirling flow.” *Renew Energy*, 162, 2259–2271.
- Hu, J., Sun, X., Xu, J., and Li, Z. (2013). “Numerical analysis of mechanical ventilation solar air collector with internal baffles.” *Energy Build*, 62, 230–238.
- Hung, T. C., Huang, T. J., Lee, D. S., Lin, C. H., Pei, B. S., and Li, Z. Y. (2017). “Numerical analysis and experimental validation of heat transfer characteristic for flat-plate solar air collector.” *Appl Therm Eng*, 111, 1025–1038.
- Hussien, S. Q., and Farhan, A. A. (2019). “The effect of metal foam fins on the thermohydraulic performance of a solar air heater.” *International Journal of Renewable Energy Research*, 9(2), 840–847.
- Hussien, S. Q., Farhan, A. A., Hussien, S. Q., Farhan, A. A., and Corresponding, ‡. (2019). International journal of renewable energy research the effect of metal foam Fins on the Thermo-hydraulic Performance of a Solar Air Heater.
- J P Holman. (1994). *Experimental methods for engineers*.
- Jadhav, P. H., G, T., Gnanasekaran, N., and Mobedi, M. (2022). “Performance score based multi-objective optimization for thermal design of partially filled high porosity metal foam pipes under forced convection.” *Int J Heat Mass Transf*, 182.
- Jadhav, P. H., and Gnanasekaran, N. (2021). “Optimum design of heat exchanging device for efficient heat absorption using high porosity metal foams.” *International Communications in Heat and Mass Transfer*, 126(July), 105475.
- Jadhav, P. H., Gnanasekaran, N., and Perumal, D. A. (2021a). “Numerical consideration of LTNE and darcy extended forchheimer models for the analysis of forced convection in a horizontal pipe in the presence of metal foam.” *J Heat Transfer*, 143(1).

- Jadhav, P. H., Gnanasekaran, N., Perumal, D. A., and Mobedi, M. (2021b). "Performance evaluation of partially filled high porosity metal foam configurations in a pipe." *Appl Therm Eng*, 194.
- Jalil, M. J., and Ali, J. S. (2021). "Thermal Investigations of Double Pass Solar Air Heater with Two Types of Porous Media of Different Thermal Conductivity." *Engineering and Technology Journal*, 39(1A), 79–88.
- Jia, B., Yang, L., Zhang, L., Liu, B., Liu, F., and Li, X. (2021). "Optimizing structure of baffles on thermal performance of spiral solar air heaters." *Solar Energy*, 224, 757–764.
- Jouybari, H. J., Saedodin, S., Zamzamian, A., Nimvari, M. E., and Wongwises, S. (2017). "Effects of porous material and nanoparticles on the thermal performance of a flat plate solar collector: An experimental study." *Renew Energy*, 114, 1407–1418.
- Jouybari, N. F., and Lundström, T. S. (2020). "Performance improvement of a solar air heater by covering the absorber plate with a thin porous material." *Energy*, 190, 116437.
- Kamath, P. M., Balaji, C., and Venkateshan, S. P. (2011). "Experimental investigation of flow assisted mixed convection in high porosity foams in vertical channels." *Int J Heat Mass Transf*, 54(25–26), 5231–5241.
- Kamath, P. M., Balaji, C., and Venkateshan, S. P. (2013). "Convection heat transfer from aluminium and copper foams in a vertical channel - An experimental study." *International Journal of Thermal Sciences*, 64, 1–10.
- Kansara, R., Pathak, M., and Patel, V. K. (2021). "Performance assessment of flat-plate solar collector with internal fins and porous media through an integrated approach of CFD and experimentation." *International Journal of Thermal Sciences*, 165.
- Kesavan, S., Arjunan, T. V., and Vijayan, S. (2019). "Thermodynamic analysis of a triple-pass solar dryer for drying potato slices." *J Therm Anal Calorim*, 136(1), 159–171.
- Koholé, Y. W., Fohagui, F. C. V., and Tchuen, G. (2021). "Flat-Plate Solar Collector Thermal Performance and Optimal Operation Mode by Exergy Analysis and Numerical Simulation." *Arab J Sci Eng*, 46(2), 1877–1897.
- Kothandaraman C P, S. S. (2018). *Heat and mass transfer data book*. New Age International Publishers.
- Krittacom, B., Bunchan, S., and Luampon, R. (2022). "Heat transfer enhancement of solar collector by placing wire mesh stainless porous material on the solar absorber plate of indirect forced convection solar dryer." *Thermal Science and Engineering Progress*, 32(August 2021), 101304.
- Kumar, D., and Layek, A. (2022). "Nusselt number and friction characteristics of solar air heater roughened with novel twisted V-shaped staggered ribs using liquid crystal thermography." *Renew Energy*, 201, 651–666.

- Kumar, P. (2012). "Effect of differential mass flow rate on the thermal performance of double duct packed bed solar air heaters." *Renewable Energy and Power Quality Journal*, 1(10), 1300–1304.
- Luampon, R., Bunchan, S., and Krittakom, B. (2019). "Specific energy consumption improvement with applying stainless wire mesh porous material for a hot air dryer." *Key Eng Mater*, Trans Tech Publications Ltd, 345–350.
- M. Jalil, J., and J. Ali, S. (2021). "Thermal Investigations of Double Pass Solar Air Heater with Two Types of Porous Media of Different Thermal Conductivity." *Engineering and Technology Journal*, 39(1A), 79–88.
- Mahdi, A. N., Hasan, M. R., and Rasheed, S. A. (2021). "Experimental Study of Forced Convection Heat Transfer through Porous Media inside a Rectangular Duct of Fully Developed Region." *IOP Conf Ser Mater Sci Eng*, 1076(1), 012073.
- Mahmoudi, Y., and Karimi, N. (2014). "Numerical investigation of heat transfer enhancement in a pipe partially filled with a porous material under local thermal non-equilibrium condition." *Int J Heat Mass Transf*, 68, 161–173.
- Mancin, S., Zilio, C., Diani, A., and Rossetto, L. (2012). "Experimental air heat transfer and pressure drop through copper foams." *Exp Therm Fluid Sci*, 36, 224–232.
- Mishra, C. B., and Sharma, S. P. (1981). "Performance study of air-heated packed-bed solar-energy collectors." *Energy*, 6(2), 153–157.
- Mittal, M. K., and Varshney, L. (2006). "Optimal thermohydraulic performance of a wire mesh packed solar air heater." *Solar Energy*, 80(9), 1112–1120.
- MNRE Government of India. (2023). "<https://mnre.gov.in/about-department/introduction/>." *Government of India*.
- Mund, C., Kumar Rathore, S., and Kumar Sahoo, R. (2023). "Experimental study of heat transfer and frictional characteristics of impinging jet solar air heater with wire-mesh attached to the absorber plate." *Thermal Science and Engineering Progress*, 46.
- Mutar, W. M., and Alaiwi, Y. (2023). "Experimental investigation of thermal performance of single pass solar collector using high porosity metal foams." *Case Studies in Thermal Engineering*, 45(March).
- Naphon, P. (2005). "Effect of porous media on the performance of the double-pass flat plate solar air heater." *International Communications in Heat and Mass Transfer*, 32(1–2), 140–150.
- Narashimhan, A. (2020). *Essentials of Heat and Fluid Flow in Porous Media*. (Arunna Narasimhan, ed.), New Delhi: Ane Books Pvt. Ltd.
- Nidhul, K., Yadav, A. K., Anish, S., and Arunachala, U. C. (2020). "Efficient design of an artificially roughened solar air heater with semi-cylindrical side walls: CFD and exergy analysis." *Solar Energy*, 207, 289–304.

- Nidhul, K., Yadav, A. K., Anish, S., and Arunachala, U. C. (2022). "Thermo-hydraulic and exergetic performance of a cost-effective solar air heater: CFD and experimental study." *Renew Energy*, 184, 627–641.
- Nowzari, R., and Aldabbagh, L. B. Y. (2017). "Experimental study on a solar air heater with various perforated covers." *Sadhana - Academy Proceedings in Engineering Sciences*, 42(9), 1585–1593.
- Nowzari, R., Mirzaei, N., and Aldabbagh, L. B. Y. (2015). "Finding the best configuration for a solar air heater by design and analysis of experiment." *Energy Convers Manag*, 100, 131–137.
- Nowzari, R., Saygin, H., and Aldabbagh, L. B. Y. (2021). "Evaluating the performance of a modified solar air heater with pierced cover and packed mesh layers." *Journal of Solar Energy Engineering, Transactions of the ASME*, 143(1), 1–8.
- Omojaro, A. P., and Aldabbagh, L. B. Y. (2010). "Experimental performance of single and double pass solar air heater with fins and steel wire mesh as absorber." *Appl Energy*, 87(12), 3759–3765.
- Parsa, H., Saffar-Avval, M., and Hajmohammadi, M. R. (2021). "3D simulation and parametric optimization of a solar air heater with a novel staggered cuboid baffles." *Int J Mech Sci*, 205(April), 106607.
- Patel, Y. M., Jain, S. V., and Lakhera, V. J. (2021). "Thermo-hydraulic performance analysis of a solar air heater roughened with discrete reverse NACA profile ribs." *International Journal of Thermal Sciences*, 167.
- Prasad, S. B., Saini, J. S., and Singh, K. M. (2009). "Investigation of heat transfer and friction characteristics of packed bed solar air heater using wire mesh as packing material." *Solar Energy*, 83(5), 773–783.
- Prasad, S. B., Saini, J. S., and Singh, K. M. (2021). "Enhancement of heat transfer characteristics of wire mesh packed bed solar air heaters." *AIP Conf Proc*, 2341(May).
- Prasanna Singh. (2023a). "Saur Energy International." *Manas Nandi, New Delhi*, 1–60.
- Prasanna Singh. (2023b). "Saur Energy International." *Manas Nandi, New Delhi*, 1–64.
- Rajarajeswari, K., Alok, P., and Sreekumar, A. (2018). "Simulation and experimental investigation of fluid flow in porous and non-porous solar air heaters." *Solar Energy*, 171, 258–270.
- Rajarajeswari, K., and Sreekumar, A. (2014). Performance evaluation of a wire mesh solar air heater.
- Rajkumar, P., Kulanthaisami, S., Raghavan, G. S. V., Gariépy, Y., and Orsat, V. (2007). "Drying kinetics of tomato slices in vacuum assisted solar and open sun drying methods." *Drying Technology*, 25(7–8), 1349–1357.

Ramani, B. M., Gupta, A., and Kumar, R. (2010). "Performance of a double pass solar air collector." *Solar Energy*, 84(11), 1929–1937.

Ranake Vinayak. (n.d.). "Data Loggers, Wireless Data Logger, Chart Recorder, Manufacturer, India." <<https://www.sunsuiprocess.com/>> (Nov. 23, 2022).

Saedodin, S., Zamzamian, S. A. H., Nimvari, M. E., Wongwises, S., and Jouybari, H. J. (2017a). "Performance evaluation of a flat-plate solar collector filled with porous metal foam: Experimental and numerical analysis." *Energy Convers Manag*, 153, 278–287.

Saravanan, A., Murugan, M., Reddy, M. S., Ranjit, P. S., Elumalai, P. V., Kumar, P., and Sree, S. R. (2021). "Thermo-hydraulic performance of a solar air heater with staggered C-shape finned absorber plate." *International Journal of Thermal Sciences*, 168.

Sharma, S. P., Chauksey, V. K., Kumar, A., Behura, A. K., and Kumar, R. (2017a). "Wire Screen Matrices Packed Bed Solar Air Heater Performance-An Exergetic and Energetic Approach." 4(4), 90–108.

Sharma, S. P., Saini, J. S., and Varma, H. K. (1991). "Thermal performance of packed-bed solar air heaters." *Solar Energy*, 47(2), 59–67.

Sharma, S., and Talukdar, P. (2022). "Thermo-mechanical analysis of a porous volumetric solar receiver subjected to concentrated solar radiation." *Solar Energy*, 247, 41–54.

Shetty Shreyas, N. Madhwesh, K. V. K. (2021). "Numerical analysis of a solar air heater with circular perforated absorber plate by Shreyas P Shetty." *Solar Energy*, 215, 416–433.

Singh, O. K., and Panwar, N. L. (2013). "Effects of thermal conductivity and geometry of materials on the temperature variation in packed bed solar air heater." *J Therm Anal Calorim*, 111(1), 839–847.

Singh, S. (2020). "Experimental and numerical investigations of a single and double pass porous serpentine wavy wiremesh packed bed solar air heater." *Renew Energy*, 145, 1361–1387.

Singh, S. (2022). "Utilising fractional porous interface for high thermal performance of serpentine wavy channel solar air heater." *Appl Therm Eng*, 205.

Singh, S., and Dhiman, P. (2018). "Analytical and experimental investigations of packed bed solar air heaters under the collective effect of recycle ratio and fractional mass flow rate." *J Energy Storage*, 16, 167–186.

Singh, S., Dhruw, L., and Chander, S. (2019). "Experimental investigation of a double pass converging finned wire mesh packed bed solar air heater." *J Energy Storage*, 21(October 2018), 713–723.

- Sopian, K., Daud, W., Othman, M., and Yatim, B. (1999). Thermal performance of the double-pass solar collector with and without porous media.
- Sözen, A., Kazancıoğlu, F. Ş., Tuncer, A. D., Khanlari, A., Bilge, Y. C., and Gungor, A. (2021). “Thermal performance improvement of an indirect solar dryer with tube-type absorber packed with aluminum wool.” *Solar Energy*, 217(February), 328–341.
- Sözen, A., Şirin, C., Khanlari, A., Tuncer, A. D., and Gürbüz, E. Y. (2020). “Thermal performance enhancement of tube-type alternative indirect solar dryer with iron mesh modification.” *Solar Energy*, 207(February), 1269–1281.
- Sukhatme, and Nayak. (2018). *Solar energy*. McGraw Hill.
- Taha, S. Y., and Farhan, A. A. (2021). “Performance augmentation of a solar air heater using herringbone metal foam fins: An experimental work.” *Int J Energy Res*, 45(2), 2321–2333.
- Thakur, N. S., Saini, J. S., and Solanki, S. C. (2003). “Heat transfer and friction factor correlations for packed bed solar air heater for a low porosity system.” *Solar Energy*, 74(4), 319–329.
- Tian, J., Kim, T., Lu, T. J., Hodson, H. P., Queheillalt, D. T., Sypeck, D. J., and Wadley, H. N. G. (2004). “The effects of topology upon fluid-flow and heat-transfer within cellular copper structures.” *Int J Heat Mass Transf*, 47(14–16), 3171–3186.
- Tiwari, P., Kumar, A., and Sarviya R M. (2013). International Conference on Energy Efficient Technologies for Sustainability (ICEETS). IEEE.
- Tuncer, A. D., Khanlari, A., Afshari, F., Sözen, A., Çiftçi, E., Kusun, B., and Şahinkesen, İ. (2023). “Experimental and numerical analysis of a grooved hybrid photovoltaic-thermal solar drying system.” *Appl Therm Eng*, 218.
- Varshney, L., and Saini, J. S. (1998). Heat transfer and friction factor correlations for rectangular solar air heater duct packed with wire mesh screen matrices.
- Velmurugan, P., and Kalaivanan, R. (2015). “Energy and exergy analysis of multi-pass flat plate solar air heater-an analytical approach.” *Int J Green Energy*, 12(8), 810–820.
- Velmurugan, P., and Ramesh, P. (2011). “Evaluation of thermal performance of wire mesh solar air heater.” *Indian J Sci Technol*, 4(1).
- Verma, P., and Varshney, L. (2015). “Parametric investigation on thermo-hydraulic performance of wire screen matrix packed solar air heater by Prashant Verma.” *Sustainable Energy Technologies and Assessments*, 10, 40–52.
- Xu, H., Gong, L., Huang, S., and Xu, M. (2014). “Non-equilibrium heat transfer in metal-foam solar collector with no-slip boundary condition.” *Int J Heat Mass Transf*, 76, 357–365.

Yadav, A. S., and Bhagoria, J. L. (2013). "Heat transfer and fluid flow analysis of solar air heater: A review of CFD approach." *Renewable and Sustainable Energy Reviews*, Elsevier Ltd.

Yadav, S., and Saini, R. P. (2020). "Numerical investigation on the performance of a solar air heater using jet impingement with absorber plate." *Solar Energy*, 208, 236–248.

Zhao, Z., Luo, L., Qiu, D., Wang, Z., and Sundén, B. (2021). "On the solar air heater thermal enhancement and flow topology using differently shaped ribs combined with delta-winglet vortex generators." *Energy*, 224.

LIST OF PUBLICATIONS BASED ON PH.D. RESEARCH WORK

Sr. No.	Title of the paper	Authors	Journal Name, Year, Volume Number, Issue, Pages	Month, year of publication	Category*
1	“Numerical Study for Enhancement of Heat Transfer Using Discrete Metal Foam with Varying Thickness and Porosity in Solar Air Heater by LTNE Method”, https://doi.org/10.3390/en15238952	Rawal Diganjit, N. Gnanasekaran*, and Moghtada Mobedi*,	Energies, 2022, 15, 8952, Impact factor: 3.2 (Q1)	26 November 2022	1
2	“Performance evaluation of single pass solar air heater with stepped type arrangement of metal foam by a numerical study”, (FMFP2022 –752)	Rawal Diganjit Shashikant, Dr N. Gnanasekaran*,	Proceedings of the 9th International and 49th National Conference on Fluid Mechanics and Fluid Power (FMFP) IIT Roorkee, Roorkee-247667, Uttarakhand, India.	December 14-16, 2022,	3
3	Experimental study on thermal performance of single-pass solar air heater using Hexagonal Aluminium wire mesh by forced convection.	Rawal Diganjit, N, Gnanasekaran*,	International conference on recent “Advances in modelling and analysis of thermal and energy systems” (RAMATES-2023), Department of Mechanical Engineering, NIT Karnataka, Surathkal, Mangalore, Karnataka, India, 575025.	10-12 May 2023	3

4	“Thermohydraulic Efficiency of a Solar Air Heater in the Presence of Graded Aluminium Wire Mesh—A Combined Experimental–Numerical Study”, https://doi.org/10.3390/en16155633 .	Rawal Diganjit, N. Gnanasekaran*, and Moghtada Mobedi*,	Energies, 2023, 16(15), 5633. Impact factor: 3.2 (Q1)	26 July 2023	1
5	“Numerical study for enhancement of heat transfer rate in single pass solar air heater using stepped arrangement of metal foam with varying the distances from absorber plate and glass”, (ISTP33 -10).	Rawal Diganjit, N, Gnanasekaran* and Moghtada Mobedi*,	The 33rd International Symposium on Transport Phenomena, Kumamoto, JAPAN.	24-27 September 2023	3
6	Energy, exergy, and economic analysis of single pass solar air heater comparing transverse and longitudinal direction graded aluminium wire mesh for drying Onion and Tomato	Rawal Diganjit, N, Gnanasekaran*	Energy (Submitted) Impact factor: 9 (Q1)	-	-

Category* 1: Journal paper, full paper reviewed

2: Journal paper, Abstract reviewed

3: Conference /Symposium paper, full paper reviewed

4: Conference /Symposium paper, Abstract reviewed

5: Others (including paper in workshop, NITK Bulletin, short notes etc.)

Rawal Diganjit Shashikant

Research Scholar

Dr. Gnanasekaran N

Research Guide

BIO-DATA

Name : Shri. Rawal Diganjit Shashikant.
 Date of Birth : 07/08/1989
 Nationality : Indian
 Marital status : Married
 Address : Plot No.8, 111/2, bypass road, Jaysingpur,
 Sambhaji Nagar, Tal- Shirol, Dist.
 Kolhapur, Maharashtra, India. 416101.
 Mob No : 9422532795
 E-Mail ID : rawaldiganjitshashikant.207me027@nitk.edu.in,
diganjitrawalgpn@yahoo.com



Details of Educational Qualifications: -

Sr. No.	Exam	Institute	Board/ University	Subject /Specialization	Year of passing	% of Marks / CGPA	Class Award
01	Ph.D.	National Institute of Technology, Karnataka, Surathkal, Mangalore, Karnataka, 575025, India	Government, Autonomous	Mechanical (Solar air heater)	-	8.25	First class with Distinction
02	ME	JSPM, Jaywantrao Sawant College of Engineering Hadapsar, Pune Maharashtra 411028, India.	Pune	Design Engineering	2013-2016	8.03	First class with Distinction
02	BE	JSPM, Jaywantrao Sawant College of Engineering, Hadapsar, Pune Maharashtra 411028, India.	Pune	Mechanical Engineering	2007-2011	67.63	First class with Distinction

Details of Employment: -

Sr. No.	Organization	Designation	Duration	Period (Years)	Work Done in Brief
01	Government Polytechnic Nashik, Maharashtra, 422101, India.	Lecturer in Automobile Engineering	24/01/2012 to Till date	12.3	Teaching
02	Jaywantrao Sawant Polytechnic, Hadapsar, Pune, Maharashtra, 411028, India.	Lecturer in Mechanical Engineering	16-09-2011 To 23-01-2012	0.34	Teaching